Durham E-Theses

Dust-enshrouded AGN: Implications for cosmological backgrounds

Gunn, Katherine Frances

Dust-Enshrouded AGN:

Implications for

Cosmological Backgrounds

Katherine Frances Gunn

A thesis submitted to the University of Durham

in accordance with the regulations for

admittance to the Degree of Doctor of Philosophy.

Department of Physics

University of Durham

February 19, 1999

Preface

The work described in this thesis was undertaken between 1995 and 1999 whilst the author was a research student under the supervision of Dr Tom Shanks in the Department of Physics at the University of Durham. This work has not been submitted for any other degree at the University of Durham or at any other University.

The work presented in the thesis is the author's own, unless where stated explicitly otherwise. Much of the work is based on the source catalogue from the Deep *ROSAT* Survey Collaboration, whose members include Drs Tom Shanks, Brian Boyle, Ioannis Georgantopoulos, Omar Almaini, Richard Griffiths, Gordon Stewart and Nathan Roche.

A number of the results presented here have appeared in the following papers:

Gunn K.F. & Shanks T., 1998, Astronomische Nachrichten, 319, 66.

Gunn K.F. & Shanks T., 1999a, Advances in Space Research, in press.

Gunn K.F. & Shanks T., 1999b, MNRAS, submitted.

Dust-Enshrouded AGN: Implications for Cosmological Backgrounds

Katherine Frances Gunn

Abstract

The goal of this thesis is to develop an obscured AGN model for the X-ray background (XRB), and then to test the model via its predictions for the intensity of the cosmic background in the far infra-red, and by searching for obscured nuclei in individual X-ray sources in the near infra-red.

A model invoking populations of obscured QSOs with a flat distribution of absorbing columns is found to give a good fit to the X-ray source counts and to the XRB spectrum. The model also accommodates the recent detection of a population of narrow-line X-ray galaxies, identifying them as low-luminosity obscured AGN. We investigate the selection effects present in optical QSO samples, and find that absorption in both the X-ray and optical wavebands combine to produce the tight observed X-ray/optical correlation, while still allowing a wide range of intrinsic column densities. X-ray sources with no obvious optical counterparts are predicted by this model, with a frequency in agreement with the numbers of these 'blank field' sources found in deep *ROSAT* surveys. We predict that in forthcoming *AXAF* surveys, $\sim$ 50 per cent of the sources detected will be optically blank and lie at $z \gtrsim 1$. Obscured QSOs are estimated to outnumber unobscured QSOs by a factor of at least four to one. At longer wavelengths, we make a conservative prediction that obscured QSOs can account for approximately ten per cent of the sub-mm number counts and the far infra-red background, which is a modest, but non-negligible fraction.

We then make observations to determine the extent of dust reddening in X-ray galaxies and QSOs, in the light of predictions of our obscured QSO model. We present $K-$band imaging of *ROSAT* and *ASCA* X-ray luminous galaxies and blank field sources. A trend is observed between the hardness of the X-ray spectra and the occurrence of red, unresolved counterparts, consistent with an obscured QSO origin for the X-ray emission. Near infra-red spectroscopy of X-ray luminous galaxies is then presented, searching for broad Pa_α emission lines. A broad line is possibly detected in one of six galaxies observed, which would indicate AGN activity. From far infra-red *ISO* photometry of X-ray galaxies and QSOs, we detect emission at $\sim$ 100μm from six narrow-line galaxies at low redshift, and from a Type 2 QSO at higher redshift. For at least two of the low redshift galaxies, there is clear proof of AGN activity on the grounds of X-ray variability and near infra-red spectroscopy. This, together with the 100μm detections, forms conclusive proof of the presence of dust-enshrouded AGN in at least some X-ray galaxies, supporting the obscured QSO explanation for the cosmic X-ray background.

Acknowledgments

"Mice, says Yuri Sen, steal eggs in pairs - pairs of mice, that is, not pairs of eggs - one will lie flat on its back, clutching the egg with its paws against the cushion of its belly, while the other takes its tail and drags his partner back to the nest.

I was not aware, I answer, that mice had any use for eggs? What on earth would they do with them?

Cheese omelettes, no doubt, replies Yuri Sen."

— *Moonlight into Marzipan,* Sunetra Gupta.

The centipede was happy, quite,

  Until a toad in fun

Said, "Pray, which leg goes after which?"

  This worked his mind to such a pitch,

He lay distracted in a ditch,

  Considering how to run.

— Ancient Chinese poem.

Contents

Chapter 1

Introduction

ABSTRACT. In this Chapter, we give a short overview of the history of X-ray astronomy, and a discussion of the nature of the X-ray background radiation (XRB). The properties of active galactic nuclei are described, in relation to their known significant contribution to the XRB, and currently favoured obscured AGN models are compared with alternative models for its origin. The content and structure of the thesis is then outlined.

1.1 Brief History of X-ray Astronomy

The era of X-ray astronomy began with a rocket flight in June 1962, aimed at detecting reflected solar X-rays from the Moon (Giacconi et al. 1962). The rocket carried three Geiger counters and measured the changes in count rate over the rotation period of the rocket, detecting an unexpected localised source of soft X-rays. This source was not consistent with the position of the Moon or any other known solar system objects, and was in addition to an isotropic diffuse background, which dominated any possible contribution from the direction of the Moon. This first extra-solar source to be discovered was in the constellation Scorpio, and was named Sco X-1. In these early rocket- and balloon-borne observations, the sources detected were primarily X-ray binary stars such as Cyg X-1, Cen X-3 and Her X-1, and pulsars such as the progenitor of the Crab Nebula. By 1966, there were seventeen known X-ray sources other than the Sun. Only one of these sources was later classified as extragalactic, when it was found to be associated with M87 and the Virgo Cluster[1]. But X-ray astronomy really "took off" with the launch in 1970 of the first dedicated X-ray satellite, *Uhuru*, which had the aim of completely mapping the X-ray sky for the first time. Many more discrete sources were soon discovered, including extragalactic sources such as active galactic nuclei (AGN), quasi-stellar objects (QSOs), and clusters of galaxies.

Initially, X-ray telescopes had very little spectral or spatial resolution, and were in essence just high-energy photon counters. In addition, the available rocket technology put constraints on the

---

[1] M87 is the galaxy at the centre of the cluster of galaxies in the constellation Virgo.
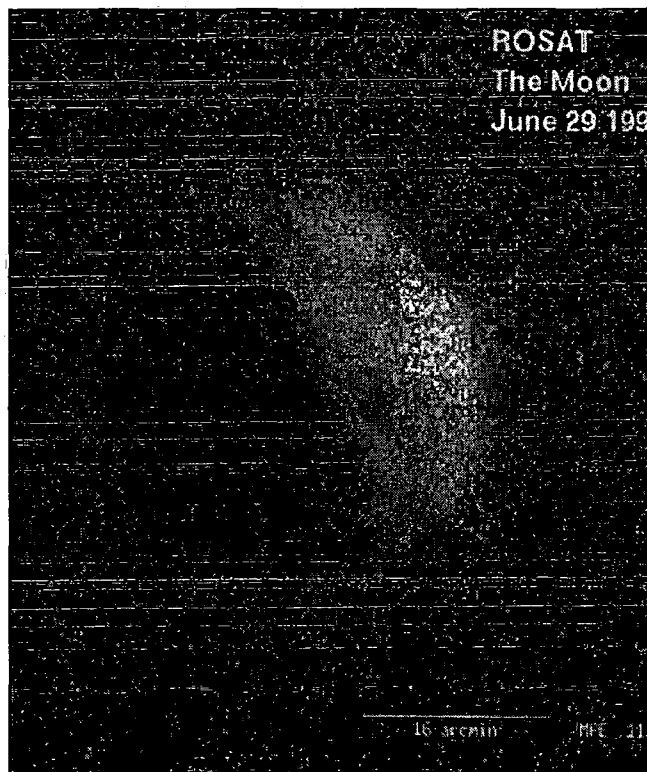
Figure 1.1: The Moon in X-rays: A *ROSAT Position Sensitive Proportional Counter* (*PSPC*) image of the Moon in soft X-rays, showing reflected solar X-rays on the bright side of the Moon, and the dark side of the Moon casting a shadow on a diffuse background radiation (Schmitt et al. 1991).

size of payload, and therefore the types of detectors that it was possible to raise above the Earth's atmosphere. But the development of new types of detector and superior mirror technology, coupled with advances in rocket science, led to huge progress in the field of X-ray astronomy. The recently deceased *Röntgen Observatory Satellite*, known as *ROSAT* (Trümper 1982, 1990), provided the first high resolution images of the soft $0.1 - 2.4 \, \mathrm{keV}$ X-ray sky. The *Advanced Satellite for Cosmology and Astrophysics, ASCA* (Tanaka, Inoue & Holt 1994), sensitive to soft and hard X-rays in the range $0.5 - 10 \, \mathrm{keV}$, was launched in 1993, enabling spectroscopic observations of faint X-ray sources with unprecedented sensitivity, and medium resolution imaging of the hard X-ray sky. More recently, the Italian/Dutch satellite *BeppoSAX*[2] (Boella et al. 1997) was launched in April 1996, with imaging capabilities below $10 \, \mathrm{keV}$, and a wide spectral coverage from $0.1 - 200 \, \mathrm{keV}$.

Future X-ray satellite missions due to be launched over the next couple of years offer the prospect of even greater advances in our knowledge of X-ray astrophysics. New types of detectors provide increased spatial and spectral resolution; modern mirror design and technology produce enormous photon collecting areas and sensitivity to very faint sources; and launch facilities using

---

[2] *BeppoSAX: Satellite per Astronomia X "Beppo"*, named in honour of Giuseppe "Beppo" Occhialini.
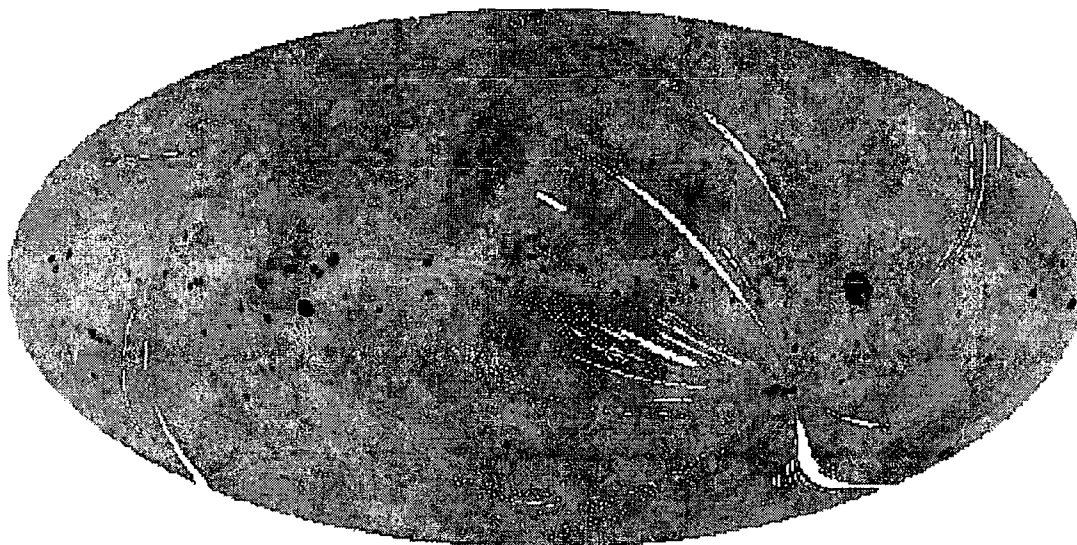
Figure 1.2: The *ROSAT* All-Sky Survey image of the entire sky in 0.1 − 2 keV soft X-rays, which was taken during the first six months of the *ROSAT* mission, 1990-91. The image is presented in an Aitoff-Hammer equal-area projection in Galactic coordinates with the Galactic centre in the middle of the image and longitude increasing to the left. Bright galactic sources along the Galactic plane and the zodiacal component can clearly be seen, with diffuse background emission dominating towards the Galactic poles. Image courtesy of MPE & S.L. Snowden.

powerful rockets or the Space Shuttle enable the resulting large observatories to be put into the required orbit. The *Advanced X-ray Astrophysics Facility, AXAF*[3], is due to be launched by NASA in mid-1999, and will have an imaging capability in 0.4 − 6 keV X-rays, comparable to that currently possible with ground-based optical telescopes. The *X-ray Multi-Mirror Mission, XMM*, is an ESA project due for launch in early 2000, which has three X-ray telescope modules, each containing 58 nested concentric mirrors. *XMM* will provide unprecedented collecting area for high resolution spectroscopy of faint sources, combined with good spatial resolution from 0.1 − 10 keV over a 30′ diameter field-of-view. Also to be launched in 2000 is the Japanese satellite, *Astro-E*, which will have outstanding spectral resolution over a wide bandpass. The use of micro-calorimeters to determine the photon energy, rather than more conventional dispersive techniques, gives an energy resolution of ∼ 12 eV FWHM[4] in the 0.4 − 10 keV energy range. This observatory also will have imaging capabilities in the 0.4 − 10 keV energy band over a similar field-of-view to *AXAF*, and a high energy detector which is sensitive up to 700 keV, enabling a wide range of astronomical applications.

The increased sensitivity made possible with the most recent X-ray telescopes has allowed the detection of increasingly faint discrete X-ray sources. However, once the contribution from

---

[3] *AXAF*: Recently renamed *Chandra*, in honour of the astrophysicist Subrahmanyan Chandrasekhar.
[4] FWHM: Full Width at Half Maximum.
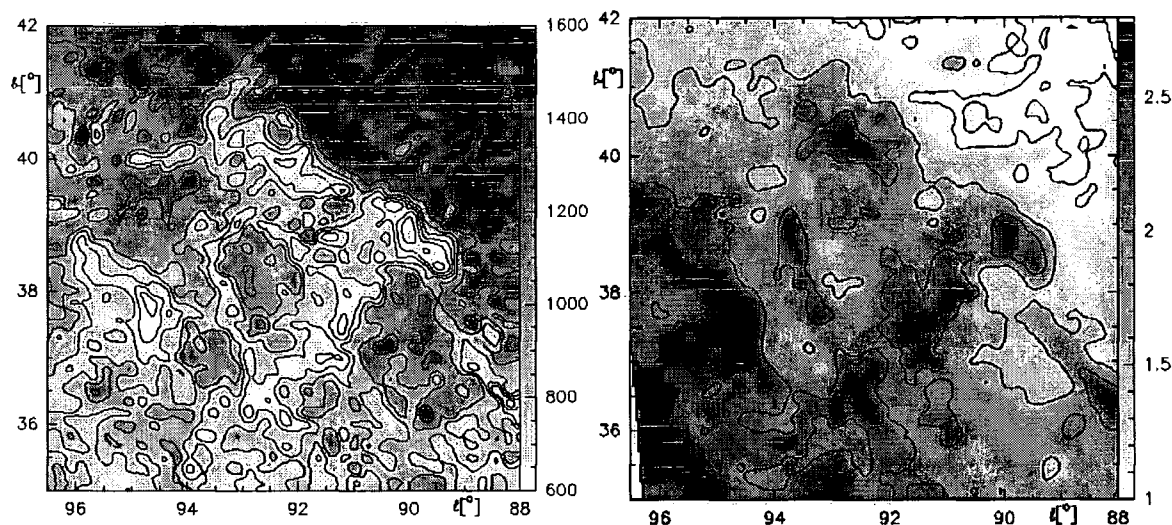
Figure 1.3: Shadowing of the 0.25 keV X-ray background by the Draco nebula (Moritz et al. 1998). The left hand panel shows a map of the Draco region taken from the *ROSAT* All-Sky Survey, where the dark areas correspond to the highest intensities. The right hand panel shows a contour map of the neutral hydrogen column density in the same region, again where dark areas indicate the highest densities. Note that the regions of lowest X-ray intensity are where the HI column density is highest, showing that the Draco nebula casts a shadow on the X-ray background.

these resolved sources is subtracted, there remains the residual strong isotropic component first detected by the 1962 rocket flight, which prompts the question as to where this emission originates. The knowledge that this background radiation is external to the solar system is illustrated in Fig. 1.1, which is an image of the Moon in X-rays, taken by *ROSAT* (Schmitt et al. 1991). The bright side of the Moon can be clearly seen in back-scattered solar X-rays, whereas the dark side casts a shadow on the isotropic background radiation, which therefore must originate from a point further away than the Moon. During the first six months of the *ROSAT* mission, an X-ray survey of the entire sky was undertaken, where the resulting image is shown in Fig. 1.2 (Snowden et al. 1995). This has been an invaluable resource for studies of the nature of the X-ray background. At hard X-ray energies, where the contamination from Galactic emission is low, it is straightforward to subtract the contribution due to resolved sources, and find that the remainder of the X-ray background is isotropic to high accuracy, implying an extra-galactic nature. However, at soft X-ray energies, hot gas within a local "super-bubble" dominates the emission, and therefore more subtle methods must be used to determine the origin of any isotropic component. *ROSAT* observations discovered that high-latitude molecular clouds in our Galaxy also cast shadows on the soft X-ray background, indicating that the source of the emission is more distant than these clouds (Burrows & Mendenhall 1991). Fig. 1.3 shows a map from Moritz et al. (1998) of the Draco nebula region taken from the *ROSAT* All-Sky Survey compared with a neutral hydrogen

column density map of the same area. Dark regions in the 0.25 keV X-ray map, indicating high X-ray counts, correspond to light regions of low HI column density in the other map, and vice versa. Extending this method, Barber, Roberts, & Warwick (1996) discovered that the nearby spiral galaxy NGC 55 also casts a shadow on the soft X-ray background, thereby confirming that it is indeed extra-galactic in origin. However, this does not give any further clues as to the exact cause of the observed emission.

1.2 The Nature of the X-ray Background

Although the X-ray Background (XRB) radiation was the first all-sky radiation field to be detected, some three years before the discovery of the Cosmic Microwave Background (CMB) by Penzias & Wilson (1965), its exact origin is still the subject of much debate (for a review, see Fabian & Barcons 1992). Much of the observed background radiation has already been resolved into discrete sources, primarily associated with X-ray binary stars, pulsars, clusters of galaxies, AGN and QSOs. Once the contribution from these bright sources is removed, there remains a residual component which, at energies below $\sim$ 2 keV, is thought to be dominated by galactic emission, whereas at higher energies, the radiation field is isotropic, indicating an extra-galactic origin. The emission in the energy range 3 − 50 keV has a hard spectrum with a power-law index of $\alpha \sim 0.4$[5] which rolls over above 40 keV. This spectrum is found to be well fitted by bremsstrahlung emission at a temperature of $kT = 40$ keV, and it was initially postulated that this was due to thermal emission from an optically thin plasma, such as hot intergalactic gas. However, the spectrum of the Cosmic Microwave Background would be measurably affected by the presence of such a medium, due to the Compton up-scattering of CMB photons by the hot plasma. *COBE* observations of the CMB spectrum (Mather et al. 1990, 1994) shows that it follows an almost perfect black-body form, which puts a stringent constraint of less than 0.01 per cent on the contribution to the XRB from intergalactic gas. As fainter X-ray flux limits are reached, more and more sources are resolved, and therefore it is now thought that almost all of the XRB is discrete in origin.

With the advent of deep X-ray surveys, the dominant source population was immediately found to be QSOs. In a deep survey of the Pavo region by the *Einstein* satellite, it was found that 60 − 80 per cent of the sources detected in the 0.1 − 4.5 keV band were QSOs or QSO candidates (Griffiths et al. 1983). The *Einstein* Medium-Sensitivity Survey (MSS) and Extended Medium-

---

[5] In this thesis, we shall use the convention for the spectral index described by $f_\nu \propto \nu^{-\alpha}$, in both the optical and X-ray regimes.

Sensitivity Survey (EMSS) found that approximately half of the $\sim$ 800 sources detected were associated with QSOs and Seyfert galaxies (Stocke et al. 1983, 1991). At even fainter flux limits, Bower et al. (1996) identified as QSOs and Seyferts at least 12 out of 18 sources detected in a single deep *ROSAT* pointing. QSOs were found to contribute at least 30 per cent of the XRB intensity at 1 keV (Shanks et al. 1991). A similar result has been found in the higher energy *ASCA* band, where QSOs provide $\sim$ 40 per cent of the 2 − 10 keV XRB (Boyle et al. 1998a).

However, since the average spectral index of QSOs is $\alpha \sim 1$ whereas the background has $\alpha \sim 0.4$, this so-called "spectral paradox" (De Zotti et al. 1982) implies that there must be another component to the XRB. For a long time, there was no known class of source with the right spectral properties required to resolve this paradox. Recently it was realised that one mechanism by which it is possible to obtain a spectral index closer to that of the background is to invoke large populations of obscured AGN. Absorption has the effect of flattening the intrinsic AGN X-ray spectrum, and this effect will be described further in Section 2.2. Nearby Type 2 AGN are known to have hard X-ray spectra, and it is plausible to extrapolate this result and assume that similar sources exist at high redshift. Recent deep X-ray surveys have found that a population of X-ray luminous galaxies starts to dominate the source counts at faint fluxes, and is thought to be responsible for a large fraction of the hard XRB (Roche et al. 1995; Romero-Colmenero et al. 1996; Almaini et al. 1997; McHardy et al. 1998). The X-ray emission mechanism within these galaxies is still uncertain, although obscured AGN and starburst galaxies are the most likely causes. Almaini et al. (1999a) find evidence for an AGN origin in one such faint X-ray galaxy. Significant variability is detected in the X-ray light curve, consistent of that seen in their sample of faint *ROSAT* QSOs, from which they infer that the X-ray emission is due to the presence of an AGN. Current theories favour an obscured AGN origin for the X-ray background.

1.3 The Deep *ROSAT* Survey

1.3.1 Observations

The motivation for the work in this thesis has evolved out of an investigation into the origin of the X-ray background radiation using a deep soft X-ray survey, the Deep *ROSAT* Survey (Shanks et al. 1991). This is a pencil-beam survey of seven pointings, with exposure times between 21 and 57 ks, taken with the *Position Sensitive Proportional Counter* (*PSPC*) on *ROSAT*, which is sensitive to 0.5 − 2 keV X-rays. The regions surveyed were chosen to have low Galactic column density, $N_H < 3 \times 10^{19}$ cm^{-2}, in order to maximise the visibility of extragalactic sources and

Field Name	Field Centre	N_H	ROSAT		ASCA	
	α (J2000) δ	(cm^{-2})	Exp. time	Date	Exp. Time	Date
GSGP4	00 57 28.7 -27 38 24	1.8×10^{19}	49 ks	7/92	50 ks	6/94
SGP2	00 52 04.8 -29 05 24	1.8×10^{19}	25 ks	6/92	50 ks	6/97
SGP3	00 55 00.0 -28 19 48	1.8×10^{19}	21 ks	7/94	50 ks	6/98
QSF1	03 42 09.6 -44 54 36	1.7×10^{19}	26 ks	7/90	50 ks	1/97
QSF3	03 42 14.3 -44 07 48	1.7×10^{19}	27 ks	7/90	109 ks	6, 9/93
BJS855	10 46 24.0 -00 21 00	2.9×10^{19}	57 ks	6, 12/93	50 ks	11/95
BJS864	13 43 43.0 -00 15 00	2.6×10^{19}	52 ks	1/93	50 ks	1/98

Table 1.1. Summary of *ROSAT* and *ASCA* X-ray observations of the Deep *ROSAT* Survey Fields, GSGP4, SGP2, SGP3, QSF1, QSF3, BJS855 and BJS864. For each field, we list the field centre co-ordinates, the Galactic column density, N_H, in the direction of each pointing, and the exposure times and dates of each observation.

minimise contamination by Galactic stars. Therefore, ultra-violet excess (UVX) QSO survey fields were picked (Boyle et al. 1990), three near the South Galactic Pole, SGP2, SGP3 and GSGP4 ($l \simeq 270°, b \simeq -88°$), QSF1 and QSF3 ($l \simeq 250°, b \simeq -52°$), plus two fields at zero declination, BJS855 ($l \simeq 250°, b \simeq 49°$) and BJS864 ($l \simeq 330°, b \simeq 59°$). This survey is unbiased as, although known quasar fields were used, these fields in themselves were originally chosen as unbiased for each respective survey: QSF and SGP – Boyle et al. (1990), and BJS – Boyle, Jones & Shanks (1991). The properties of the X-ray observations taken in these fields are summarised in Table 1.1.

The survey covers a total area of $\sim 2.4 \deg^2$, detecting over 400 sources above a 4σ threshold of $S(0.5 - 2\,keV) \sim 4 \times 10^{-15}\,erg\,cm^{-2}\,s^{-1}$, where the area surveyed is a function of the sensitivity. Optical identifications of the X-ray sources were obtained using the AUTOFIB fibre-fed spectrograph (Sharples, Gray & Hatzidimitriou 1991) on the Anglo-Australian Telescope (AAT). This led to identifications for ~ 60 per cent of the ~ 500 sources in total, as catalogued in Shanks et al. (in preparation).

With the launch of the *ASCA*, which is sensitive to hard X-rays in the range $2 - 10\,keV$, this survey was extended through the acquisition of deep *ASCA* exposures of all seven pointings. A 50 ks exposure was taken of each field, and for QSF3, additional data was available from the archive, making a total of 109 ks. The data are taken with the *Gas Imaging Spectrometer* (*GIS*) instrument on board *ASCA*. Sources are extracted from the inner $20'$ radius of each field to match the *ROSAT* central field of view, to a mean flux limit of $S(2 - 10\,keV) \sim 5 \times 10^{-14}\,erg\,cm^{-2}\,s^{-1}$. Of the three fields analysed so far, a total of 26 sources were detected, as catalogued in Boyle et al. (1998a).

1.3.2 Aims and Results

The primary aim of the Deep *ROSAT* Survey was to determine the nature of the source populations responsible for the soft X-ray background radiation, extending earlier surveys from satellites such as *Einstein* (0.3 − 3.5 keV) and *HEAO-1* (2 − 10 keV). Initial results showed that QSOs contribute between 30 and 50 per cent of the soft XRB (Shanks et al. 1991; Boyle et al. 1994), however the origin of the remainder of the XRB was still unknown. From the sample of X-ray selected QSOs obtained from this survey, the QSO X-ray luminosity function was derived (Boyle et al. 1993), and a limit of $\sim$ 50 per cent was placed on the total QSO contribution to the XRB using isotropy arguments and the known clustering properties of QSOs (Georgantopoulos et al. 1993).

Measurements of the numbers of *ROSAT* X-ray sources as a function of flux showed that while the total number of sources continued to increase towards faint fluxes, the fraction of QSOs and Seyfert 1 galaxies decreased, and their contribution became less important at the very faintest flux limits (Georgantopoulos et al. 1996). Moreover, if extrapolated to higher energies, the soft *ROSAT* source counts were found to lie significantly lower than those observed in hard X-rays. These two facts suggest that there exists an additional source population which dominates at higher energies and fainter fluxes, and which could provide the remaining 50 per cent of the soft X-ray background. A number of the non-QSO *ROSAT* sources are identified with narrow emission-line galaxies, for which the origin of the X-ray emission is ambiguous, and may be due to AGN activity or some other mechanism. Roche et al. (1995) performed a cross-correlation analysis between X-ray sources and $B < 21$ mag galaxies, finding that such galaxies comprise $\sim$ 5 per cent of the X-ray sources. Furthermore, cross-correlating the *ROSAT* X-ray background photons with $B < 23$ mag galaxies from photographic plates, gives a strong signal (5σ), implying that these galaxies contribute $\sim$ 17 per cent of the XRB, or more if extrapolated to fainter galaxy magnitudes. *ROSAT* X-ray luminous galaxies are found to have much harder spectra than QSOs, consistent with the XRB spectrum, and they are therefore postulated as the source of the remainder of the XRB (Almaini et al. 1997).

ASCA observations of the deep *ROSAT* fields confirmed that the hard X-ray source counts are a factor of three above the soft counts (Georgantopoulos et al. 1997), supporting the existence of an additional population of X-ray sources making a significant contribution to the hard XRB. Follow-up of unidentified *ASCA* sources in the first three fields to be observed, yielded the result that half of the 26 sources were broad-line QSOs, and a further six sources were associated with narrow emission-line galaxies, with a combined contribution to the 2 − 10 keV XRB of 50 − 80 per cent (Boyle et al. 1998a). One of the brightest *ASCA* sources in a fourth *ASCA* field was identified as

a Type 2 obscured AGN at redshift $z = 0.67$ (Boyle et al. 1998b), suggesting that this population might also contribute to the hard X-ray background.

In the next Section, we therefore describe the properties of QSOs and AGN, in relation to their significant contribution to the X-ray background. In Sections 1.5 and 1.6, we then discuss the relative merits of various proposed models for the origin of the XRB, in particular obscured AGN models, which are invoked in order to explain the observed properties of X-ray sources at both soft and hard energies.

1.4 Multiwavelength description of Active Galactic Nuclei

1.4.1 The Nucleus: Black Holes and Accretion Discs

With the advent of satellite-borne X-ray telescopes came the first detections of AGN and QSOs at X-ray energies. Previously, the only extra-solar sources had been X-ray binary stars, with luminosities of $L_X \sim 10^{37}\,\mathrm{erg\,s^{-1}}$, and supernova remnants, with $L_X \sim 10^{35}\,\mathrm{erg\,s^{-1}}$. The enormous luminosities found for QSOs, $L_X \lesssim 10^{46}\,\mathrm{erg\,s^{-1}}$, meant that a large and efficient source of energy was required in order to fuel the enormous output of these objects. It was realised that it would be extremely difficult to create this quantity of energy through stellar processes alone: converting rest mass into energy by thermonuclear fusion of hydrogen into helium has an efficiency of only $\epsilon \sim 0.007$. The X-ray emission of AGN is know to be highly variable over a wide range of temporal frequencies (Lawrence & Papadakis 1993). In particular, the X-ray intensity can vary substantially on extremely short time-scales, as shown in Fig. 1.4 for the Seyfert 1 galaxy MCG 6-30-15 (Yaqoob et al. 1997). In some cases, a fluctuation of $\Delta I / I > 1$ is seen in $10^3\,\mathrm{s}$ or less, from which it is possible to infer an upper limit on the size of the emitting region, $R < c\,\Delta T \sim 10^{12-13}\,\mathrm{m}$, where the light crossing time is ΔT, and c is the speed of light. Assuming that QSOs are radiating at the Eddington limit, which is the maximum luminosity attainable before losing mass by radiation pressure:

$$L_{\mathrm{EDD}} = \frac{4\pi G M c m_H}{\sigma_T} = 1.25 \times 10^{38}\,\mathrm{erg\,s^{-1}}\left(\frac{M}{\mathrm{M_\odot}}\right), \qquad (1.1)$$

where m_H is the mass of a hydrogen atom and σ_T is the Thompson cross-section of an electron, a central mass of $10^6 - 10^9\,\mathrm{M_\odot}$ can be inferred[6] from the measured luminosities. Since this mass must be concentrated inside a region much smaller than the size of our solar system, the only feasible state must be that of a black hole. Since accretion onto a compact object is a much more

---

[6] $\mathrm{M_\odot}$ = solar mass unit.
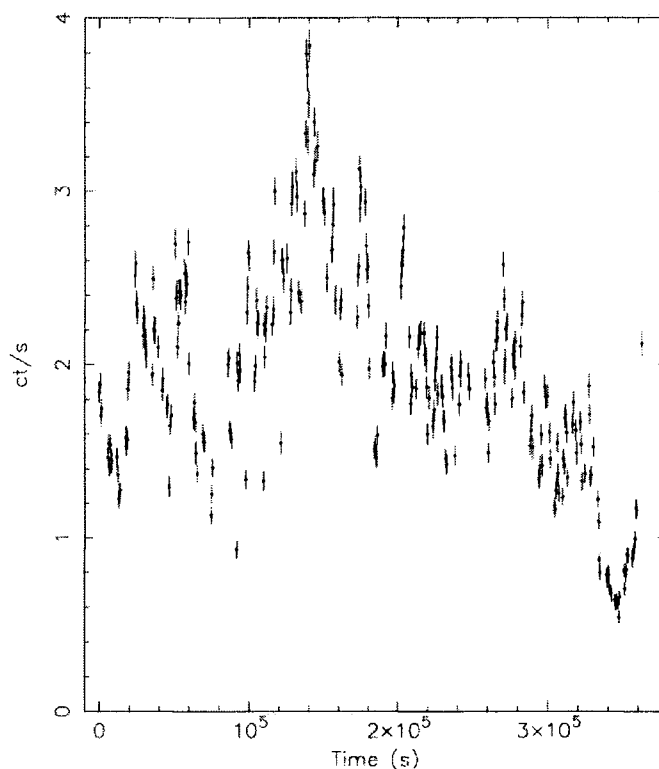
Figure 1.4: The X-ray light-curve of the Seyfert 1 galaxy MCG 6-30-15 showing variability on very short time-scales. The observations, covering a time period of 400, 000 s, are taken with the *SIS 0* detector on board the *ASCA* satellite, in the energy range 0.5 − 10 keV (Yaqoob et al. 1997).

efficient method of converting rest mass into radiation, with $\epsilon \sim 0.1$, this is a much more likely source of QSO luminosity.

To estimate the amount of matter that must be accreted in this manner in order to fuel a QSO, we take the rest mass energy of the Sun, 1.8×10^{54} erg, and using a rest energy to radiation conversion efficiency of $\epsilon = 0.1$, calculate that the accretion of one solar mass per year corresponds to a luminosity of 5.7×10^{45} erg s^{-1}. Therefore, for AGN luminosities in the range $L = 10^{42-47}$ erg s^{-1}, accretion rates of $10^{-4} - 20 \, M_\odot \, \mathrm{yr}^{-1}$ are implied.

The principle of conservation of momentum requires that in order for such accretion to occur, any matter falling into the black hole must first lose its angular momentum. The matter therefore forms a disc around the black hole, which enables angular momentum to be lost outwards, and matter to be transferred inwards, in the process losing vast amounts of energy and thereby fuelling the AGN emission. An accretion disc around a black hole is thought to be geometrically thin, *i.e.*, the thickness or height of the disc is much smaller than its radius, and optically thick, *i.e.*, a photon
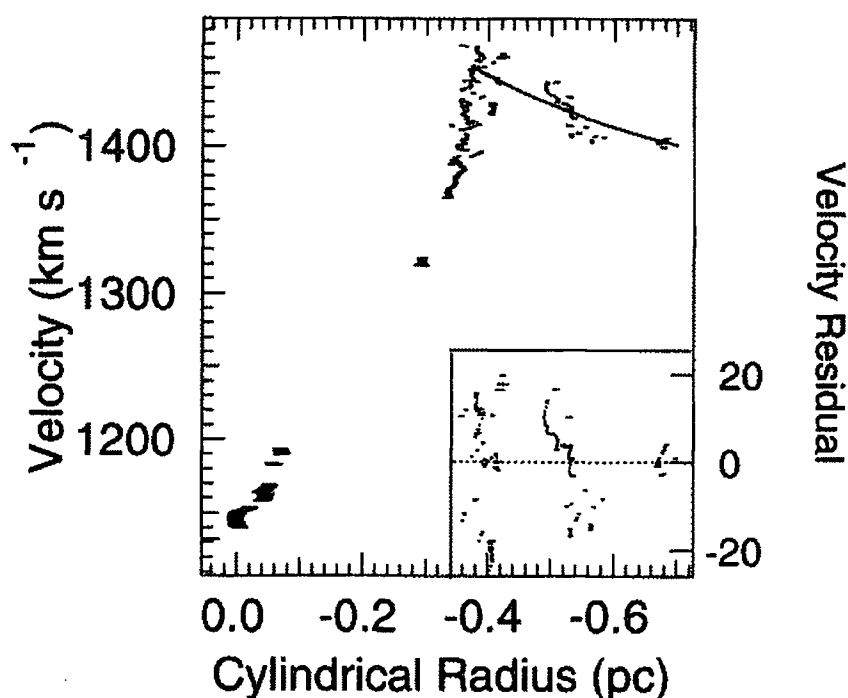
Figure 1.5: The position-velocity relationship of the maser emission in NGC 1068, taken from Greenhill et al. (1996), showing the Keplerian motion of the very inner regions of the AGN. The inset panel shows the residuals to the fitted curve.

hitting the disc will be either absorbed or scattered on average. The motion of the disc is thought to be Keplerian, for which:

$$v_{circ} = \left(\frac{GM}{R}\right)^{\frac{1}{2}}.$$

(1.2)

Although this motion has not been detected directly on the scale of the accretion disc, Keplerian motion has been observed at larger scales via the detection of velocity gradients in water maser emission, for example in NGC 4258 (Greenhill et al. 1995) and NGC 1068 (Greenhill et al. 1996; see Fig. 1.5), and it is thought that this can be extrapolated towards the smaller radii occupied by the accretion disc. Since there is differential rotation within the disc, shear forces occur between material at adjacent radii, creating the required viscosity. In addition, since material closer in to the black hole is moving much more rapidly, it has a much higher temperature than material further out. The superposition of black body radiation of different temperatures at different positions in the disc creates the observed "big blue bump". Thermal arguments predict that for AGN, the average temperature of the accretion disc will be of the order of 10^5 K, or $\sim 10\,\text{eV}$, which means that the bulk of the direct emission will be in the ultra-violet part of the spectrum.

1.4.2 Emission line properties

The most striking feature of AGN at optical wavelengths is the presence of strong emission lines. These can be used to divide AGN into two categories: those which have both broad emission lines (FWHM $\gtrsim$ 1000 km s^{-1}) and narrow emission lines (FWHM $\lesssim$ 1000 km s^{-1}); and those which have narrow lines only (Osterbrock 1989). At low redshift, these types of objects are classified as Seyfert galaxies, where Type 1 Seyfert galaxies (Sy 1, hereafter) present both broad and narrow emission lines, and Type 2 Seyfert galaxies (Sy 2) present only narrow lines. Examples of typical Type 1 and Type 2 spectra are shown in Fig. 1.6. The definition of a QSO requires the presence of broad emission lines with FWHM $\gtrsim$ 1000 km s^{-1} and an absolute magnitude of $M_B < -23$. If the width of these lines is interpreted as a velocity dispersion due to Doppler broadening, then it can be inferred that the emission regions are at different distances from the central black hole, with the broad line region (BLR) closer in, and therefore with material moving at faster speeds, and the narrow line region (NLR) further out. It is thought that these regions contain clouds of material irradiated by emission from the nucleus, which excites the atoms present. These atoms then de-excite, emitting line radiation.

The species of lines present can give information on the conditions prevailing in the emission regions. For example, narrow emission lines of certain "forbidden" transitions can be detected, so-called because under most circumstances, these lines are extinguished by collisional de-excitation and are never seen. A upper limit can therefore be placed on the density of the emission region, so that collisional effect are negligible, and we therefore obtain $\rho_{NLR} < 10^{5-10}$ cm^{-3}, depending on the transitions seen. However, the only broad lines detected are for "permitted" transitions, and therefore this emission region is more dense, with $\rho_{BLR} > 10^{9-10}$ cm^{-3}. In addition, the presence of huge quantities of X-ray and ultra-violet emission creates very highly ionized species, which are a useful diagnostic, as they are only seen in the extreme environments present in AGN. These are often called "coronal" lines, such as [Si VI] at 1.96μm.

1.4.3 The Unified Model of AGN

The narrow line properties of Sy 1 and Sy 2 galaxies are to first order very similar, and it was therefore postulated that the differences between the two classes was due to the orientation of the line of sight to the nucleus. This is the so-called "Unified Model of AGN" (Antonucci 1993), in which it is proposed that in Type 2 objects the BLR, lying close in to the nucleus, is hidden by obscuring matter in the line of sight, whereas the NLR is external to this obcuration, and therefore is visible in both classes. The geometry of this matter is taken to be toroidal for convenience, and
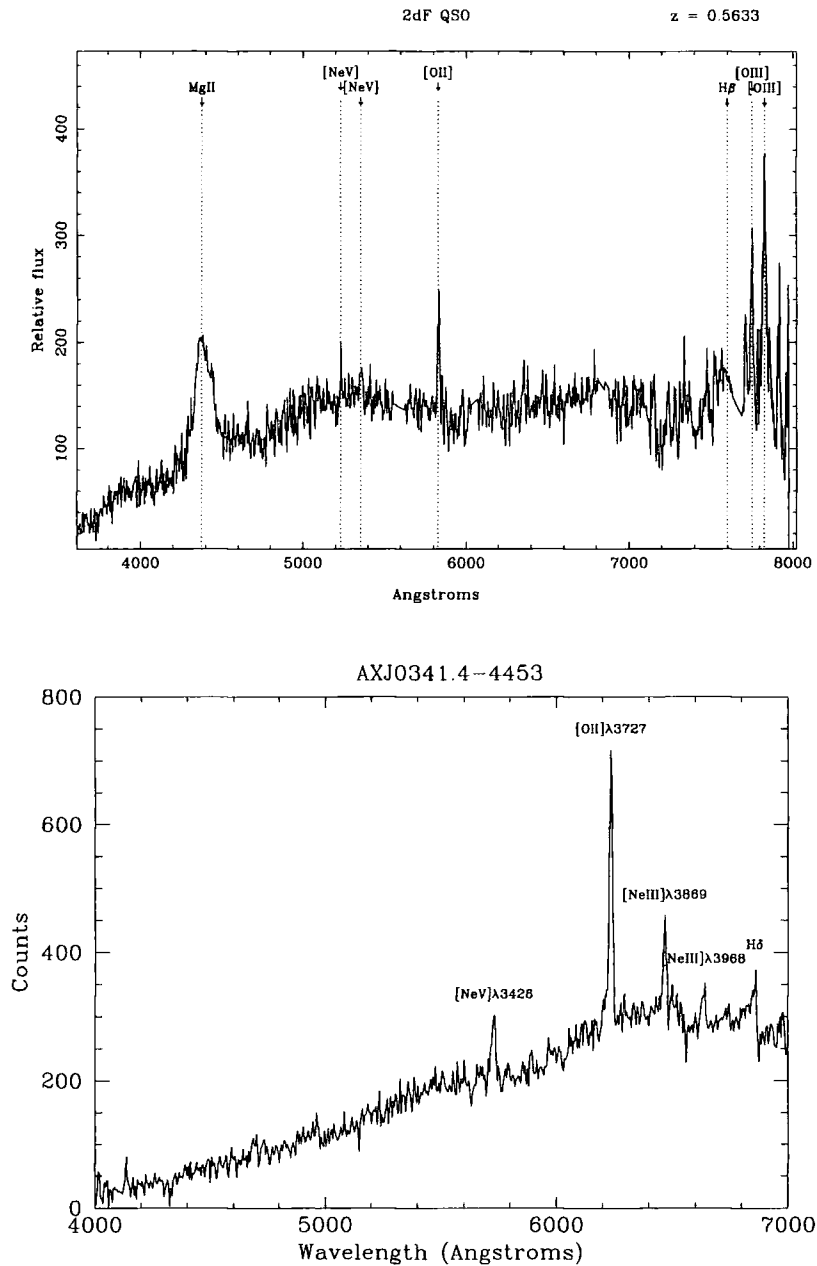
Figure 1.6: Optical spectra illustrating the differences between the broad and narrow emission lines properties of Type 1 and Type 2 objects. The upper panel shows the spectrum of a redshift $z = 0.563$ QSO from the 2dF QSO Survey (Croom 1999, private communication). A broad MgII λ2798 emission line can clearly be seen, showing that this is a Type 1 object. Broad H_β is also present, although affected by sky absorption bands. Narrow emission lines of [OII] λ3727 and [OIII] λ4959, λ5007 can be seen, and in addition, [NeV] emission lines which are only present in the spectra of AGN. The lower panel is the Sy2 galaxy, AXJ0341.4-4453, discovered in a deep *ASCA* survey by Boyle et al. (1998b). The galaxy is at redshift $z = 0.672$, and presents narrow emission lines of [OII] λ3727, [NeIII] λ3869, [NeIII] λ3968 and H_δ. The presence of strong [NeV] emission indicates that this object is an AGN, and the absence of broad MgII λ2798, confirms that this is a Type 2 object.

Scattered X-ray Spectrum
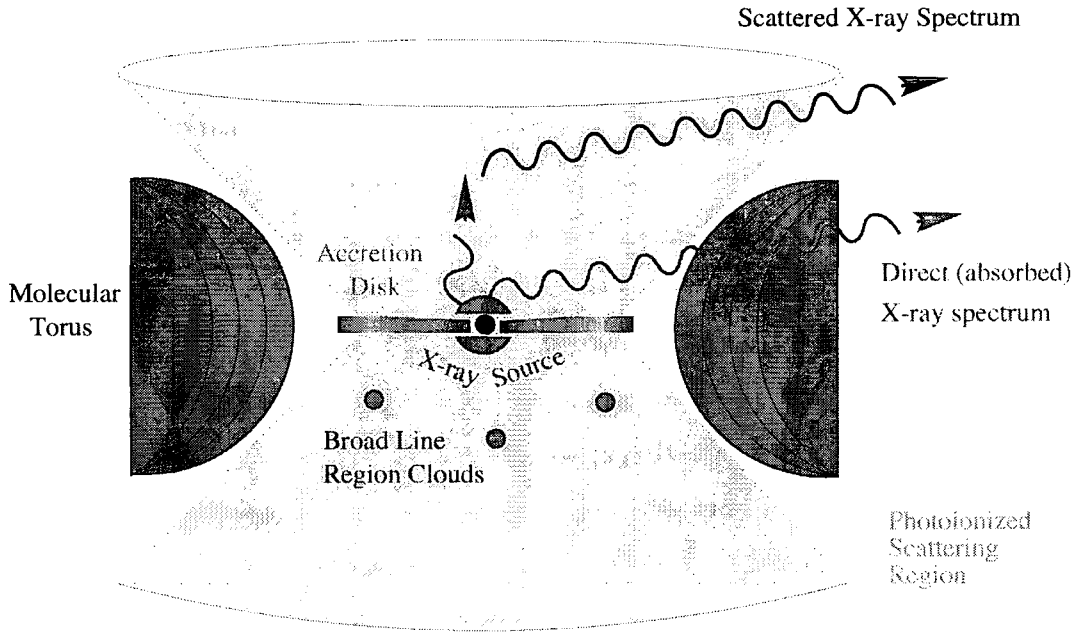
Figure 1.7: Schematic diagram of the Unified Model of AGN, showing the relationship between the nuclear X-ray source, accretion disc, broad line region, molecular torus and photo-ionized scattering medium. The narrow line region is on much larger scales than this diagram. Possible photon paths are also shown, illustrating that a photon may be absorbed, scattered, or escape directly. Figure courtesy of C. Done.

Incident X-rays   6.4 keV Fe Kα fluorescence line

Optically thick material
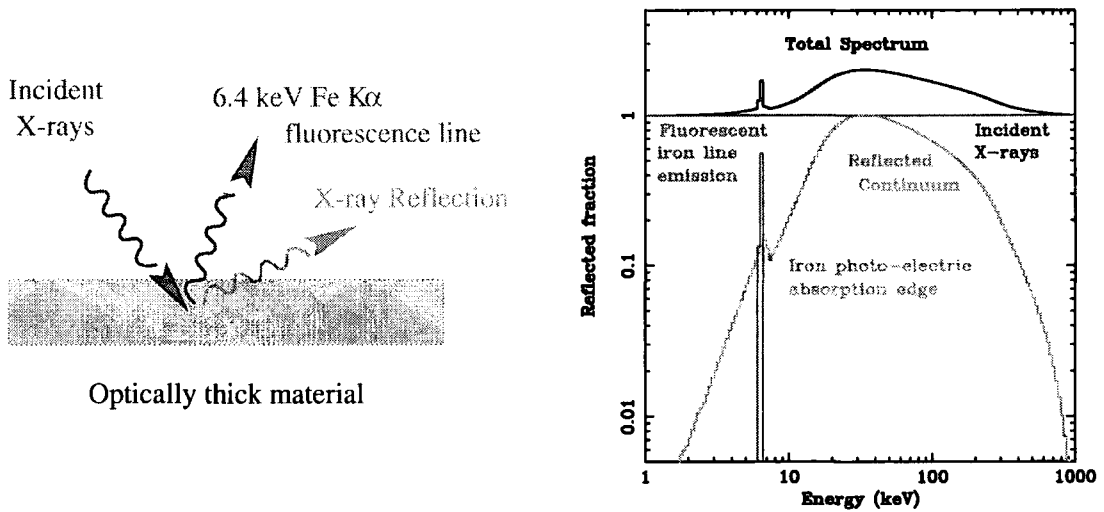
Figure 1.8: Schematic diagram showing the origin of the reflection spectrum seen in X-ray observations of AGN. X-ray photons impinge on optically thick material in the accretion disc, and are reprocessed. At low energies, the photons are mostly absorbed, and their energy goes into ionizing the accretion disc. At 7.1 keV, an absorption edge due to neutral iron atoms can be seen, plus the emission line at 6.4 keV from the resulting iron K_α transition. As the photon energy approaches the rest mass energy of an electron, the process of Compton down-scattering becomes important, by which photons lose energy through collisions with free electrons, thereby removing the highest energy photons, and creating a "bump" at around 30 keV. Figure courtesy of C. Done.
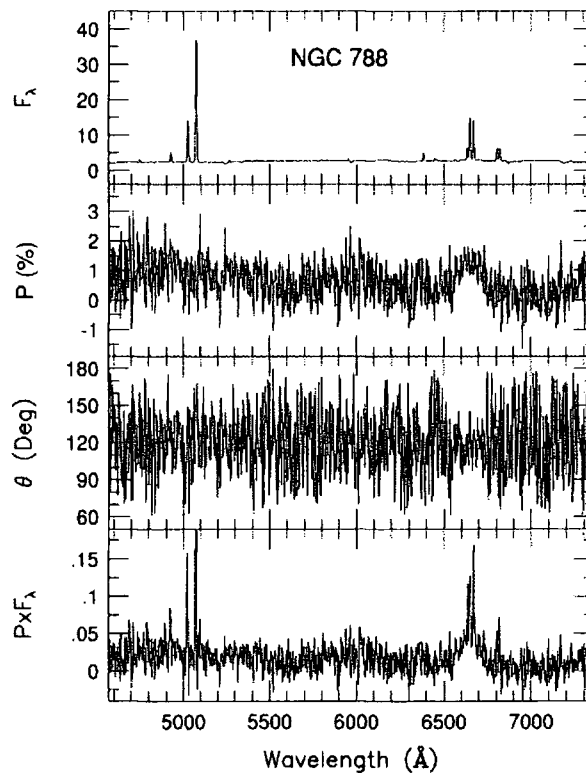
Figure 1.9: Spectropolarimetric observations of the Seyfert 2 galaxy, NGC 788, showing the detection of a broad H_α emission line in the polarized flux spectrum, which indicate the presence of an obscured Seyfert 1 nucleus (Kay & Moran 1998). The top panel contains the spectrum of the galaxy in total light, where the strong narrow emission lines typical of a Seyfert 2 galaxy can be clearly seen; the second and third panel show respectively the percentage polarization and the polarization position angle, as a function of wavelength; and the bottom panel gives the spectrum of the polarized light, with the broad H_α emission line.

for most purposes this is an adequate description. However, a more realistic picture would require a more sophisticated geometry and the structure is likely to be stratified with a range of different properties.

A schematic picture of the Unified Model of AGN is shown in Fig. 1.7. Here, the black hole is surrounded by a coronal emission region, from which the X-radiation emanates, and either escapes immediately or impinges on the accretion disc and is reprocessed, producing the X-ray reflection spectrum shown in Fig. 1.8. Close in to the nucleus are clouds of material in the broad line region, producing broad emission lines at optical wavelengths. If this emission is viewed within the opening angle of the torus, a Type 1 object is seen, whereas if the line of sight to the nucleus passes through the torus, an absorbed, or Type 2, spectrum is observed. The narrow line region lies at a larger distance from the nucleus, not shown on this diagram, and is therefore unaffected by the obscuration.

Evidence for the Unified Model was strengthened by the detection of broad emission lines in polarized light in the spectrum of the Sy 2 galaxy NGC 1068 (Antonucci & Miller 1985), showing that a Sy 1 nucleus did indeed exist in the galaxy, but was not visible in direct emission from the nucleus. This result was confirmed by the detection of the broad-line region in a further four Sy 2 galaxies by Miller & Goodrich (1990). This effect is explained by a type of periscope effect, by which emission from the nucleus escapes through the opening angle of the torus and is then scattered into our line of sight by diffuse material surrounding the central regions (see Fig. 1.7). Electron scattering in an ionized medium causes polarization in scattered radiation, and since this medium is in the intense radiation field of the AGN, photo-ionization is a likely mechanism. This effect is shown in Fig. 1.9, where for the narrow-line Seyfert 2 galaxy, NGC 788, a broad H_α emission line is detected in polarized light. A fractional classification of AGN can then be defined, according to the degree of obscuration and the types of properties exhibited. By measuring the relative strengths of the broad and narrow components of the H_α line, a Sy 1 will be dominated by the broad emission, a Sy 2 will have only a narrow line, and a Sy 1.5 will have broad and narrow H_α components of equal strength.

A further consequence of this model is that the torus, which is made up of molecular gas and dust, absorbs large quantities of X-ray and ultra-violet radiation, heats up, and re-radiates this energy as a quasi-black body at far infra-red wavelengths. This has implications on the origins of the extragalactic background radiation and source counts in the far infra-red/sub-mm part of the spectrum. The effects of an obscuring torus on the observed AGN spectrum are described in more detail in Sections 2.2, 3.2 and 4.3, in the X-ray, optical and sub-mm wavebands respectively.

1.4.4 Properties of Radio-Loud AGN

Approximately ten per cent of AGN have strong radio-emission associated with jets from the nucleus. The unified picture holds for such radio-loud AGN, where the properties are the same as for radio-quiet AGN but with the addition of a jet. Radio emission from the jet can be seen whatever the incident angle, whereas many other observed properties of AGN depend significantly on the viewing angle. If the line of sight to the nucleus is within the opening angle of the jet, a blazar or BL Lac will be seen, for which relativistic beaming totally dominates the emission. When the line of sight is within the opening angle of the torus but not of the jet, this gives a Type 1 radio-loud AGN or QSO. If the nucleus is obscured fully by the torus, then the object will be classified as a radio galaxy. However, as most of the sources under consideration in this work are selected using X-ray techniques, we will usually only be concerned with radio-quiet AGN.
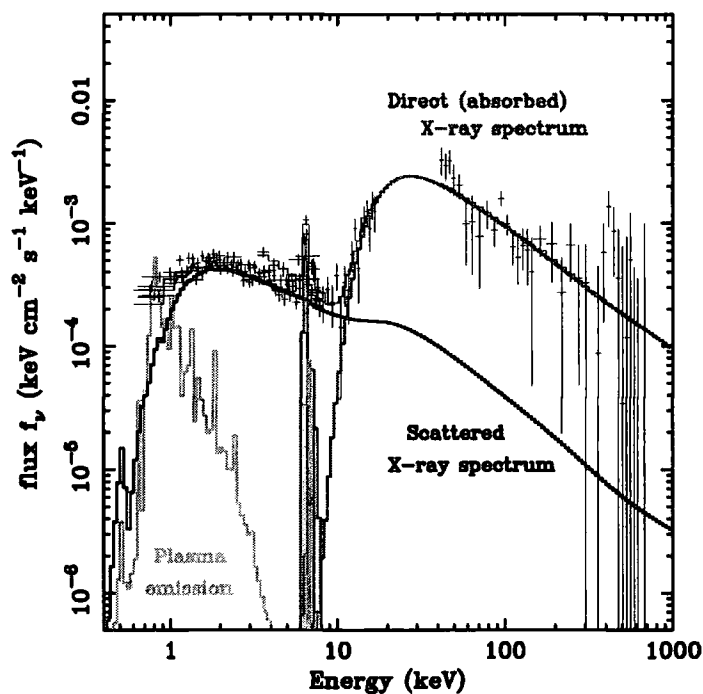
Figure 1.10: The broad-band X-ray spectrum of NGC 4945, a local example of an obscured AGN (Done, Madejski & Smith 1996). The components making up the spectrum are the direct (absorbed) flux, emerging at energies $\gtrsim 10$ keV, a scattered component below 10 keV which has also undergone reflection, plus a contribution from a Raymond-Smith hot plasma below 3 keV. The total spectrum is then compared with the data from *ASCA*, *Ginga* and *OSSE*. Figure courtesy of C. Done.

1.5 Obscured AGN Models for the X-ray Background

The size of the obscured AGN contribution to the XRB is still highly controversial. Madau, Ghisellini & Fabian (1994) and Comastri et al. (1995), have modelled the XRB from 2 keV to 100 keV using significant populations of obscured AGN. The Madau et al. model uses two populations of objects: unobscured QSOs and heavily obscured QSOs ($N_H \sim 10^{24}\,\mathrm{cm^{-2}}$). The Comastri et al. model uses a more continuous distribution of column densities ($10^{21}\,\mathrm{cm^{-2}} - 10^{25}\,\mathrm{cm^{-2}}$) for the obscured populations. In both models the space density of obscured QSOs is larger than that of unobscured QSOs. Webster et al. (1995) find evidence of a wide dispersion in $B - K$ colours for radio-loud QSOs, possibly caused by reddening from intrinsic dust. However, Boyle & Di Matteo (1995) observe a tight relationship between X-ray and optical fluxes for both X-ray and optically selected QSO samples. The spread in the relation is used to place a limit on the maximum column density present in these objects, and the extinction inferred from these data is at most $A_B = 2$ mag. This is interpreted as implying that the majority of QSOs are unaffected by dust.

The hypothesis that obscured AGN may make a significant contribution to the XRB seems to be very successful in theory, but until recently, very few such objects were actually known, particularly at high redshift, where a large fraction of the emission is known to originate. Local examples of AGN with moderate amounts of obscuration have been known for a while, but when the column density becomes greater than $N_H \gtrsim 10^{23} \, \mathrm{cm}^{-2}$, no radiation escapes directly from the nucleus in the $2 - 10 \, \mathrm{keV}$ range most commonly observed, and such objects are only seen in scattered light, and therefore at a much lower flux level. However, higher energy *Ginga* and *OSSE* observations of the nearby galaxy NGC 4945, which appears to be an unremarkable X-ray galaxy below $\sim 10 \, \mathrm{keV}$, reveal the direct flux from the nucleus to be a factor of ten higher than the scattered flux, showing that this is indeed a heavily obscured AGN (Done, Madejski & Smith 1996). The broad-band X-ray spectrum of NGC 4945, from $0.6 - 500 \, \mathrm{keV}$, is shown in Fig. 1.10.

The feasibility of obscured AGN models for the XRB was reinforced by the discovery of high redshift counterparts of NGC 4945, such as RXJ 1343.4+0001, a $2 \times 10^{45} \, \mathrm{erg \, s}^{-1}$ X-ray source in the Deep *ROSAT* Survey of Shanks et al. (in preparation). In Fig. 1.11, the optical spectrum of RXJ 1343.4+0001 shows narrow Ly_α and C IV emission lines at $z = 2.35$ (Almaini et al. 1995). Further observations in the infra-red, shown in Fig. 1.12, then revealed broad H_α at $2.2\mu\mathrm{m}$ (Shanks et al. 1995, 1996), confirming that this is indeed an obscured QSO, with $N_H \sim 3 \times 10^{21} \, \mathrm{cm}^{-2}$. Follow-up observations using *ASCA* (Georgantopoulos et al. 1999) found that the hard X-ray data were more in agreement with a much larger column density, $N_H \sim 10^{23} \, \mathrm{cm}^{-2}$ for an intrinsic spectral index of $\alpha \sim 0.9$, when combined with the *ROSAT* soft energy data. This can be interpreted in one of two different ways. First, that there is a large obscuring column seen by the X-ray photons, and the soft X-ray emission is only seen through scattering. Although this is not consistent with the more modest amount of absorption inferred from the optical/infra-red extinction, this effect can be explained by high gas-to-dust ratios (Granato, Danese & Franceschini 1997) or high gas metallicities. Alternatively, if the possibility of variability between the *ROSAT* and *ASCA* observations is taken into account, then the data can be fitted by an intrinsically flat spectrum, $\alpha \sim 0.4$, with a moderate amount of absorption, in line with the reddening estimates.

Further examples of obscured QSOs have been found, including a more highly obscured object, AXJ 0341.4-4453, which was discovered by Boyle et al. (1998b) in a deep *ASCA* survey (see the lower panel of Fig. 1.6 for the LDSS spectrum). Although there was no detection in the soft $1 - 2 \, \mathrm{keV}$ band, this source was one of the most luminous objects in the field above $2 \, \mathrm{keV}$, implying a very hard X-ray power-law consistent with an intrinsic spectral index $\alpha < 0.1$, or heavy absorption. Optical spectroscopy revealed that the object had no broad emission lines, but
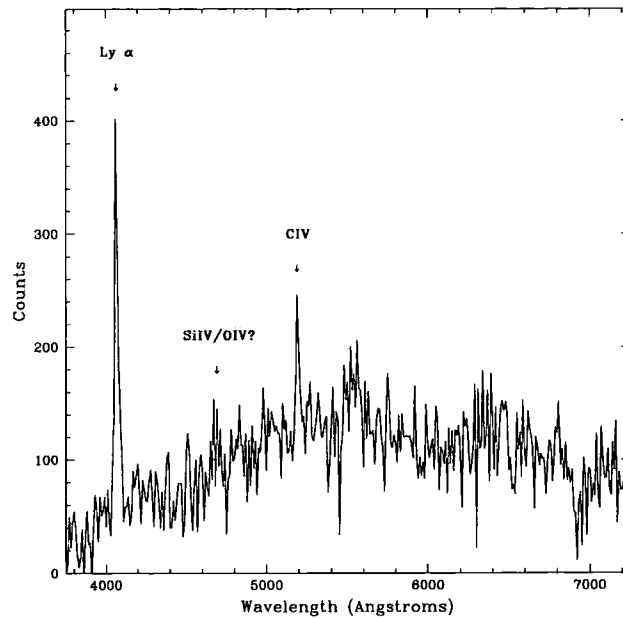
Figure 1.11: Low resolution (12Å) optical spectrum of the obscured QSO RXJ 1343.4+0001, obtained using the AUTOFIB instrument on the Anglo-Australian Telescope. The prominent emission lines of Ly_α and C IV are shown, giving a redshift of $z = 2.35$ (Almaini et al. 1995).
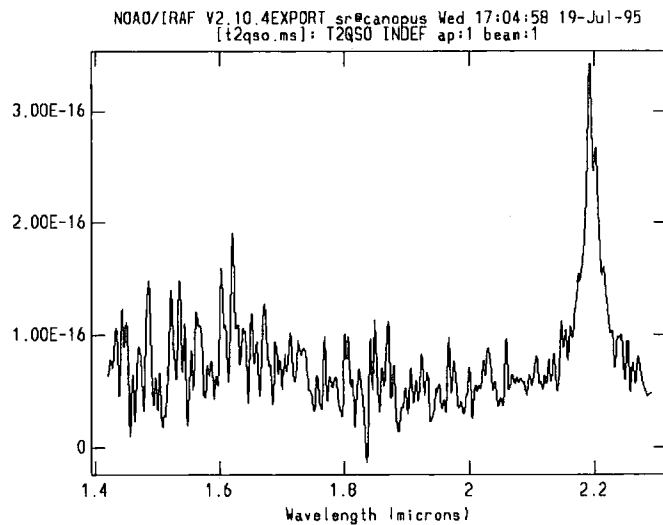
Figure 1.12: Near infra-red spectrum of the obscured QSO RXJ 1343.4+0001, obtained using the CGS4 instrument on the United Kingdom Infra-red Telescope telescope in Hawaii. The broad H_α emission line at 2.2μm confirms the presence of a QSO nucleus, and that dust is obscuring the broad line region at rest-frame ultra-violet wavelengths (Shanks et al. 1995, 1996; Georgantopoulos et al. 1999).

showed high-ionization, narrow emission lines characteristic of Seyfert 2 galaxies. The galaxy is at redshift $z = 0.67$ and therefore if the hard X-ray spectrum is caused by photo-electric absorption, the column density required is $N_H > 4 \times 10^{22}\,\mathrm{cm}^{-2}$ for an intrinsic spectral slope of $\alpha = 1$. Another such object is the Type 2 QSO at $z \sim 0.9$ found using *ASCA* by Ohta et al. (1996).

Additional evidence supporting an obscured AGN origin for the XRB include results obtained from studying supermassive black holes at the centres of non-active galaxies. Franceschini, Vercellone & Fabian (1998) use the correlation between radio emission of galaxies and the mass of the central black hole in order to estimate the mass function of black holes in the local universe. In a framework in which short-lived QSO activity occurs in most galaxies, as opposed to long-lived activity in only a fraction of galaxies, these black holes are thought to be "dead" QSOs, in which the central activity is now switched off. Using the black hole mass function, the emission from these galaxies in their active phase is then found to be in excellent agreement with the observed hard X-ray background. Fabian & Iwasawa (1999) perform this calculation in the reverse direction, by calculating the black hole mass density inferred by the intensity of the XRB, which they find to be in excellent agreement with the optically measured value. Considerations of the spectrum of the XRB implies that ~ 85 per cent of the energy released by accretion in the Universe is absorbed.

There are however, some criticisms of obscured AGN models for the X-ray background. One such doubt is whether the observed smooth slope of the XRB, which can be approximated by a power-law to very high accuracy, can be made by a superposition of many sources which are known to contain emission lines in their X-ray spectra, in particular, strong iron K features. Although these sources are at a large range of redshifts, and therefore one would expect emission lines to be smeared out when looking at an ensemble of objects, this should have a measurable effect on the shape of the XRB spectrum (Matt & Fabian 1994). Gendreau et al. (1995a) use *ASCA* measurements of the XRB spectrum to put strong constraints on the allowed parameter space for AGN synthesis models. They find however, that the small area of parameter space which gives acceptable models for the XRB is consistent with independently derived AGN data, and therefore that obscured AGN models for the XRB cannot be ruled out in this way.

1.6 Alternative Models for the X-ray Background

The above problem has led to the development of alternative models for the XRB. However, in order to explain the origin of the X-ray background as due to something other than QSOs and AGN, a new class of source must be postulated which not only has the correct spectral shape,

but exists out to high redshifts, in order to produce the observed isotropy and smoothness of the background. There are many such models, but presented here are a few of the more plausible.

1.6.1 Starburst Models

Starburst models for the XRB were first proposed by Griffiths & Padovani (1990), using the properties of galaxies for which the star-formation rate is much greater than in normal galaxies. These starburst galaxies contain large numbers of massive hot young stars which produce copious quantities of X-rays. Terlevich et al. (1992) used these types of model to explain the AGN phenomenon. The evolutionary end-point of these massive stars is a supernova, and an ensemble of such stars would produce a stochastic series of supernovae explosions, causing the observed variability in the lightcurves. In this picture, the broad emission lines are caused by the supernovae exploding in a very dense medium, with the remnants expanding at several thousand $km\,s^{-1}$. The X-ray emission comes from stellar outflows, X-ray binary stars, the supernova explosion itself, and shock-heating of the inter-stellar medium.

It is now known that starbursts and AGN are two distinct, although not necessarily unrelated, properties of a galaxy, and the conditions prevailing in each result in slightly different emission line species and strengths to be present in the spectrum. To differentiate between starbursts and AGN, it is possible to use certain diagnostic diagrams (Veilleux & Osterbrock 1987), in which a comparison is made of the emission line strength ratios of various pairs of lines close together in the spectrum. The classification as either starburst or AGN then depends on the position of the galaxy in the diagram.

However, starbursts do not provide a good fit to the XRB, as they do not possess the right spectrum. Although massive X-ray binary stars have a similar spectral slope to the XRB, their spectra have a turnover at around 20 keV (White, Swank & Holt 1983; White, Nagase & Parmer 1995), which will be shifted to even lower energies for high redshift objects. This is inconsistent with the fact that a large fraction of the XRB must come from high redshifts, and therefore cannot account for the significant intensity of the background at 30 keV.

1.6.2 Composite Models

Hybrid models, in which an active nucleus and star-formation co-exist within the same galaxy, are likely to be a far more likely scenario than treating Seyfert and starburst activity as two mutually exclusive phenomena, and several such objects have already been discovered. Iwasawa et al. (1997) found that spatially resolved optical spectroscopy of a hard spectrum *ASCA* source at

$z = 0.05$ revealed signatures of both AGN and star-forming activity present in differing amounts, which they interpret as a starburst galaxy containing a hidden Seyfert nucleus. A further hypothesis is that for low luminosity AGN, obscuration can actually be caused by the dust in a circumnuclear starburst region (Fabian et al. 1998).

1.6.3 Advection-Dominated Accretion Flows

A recent hypothesis for the emission mechanism in X-ray luminous galaxies is an advection-dominated accretion flow (ADAF; see Narayan, Mahadevan & Quataert 1998), characterised by low radiative efficiency, *i.e.*, matter is accreted onto a black hole before it has the chance to lose all its energy. At low accretion rates, the X-ray emission is predominantly due to bremsstrahlung from hot electrons. As the accretion rate increases until it is of the order of the critical rate for advective flow, $\dot{m} \sim \dot{m}_{crit}$, the thermal spectrum is Comptonized, which creates a hard X-ray spectrum, similar to that of the XRB above $\sim 5\,\mathrm{keV}$. ADAFs have been used to provide good fits to the hard XRB spectrum (Di Matteo et al. 1999), although a prediction of the ADAF model is a characteristic peak at sub-mm wavelengths due to thermal synchrotron radiation, which as yet has not been observed in individual sources (Di Matteo et al. 1998). This may prove to rule out ADAF models for the XRB. In addition, the particular ADAF models of Di Matteo et al. (1999) used to fit the XRB, are constrained to have an accretion disc with an inner, or transition, radius of $R_{tr} \sim 500$ Schwarzschild radii (R_s), and $\dot{m} \sim \dot{m}_{crit}$. Since the nuclear emission is primarily at hard energies, whereas the accretion disc is distant from the nucleus and therefore only radiating weakly in the ultra-violet, a very hard spectrum is produced, containing very few soft X-ray photons. This is in contrast to less specific ADAF models for which the transition radius is not constrained. The inner edge of the accretion disc approaches the nucleus much more closely, therefore intercepts and reprocesses a larger fraction of the nuclear emission, producing copious soft X-ray emission. Esin, McClintock & Narayan (1997) find that $\dot{m} \sim \dot{m}_{crit}$ implies that $R_{tr} \sim 3R_s$. The resulting spectrum is much softer, which is then inconsistent with the XRB spectrum, making ADAFs unlikely to be the source of the XRB.

1.7 Thesis outline

The main aim of this thesis is therefore to investigate obscured AGN models for the X-ray background in the light of the most recent observations at a range of wavelengths. Two approaches are used, the first involving the determination of ensemble properties for populations of obscured AGN, and the second investigating the properties of individual objects. In Chapter 2, we develop

our own model for the X-ray background, using populations of both obscured and unobscured AGN, which we test for consistency against the available data in the form of X-ray source counts and the XRB spectrum. Using this model, in Chapter 3 we investigate the selection effects present in various QSO samples, at both optical and near infra-red wavelengths, in order to explain recent conflicting results concerning the existence of such obscured AGN. The number-redshift relation predicted by our model is compared with the results from X-ray surveys at both soft and hard energies, and at a range of flux limits. The existence of highly obscured sources in our models implies that a number of X-ray sources will be detected for which there will be no obvious optical counterpart from optical imaging and spectroscopic data, and the number of these so-called "blank field" sources are compared with the data. In addition, we make predictions of the number-redshift distribution and numbers of blank fields expected in proposed deep observations with *AXAF*. In this framework, significant populations of obscured AGN are required to explain the origin of the hard XRB. One major consequence of this model is that large quantities of dust must be invoked to provide the medium in which this absorption occurs. The energy absorbed by the dust in this way is then re-radiated in the thermal infra-red. These sources will therefore be detectable as sub-millimetre sources and will contribute to the intensity of the far infra-red background. In Chapter 4, we therefore model the far infra-red emission expected from obscured AGN, as observational constraints at these wavelengths may prove to place strict limits on the numbers of such objects which can exist. We make predictions of the maximum contribution to the sub-mm number counts and far infra-red background spectrum from our obscured AGN model. An observational program to test these hypotheses is presented in Chapters 5, 6, and 7, involving near infra-red imaging, near infra-red spectroscopy, and far infra-red photometry of *ROSAT* X-ray sources. In Chapter 8, we present preliminary results from a hard X-ray *BeppoSAX* observation of the field BJS864, and describe the source population detected at these fluxes. Finally in Chapter 9, our conclusions are then discussed in the context of future technological developments and the anticipated results from forthcoming X-ray satellites *AXAF* and *XMM*, which should help to solve many outstanding problems in this subject.

References

Almaini O., Boyle B. J., Griffiths R. E., Shanks T., Stewart G. C., Georgantopoulos I., 1995, MNRAS, 277, L31

Almaini O., Lawrence A., Shanks T., Edge A., 1999a, MNRAS submitted.

Almaini O., Shanks T., Griffiths R. E., Boyle B. J., Roche N., Georgantopoulos I., Stewart G. C., 1997, MNRAS, 291, 372

Antonucci R., 1993, ARA&A, 31, 473

Antonucci R. R. J., Miller J. S., 1985, ApJ, 297, 621

Barber C. R., Roberts T. P., Warwick R. S., 1996, MNRAS, 282, 157

Boella G., Butler R. C., Perola G. C., Piro L., Scarsi L., Bleeker J. A. M., 1997, A&AS, 122, 299

Bower R. G. et al., 1996, MNRAS, 281, 59

Boyle B. J., Almaini O., Georgantopoulos I., Blair A. J., Stewart G. C., Griffiths R. E., Shanks T., Gunn K. F., 1998b, MNRAS, 297, L53

Boyle B. J., Di Matteo T., 1995, MNRAS, 277, L63

Boyle B. J., Fong R., Shanks T., Peterson B. A., 1990, MNRAS, 243, 1

Boyle B. J., Georgantopoulos I., Blair A. J., Stewart G. C., Griffiths R. E., Shanks T., Gunn K. F., Almaini O., 1998a, MNRAS, 296, 1

Boyle B. J., Griffiths R. E., Shanks T., Stewart G. C., Georgantopoulos I., 1993, MNRAS, 260, 49

Boyle B. J., Jones L. R., Shanks T., 1991, MNRAS, 251, 482

Boyle B. J., Shanks T., Georgantopoulos I., Stewart G. C., Griffiths R. E., 1994, MNRAS, 271, 639

Burrows D. N., Mendenhall J. A., 1991, Nat, 351, 629

Comastri A., Setti G., Zamorani G., Hasinger G., 1995, A&A, 296, 1

Croom S. M., 1999, private communication.

De Zotti G., Boldt E. A., Marshall F. E., Swank J. H., Szymkowiak A. E., Cavaliere A., Danese L., Franceschini A., 1982, ApJ, 253, 47

Di Matteo T., Esin A., Fabian A. C., Narayan R., 1999, MNRAS submitted. (astro-ph/9812134)

Di Matteo T., Fabian A. C., Rees M. J., Carilli C. L., Ivison R. J., 1998, MNRAS submitted. (astro-ph/9807245)

Done C., Madejski G. M., Smith D. A., 1996, ApJL, 463, L63

Esin A. A., McClintock J. E., Narayan R., 1997, ApJ, 489, 865

Fabian A. C., Barcons X., 1992, ARA&A, 30, 429

Fabian A. C., Barcons X., Almaini O., Iwasawa K., 1998, MNRAS, 297, L11

Fabian A. C., Iwasawa K., 1999, MNRAS, 303, L34

Franceschini A., Vercellone S., Fabian A. C., 1998, MNRAS, 297, 817

Gendreau K., Yaqoob T., Mushotzky R., Fabian A., 1995, American Astronomical Society Meeting, 187, 5007

Georgantopoulos I., Almaini O., Shanks T., Stewart G. C., Griffiths R. E., Boyle B. J., Gunn K. F., 1999, MNRAS, 305, 125

Georgantopoulos I., Stewart G. C., Blair A. J., Shanks T., Griffiths R. E., Boyle B. J., Almaini O., Roche N., 1997, MNRAS, 291, 203

Georgantopoulos I., Stewart G. C., Shanks T., Boyle B. J., Griffiths R. E., 1996, MNRAS, 280, 276

Georgantopoulos I., Stewart G. C., Shanks T., Griffiths R. E., Boyle B. J., 1993, MNRAS, 262, 619

Giacconi R., Gursky H., Paolini F., Rossi B., 1962, Phys.Rev.Letters, 9, 439

Granato G. L., Danese L., Franceschini A., 1997, ApJ, 486, 147

Greenhill L. J., Gwinn C. R., Antonucci R., Barvainis R., 1996, ApJL, 472, L21

Greenhill L. J., Jiang D. R., Moran J. M., Reid M. J., Lo K. Y., Claussen M. J., 1995, ApJ, 440, 619

Griffiths R. E. et al., 1983, ApJ, 269, 375

Griffiths R. E., Padovani P., 1990, ApJ, 360, 483

Iwasawa K., Fabian A. C., Brandt W. N., Crawford C. S., Almaini O., 1997, MNRAS, 291, L17

Kay L. E., Moran E. C., 1998, PASP, 110, 1003

Lawrence A., Papadakis I., 1993, ApJL, 414, L85

Madau P., Ghisellini G., Fabian A., 1994, MNRAS, 270, L17

Mather J. C. et al., 1994, ApJ, 420, 439

Mather J. C. et al., 1990, ApJL, 354, L37

Matt G., Fabian A. C., 1994, MNRAS, 267, 187

McHardy I. M. et al., 1998, MNRAS, 295, 641

Miller J. S., Goodrich R. W., 1990, ApJ, 355, 456

Moritz P., Wennmacher A., Herbstmeier U., Mebold U., Egger R., Snowden S. L., 1998, A&A, 336, 682

Narayan R., Mahadevan R., Quataert E., 1998, *The Theory of Black Hole Accretion Discs*. Cambridge University Press

Ohta K., Yamada T., Nakanishi K., Ogasaka Y., Kii T., Hayashida K., 1996, ApJL, 458, L57

Osterbrock D. E., 1989, *Astrophysics of gaseous nebulae and active galactic nuclei*. University Science Books, University of Minnesota, Mill Valley, CA.

Penzias A. A., Wilson R. W., 1965, ApJ, 142, 419

Roche N., Shanks T., Georgantopoulos I., Stewart G. C., Boyle B. J., Griffiths R. E., 1995, MNRAS, 273, L15

Romero-Colmenero E., Branduardi-Raymont G., Carrera F. J., Jones L. R., Mason K. O., McHardy I. M., Mittaz J. P. D., 1996, MNRAS, 282, 94

Schmitt J. H. M. M., Snowden S. L., Aschenbach B., Hasinger G., Pfeffermann E., Predehl P., Trümper J., 1991, Nat, 349, 583

Shanks T. et al., 1996, in Zimmerman U., Truemper J.E., Yorke H., eds, *Roentgenstrahlung from the Universe*, Vol. MPE Report 263, p. 341

Shanks T., Almaini O., Boyle B. J., Done C., Georgantopoulos I., Griffiths R. E., Rawlings S., Stewart G. C., 1995, Spectrum, Newsletter of the Royal Observatories, vol. 7, 7

Shanks T., Georgantopoulos I., Stewart G. C., Pounds K. A., Boyle B. J., Griffiths R. E., 1991, Nat, 353, 315

Shanks T. et al., 1999, in preparation.

Sharples R., Gray P., Hatzidimitriou D., 1991, *Autofib Manual*. Anglo-Australian Observatory User Manual 26

Snowden S. L. et al., 1995, ApJ, 454, 643

Stocke J. T., Liebert J., Gioia I. M., Maccacaro T., Griffiths R. E., Danziger I. J., Kunth D., Lub J., 1983, ApJ, 273, 458

Stocke J. T., Morris S. L., Gioia I. M., Maccacaro T., Schild R., Wolter A., Fleming T. A., Henry J. P., 1991, ApJS, 76, 813

Tanaka Y., Inoue H., Holt S. S., 1994, PASJ, 46, L37

Terlevich R., Tenorio-Tagle G., Franco J., Melnick J., 1992, MNRAS, 255, 713

Trümper J., 1982, Advances in Space Research, 2, 241

Trümper J., 1990, in *High resolution X-ray spectroscopy of cosmic plasmas*, Cambridge University Press, p. 291

Veilleux S., Osterbrock D. E., 1987, ApJS, 63, 295

Webster R. L., Francis P. J., Peterson B. A., Drinkwater M. J., Masci F. J., 1995, Nat, 375, 469

White N. E., Nagase F., Parmer A. N., 1995, in Lewin W. H. G., van Paradijs J., van den Heuvel E., eds, *X–Ray Binaries*, Cambridge: Cambridge Univ. Press, p. 1

White N. E., Swank J. H., Holt S. S., 1983, ApJ, 270, 711

Yaqoob T., McKernan B., Ptak A., Nandra K., Serlemitsos P. J., 1997, ApJL, 490, L25

Chapter 2

Observational Tests of

Obscured QSO Models

ABSTRACT. In this Chapter, we develop a model for the X-ray Background (XRB) using populations of obscured QSOs, following Madau et al. (1994) and Comastri et al. (1995). We find that for a flat distribution of absorbing columns, reasonable fits to the XRB spectrum and X-ray source counts can be obtained using our model. In addition, since this model fits the XRB all the way down to $0.5\,\mathrm{keV}$, it can therefore be said to accommodate the new X-ray bright, narrow-line galaxy population (Roche et al. 1995) as a low luminosity, obscured AGN population. For a $q_0 = 0.5$ universe, we find that skewing the column density distribution to higher densities improves the fit.

2.1 Motivation & Background

At the X-ray fluxes probed by *ROSAT*, the majority of the resolved sources which contribute to the XRB are QSOs, amounting to at least 30 per cent at $1\,\mathrm{keV}$ (Shanks et al. 1991). Studies of the QSO X-ray luminosity function and its evolution indicate a total QSO contribution of $34 - 53$ per cent of the $1 - 2\,\mathrm{keV}$ extragalactic background (Boyle et al. 1994). In the higher energy *ASCA* band, Boyle et al. (1998a) find that QSOs may provide ~ 40 per cent of the $2 - 10\,\mathrm{keV}$ XRB, and the whole background intensity can be accounted for if the contribution from Seyfert 2 and narrow-line galaxies is included. However, since the average photon index of QSOs is $\Gamma \sim 2$[1] whereas the background has $\Gamma \sim 1.4$, then QSOs or sources with similar spectra cannot provide all of the XRB. This "spectral paradox" (De Zotti et al. 1982) implies that there must be another population of sources making a significant contribution to the XRB.

The contribution of galaxies to the XRB was investigated by Roche et al. (1995), who found a $2 - 3\sigma$ cross-correlation between $B = 21 - 23\,\mathrm{mag}$ galaxies and X-ray sources in deep *ROSAT*

---

[1] By convention, the photon index Γ defines the number of incident photons as a function of frequency, $n(\nu) \propto \nu^{-\Gamma}$.
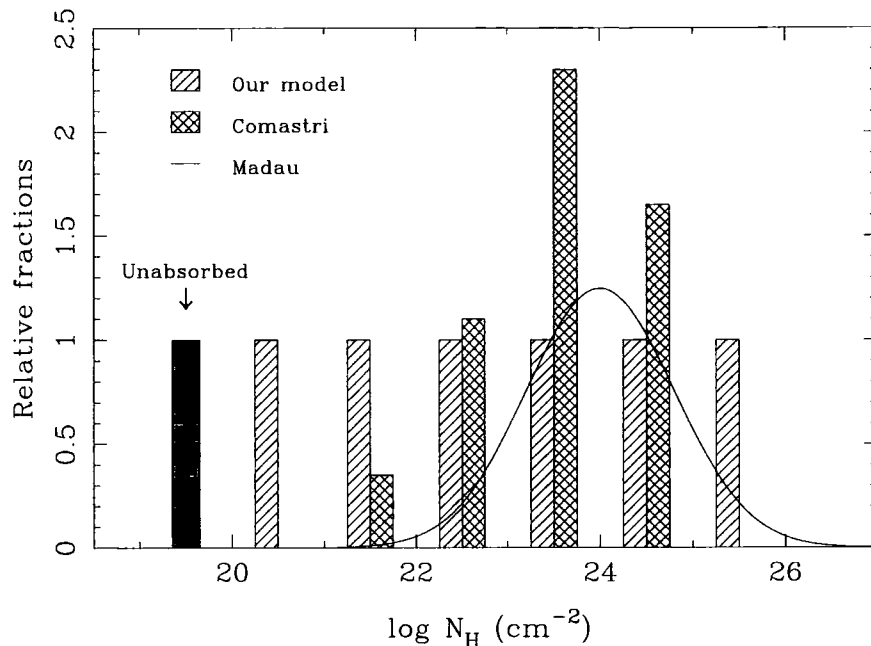
Figure 2.1: Comparisons of the different distributions of obscured QSO populations used by various authors. Each is scaled to the same amount of unobscured objects (shown here at $N_H = 10^{19.5}$ cm^{-2}) and overlaid as a solid box. Our model of a flat distribution of columns is shown as hatched regions; the Comastri et al. (1995) model is shown as cross-hatched regions; these two models are shown slightly offset from one another for clarity. The Madau et al. (1994) model is shown as the solid line describing a Gaussian distribution.

survey fields, with these galaxies accounting for ~ 5 per cent of the sources. Furthermore, a 5σ cross-correlation signal was found between these galaxies and the background photons, implying that faint galaxies may contribute ~ 20 per cent or more of the XRB intensity (Roche et al. 1996; Almaini et al. 1997). Some of the brighter X-ray galaxies were found to be Narrow Emission Line Galaxies (NELGs) (Almaini et al. 1996; Romero-Colmenero et al. 1996), which as a population have much harder spectra than QSOs, $\Gamma \sim 1.5$, suggesting that they may provide a solution to the missing component of the XRB. The emission mechanism is not known for certain, but may be due to obscured active galactic nuclei (AGN), starburst activity (Griffiths & Padovani 1990), or a mixture of both.

Our aim therefore, is to create a model for the X-ray background using populations of obscured and unobscured AGN, in order to replicate the observed spectrum of the XRB. Such a model should also be able to fit the numbers of sources detected in surveys at a range of different energies and flux limits. In addition, extending our XRB fit into the *ROSAT* energy band, our model can test whether it is possible to incorporate the observed X-ray luminous galaxies described above into a single coherent framework of obscured sources. This unification has not been attempted by

previous authors, and would provide powerful motivation for studies of the physical origin of the XRB.

In earlier model fits to the background, several different distributions have been proposed: for example, Madau et al. (1994) used a bimodal model, consisting of a population of unabsorbed sources plus 2.5 times as many absorbed sources with a Gaussian distribution of column densities with mean $N_H = 10^{24\pm0.8}\,\mathrm{cm}^{-2}$. By contrast, Comastri et al. (1995) used four sub-classes of absorbed populations, each with a different normalization with respect to the unabsorbed population. However, the Madau et al. model does not include sources with moderate columns that are known to exist (see Sections 1.5 and 1.6; Almaini et al. 1995; Boyle et al. 1998b; Ohta et al. 1996; Iwasawa et al. 1997), and the Comastri et al. model requires fine tuning of the sizes of each population. We have therefore tested a simple model of a flat distribution of columns, comprising seven populations evenly spaced in log space:

$$N_H = 10^{19.5}, 10^{20.5}, 10^{21.5}, 10^{22.5}, 10^{23.5}, 10^{24.5} \text{ and } 10^{25.5}\,\mathrm{cm}^{-2},$$

each containing the same number and intrinsic luminosity function of AGN. The unabsorbed population is represented here by $N_H = 10^{19.5}\,\mathrm{cm}^{-2}$, typical of the column present in a host galaxy. At the energies under consideration, this has the same effect as zero absorption, and can be more easily compared with the other populations in log space. In Fig. 2.1, we show our model compared with those of Madau et al. and Comastri et al., where each is normalised to the same number of unabsorbed sources ($N_H = 10^{19.5}\,\mathrm{cm}^{-2}$, solid region). It can be seen that neither of the distribution functions used by previous authors allows for many objects with columns of $N_H \sim 10^{21}\,\mathrm{cm}^{-2}$, are are therefore unable to explain fully the observed obscured source distribution.

In addition, these authors concentrated on fitting the hard XRB spectrum above $\sim 2\,\mathrm{keV}$, since at the time the lower energy determination of the background from *ROSAT* data was not in agreement with other measurements. However, a more recent treatment of the *ROSAT* data, taking careful account of Galactic contamination, has found that the XRB spectrum below $\sim 2\,\mathrm{keV}$ to be much flatter than previously thought (Georgantopoulos et al. 1996), and it is with this measurement that we have compared our predictions.

In what follows, the differences in the observed properties of each population of sources are attributable solely to the effects of absorption by neutral gas, as parametrized by the column density of hydrogen. However, the geometry of this obscuring medium is not known. Two possible geometries considered here are firstly an isotropic absorber, in which the object looks the same
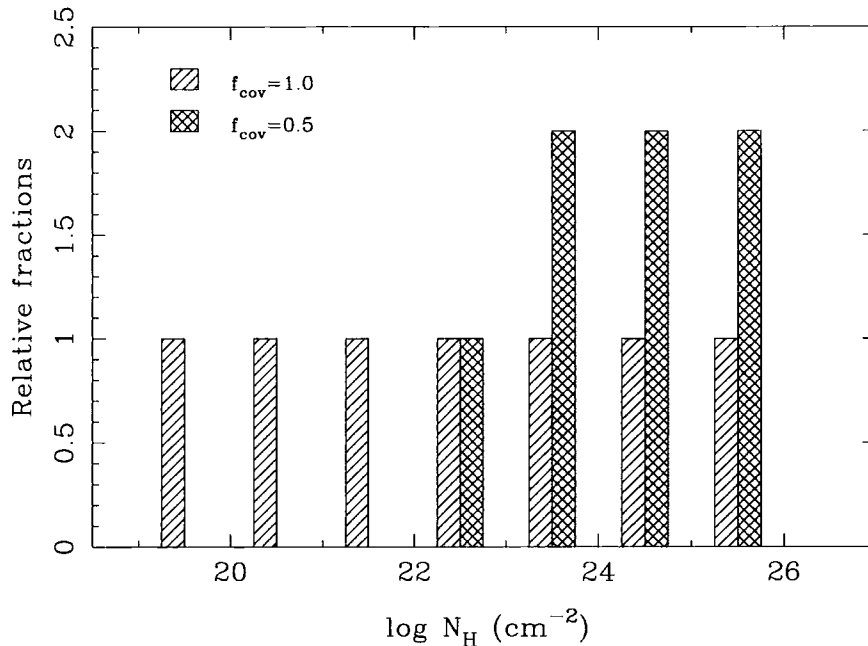
Figure 2.2: Comparisons of two different intrinsic column density distributions of obscured QSO populations, which give rise to the same *perceived* flat distribution. For an isotropic absorber, the covering factor is unity, *i.e.*, $f_{cov} = 1$, and therefore an intrinsic flat distribution will also be perceived as flat (hatched regions); however, for an absorber for which $f_{cov} = 0.5$, a larger number of obscured sources are required, as half will be observed to be unobscured (cross-hatched regions); the two distributions are shown slightly offset from one another for clarity. For the tilted distribution of columns used in $q_0 = 0.5$ scenarios (see Section 2.6), a similar correction must be made when $f_{cov} = 0.5$ is assumed.

from all directions, and secondly a toroidal structure, in which the observed properties depend critically on viewing angle. At X-ray and optical energies, the observed spectrum depends on whether or not the line of sight to the source of the emission intersects the absorber, and therefore it is the fraction of obscured lines of sight to the nucleus which is important. However, although a toroidal obscuring medium will be absorbing X- and optical radiation anisotropically, this energy will be re-radiated *iso*tropically at longer wavelengths. It is therefore important to take the geometry of the obscurer into account here, in order to be consistent with the work presented in Chapter 4 on the properties of such obscured AGN at sub-mm wavelengths.

At X-ray and optical energies, the *perceived* column density distribution is effectively the convolution of the fraction of sources of each column density with the covering factor of the obscuring material at this density. However to disentangle these effects, in order to derive the underlying true column density distribution, would require knowledge of the geometry of the absorber, of which very little is known. It is therefore usually assumed either that the absorber is isotropic, in which case any line of sight will have the same N_H, or that the absorber has a toroidal geometry.

In the latter case a covering factor, f_{cov}, must be assumed, such that a fraction f_{cov} of lines of sight will intersect the torus, thereby affecting the transmitted flux, and the remaining lines of sight will be effectively unabsorbed, enabling the flux to escape unattenuated. For instance, if the covering factor is assumed to be unity, *i.e.*, the absorber is isotropic, then the perceived column distribution will be identical to the intrinsic column distribution. However, if the covering factor is for example, $f_{cov} \sim 0.5$, then statistically, an object with a high N_H will be detected as absorbed in ~ 50 per cent of cases and unabsorbed in the remaining ~ 50 per cent. This implies that the intrinsic column distribution is skewed with respect to the observed distribution (*i.e.*, here, our flat distribution), with more highly obscured objects than actually detected. Figure 2.2 shows column distributions for $f_{cov} \sim 1$ and $f_{cov} \sim 0.5$ which both give rise to the same observed flat distribution. For $f_{cov} \sim 0.5$, twice as many highly obscured sources are required, as they will appear unobscured for half the lines of sight, thereby reproducing a flat distribution perceived at X-ray and optical energies.

For the predictions made in this and the following Chapter, it is only the observed or line of sight column density distribution which affects our results. Whereas for consistency, in Chapter 4 we shall have to make assumptions about the geometry in order to estimate the possible intrinsic distributions.

The rest of this Chapter is concerned with the consequences of this obscured QSO model at X-ray energies. In Section 2.2, we show how the presence of a dusty molecular torus affects a QSO spectrum through photo-electric absorption, then in Section 2.3, the method of predicting the X-ray source counts is described, together with the QSO luminosity function and evolutionary parameters used. The results for the number counts of QSOs are presented in Section 2.4, and the XRB spectrum predicted by our model is shown in Section 2.5: both are compared with the observational constraints. Additional model fits for a $q_0 = 0.5$ universe, using a tilted distribution of column densities, is presented in Section 2.6. The main conclusions are given in Section 2.7.

2.2   The effects of photo-electric absorption on QSO spectra

In Fig. 2.3, the effect of obscuring columns of $N_H = 10^{21}, 10^{22}, 10^{23}$ and $10^{24}\,\mathrm{cm}^{-2}$ on an $\alpha_x = 1$ ($\Gamma = 2$)[2] intrinsic QSO spectrum can be seen. The XSPEC spectral fitting package (Arnaud 1996) uses the Wisconsin energy-dependent absorption cross-sections from Morrison & McCammon (1983) to calculate the X-ray photo-electric absorption, and hence the transmitted

---

[2]   By convention, the spectral index α is defined by $f_\nu \propto \nu^{-\alpha}$ in both the optical and X-ray regimes. The spectral index is related to the photon index by $\alpha = \Gamma - 1$.
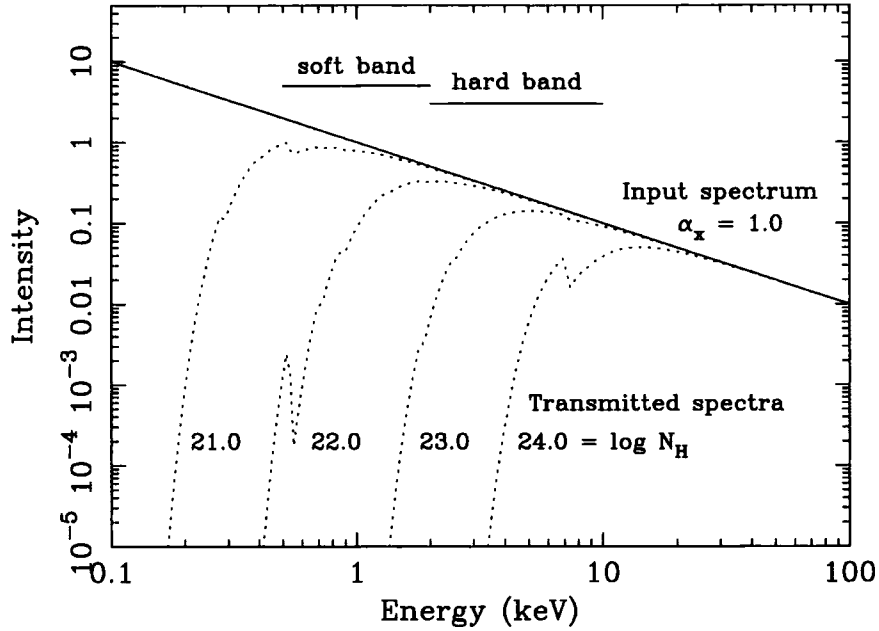
Figure 2.3: Absorption at X-ray energies for column densities of $N_H = 10^{21}, 10^{22}, 10^{23}$ and 10^{24} cm^{-2}, derived using XSPEC. The incident spectrum is a power-law, $I \propto \nu^{-\alpha_x}$, with spectral index $\alpha_x = 1$.

flux. For instance, in the soft X-ray $0.5 - 2$ keV band, as the absorbing column increases the observed spectrum is gradually hardened (*i.e.*, decreasing α_x) until no flux is transmitted in this band. Even in the hard X-ray band, once the column density gets as high as $N_H \sim 10^{23}$ cm^{-2}, the spectrum is much harder, as shown in Fig. 2.3. It then becomes more difficult to detect such objects unless they lie at high redshifts, in which case a higher energy part of the spectrum is shifted into the observed band. This property of higher absorbing columns leading to harder QSO spectra provides the correct behaviour to allow a model containing obscured AGN to fit the spectral shape of the XRB.

2.3 Modelling of the X-ray number counts

A complete model of the XRB should accurately predict the number of sources actually observed per area of sky as a function of the limiting flux of a survey. If we assume that the majority of sources contributing to the XRB are QSOs, then we can estimate their total integrated emission by integrating their X-ray luminosity function (XLF), $\Phi_X(L_X, z)$, over both luminosity and redshift in a co-moving volume element:

$$N_Q = \int_L \int_z \Phi_X(L_X, z) \frac{dV_{com}}{dz} \, dz \, dL,$$

$$= \int_L \int_z \Phi_X(L_X, z) \frac{c}{H_0} \frac{d_L{}^2}{(1+z)^3} \frac{d\Omega}{\sqrt{1+2q_0 z}} \, dz \, dL,$$

where

$$d_L = \frac{c}{H_0} \begin{cases} q_0^{-2} \left\{ q_0 z + (1 - q_0)\left(1 - \sqrt{1 + 2q_0 z}\right)\right\} & q_0 > 0, \\ 1 + \frac{1}{2}z & q_0 = 0. \end{cases}$$

The XLF measures the number density of QSOs in a certainly luminosity range. The zero redshift XLF can be approximated by a double power-law form as in Boyle et al. (1994):

$$\Phi_X(L_X, z = 0) = \begin{cases} \Phi_X^* L_{X_{44}}^{-\gamma 1} & L_X < L_X^*(z = 0), \\ \Phi_X^* L_{X_{44}}^{-\gamma 2} L_{X_{44}}^{*(\gamma 2 - \gamma 1)} & L_X > L_X^*(z = 0), \end{cases}$$

where Φ_X^* is the normalization of the XLF, measured in units of $\mathrm{Mpc}^{-3}(10^{44}\,\mathrm{erg\,s}^{-1})^{-1}$, and $L_{X_{44}}$ is the $0.3 - 3.5\,\mathrm{keV}$ X-ray luminosity in units of $10^{44}\,\mathrm{erg\,s}^{-1}$. In order to convert between the $0.3 - 3.5\,\mathrm{keV}$ XLF and those of other wavebands, it is necessary to take the assumed form for the QSO spectrum, and calculate the relationship between the observed luminosity in the new waveband compared to that in the $0.3 - 3.5\,\mathrm{keV}$ band. Since Φ_X is a number density per unit logarithmic luminosity, then this value remains constant, and the transformation reflects the change in luminosity alone, *i.e.*, a shift of the XLF with respect to the luminosity axis.

We assume that the number density of QSOs does not evolve, and that they undergo pure luminosity evolution alone. The luminosity evolution can be parametrized by the evolution of the characteristic "knee" in the luminosity function, L_X^*, such that:

$$L_X^*(z) = L_X^*(0)\, f_{evol}(z).$$

Following Boyle et al. (1994), we have chosen to adopt two forms for the evolution, one of which they term "polynomial" evolution:

$$L_X^*(z) = L_X^*(0)\, 10^{(\gamma_z z + \gamma_z' z^2)}, \tag{2.1}$$

and the other being "power-law" evolution:

$$L_X^*(z) = L_X^*(0)(1 + z)^{\gamma_z}. \tag{2.2}$$

For the power-law model, we can also incorporate some maximum redshift, z_{cut}, at which the evolution stops, such that:

$$L_X^*(z) = L_X^*(z_{cut}) \qquad z > z_{cut}.$$

These forms for the evolution are summarised in Fig. 2.4.
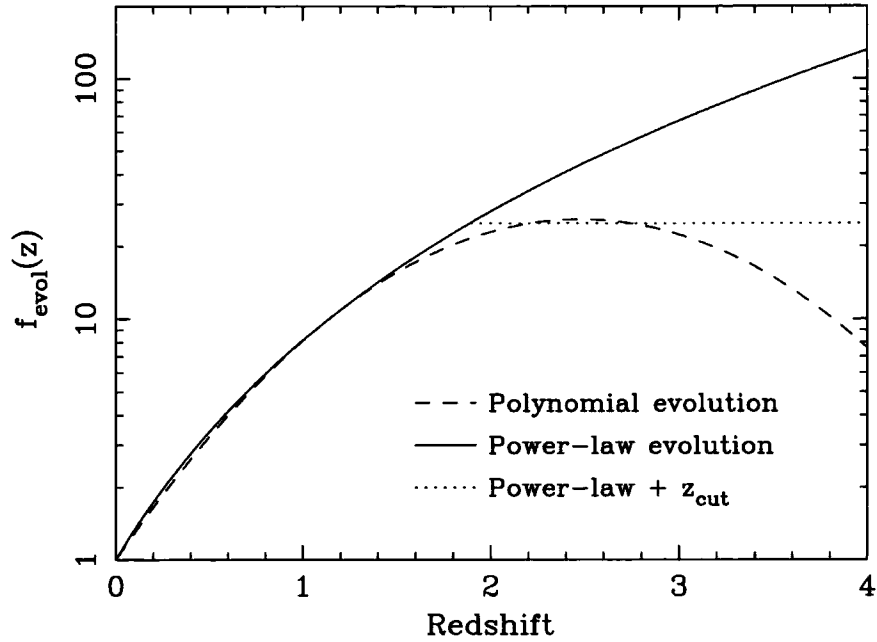
Figure 2.4: Luminosity evolution of QSOs with redshift. The evolution factor, $f_{evol}(z) = L_X^*(z)/L_X^*(0)$, is parametrized either as having a polynomial or a power-law dependence on redshift, as described in Eqns 2.1 and 2.2. Here we plot a polynomial evolutionary model (dashed line) compared with a power-law model with a redshift cutoff at $z_{cut} \sim 1.7$ (dotted line), both fit to the same data. For comparison, we also show the power-law model without a redshift cutoff (solid line), demonstrating why a cutoff is required to keep the luminosity evolution within sensible limits.

To simplify the calculation, rather than re-calculating the XLF at each redshift, an alternative method is to vary only the limits of integration. We wish to know the number of sources visible above a certain observed flux limit, S_{lim}, and this is related to the emitted luminosity, L_e, via:

$$S_{lim} = \frac{L_e}{4\pi d_L^2} = \left(\frac{L_e}{L_o}\right)\frac{L_o}{4\pi d_L^2},$$

where L_e/L_o is the k-correction term, due to the redshifting of a higher energy part of the spectrum into the observed band for more distant sources. For a power-law spectrum of index α_x, this term has the form $(1+z)^{1-\alpha_x}$, but here we shall denote it as $f_k(z)$, as in all other cases it has to be calculated explicitly. The observed luminosity also evolves with redshift as $f_{evol}(z)$, therefore the full expression relating luminosity and flux limit is:

$$L_o = \frac{4\pi d_L^2 S_{lim}}{f_k(z)\, f_{evol}(z)}, \tag{2.3}$$

and is used in the calculation of the integral form of the luminosity function,

$$\Psi(L_o) = \int_{L_o}^{L_{max}} \Phi_X(L_X, 0)\, \mathrm{d}L.$$

Model	B94	q_0	Evolution	γ_1	γ_2	$\log L_X^*(0)^\dagger$	γ_z	z_{cut}	γ_z'	$\Phi_X^{*\ddagger}$
POW(0.0)	G	0.0	$(1+z)^{\gamma_z} + z_{cut}$	1.53	3.38	43.70	3.03	1.89		0.79
POW(0.5)	H	0.5	$(1+z)^{\gamma_z} + z_{cut}$	1.36	3.37	43.57	2.90	1.73		1.45
POL(0.0)	K	0.0	$\gamma_z z + \gamma_z' z^2$	1.50	3.35	43.71	1.14		-0.23	0.84
POL(0.5)	L	0.5	$\gamma_z z + \gamma_z' z^2$	1.26	3.32	43.52	1.15		-0.26	1.89

†where $L_X^*(0)$ is the $0.3 - 3.5\,\mathrm{keV}$ luminosity in units of $\mathrm{erg\,s^{-1}}$.

‡where Φ_X^* is in units of $10^{-6}\,\mathrm{Mpc^{-3}}(10^{44}\,\mathrm{erg\,s^{-1}})^{-1}$.

Table 2.1. Parameters of four Boyle et al. (1994) model fits to the *ROSAT* and *Einstein* EMSS QSO X-ray luminosity function and its evolution, as used in our calculations. The first column contains our adopted descriptive model name, POW(q_0) or POL(q_0), with the corresponding model name from Boyle et al. (1994) in the column headed B94. As described in Section 2.3, the XLF is parametrized by a broken power-law, with indices γ_1 and γ_2 below and above the break luminosity L_X^*. The evolution is described by either power-law or polynomial evolution, in both $q_0 = 0.0$ and $q_0 = 0.5$ universes.

The final expression for the number counts per steradian is therefore:

$$N_Q(> S_{lim}) = \frac{c}{H_0} \int_0^{z_{max}} \Psi(L_o) \frac{d_L{}^2}{(1+z)^3\sqrt{1+2q_0 z}}\, \mathrm{d}z.$$

where L_o is calculated from Equation 2.3.

To extend this method in order to calculate the effect of obscuration on the number of sources detected, it is necessary to evaluate the k-correction at each redshift for the column density used for each population, $f_k(z, N_H)$:

$$f_k(z, N_H) = \frac{L_e}{L_o} = \frac{L_X(z = z', N_H)}{L_X(z = 0, N_H)}.$$

In this way, we can calculate the amount by which each AGN in the population is dimmed, and this can be represented by a reduction in the value of L^*. The number counts are then calculated in the same manner, using the XLF modified by $f_k(z, N_H)$.

The parameters for the X-ray luminosity function and its evolution have been taken from the fits to *ROSAT* and *Einstein* EMSS QSO number counts by Boyle et al. (1994). We have used existing model fits in order to see whether the addition of obscured populations of QSOs, in both the soft and hard X-ray bands, provides a better match to the data. We have taken descriptions of the XLF (from table 3 from Boyle et al. 1994) for two different cosmologies, $q_0 = 0.0$ and $q_0 = 0.5$, and for two different forms of the luminosity evolution, both power-law evolution with a redshift cutoff and polynomial evolution (see Equations 2.1 and 2.2). We have adopted model names of POW and POL for the power-law and polynomial evolution respectively, with the value of q_0 in parentheses.

The correspondence between these model names and Models G to L from Boyle et al. are detailed in Table 2.1. These four models were chosen as they were the best fits to the combined *ROSAT* and *Einstein* samples, without excluding certain sections of the data.

These parametrizations of the XLF and its evolution have been calculated under the assumption that the QSOs have the same spectral index of $\alpha_x = 1$. It is also possible to vary the intrinsic spectral index within each QSO population. Boyle et al. (1994) found that allowing α_x to vary does not significantly increase the acceptability of the fit for standard power-law and polynomial evolution. In our models, we have chosen not to introduce variation in observed spectral index artificially, as this is produced naturally by the obscuration (as described in Section 2.2) and is taken into account in our calculations.

At the energies under consideration, we have assumed that the observed luminosity function incorporates just the populations at $N_H = 10^{19.5}\,\mathrm{cm}^{-2}$ and $10^{20.5}\,\mathrm{cm}^{-2}$, so we take a normalization of $\frac{1}{2}\Phi^*$ for each population, where this and all other parameters for each model have been summarized in Table 2.1.

2.4 LogN:LogS Results

In Fig. 2.5, we compare our obscured QSO model predictions with the deepest available X-ray source count data, by plotting LogN:LogS graphs in both (a) soft and (b) hard energy bands, for the Boyle et al. (1994) models detailed in Table 2.1. These use power-law and polynomial luminosity evolution, for $q_0 = 0.0$ and $q_0 = 0.5$ cosmologies, and are denoted here as POW(0.0), POW(0.5), POL(0.0) and POL(0.5) respectively.

In the soft (0.5-2 keV) band, we have plotted *ROSAT PSPC* observations to fluxes of $S > 4 \times 10^{-15}\,\mathrm{erg\,s}^{-1}$ (Georgantopoulos et al. 1996), for all sources and QSOs respectively. The *Einstein* deep survey result of Primini et al. (1991) is also shown. At fainter fluxes, $S > 10^{-15}\,\mathrm{erg\,s}^{-1}$, we plot the 880 ksec *ROSAT* HRI Lockman Hole source counts (Hasinger et al. 1998). The number of X-ray galaxies lies an order of magnitude below the QSO contribution at $6 \times 10^{-15}\,\mathrm{erg\,s}^{-1}$, and we propose that these correspond to objects with moderate column densities which are not identified as broad-line QSOs in any spectroscopic follow-up.

In the hard (2-10 keV) band, the data are from *ASCA* (Georgantopoulos et al. 1997; Inoue et al. 1996), *BeppoSAX* (Giommi et al. 1998), and a *Ginga* fluctuation analysis (Butcher et al. 1997). Forthcoming observations should help to clarify whether the steep slope at the faintest fluxes is a real feature, or an artifact of the small sky coverage to this depth available at present. We also
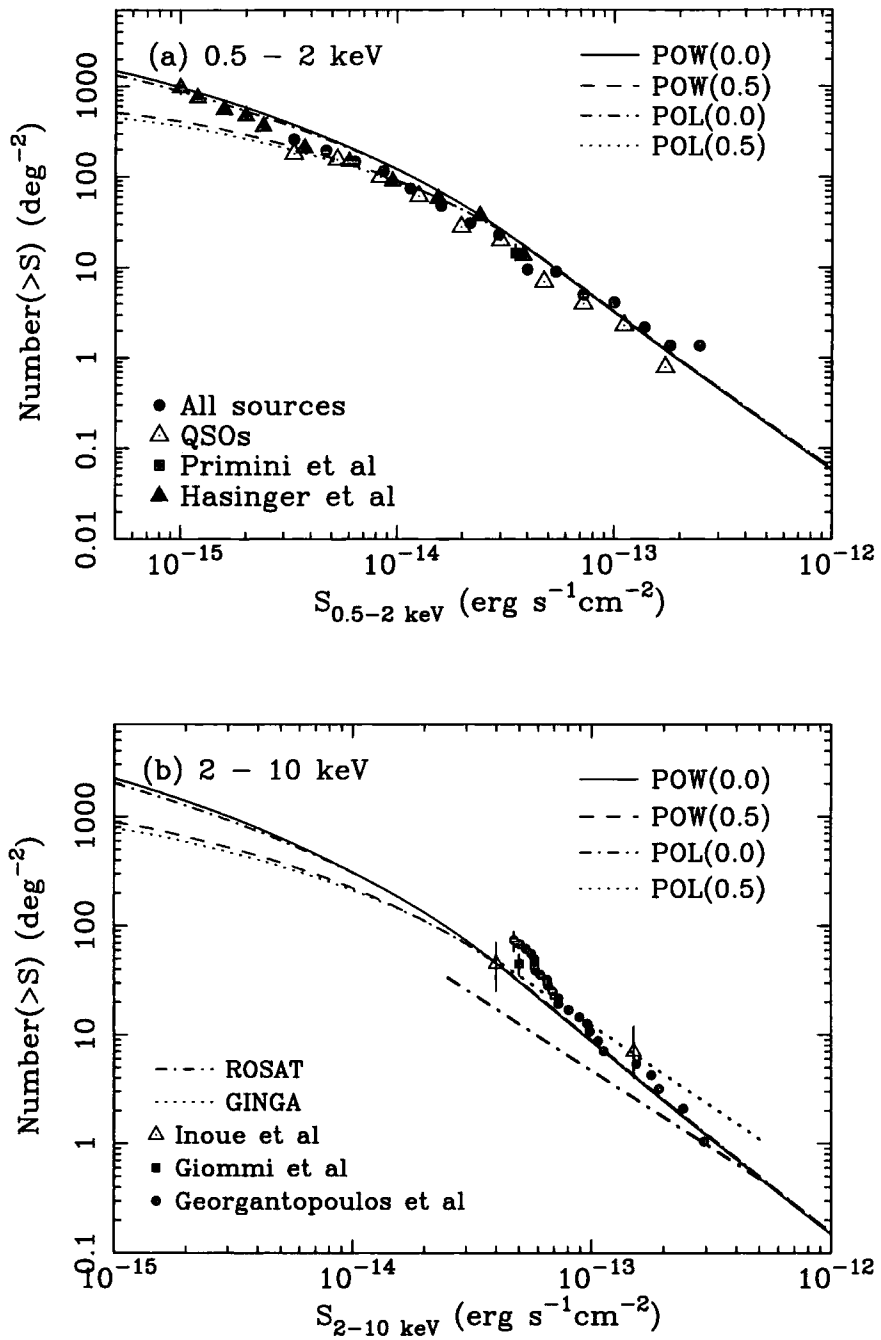
Figure 2.5: Predicted X-ray LogN:LogS relationship for (a) $0.5 - 2\,\mathrm{keV}$, (b) $2 - 10\,\mathrm{keV}$, for both power-law and polynomial evolution, and both $q_0 = 0.0$ and $q_0 = 0.5$ cosmologies, compared with the data described in Section 2.4. Models POW(0.0), POW(0.5), POL(0.0) and POL(0.5) are denoted by solid, dashed, dot-dashed and dotted lines respectively.
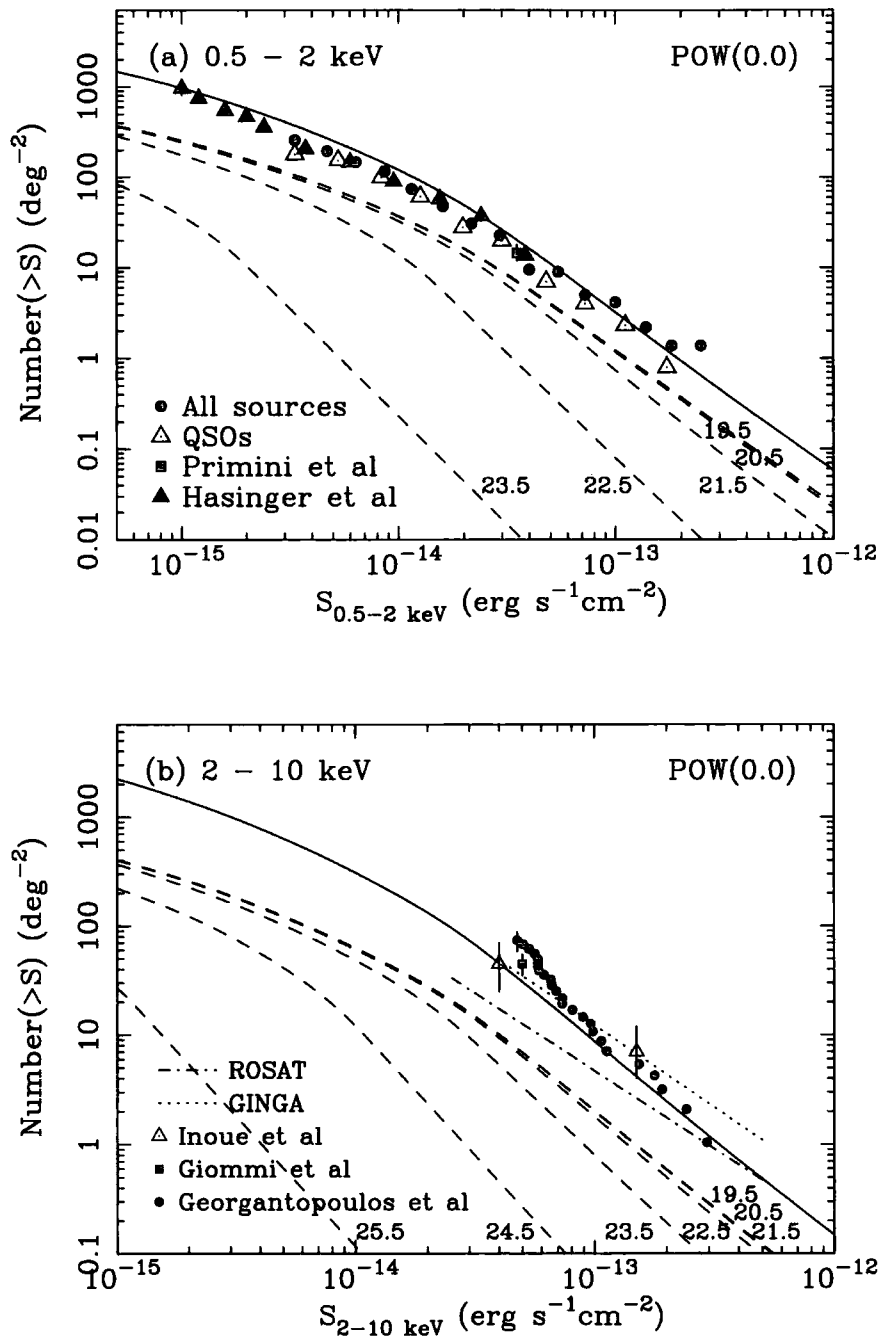
Figure 2.6: Predicted X-ray LogN:LogS relationship for (a) $0.5 - 2\,\mathrm{keV}$, (b) $2 - 10\,\mathrm{keV}$, compared with the data described in Section 2.4. is assumed for $q_0 = 0.0$, with parameters from Boyle et al. (1994). Each population of sources is plotted separately as a dashed line, with the column density marked in logarithmic units. The total contribution is plotted as a solid line.

show an extrapolation of the *ROSAT* 0.5 − 2 keV source counts to the 2 − 10 keV band, taken from Georgantopoulos et al. (1996).

As can be seen in Fig. 2.6(a) and (b), the absorption affects the counts in the 0.5 − 2 keV band to a greater extent than in the 2 − 10 keV band. Each population of sources is shown as a separate dashed line, marked with the value of $\log N_H$. Fewer sources can be detected as the column density is increased, with this effect being most significant at lower energies. At low redshift, a large proportion of objects are lost due to the fact that the most highly absorbed part of the X-ray spectrum is observed. At higher redshifts however, the rest frame energies which are redshifted into the observed passband are less affected by absorption and therefore the counts are not decreased to the same extent. These effects combine to steepen the observed LogN:LogS slope with increasing column density. As a consequence, highly absorbed sources at high redshift will provide a significant fraction of the XRB intensity at very faint fluxes and also at harder energies, but may not be resolved into individual sources at the limits of current detectors.

From Fig. 2.6(a), it can also be seen that QSOs with more than a small obscuring column make very little contribution to the source counts below 2 keV. In this band, the majority of sources are identified as unobscured broad-line QSOs, and it is only at the faintest fluxes that AGN with moderate $(N_H \sim 10^{22}\,\mathrm{cm}^{-2})$ columns, (which would be identified as NELGs in optical surveys; discussed in full in Chapter 3), have more of an effect.

Purely unobscured models fail to reproduce the observed hard X-ray number counts, and therefore the addition of the obscured populations to our model is vital. In addition, the data in Fig. 2.6(b) may imply that we need even more obscured QSOs than already included in our model, to steepen the bright end slope still further. However this may introduce problems with the fit to the XRB spectrum.

In a $q_0 = 0.5$ universe, the soft counts are underpredicted at faint fluxes, which in turn means that the contribution to the background intensity is too low (as described later in Section 2.5). A better fit is obtained in a $q_0 = 0.0$ universe, due to the increased volume present at high redshifts, and hence higher number counts at faint fluxes. For a $q_0 = 0.5$ universe, we find that skewing the column density distribution to higher columns improves the fit (see Section 2.6).

2.5 XRB spectrum

The spectrum of the background is calculated as in Matt & Fabian (1994) by assuming an intrinsic spectral shape for the local volume emissivity of an unabsorbed population of sources. A first ap-
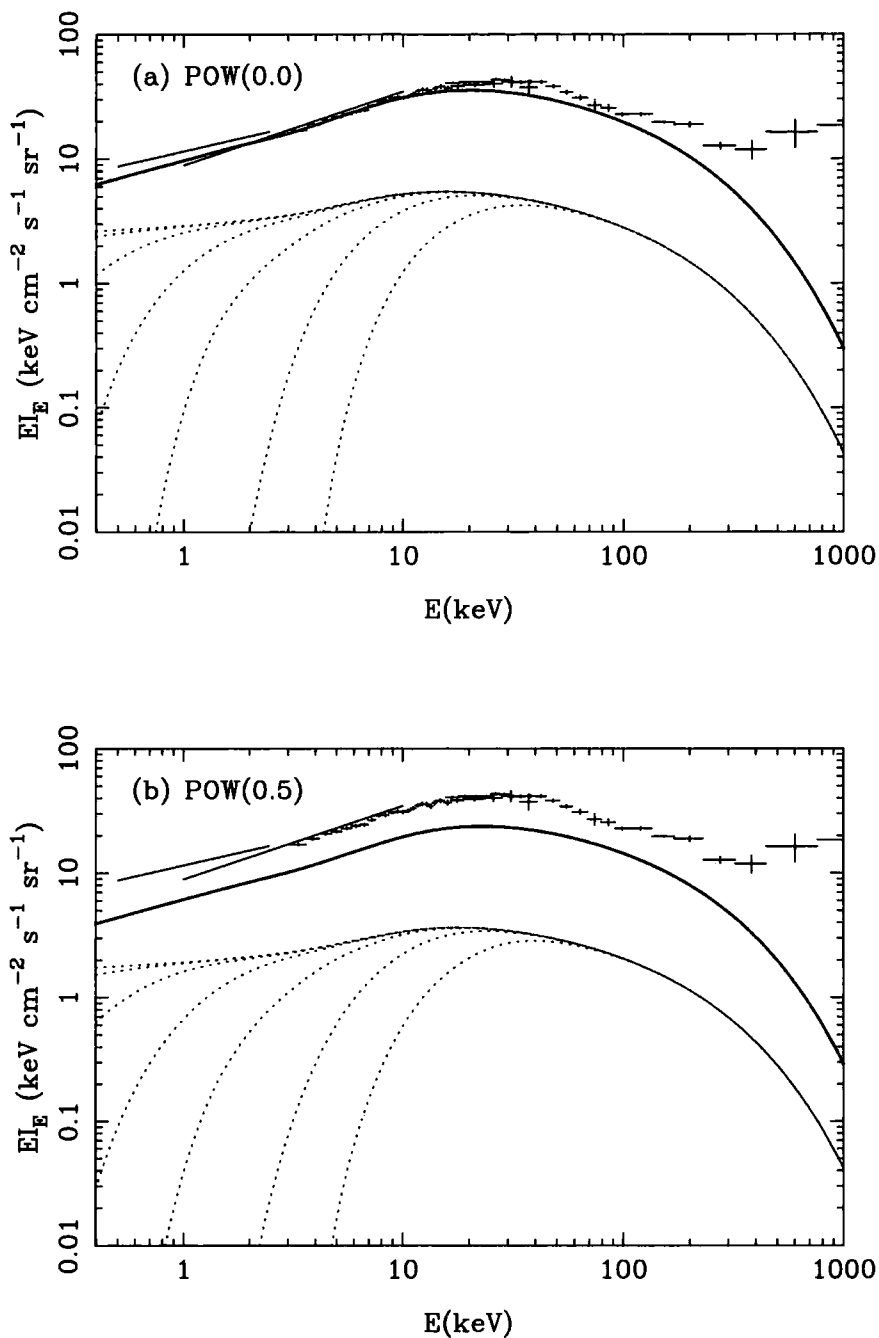
Figure 2.7: Predicted obscured AGN contribution to the XRB intensity, for power-law luminosity evolution models with (a) $q_0 = 0.0$ and (b) $q_0 = 0.5$. An intrinsic spectrum of $\alpha_x = 0.9$ and $kT = 360\,\text{keV}$ is assumed. Seven populations of columns have been used: $N_H = 10^{19.5}$ to $10^{25.5}\,\text{cm}^{-2}$. Each is represented by a separate dotted line, and the sum of their contributions is shown by the dashed line. Observations in the range $3\,\text{keV} - 1\,\text{MeV}$ are from *HEAO-1* A2 & A4 (Gruber 1992); $1 - 10\,\text{keV}$ from *ASCA* (Gendreau et al. 1995); and $0.5 - 2.4\,\text{keV}$ from *ROSAT* (Georgantopoulos et al. 1996).
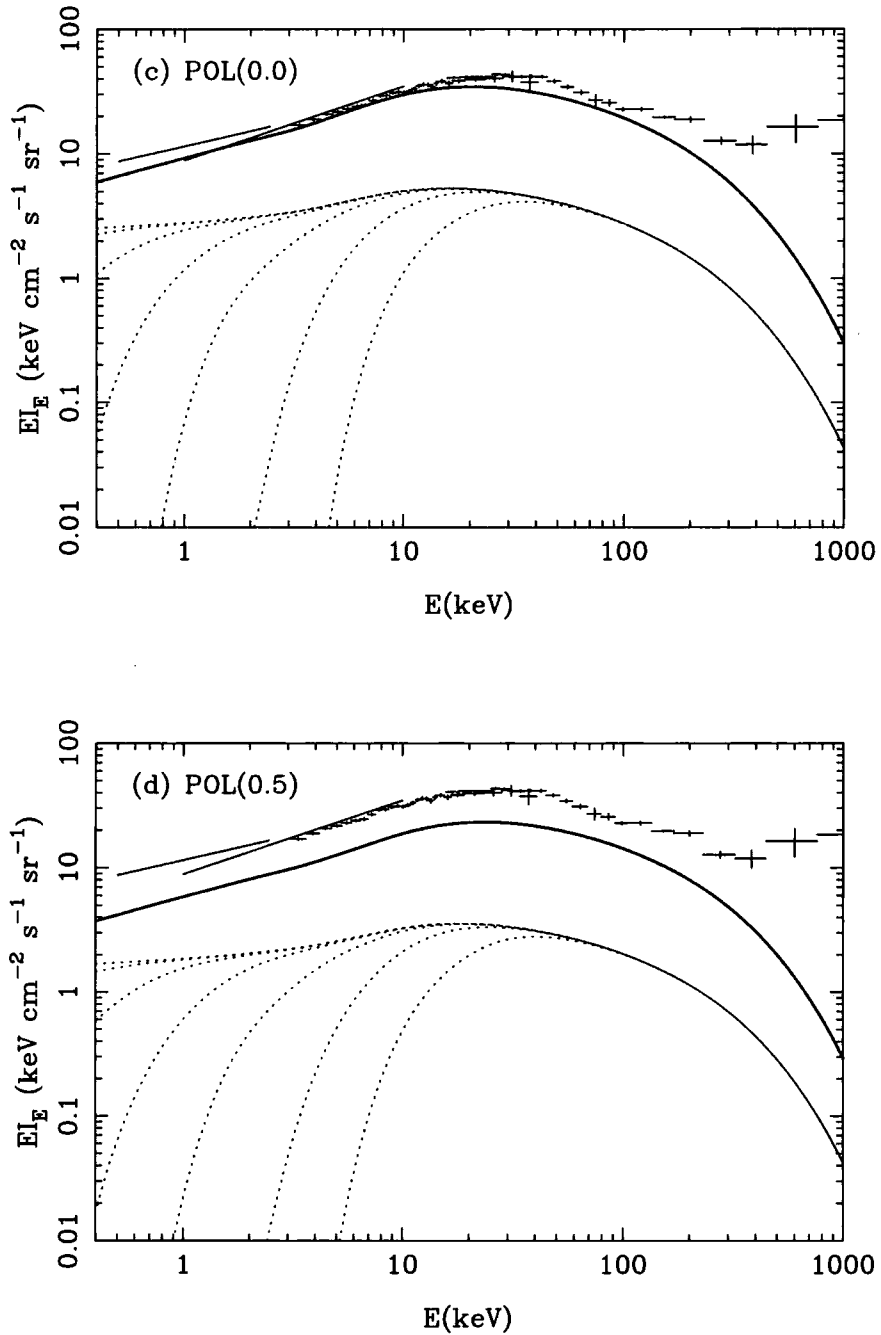
Figure 2.7: (c,d) Obscured AGN contribution to the XRB intensity predicted by polynomial luminosity evolution models, using $q_0 = 0.0$ and $q_0 = 0.5$ respectively.

proximation is a power-law with spectral index $\alpha_x = 0.9$ and exponential cutoff at high energies, $kT \sim 360\,\text{keV}$:

$$\rho(E) = AE^{-\alpha_x} \exp\left(-\frac{E}{kT}\right).$$

However, here we have chosen to use XSPEC to add a component to the spectrum due to reflection from an accretion disc, as in Madau et al. (1994).

Invoking the Unified Theory of AGN, we then take this shape for the intrinsic spectrum of obscured populations of objects and then use XSPEC to calculate the photo-electric absorption for each column used. (We note here that a more rigorous treatment should include the fact that for column densities above $N_H \sim 10^{24.5}\,\mathrm{cm}^{-2}$, the absorbing material becomes Compton thick, and only a small fraction of the flux is transmitted. However, we have chosen not to include this, as we are not aiming to provide a perfect fit at the high energies where these types of objects start to contribute. Our conclusions are not affected by the exclusion of such large column densities.)

A weighted average emissivity, ρ_{loc}, is then constructed containing the emission due to each population. This emissivity is then integrated over redshift, $0 < z < z_{max}$, to calculate the intensity of the XRB (Weinberg 1972; Schwartz & Gursky 1974).

$$I(E_0) = \frac{c}{4\pi H_0} \int_0^{z_{max}} \frac{f_{evol}(z)}{(1+z)^2} \frac{\rho[E_0(1+z)]}{\sqrt{1+2q_0 z}} dz.$$

The dependence of evolution on redshift, $f_{evol}(z)$, can be parametrized as in Equations 2.1 and 2.2 as either polynomial or power-law, where we have used power-law evolution with a redshift cutoff, z_{cut}.

In Fig. 2.7, the spectral shape predicted by our model is compared with current observations, where the data are as follows: $3\,\mathrm{keV} - 1\,\mathrm{MeV}$ from *HEAO-1* A2 and A4 experiments (Gruber 1992); between $1 - 10\,\mathrm{keV}$ is the *ASCA* result (Gendreau et al. 1995); $0.5 - 2.4\,\mathrm{keV}$ from *ROSAT* data (Georgantopoulos et al. 1996). Each of our model populations is represented by a separate dotted line, with (from left to right on the diagram) $N_H = 10^{19.5}\,\mathrm{cm}^{-2}$ up to $10^{25.5}\,\mathrm{cm}^{-2}$, and the total contribution is plotted as a dashed line.

It can be seen that for a $q_0 = 0.0$ cosmology, both power-law and polynomial forms for the luminosity evolution provide a good fit to the XRB spectrum between 0.5 and $100\,\mathrm{keV}$, above which different types of object start to contribute. We have not allowed the normalizations of each individual population to vary in order to achieve a better fit, as this has been performed by previous authors (see *e.g.* Comastri et al. 1995). However, having shown that this simple model does give good agreement with the available X-ray data, we can now use it to test various selection effects in existing X-ray surveys and to make predictions for future X-ray and sub-mm surveys, as will be described in Chapters 3 and 4.

With a $q_0 = 0.5$ cosmology, the intensity of the background is too low by about a third, as expected given the fact that the faint number counts are underpredicted. Looking more closely at the soft LogN:LogS predictions for low q_0 in Fig. 2.5(a), it can be seen that the counts are slightly overpredicted in the region around $S(0.5 - 2\,\mathrm{keV}) \sim 4 \times 10^{-15}\,\mathrm{erg\,cm^{-2}\,s^{-1}}$, which is where
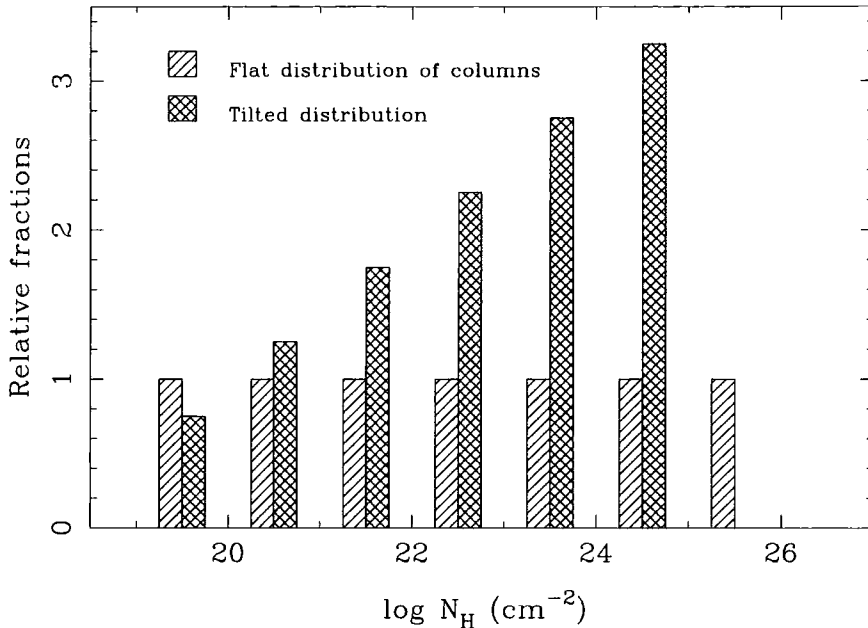
Figure 2.8: The tilted column density distribution (cross-hatched regions) used in order to achieve better fits to the data in a $q_0 = 0.5$ universe, compared with the flat distribution (hatched regions) used in Section 2.1. The two models are shown slightly offset from one another for clarity

the largest contribution to the total intensity comes from: a small increase here has a measurable effect. If this is the case, then this motivates the investigation of tilted distributions of column densities, in order to increase the relative contribution from absorbed objects while keeping the same unabsorbed numbers. This pushes the faint end counts higher, while retaining the bright end slope, and is discussed further in Section 2.6.

2.6 An alternative column distribution for $q_0 = 0.5$

From Sections 2.4 and 2.5, we have seen that for a $q_0 = 0.5$ universe, it is difficult to simultaneously fit both the bright and faint X-ray source counts in the $0.5 - 2$ keV band, which leads to the underprediction of the total intensity of the background at these energies (see Fig. 2.5(c) and (d)). This is due to the decreased volume present at high redshifts, compared to the $q_0 = 0.0$ case. Here we investigate a number of alternative column density distributions, in order to see how the fit of the $q_0 = 0.5$ model can be improved.

We cannot increase the population of unabsorbed objects, as the source counts at bright fluxes place limits on the numbers that may be present. However at faint fluxes, where high redshift and more absorbed sources start to dominate, it is possible to increase their contribution, and we
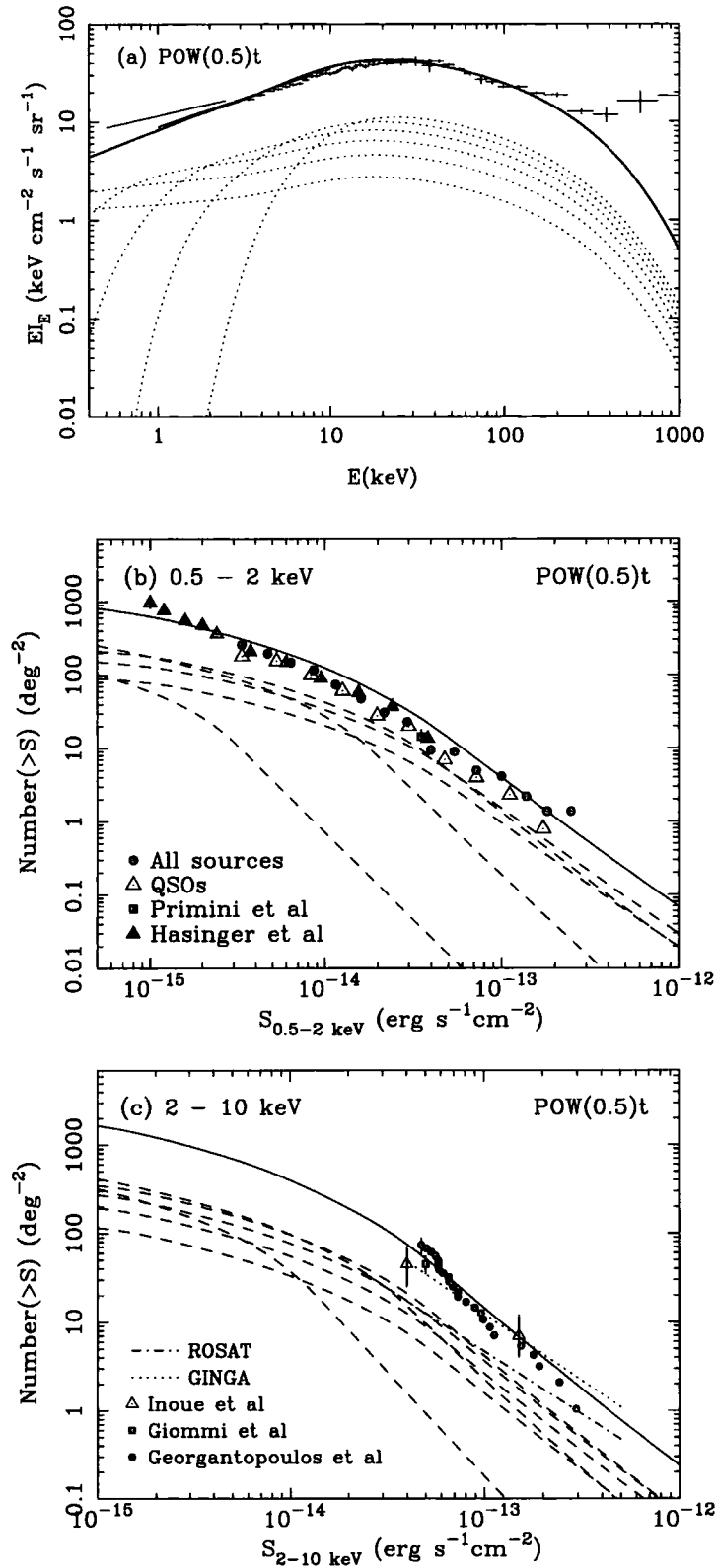
Figure 2.9: The results of using a tilted distribution of column densities in order to achieve better fits to the data in a $q_0 = 0.5$ universe, using power-law evolution parameters. (a) Fit to the XRB spectrum. (b,c) Soft and hard LogN:LogS distributions respectively, where the populations $N_H = 10^{19.5-23.5}$ cm^{-2} are visible in (b), and all six populations are visible in (c).
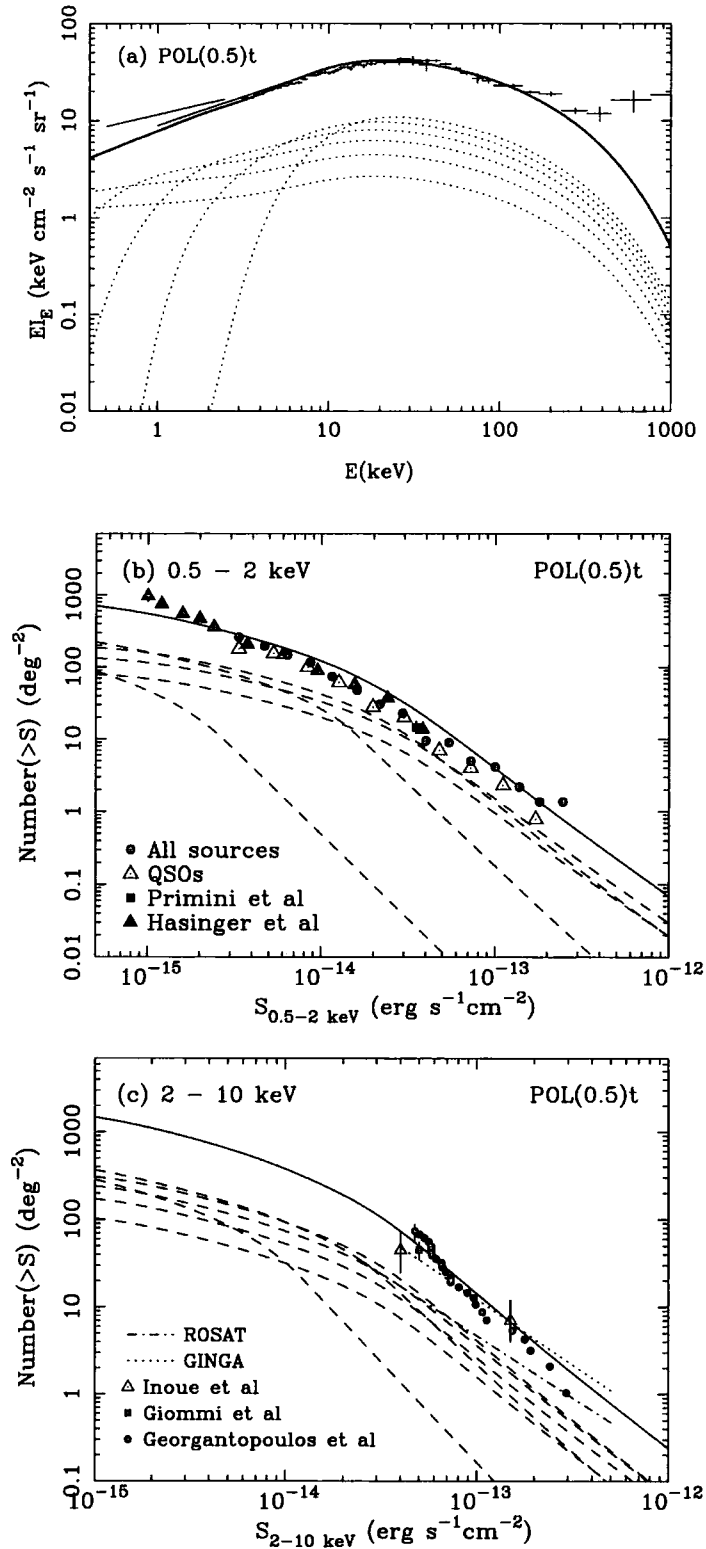
Figure 2.10: The results of using a tilted distribution of column densities in order to achieve better fits to the data in a $q_0 = 0.5$ universe, using polynomial evolution parameters. (a) Fit to the XRB spectrum. (b,c) Soft and hard LogN:LogS distributions respectively, where the populations $N_H = 10^{19.5-23.5}$ cm^{-2} are visible in (b), and all six populations are visible in (c).

find that skewing the column density distribution to higher densities improves the fit. This can be modelled in many different ways, but we have chosen to look at three simple cases.

First, we take two populations only, unabsorbed ($N_H = 10^{19.5} \, \mathrm{cm}^{-2}$) and absorbed ($N_H = 10^{23} \, \mathrm{cm}^{-2}$), and vary their respective normalizations. In this way, it is easy to steepen the faint end of the soft source counts to match the data. However, the slope obtained is not sufficiently steep to avoid overpredicting the counts at intermediate fluxes, and the increased contribution from absorbed sources is immediately too high for the hard counts and the background intensity above 1 keV. There are two further disadvantages to such a model: its bimodal nature means that, not only is it not possible to reproduce the observed smooth power-law dependence on energy of the background intensity, as a distinct jump occurs in the spectrum, but also this very bimodality leaves no room for the moderately absorbed X-ray galaxies that we know exist with column densities of $N_H \sim 10^{21} \, \mathrm{cm}^{-2}$.

Therefore, we return to a broader distribution of column densities, and assume that more heavily absorbed populations have a higher space density than the unabsorbed populations, for example, let populations with $N_H < 10^{22} \, \mathrm{cm}^{-2}$ have normalizations of Φ^* and populations with $N_H > 10^{22} \, \mathrm{cm}^{-2}$ have normalizations of $2 \times \Phi^*$. This certainly helps to boost the faint soft counts and the background intensity, but still does not account for the entire XRB. Further increasing the absorbed contribution to $3 \times \Phi^*$ gives a better fit to the counts, but starts to overpredict the background intensity at higher energies, due to the large numbers of highly absorbed sources.

Lastly, we investigate the possibility of using tilted distributions of column densities, so that there is no longer a discontinuity in their relative contributions, making it easier to reproduce the smooth shape of the XRB spectrum. We present one particular case, not necessarily unique, where we have chosen to retain our smooth column distribution, but to tilt it towards higher densities. In this way, we use the relationship:

$$\Phi(N_H) = \left\{ 1 + A \log\left(\frac{N_H}{10^{20}}\right) \right\} \Phi^*,$$

such that $A = 0$ corresponds to our original flat distribution, and $A > 0$ means that the highest column densities have the largest normalization. For example, for a model using six populations, $N_H = 10^{19.5}, 10^{20.5}, 10^{21.5}, 10^{22.5}, 10^{23.5}, 10^{24.5} \, \mathrm{cm}^{-2}$, with $A = 0.5$ (as in Fig. 2.8), we obtain good fit to the data. The results are shown in Fig. 2.9 and 2.10, for power-law and polynomial evolution models respectively. We denote these tilted models by POW(0.5)t and POL(0.5)t hereafter, in order to distinguish them from models using flat columns distribution.

The use of tilted column distributions proves to be a reasonable way of making a $q_0 = 0.5$ universe consistent with the data, being in better agreement with the *ASCA* number counts, although it still has difficulties in attaining the steep faint soft counts simultaneously with the hard counts and XRB spectral constraints.

2.7 Conclusions

In this Chapter, we have developed an obscured QSO model for the X-ray background, which can fit the source counts both at soft and hard X-ray energies, and the background spectrum. This model incorporates the X-ray galaxies detected in faint *ROSAT* surveys (Roche et al. 1995; Griffiths et al. 1996; McHardy et al. 1998) into the obscured QSO framework. Here they appear generally as intrinsically low luminosity objects with modest amounts of absorption ($N_H <$ $10^{21}\,\mathrm{cm}^{-2}$). We can claim this because in Fig. 2.7(a) and (c), we see that our model with a flat N_H distribution for the obscured QSO populations fits the total *ROSAT* X-ray background in the range $0.5 - 2\,\mathrm{keV}$, in a low q_0 universe. Madau et al. (1994) did not attempt to fit this soft X-ray region, as at the time, the *ROSAT* result was not in agreement with the *ASCA* measurement. More recently, the *ROSAT* XRB spectrum has been found to be considerably flatter, when Galactic contamination is taken into account in the correct manner (Georgantopoulos et al. 1996). Of course, the bimodal model of Madau et al., peaking at a column of $N_H = 10^{24}\,\mathrm{cm}^{-2}$, makes it difficult to accommodate the low redshift X-ray galaxies, given the upper limits of $N_H < 10^{21}\,\mathrm{cm}^{-2}$ inferred from their X-ray spectra. However, it is easier to incorporate such galaxies into the model of Comastri et al., which has a broader range of absorbing columns. These authors also concentrated on fitting the hard XRB spectrum and did not try to fit the softer *ROSAT* range. Therefore, before this work, it remained unproven that this type of model could simultaneously fit the hard and soft XRB spectra.

For high density universes, a flat distribution of obscuring columns has greater difficulty in reproducing the observations, and therefore in Section 2.6, we have biased the column distribution towards higher N_H, which simultaneously increases the soft counts and contribution to the XRB, while not overproducing the hard X-ray counts. This retains the unifying feature of the flat column distribution, in that the X-ray galaxies are an intrinsic part of the model.

We have shown here that obscured QSOs may outnumber unobscured QSOs in the approximate ratio 4:1, and that such models can give good fits to the XRB spectrum and the source counts, LogN:LogS. In the next Chapter, we use our obscured QSO model to make predictions at optical wavelengths of the numbers of QSOs, NELGs and blank fields that may be detected both in existing surveys, and in future much deeper X-ray survey with satellites such as *AXAF* and *XMM*.

References

Almaini O., Boyle B. J., Griffiths R. E., Shanks T., Stewart G. C., Georgantopoulos I., 1995, MNRAS, 277, L31

Almaini O., Shanks T., Boyle B. J., Griffiths R. E., Roche N., Stewart G. C., Georgantopoulos I., 1996, MNRAS, 282, 295

Almaini O., Shanks T., Griffiths R. E., Boyle B. J., Roche N., Georgantopoulos I., Stewart G. C., 1997, MNRAS, 291, 372

Arnaud K. A., 1996, in Jocoby G.H., Barnes J., eds, *Proc. of the ADASS V Conference*: ASP Conf. Series 101: San Francisco, Vol. 5, p. 17

Boyle B. J., Almaini O., Georgantopoulos I., Blair A. J., Stewart G. C., Griffiths R. E., Shanks T., Gunn K. F., 1998b, MNRAS, 297, L53

Boyle B. J., Georgantopoulos I., Blair A. J., Stewart G. C., Griffiths R. E., Shanks T., Gunn K. F., Almaini O., 1998a, MNRAS, 296, 1

Boyle B. J., Shanks T., Georgantopoulos I., Stewart G. C., Griffiths R. E., 1994, MNRAS, 271, 639

Butcher J. A. et al., 1997, MNRAS, 291, 437

Comastri A., Setti G., Zamorani G., Hasinger G., 1995, A&A, 296, 1

De Zotti G., Boldt E. A., Marshall F. E., Swank J. H., Szymkowiak A. E., Cavaliere A., Danese L., Franceschini A., 1982, ApJ, 253, 47

Gendreau K. C. et al., 1995, PASJ, 47, L5

Georgantopoulos I., Stewart G. C., Blair A. J., Shanks T., Griffiths R. E., Boyle B. J., Almaini O., Roche N., 1997, MNRAS, 291, 203

Georgantopoulos I., Stewart G. C., Shanks T., Boyle B. J., Griffiths R. E., 1996, MNRAS, 280, 276

Giommi P., Fiore F., Ricci D., Molendi S., Maccarone M. C., Comastri A., 1998, Nucl. Phys. Proc. Suppl., 69, 591

Griffiths R. E., Della Ceca R., Georgantopoulos I., Boyle B. J., Stewart G. C., Shanks T., Fruscione A., 1996, MNRAS, 281, 71

Griffiths R. E., Padovani P., 1990, ApJ, 360, 483

Gruber D. E., 1992, in Barcons X., Fabian A.C., eds, *The X-ray Background*, p. 44

Hasinger G., Burg R., Giacconi R., Schmidt M., Trümper J., Zamorani G., 1998, A&A, 329, 482

Inoue H., Kii T., Ogasaka Y., Takahashi T., Ueda Y., 1996, in Zimmerman U., Truemper J.E., Yorke H., eds, *Roentgenstrahlung from the Universe*, Vol. MPE Report 263, p. 323

Iwasawa K., Fabian A. C., Brandt W. N., Crawford C. S., Almaini O., 1997, MNRAS, 291, L17

Madau P., Ghisellini G., Fabian A., 1994, MNRAS, 270, L17

Matt G., Fabian A. C., 1994, MNRAS, 267, 187

McHardy I. M. et al., 1998, MNRAS, 295, 641

Morrison R., McCammon D., 1983, ApJ, 270, 119

Ohta K., Yamada T., Nakanishi K., Ogasaka Y., Kii T., Hayashida K., 1996, ApJL, 458, L57

Primini F. A., Murray S. S., Huchra J., Schild R., Burg R., Giacconi R., 1991, ApJ, 374, 440

Roche N., Griffiths R. E., Della Ceca R., Shanks T., Boyle B. J., Georgantopoulos I., Stewart G. C., 1996, MNRAS, 282, 820

Roche N., Shanks T., Georgantopoulos I., Stewart G. C., Boyle B. J., Griffiths R. E., 1995, MNRAS, 273, L15

Romero-Colmenero E., Branduardi-Raymont G., Carrera F. J., Jones L. R., Mason K. O., McHardy I. M., Mittaz J. P. D., 1996, MNRAS, 282, 94

Schwartz D., Gursky H., 1974, in *X-ray Astronomy*, eds. Giacconi R., Gursky H.; Reidel, Dordrecht; Astrophysics and Space Science Library. Volume 43, p, 359

Shanks T., Georgantopoulos I., Stewart G. C., Pounds K. A., Boyle B. J., Griffiths R. E., 1991, Nat, 353, 315

Weinberg S., 1972, *Gravitation and cosmology: Principles and applications of the general theory of relativity.* New York: Wiley

Chapter 3

Optical consequences of

Obscured QSO Models

ABSTRACT. Using our obscured QSO model for the XRB, we investigate the selection effects present in QSO samples to see whether these can cause the observed narrow dispersion in the X-ray/optical flux ratio *vs* redshift relation. We find that even for a flat distribution of absorbing columns, reasonable fits to the XRB can be obtained while both optical and X-ray absorption combine to produce the tight observed X-ray/optical correlation. X-ray sources with no obvious optical counterparts are predicted by this obscured QSO model, both at soft and hard energies, and the models show good agreement with the numbers of these 'blank field' sources found in deep *ROSAT* surveys. Our obscured QSO model also predicts that > 50 per cent of *AXAF* sources will be optically blank, at redshifts $z > 1$, with a nuclear flux fainter than $B = 24.5$ mag. Such 'blank fields' will be as numerous as unobscured broad line QSOs and could dominate low redshift NELGs by a factor of four to one.

3.1 Motivation

Our investigation into the effect of absorption on QSO samples from different wavelength regimes is prompted by two conflicting results in recent literature; the first being the work of Webster et al. (1995) who find evidence for a wide dispersion in $B - K$ colours in radio-loud QSOs. When plotting the colour-magnitude diagram for the Parkes QSOs, they find a huge spread in the range $1 < B - K < 8$, compared with the much smaller dispersion found in optically selected QSOs from the Large Bright Quasar Survey (LBQS; Morris et al. 1991; Hewett et al. 1991) of $2 < B - K < 4$. The scatter in the radio-selected sample could be caused by reddening from intrinsic dust, which would be consistent with AGN unification schemes (Antonucci 1993) and models for the formation of the X-ray background which invoke large populations of dust-obscured AGN (Madau et al. 1994; Comastri et al. 1995). However, an opposing view is held by

Boyle & Di Matteo (1995), who argue that the tightness of the X-ray/optical flux ratio relationship for X-ray and optically selected QSOs implies that only a small fraction of objects may be obscured by significant amounts of intrinsic dust.

In their work, Boyle & Di Matteo (1995) look at the X-ray and optical properties of a sample of 68 X-ray selected QSOs from the Cambridge-Cambridge *ROSAT* Serendipity Survey (CRSS; catalogued in Boyle, Wilkes & Elvis 1997). The CRSS comprises 123 *ROSAT* X-ray sources with soft X-ray fluxes of $S(0.5 - 2\,\mathrm{keV}) > 2 \times 10^{-14}\,\mathrm{erg\,cm^{-2}\,s^{-1}}$, with a spectroscopic identification rate of 90 per cent. If the Webster et al. interpretation is true and the $B - K$ scatter is caused by intrinsic dust, then a similar range of values would be expected in the equivalent quantity for these QSOs, which is the X-ray/optical flux ratio, f_X/f_B.

However, Boyle & Di Matteo find that the dispersion in X-ray/optical flux ratios for the CRSS X-ray selected QSOs is low, $\sigma[\log(f_X/f_B)] \sim 0.4$, reflecting the fact that virtually the same QSOs are selected in optical and soft X-ray selected samples. The spread in the relation is used to place a limit on the maximum column density present in these objects, and the extinction inferred from these data is at most $A_B = 2\,\mathrm{mag}$. This is interpreted as implying that the majority of QSOs are unaffected by dust. If there existed a large population of obscured QSOs, Boyle & Di Matteo suggest that the small scatter in f_X/f_B would be unexpected since absorption could produce very different selection effects in the optical and X-ray regimes.

We now discuss these two observations in more detail. The Webster et al. (1995) work is concerned with the optical identification of a complete sub-sample of Parkes flat spectrum sources, with spectral index $\alpha_r < 0.5$, fluxes of $S(2.7\mathrm{GHz}) > 0.5\,\mathrm{Jy}$, galactic latitude $|b| > 20°$, and declination $-45° < \delta < +3°$. Of the 323 sources in this sample, the spectroscopic identifications obtained to $B < 22.5\,\mathrm{mag}$ included 218 QSOs[1]. Webster et al. also obtained $K-$band imaging to $K < 19.5\,\mathrm{mag}$, in order to compare the optical/infra-red colours of these sources. The observed wide range of $B - K$ colours could be an intrinsic property of the radio-loud QSOs, in which dust is an integral component in radio-selected QSOs. Alternatively, the scatter in $B - K$ could be interpreted as due to varying amounts of dust along the line of sight to the QSOs, in which case, one would expect the optical sample to have a similarly large scatter. In support of the hypothesis that the dust is intrinsic to the QSOs is the absence of a correlation between the equivalent widths of the photo-ionized emission lines. If the observed red QSO colours were representative of the relative fluxes at ultra-violet and optical wavelengths, then a red QSO would have lower ultra-

---

[1] The sample of 323 sources comprises 218 QSOs, 18 BL Lacs, 37 galaxies/planetary nebulae/etc., and 50 with no spectroscopic IDs at present.

violet ionizing continuum and therefore weaker emission lines. As the observed emission line equivalent widths appear to be independent of QSO colour, then the cause of the spread in colours must be exterior to the nuclear emission region, with a likely mechanism being the presence of dust.

It has also been shown that a similar population of radio-quiet red QSOs exists. Kim & Elvis (1999) selected a sample of 45 radio-quiet, optically red ($O - E > 2, O \leq 20$ from the APM catalogue) *ROSAT* sources with *PSPC* fluxes brighter than $10^{-13} \, \mathrm{erg \, cm^{-2} \, s^{-1}}$, for which they obtained spectroscopic identifications. Of these candidates, seven were found to be red QSOs, with spectra and Balmer line ratios consistent with absorption, rather than being intrinsic properties of the emission. The degree of obscuration is only mild in this case, with $A_V \sim 2$, but suggests that more heavily absorbed sources will exist, but that would not be picked up using these selection criteria.

Here, our aim is to ascertain whether the obscured QSO model developed in Chapter 2 which fits both the XRB spectrum and X-ray source counts, can simultaneously produce the observed low dispersion in the X-ray/optical flux ratio. In particular, we shall investigate whether X-ray and optical absorption will produce the Boyle & Di Matteo (1995) result as a selection effect. We also verify that our models are consistent with the $B - K$ colours found by Webster et al. (1995) for a radio-selected QSO sample.

In Section 3.2, we show how a QSO spectrum is affected by dust extinction due to the presence of a dusty molecular torus. The X-ray number-redshift or $n(z)$ relation predicted by our models is presented in Section 3.3, and compared with the redshift distributions and numbers of blank field sources (defined here as having a nuclear magnitude of $B > B_{lim}$, where B_{lim} depends on the survey parameters) observed in existing surveys. Then in Section 3.4, we use these methods in order to investigate the selection effects present in X-ray and optically selected QSO samples, and determine the X-ray/optical flux ratio versus redshift relation predicted by our obscured QSO model. In Section 3.5, we use our obscured QSO model to predict both the X-ray/optical (f_X/f_K) and optical/infra-red ($B - K$) colour distributions expected for an X-ray selected sample of QSOs. The f_X/f_K distribution is then compared directly with the results of Boyle & Di Matteo (1995) and our predictions in the B-band, as described in Section 3.4, and the $B - K$ distributions are compared with the Webster et al. (1995) results. Finally, we present model predictions for future deep X-ray surveys with *AXAF* and *XMM*, together with our conclusions in Section 3.6.

3.2 Modelling the Optical Properties of QSOs

3.2.1 Canonical optical QSO spectrum

Assuming that the optical spectrum of a QSO can be modelled as a power-law, we take $\alpha_{opt} = 0.8$ (Francis 1993) as our canonical value. We relate the optical luminosity to the X-ray luminosity by introducing a hypothetical optical/X-ray power-law, of spectral index α_{ox}. This is defined in the rest frame of the QSO as follows:

$$\alpha_{ox} = -\frac{\log[l(\nu_x)/l(\nu_{opt})]}{\log(\nu_x/\nu_{opt})} = -0.384 \, \log[l(\nu_x)/l(\nu_{opt})]. \tag{3.1}$$

where the monochromatic luminosities in the X-ray and optical, $l(\nu_x)$ and $l(\nu_{opt})$ are measured at $\nu_x = 2 \, \text{keV}$ and $\nu_{opt} = 2500 \, \text{Å}$ respectively. Here we take an average value from the literature of $\alpha_{ox} = 1.5$ (Tananbaum et al. 1979; Green et al. 1995; Laor et al. 1997; Yuan et al. 1998a). There is evidence to suggest that α_{ox} is related to the intrinsic optical luminosity (Yuan, Siebert & Brinkmann 1998b), but as the determination of this relationship will be affected by the selection effects that we are investigating here, we do not include this in our models.

The adoption of a mean value for α_{ox} means that we can directly calculate the intrinsic optical properties for a sample of QSOs taken from a known X-ray luminosity function. From this, we can then evaluate the effects of dust obscuration on X-ray selected QSOs.

3.2.2 The effects of dust extinction on QSO spectra

The relationship between the strength of the absorption by gas of X-ray photons, and the absorption by dust of optical photons, is determined by the gas to dust ratio. For our modelling, we have chosen to use the Galactic gas to dust ratio. However, we note that there is evidence to suggest that this ratio may differ for a small fraction of AGN (Granato, Danese & Franceschini 1997).

The variation in the strength of dust absorption in the infra-red, optical and ultra-violet can be crudely approximated by the relationship $A_\lambda \propto 1/\lambda$. However, a more reliable technique and one we have adopted in our models, is to use the empirically determined fit to the extinction in the infra-red and optical taken from Howarth (1983), and in the ultra-violet from Seaton (1979). This takes into account such departures from the $1/\lambda$ law as the 2200 Å graphite feature. Nevertheless, we note that using the simpler $1/\lambda$ form does not affect our broad conclusions, which indicates that our results are robust with respect to changes in the extinction law at this level. Defining $x = 1/\lambda$
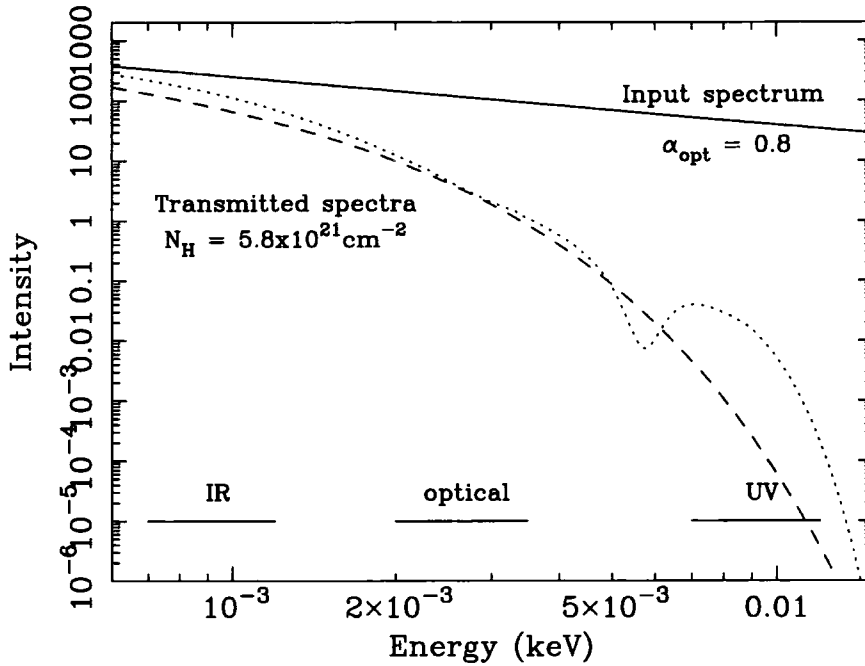
Figure 3.1: Extinction at infra-red, optical and ultra-violet energies for a column of $N_H = 5.8 \times 10^{21}$ cm^{-2}. The incident spectrum is a power-law, $I \propto \nu^{-\alpha_{opt}}$, with spectral index $\alpha_{opt} = 0.8$ (solid line). We show an approximation to the extinction of $A_\lambda \propto 1/\lambda$ (dashed line), and a polynomial fit to the results of Howarth (1983) and Seaton (1979) (dotted line).

with λ measured in μm, and $X(x) = A_\lambda/E_{B-V}$, the extinction has the following polynomial form:

$$
X(x) = \begin{cases}
[(1.86 - 0.48x)x - 0.1]x & 0 \le x < 1.83, \\
3.1 + 2.56(x - 1.83) - 0.993(x - 1.83)^2 & 1.83 \le x < 2.75, \\
1.56 + 1.048x + 1.01/[(x - 4.60)^2 + 0.280] & 2.70 \le x < 3.65, \\
2.29 + 0.848x + 1.01/[(x - 4.60)^2 + 0.280] & 3.65 \le x < 7.14, \\
16.17 - 3.20x + 0.2975x^2 & 7.14 \le x \le 10.0.
\end{cases}
\tag{3.2}
$$

In Fig. 3.1, we show these two forms for the extinction due to an absorbing column of $N_H = 5.8 \times 10^{21}$ cm^{-2}, acting on a canonical power-law of spectral index $\alpha_{opt} = 0.8$ (Francis 1993).

3.2.3 Magnitude calculation

Once the transmitted spectrum of an obscured QSO has been calculated, then it is possible to find the received flux and hence the observed magnitude. A combination of CCD and B-band filter can be approximated by a central wavelength, $\lambda_0 = 0.44\mu$m, and an effective FWHM, $\Delta\lambda_0 = 0.1\mu$m (Allen 1973), and we choose to approximate this by a rectangular filter, $0.4 - 0.5\mu$m. To convert from measured fluxes to magnitudes, we use the monochromatic flux for a zero magnitude

z	A_K	A_B	A_{SX}	A_{HX}
0.0	0.38	4.20	1.51	0.061
0.5	0.60	5.67	0.54	0.022
1.0	1.00	9.45	0.27	0.011
2.0	2.20	8.20	0.09	0.004

Table 3.1. Absorption in magnitudes for $N_H = 5.8 \times 10^{21}$ cm^{-2} (corresponding to $E_{B-V} = 1$ mag) for observations in the: A_K - near infra-red; A_B - optical; A_{SX} - soft X-ray (*i.e.*, *ROSAT*); and A_{HX} - hard X-ray (*i.e.*, *ASCA, BeppoSAX*) bands of a source absorbed in its restframe at a range of redshifts (from Howarth 1983; Seaton 1979; Morrison & McCammon 1983).

star, $f_B(0) = 6.61 \times 10^{-9}$ erg cm^{-2} s^{-1} Å^{-1}, and obtain the relationship between observed magnitude, B, and received broad-band flux, f_B, of:

$$B = -2.5 \log f_B + 2.5 \log (f_B(0) \times \Delta\lambda_0) = -2.5 \log f_B - 12.97. \tag{3.3}$$

where $f_B = \int f(\lambda) \, d\lambda$ for 0.4μm $< \lambda < 0.5\mu$m. Similarly, a combination of infra-red detector and $K-$band filter can be approximated by a central wavelength, $\lambda_0 = 2.2\mu$m, and an equivalent FWHM, $\Delta\lambda_0 = 0.4\mu$m (Zombeck 1990), and we approximate this by a rectangular filter, $2.0 - 2.4\mu$m. The monochromatic flux for a zero magnitude star is $f_K(0) = 4.17 \times 10^{-11}$ erg cm^{-2} s^{-1} Å^{-1}, giving:

$$K = -2.5 \log f_K + 2.5 \log (f_K(0) \times \Delta\lambda_0) = -2.5 \log f_K - 16.94. \tag{3.4}$$

These two relationships are used to convert the received flux from an obscured QSO, whose spectrum has been calculated using the extinction in Equation 3.2, into an observed magnitude in either the $B-$ or $K-$band , or vice versa.

3.2.4 Comparison with X-ray absorption

The effects of photo-electric absorption on a QSO spectrum at X-ray energies has been described in Section 2.2. This is compared with the dust extinction in Table 3.1, which gives the absorption in magnitudes in four energy ranges: infra-red, optical, soft X-rays ($0.5 - 2$ keV) and hard X-rays ($2 - 10$ keV). The extinction has been calculated for a fiducial column of $N_H = 5.8 \times 10^{21}$ cm^{-2}, which corresponds to an extinction of $E_{B-V} = 1$ mag, assuming Galactic gas to dust ratios. These broad-band values can be approximately scaled to other column densities using the

direct proportionality between the absorption, A_λ, and the column density, N_H, where the exact relationship for monochromatic radiation is:

$$A_\lambda(N_H) = \frac{N_H}{5.8 \times 10^{21}\,\mathrm{cm}^{-2}}\, X(x),$$

and $X(x)$ is defined in Equation 3.2. For absorbed sources at low redshifts, even at a moderate column of $N_H = 5.8 \times 10^{21}\,\mathrm{cm}^{-2}$, there is a significant amount of absorption both in the B-band and soft X-rays, but much less in the K-band. At high redshifts, the X-ray absorption decreases while the B- and K-band absorption both increase. In the X-ray this is because a higher energy part of the spectrum, less susceptible to photo-electric absorption is being redshifted into the observed passband. In the B-band, the ultra-violet part of the spectrum is redshifted into the observed passband and this is heavily affected by the presence of dust. Thus it seems that while at low redshift, the selection effects at optical and X-ray energies may well be similar, at high redshift, the effects of X-ray absorption become weaker while the optical absorption continues to strengthen. In Section 3.4, we investigate whether the dust selection effect in the optical on its own is enough to satisfy the X-ray/optical dispersion constraint.

If the column rises to $N_H \sim 10^{24}\,\mathrm{cm}^{-2}$ as used in Madau et al. (1994) then the values in Table 3.1 have to be multiplied by a factor of ~ 170 ($\Delta B \sim 1000\,\mathrm{mag}$) which means that the QSOs will be visible only in the hard X-ray band, whatever their redshift! Thus the hard $(2 - 10\,\mathrm{keV})$ XRB spectrum and source counts may provide the strongest constraint on the existence of a highly obscured QSO population.

3.3 Blank field sources and the X-ray $n(z)$ relation

Our obscured model discussed in Chapter 2 satisfies the conditions imposed by the XRB spectrum and X-ray source counts, and we can now consider what can be learned from the optical information available for our X-ray sources. This third observational constraint on our model takes two forms: the X-ray number-redshift or $n(z)$ relation, for those sources for which an optical counterpart can be identified; and the number of so called *blank field* sources, for which no obvious optical counterparts can be found, and hence no redshift information exists. The $n(z)$ relation gives information about the populations with low to moderate obscuration, whereas the number of blank field sources will give information about the highly obscured source populations.
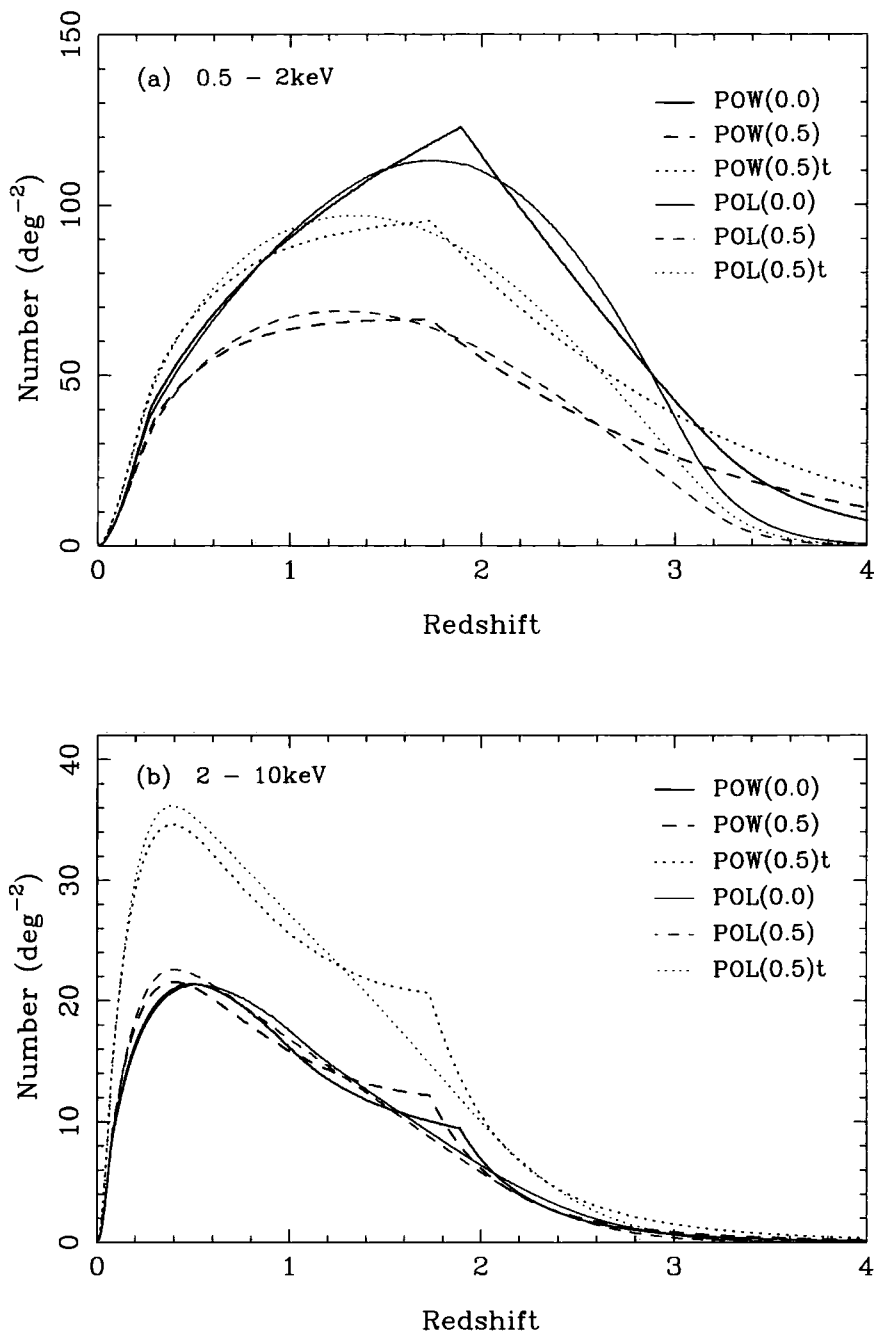
Figure 3.2: Predicted total number-redshift distribution for (a) a soft X-ray survey with $S(0.5 - 2\,\mathrm{keV})$ $> 5 \times 10^{-15}\,\mathrm{erg\,cm^{-2}\,s^{-1}}$, and (b) a hard X-ray survey with $S(2 - 10\,\mathrm{keV}) > 5 \times 10^{-14}\,\mathrm{erg\,cm^{-2}\,s^{-1}}$. These are equivalent to the *ROSAT* and *ASCA/BeppoSAX* source count predictions from Table 3.3. We have plotted the predictions for both power-law (POW) and polynomial (POL) evolution, $q_0 = 0, 0.5$ (given in brackets), plus the tilted column distribution (t) for the $q_0 = 0.5$ case. Note that at the deeper flux limits currently reached by surveys in the soft X-ray band (Hasinger et al. 1998), it is volume effects which dominate, with the low q_0 models producing the largest number of sources at redshifts $z > 1$. This is consistent with the steeper faint-end slope of the LogN:LogS relation for a low q_0 universe. At the brighter flux limits of surveys undertaken in the $2 - 10\,\mathrm{keV}$ band, the highest source densities are predicted from the models using the tilted column distribution, as more bright moderately obscured sources can be detected.
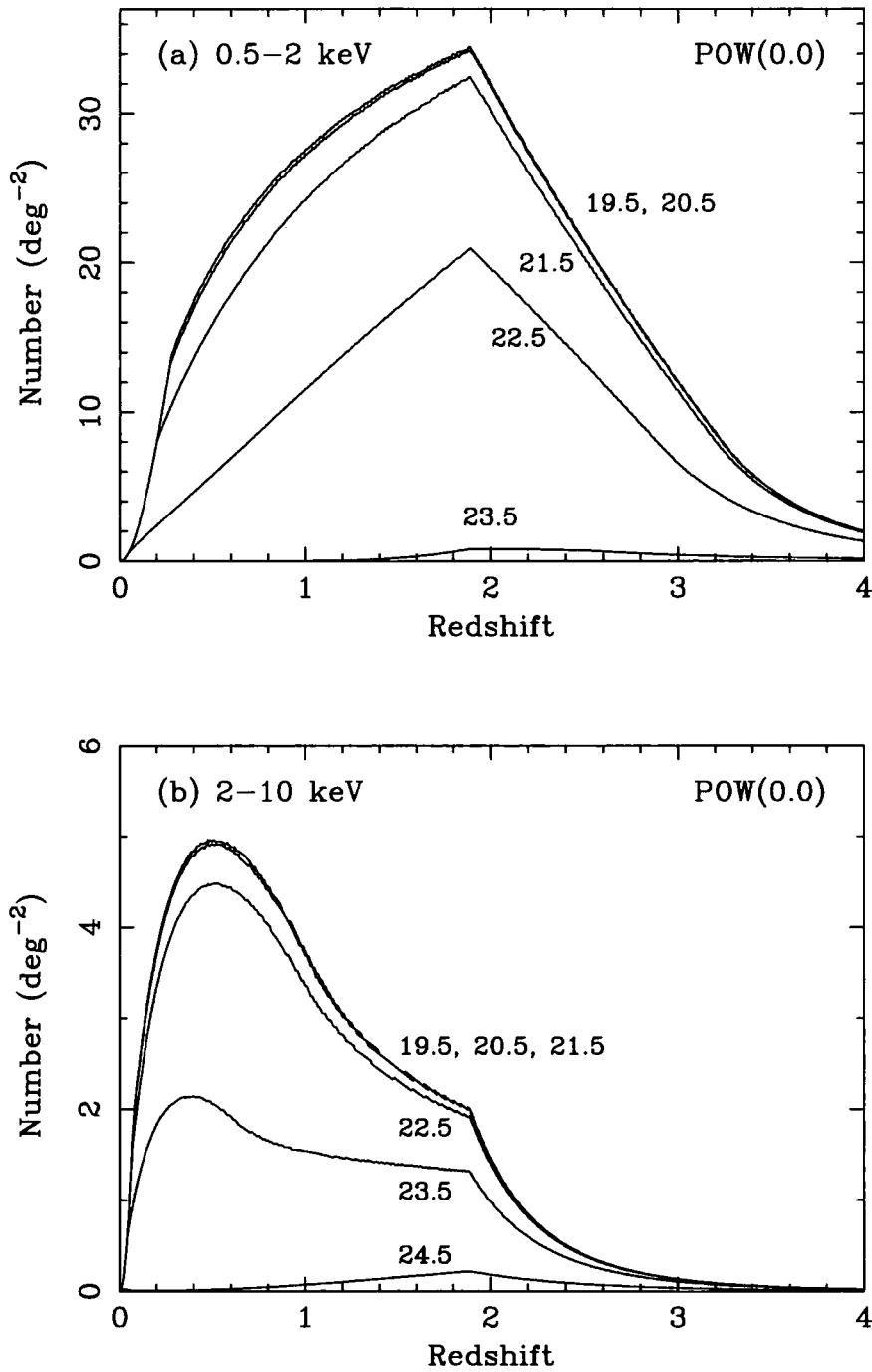
Figure 3.3: Predicted number-redshift distribution for the power-law evolution, low q_0 model, showing the relative contribution from each population of obscured AGN. Each population of sources is plotted separately, with the column density marked in logarithmic units. The predictions are shown for (a) a soft X-ray survey with $S(0.5 - 2\,\mathrm{keV}) > 5 \times 10^{-15}\,\mathrm{erg\,cm^{-2}\,s^{-1}}$, and (b) a hard X-ray survey with $S(2 - 10\,\mathrm{keV}) > 5 \times 10^{-14}\,\mathrm{erg\,cm^{-2}\,s^{-1}}$. These sum to the total $n(z)$ predictions in Fig. 3.2 and are equivalent to the *ROSAT* and *ASCA* or *BeppoSAX* source count predictions from Table 3.3.

3.3.1 Predicted $n(z)$ distributions

Fig. 3.2 shows the $n(z)$ relation predicted by a selection of models, for X-ray surveys equivalent to those currently possible (a) with *ROSAT*, and (b) with *ASCA* or *BeppoSAX*. In the soft band, for the models using power-law evolution, the most prominent feature is the strong rise out to the redshift cutoff where the pure luminosity evolution stops at $z \sim 1.8$. For models using the polynomial form for the luminosity evolution, the luminosity increases out to $z \sim 2.5$ and then decreases towards higher redshifts (see Fig. 2.4). Volume effects dominate at the flux limits currently achieved in the soft X-ray band, with the low q_0 models producing the largest number of sources at redshifts $z > 1$. This is consistent with the steeper faint-end slope of the LogN:LogS relation for a low q_0 universe. In the hard X-ray band, only comparatively shallow surveys have been completed, in which the source counts are dominated by nearby objects. This can be seen in Fig. 3.2(b), in which the assumed form for the luminosity evolution has virtually no effect on the $n(z)$ distribution for a flat column distribution. Models POW(0.5)t and POL(0.5)t, which use a tilted column distribution, predict a higher source density, as there are more bright moderately obscured sources which can be detected.

In Fig. 3.3, we use a low q_0 power-law model, POW(0.0), as our canonical example to show the contribution to the total number counts from each population of absorbed sources. It can be seen that the greatest contribution comes from objects with low to moderate absorption, and the most highly absorbed sources are not detected, particularly at soft energies. However, populations with higher column densities have negative X-ray k-corrections which increase with redshift, such that by $z \sim 2$, their space density is approaching that of the unabsorbed objects. In the absence of a redshift cutoff in the luminosity evolution, this would inevitably produce many sources with no obvious optical counterpart (blank fields). The redshift cutoff, which was initially implemented in the soft band, has an even more drastic effect in cutting the numbers of high redshift objects in the hard band. By definition, the $n(z)$ predictions can only be compared with objects for which we have redshift information, therefore, for obscured QSOs, our models must be in agreement with the combined constraints from both the $n(z)$ distribution and the number of blank field sources.

3.3.2 Consistency tests

We next check the model predictions for the redshift distribution of X-ray sources and the sky density of blank field sources, for surveys from satellites such as *ROSAT*, *ASCA* and *BeppoSAX*. We also make predictions for the numbers of blank field sources expected in surveys with the forthcoming *AXAF* and *XMM* satellites.

Here, we take unobscured AGN to be those sources for which the predicted apparent magnitude from the nucleus is greater than a spectroscopic B-band magnitude limit, enabling detection of the broad-line emission. Obscured AGN are classed as those objects where no nuclear flux can be detected, and are sub-divided further into low redshift objects, which would be identified optically as galaxies and NELGs, and high redshift objects, which would have $B \gtrsim 22.5\,\mathrm{mag}$, and thus would appear as blank fields in current surveys.

As a consistency check, we first calculate the expected numbers of blank fields at bright X-ray flux limits and $B > 22.5\,\mathrm{mag}$, and compare this with the results of Georgantopoulos et al. (1996). Assuming Model POW(0.0) parameters and our flat column density distribution, we predict the number of sources at a bright *ROSAT* flux limit of $S(0.5 - 2\,\mathrm{keV}) > 5 \times 10^{-14}\,\mathrm{erg\,cm^{-2}\,s^{-1}}$, and find that we expect to detect $1.7\,\mathrm{deg}^{-2}$ (~ 15 per cent) with optical magnitudes fainter than $B = 22.5\,\mathrm{mag}$, in agreement with Georgantopoulos et al.

In the hard band, we compare our predictions with the *HEAO 1* A-2 all sky survey data (Piccinotti et al. 1982), which has a very bright flux limit of $S(2 - 10\,\mathrm{keV}) > 3 \times 10^{-11}\,\mathrm{erg\,cm^{-2}\,s^{-1}}$. Our model accounts for ~ 65 per cent of the total numbers of sources observed in this survey, in the proportion of three times as many unobscured as obscured sources. If we relate our unobscured sources to Sy 1 galaxies, and obscured sources to Sy 2 galaxies, then this is in agreement with the data, in which Sy 1 and Sy 2 galaxies are observed in the ratio of three to one. In this survey, the remaining ~ 35 per cent of sources were clusters of galaxies.

At deeper fluxes, we compare our predictions with the *ROSAT* Deep Survey (Schmidt et al. 1998) which presents a complete sample of 47 extragalactic X-ray sources in a 207 ksec observation of the *Lockman Hole* region. The sample consists of all PSPC sources with $S(0.5 - 2\,\mathrm{keV}) > 5.60 \times 10^{-15}\,\mathrm{erg\,cm^{-2}\,s^{-1}}$ within the central $12'\!.5$ radius of the field, plus sources with $S(0.5 - 2\,\mathrm{keV}) > 1.11 \times 10^{-14}\,\mathrm{erg\,cm^{-2}\,s^{-1}}$ in the annulus $12'\!.5 < \theta < 18'\!.5$. This ensures that all the sources lie in the centre of the *ROSAT* field-of-view, which is unaffected by obscuration from the window support structure, and takes advantage of the best point-spread function of the telescope at small off-axis angles. The source type and distribution are compared with the number of objects in such a survey predicted by our models, and the results are displayed in Table 3.2. We put sources classified as NELGs, galaxies, groups and 'no IDs', together into an obscured category with $B > 22.5\,\mathrm{mag}$, and compare our predictions with the observations, assuming that the 'no IDs' are most likely to be at high redshift. We also assume that at $z > 0.5$, the host galaxy cannot be detected and therefore the source is classified as a 'blank fields' rather than as a 'galaxy'. We find that the predictions of Model POW(0.0) are consistent with the

			Unobscured AGN		Obscured AGN			Total
			$z < 0.5$	$z > 0.5$	$z < 0.5$	$z > 0.5$	Class	
ROSAT Deep Survey			4	27	-	6	NELGs	
					2	3	Groups	
					1	-	Galaxy	
					-	4	No IDs	
			4	27	3	13		47
Predictions:	POW(0.0)	(B=22.5)	3.1	27.3	0.7	18.3		49.4
	POW(0.5)t	(B=22.5)	3.2	18.3	1.3	24.8		47.6
	POW(0.5)t	(B=24.5)	3.8	24.1	0.7	19.0		47.6

Table 3.2. Comparison of our model predictions with the *ROSAT* Deep Survey (Schmidt et al. 1998) observational data: a complete sample of 47 extragalactic PSPC sources with $S(0.5 - 2\,\mathrm{keV}) > 5.60 \times 10^{-15}\,\mathrm{erg\,cm^{-2}\,s^{-1}}$ at off-axis angles of $\theta < 12\!.'5$ and $S(0.5 - 2\,\mathrm{keV}) > 1.11 \times 10^{-14}\,\mathrm{erg\,cm^{-2}\,s^{-1}}$ at $12\!.'5 < \theta < 18\!.'5$. We divide their identifications into unobscured AGN and potential obscured AGN, using the extreme case that this second category of objects contains all galaxies, NELGs, groups of galaxies, and objects with no identifications, for which no emission lines can be detected to the B-magnitude limit specified.

results of Schmidt et al. (1998). Model POW(0.5), which uses a flat distribution of columns, underpredicts the total number of sources, whereas Model POW(0.5)t, which uses the tilted distribution, predicts too many blank fields with $B > 22.5\,\mathrm{mag}$. There is no well-defined spectroscopic limit for this survey (but we would expect it to be $B \sim 23.5\,\mathrm{mag}$), and we find that we require a limit of $B > 24.5\,\mathrm{mag}$ to reproduce the observed source distribution, which is definitely too faint.

We now compare our blank field predictions for current *ASCA* or *BeppoSAX* $(2 - 10\,\mathrm{keV})$ and future *AXAF* $(0.4 - 6\,\mathrm{keV})$ surveys, presenting the results in Table 3.3. We have chosen the optical magnitude limit used for the predictions for each survey individually, as follows. In the past, most *ROSAT* survey follow-up has been performed on 4m-class telescopes, obtaining spectra to a limit of $B = 22.5\,\mathrm{mag}$. For hard X-ray sources detected by *ASCA* or *BeppoSAX*, the error box is comparatively large ($1\sigma \sim 60''$ radius r.m.s.), limiting an efficient identification program also to $B = 22.5\,\mathrm{mag}$. However, for *AXAF* surveys, both the anticipated sub-arcsecond X-ray spatial resolution and the fact that the optical follow-up is likely to be performed using the multi-object spectroscopic facilities on 8m-class telescopes, means that a much deeper limit of $B \sim 24.5\,\mathrm{mag}$ can be realistically attained.

From Table 3.3, it can be seen that for a relatively shallow survey (from *ASCA* or *BeppoSAX*), Model POW(0.5)t predicts a larger number of obscured sources than Model POW(0.0), corre-

Mission	Energy range	X-ray flux limit ($\mathrm{erg\,cm^{-2}\,s^{-1}}$)	B_{lim} (mag)	Model	Unobscured AGN $z<1$	Unobscured AGN $z>1$	Obscured AGN $z<1$	Obscured AGN $z>1$	Total ($\mathrm{deg^{-2}}$)
ROSAT	0.5 – 2 keV	5.0×10^{-15}	22.5	POW(0.0)	37.5	117.1	17.4	88.9	260.9
				POW(0.5)	29.6	66.4	14.0	54.4	164.4
				POL(0.0)	36.6	112.2	17.2	85.5	251.5
				POL(0.5)	29.8	60.5	14.5	48.8	153.6
ASCA/BeppoSAX	2 – 10 keV	5.0×10^{-14}	22.5	POW(0.0)	10.8	6.3	6.8	8.0	31.9
				POW(0.5)	10.7	6.7	6.8	8.5	32.7
				POL(0.0)	10.8	6.5	7.0	8.1	32.4
				POL(0.5)	11.3	6.0	7.1	7.6	32.0
AXAF	0.4 – 6 keV	1.0×10^{-15}	24.5	POW(0.0)	160.1	928.8	150.5	1225.9	2465.3
				POW(0.5)	97.6	351.4	95.5	491.3	1035.8
				POL(0.0)	155.2	837.5	145.6	1086.4	2224.7
				POL(0.5)	93.9	307.3	91.8	423.9	916.9

Table 3.3. Model predictions of the numbers of AGN present to the limits of existing and forthcoming X-ray surveys, with *ROSAT*, *ASCA/BeppoSAX* and *AXAF*. Unobscured and obscured AGN are classified according to whether their nuclear optical flux is brighter or fainter than the limiting magnitude, B_{lim}, chosen individually for each survey, as described in Section 3.3. Obscured AGN are divided at $z = 1$ into low redshift galaxies/NELGs, and high redshift blank field sources. For *ROSAT* and *ASCA/BeppoSAX* surveys to these limits, the predicted $n(z)$ distribution is shown in Fig. 3.3, and the predicted numbers of obscured and unobscured AGN for an *AXAF* survey are compared in Fig. 3.11.

sponding to the increased contribution from higher column populations. Current observations are consistent with either of these models. For example, in a recent deep *ASCA* survey, Boyle et al. (1998a) find that between 4 and 9 out of 26 *ASCA* sources (15 − 35 per cent, taking the two extreme cases) have no reliable identification, and which are the most likely candidates for high redshift obscured AGN. To summarise, we predict ∼ 40 per cent blank field sources in *ROSAT* surveys, compared with only ∼ 25 per cent in shallower *ASCA/BeppoSAX* surveys, but this fraction rises as we go to fainter limits, as we shall see when we discuss the predictions for *AXAF* in Section 3.6.

3.4 X-ray/Optical Dispersion from Obscured QSO Models

In this Section, we use our canonical power-law evolution, $q_0 = 0$ model, together with a flat distribution of column densities in obscured QSOs is used to predict the strength of the selection effects present in samples chosen in different wavelength regimes. In particular, we investigate whether the effects of dust extinction and photo-electric absorption can conspire to produce the small observed X-ray/optical dispersion of Boyle & Di Matteo (1995), even in the presence of a significant obscured QSO population.

We have calculated how the observed fluxes in both the X-ray and optical regimes for each population of QSOs varies with redshift. In order to do this, we relate the fluxes at 2500Å and 2keV using a spectral index $\alpha_{ox} = 1.5$ (as defined in Section 3.2.1), and we use the optical extinction laws and X-ray photo-electric absorption properties as described in Section 3.2.2. We have combined these values in order to determine the X-ray to optical flux ratio for AGN of a certain column density, as a function of redshift. This is plotted in Fig. 3.4(a) for columns of $N_H = 0, 0.25, 0.5, 0.75, 1.0 \times 10^{22} \, \mathrm{cm}^{-2}$. A restricted linear column distribution has been shown here for clarity, as the ratios obtained become extremely high very quickly with increasing column, due to the huge amounts of optical absorption. Our results are not affected by this increased resolution, as the number densities in each population remain consistent with our original model.

Since we are assuming that $f_\nu \propto \nu^{-\alpha}$ at both X-ray and the optical frequencies, and $\nu_e \propto (1 + z)\nu_o$, it can be shown that for an unabsorbed AGN:

$$\log(f_X/f_B) \propto (\alpha_{opt} - \alpha_x) \log(1 + z).$$

We have adopted values of $\alpha_{opt} = 0.8$ and $\alpha_x = 0.9$, and therefore expect the relationship $\log(f_X/f_B) \propto -0.1 \log(1+z)$, which is why very little correlation can be seen between (f_X/f_B) and redshift. Taking an AGN with moderate column density, moving it to higher redshifts and recalculating the observed fluxes, we find that the restframe extinction in the observed optical
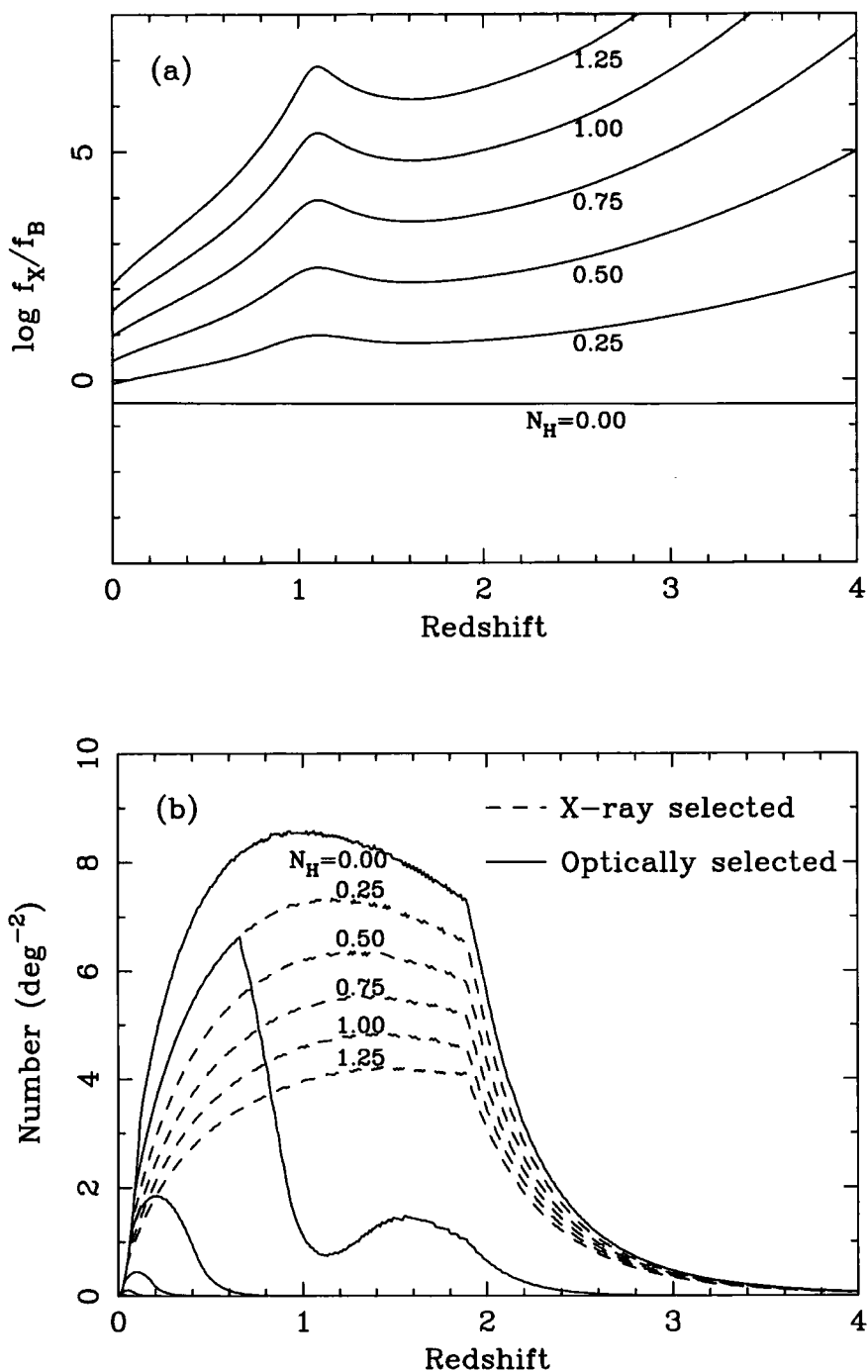
Figure 3.4: (a) Soft $(0.5 - 2\,\text{keV})$ X-ray to optical flux ratio is plotted against redshift, for column densities of $N_H = 0, 0.25, 0.5, 0.75, 1.0, 1.25 \times 10^{22}\,\text{cm}^{-2}$ (as marked, in units of $10^{22}\,\text{cm}^{-2}$), with $\alpha_{opt} = 0.8$ and $\alpha_x = 0.9$. (b) The X-ray selected $n(z)$ relation is plotted with dashed lines for the same column densities, while the X-ray sources selected above the optical spectroscopic limit of $B < 22.5\,\text{mag}$ are denoted by solid lines. Low q_0, power-law evolution parameters are used.
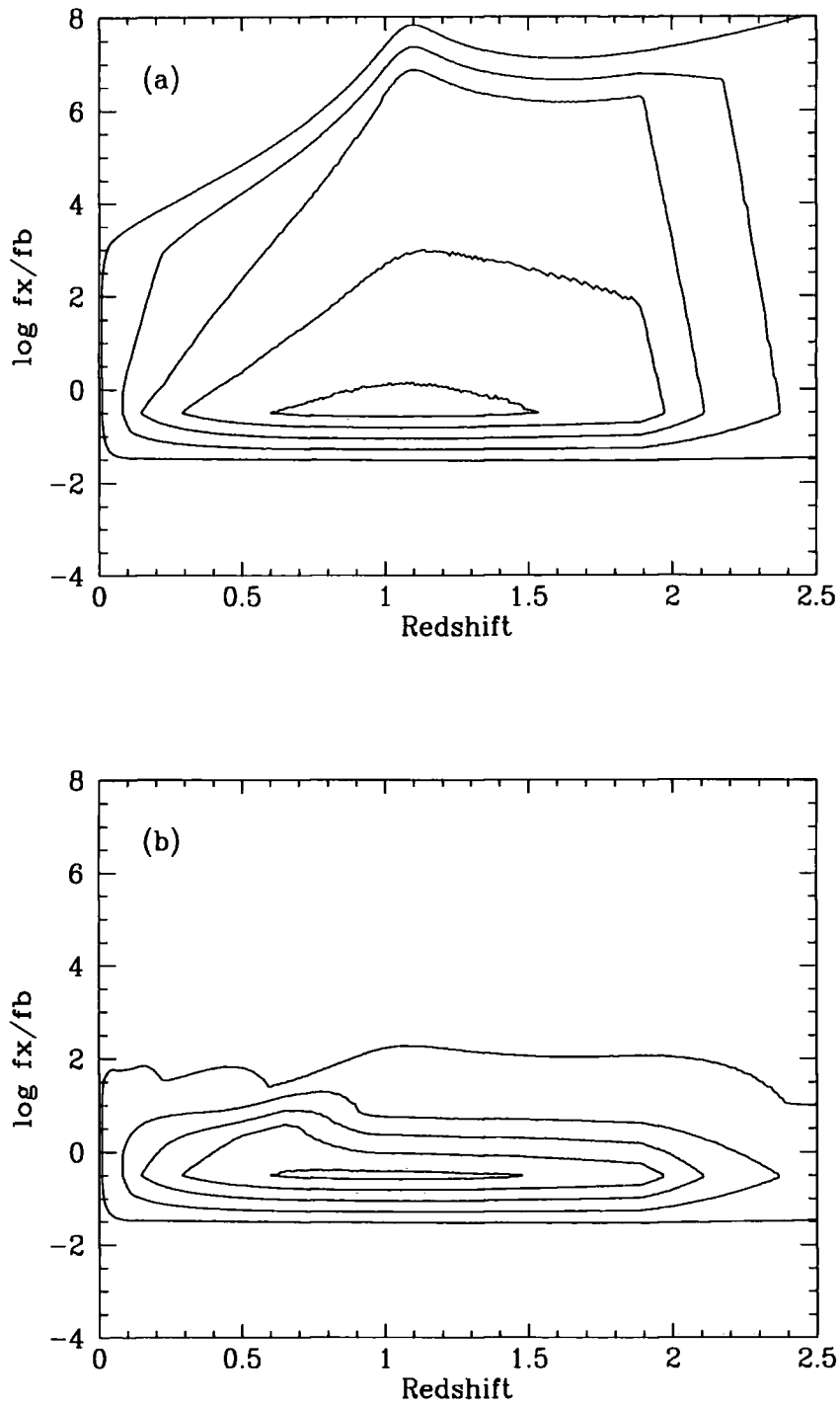
Figure 3.5: The distribution of AGN in the $\log f_X/f_B$ *vs* redshift plane (a) after X-ray selection with a flux limit of $S(0.5 - 2\,\mathrm{keV}) = 2 \times 10^{-14}\,\mathrm{erg\,cm^{-2}\,s^{-1}}$, and (b) after both X-ray and B-band selection with a spectroscopic magnitude limit of $B_{lim} = 22.5\,\mathrm{mag}$. Contours are at 0.01, 2.0, 4.0, 6.0, 8.0 deg^{-2}. The application of both selection criteria reproduces the observed tight correlation between X-ray and optical fluxes in such QSO samples, as in Fig. 1 from Boyle & Di Matteo (1995).

(restframe ultra-violet) increases while the absorption in the X-ray decreases, causing the ratio f_X/f_B to increase significantly. In Fig. 3.4(a), the prominent 2200Å feature in the absorption law due to graphite can also be seen, redshifted into the $B-$ band at $z \sim 1.2$.

Having calculated the f_X/f_B ratio as a function of redshift, we then combine this with the $n(z)$ relation as described in Section 3.3 for each population of AGN. In order to compare our results with those of Boyle & Di Matteo (1995), we use our canonical model and a flux limit of $S(0.5 - 2 \, \text{keV}) = 2 \times 10^{-14} \, \text{erg} \, \text{cm}^{-2} \, \text{s}^{-1}$. We calculate the expected number of X-ray sources as a function of redshift for each column, and plot the results in Fig. 3.4(b). The f_X/f_B ratio, at the given redshift and column, is then used to calculate the number of those sources which can be detected brighter than the spectroscopic magnitude limit, $B < 22.5 \, \text{mag}$, denoted by solid lines.

Combining the f_X/f_B information with the predicted $n(z)$ relations, it is possible to show the distribution of objects as a function of both redshift and X-ray/optical ratio. In Fig. 3.5(a), the distribution of objects in an X-ray selected sample is shown (same contour levels as in Fig. 3.4b). The number of AGN decreases as the redshift increases and also as the absorption increases.

If we then add in the effect of B-band selection at a spectroscopic magnitude limit of $B < 22.5 \, \text{mag}$, the objects with a high f_X/f_B ratio drop out of the sample. Fig. 3.5(b) shows that this produces a distribution of objects very similar to the tight correlation seen in Fig. 1 from Boyle & Di Matteo (1995). Thus the tight X-ray/optical flux ratio may be produced by selection effects, even in the presence of a significant obscured QSO population with a flat distribution of column densities. For a $q_0 = 0.5$ universe, we obtain very similar results to the $q_0 = 0$ case, for both flat and tilted distributions of column densities.

3.5 Near Infra-Red Properties from Obscured QSO Models

Assuming that the intrinsic QSO spectrum at near infra-red wavelengths is a continuation of the optical power-law continuum, the observed $K-$ band flux is therefore related to the X-ray flux via α_{ox} (as defined in Section 3.2.1). We have adopted a spectral index in the optical/near infra-red of $\alpha_{opt} \sim 0.8$, calculated from observations of LBQS QSOs (Francis 1993). By contrast, Webster et al. (1995) used the value predicted by the free-free continuum radiation model of $\alpha_{opt} \sim 0.3$ (Barvainis 1993), and we assess whether making this assumption will have a noticeable effect on our results. We note however, that this bremsstrahlung (free-free) model for the optical emission from the accretion disc of an AGN is not viable (Laor et al. 1997).
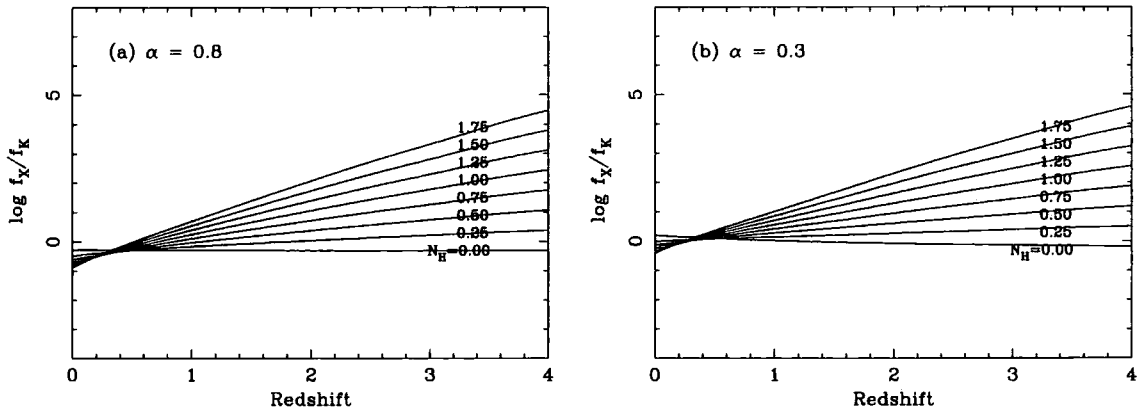
Figure 3.6: Soft $(0.5 - 2\,\mathrm{keV})$ X-ray to infra-red flux ratio is plotted against redshift, for column densities of $N_H = 0 - 1.75 \times 10^{22}\,\mathrm{cm}^{-2}$ (as marked, in units of $10^{22}\,\mathrm{cm}^{-2}$), with $\alpha_x = 0.9$ and (a) $\alpha_{opt} = 0.8$, (b) $\alpha_{opt} = 0.3$.
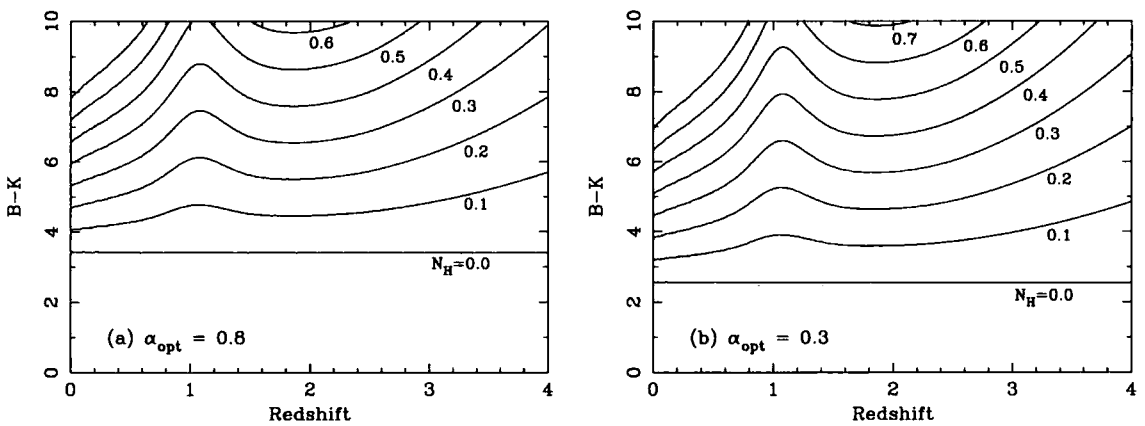
Figure 3.7: The relationship between $B - K$ colour and redshift for obscured QSOs, using a spectral index of (a) $\alpha_{opt} = 0.8$ and (b) $\alpha_{opt} = 0.3$. The predicted colours for unobscured QSOs are independent of redshift as a power-law spectrum has been assumed, giving colours of $B - K = 3.40$ and 2.54 respectively. The column density for each population is marked in units of $10^{22}\,\mathrm{cm}^{-2}$, for $N_H = 0.0 - 0.7 \times 10^{22}\,\mathrm{cm}^{-2}$ (again with linear increments for clarity).

3.5.1 The f_X / f_K vs redshift relation

The relationship between soft X-ray/K–band flux ratio and redshift is plotted in Fig. 3.6, for (a) $\alpha_{opt} = 0.8$ and (b) $\alpha_{opt} = 0.3$, respectively. It can be seen that the value adopted for α_{opt} makes virtually no difference to the X-ray/infra-red colour, just a small tilt in the curves, as to be expected from the relationship $\log(f_X / f_K) \propto (\alpha_{opt} - \alpha_x) \log(1 + z)$. We obtain a similar relationship to that found in the B–band, as in Fig. 3.4(a), but as expected, the relationship is much tighter in the infra-red than in the optical, due to the reduced absorption at longer wavelengths. Also, we can see that the effects of absorption on the observed K–band flux of a QSO becomes larger than the

effect on the soft X-ray flux when the QSO lies at redshifts $z \gtrsim 0.4$, which is consistent with the tabulated extinction values in Table 3.1.

3.5.2 The $B - K$ vs redshift relation

The observed $B - K$ colour of a QSO is equivalent to the f_B / f_K ratio. Using the two values of α_{opt}, we can calculate the expected $B - K$ colour for an unobscured QSO. Taking the relationship between $B-$ and $K-$magnitudes and flux from Eqns 3.3 and 3.4, we obtain:

$$
\begin{aligned}
B - K &= (-2.5 \log f_B - 12.97) - (-2.5 \log f_K - 16.94), \\
&= -2.5 \log \left(\tfrac{f_B}{f_K}\right) + 3.97, \\
&= 2.54 \, \text{mag}, \qquad\qquad \alpha_{opt} \sim 0.3, \\
&= 3.40 \, \text{mag}, \qquad\qquad \alpha_{opt} \sim 0.8.
\end{aligned}
$$

From Fig. 3.7, it can be seen that the optical spectral index does not significantly change the relationship between $B - K$ colour and redshift. The primary effect is a shift in the observed colour of an unobscured AGN, from $B - K = 2.54$ for $\alpha_{opt} = 0.3$, and $B - K = 3.40$ for $\alpha_{opt} = 0.8$, which is independent of redshift as the spectrum is assumed to have a power-law slope. Once absorption starts to take effect, then the intrinsic spectrum of the AGN and hence α_{opt} becomes almost irrelevant, and it is the column density which dominates the observed colour.

3.5.3 $K-$band $n(z)$ relation

Here we consider the number-redshift or $n(z)$ relation that is predicted for a sample of X-ray QSOs, after X-ray selection alone, and then X-ray and near infra-red selection combined. In Fig. 3.8, we plot the predicted distribution from our obscured QSO model, for a deep soft X-ray survey with a flux limit $S(0.5 - 2 \, \text{keV}) > 5 \times 10^{-15} \, \text{erg} \, \text{cm}^{-2} \, \text{s}^{-1}$ (dashed lines). These are compared with the numbers of those QSOs which have a nuclear flux above $K \sim 19.5 \, \text{mag}$ (solid lines). The column densities are marked in units of $10^{22} \, \text{cm}^{-2}$. For comparison, we also plot the numbers of sources which have nuclear fluxes above an optical limit of $B \sim 22.9$ (dotted lines). This limit is chosen to correspond to the $B - K = 3.4$ colour of an unobscured QSO with spectral index $\alpha_{opt} = 0.8$. It can clearly be seen that far fewer sources are detected in the optical than in the infra-red, and lie at lower redshift.

From Figs 3.6 and 3.7, it has been shown that the effect of changing the assumed optical spectral index for QSOs is small. But there is a noticeable change in the $n(z)$ distribution with α_{opt}, since for a bluer spectrum such as $\alpha_{opt} = 0.3$ for which the spectrum rises towards shorter wavelengths, then the k-correction is more favourable and it becomes easier to pick up high redshift objects than
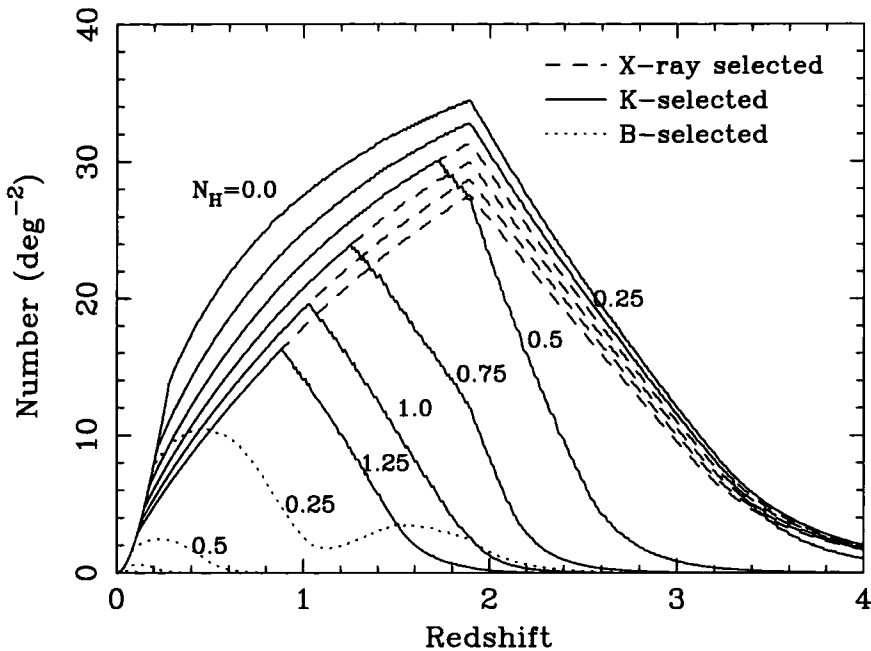
Figure 3.8: The QSO $n(z)$ relation for a soft X-ray selected sample with $S(0.5 - 2\,\mathrm{keV}) > 5 \times 10^{-15}\,\mathrm{erg\,cm^{-2}\,s^{-1}}$. We plot with dashed lines the predicted numbers of X-ray sources for column densities of $N_H = 0 - 1.25 \times 10^{22}\,\mathrm{cm^{-2}}$ (as marked, in units of $10^{22}\,\mathrm{cm^{-2}}$). The X-ray sources selected above a K-band magnitude limit of $K < 19.5\,\mathrm{mag}$, are denoted by solid lines, and those selected in the optical with a nuclear flux of $B < 22.9\,\mathrm{mag}$ are shown by dotted lines. Spectral indices of $\alpha_x = 0.9$ and $\alpha_{opt} = 0.8$ respectively are assumed. Power-law evolution and $q_0 = 0.0$ are used.

in the $\alpha_{opt} = 0.8$ case. This effect is still quite small, and therefore we adopt $\alpha_{opt} = 0.8$, in order to remain consistent with the work on absorption at optical wavelengths in Sections 3.3 and 3.4. We note that this means that the number counts of distant sources would be lower limits compared to the $\alpha_{opt} = 0.3$ case.

3.5.4 QSO $n(z)$ distribution in the f_X/f_K vs redshift plane

Combining the $n(z)$ distribution with the f_X/f_K *vs* redshift relations for each population of obscured QSOs, Fig. 3.9 shows where these objects lie for both X-ray and K-selected samples.

For an X-ray selected sample, it is likely that the source identification will be undertaken at optical wavelengths due to the relative ease of observation. In addition, the wide wavelength coverage available in the optical optimises the detection of spectral features. Therefore, to improve the consistency of these results, a B-band spectroscopic limit should be imposed on the sample, in addition to the near infra-red imaging depth. As long as the B-selection limit is more than 3.4 mag deeper (2.5 mag for $\alpha_{opt} = 0.3$) than the K-selection limit, you will always pick up more unobscured objects in B than in K, if the X-ray sample is deep enough. In this case, you can
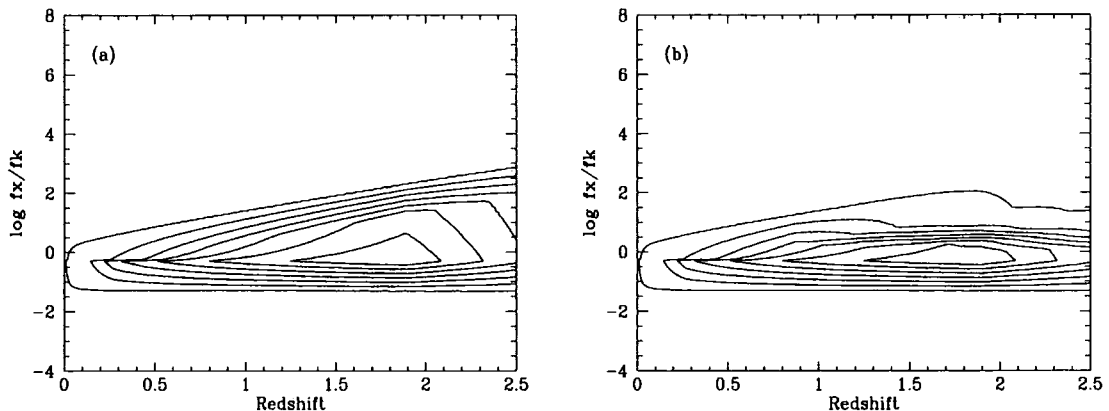
Figure 3.9: The distribution of AGN in the log f_X/f_K vs redshift plane (a) after X-ray selection with a flux limit of $S(0.5 - 2\,\text{keV}) = 5 \times 10^{-15}\,\text{erg}\,\text{cm}^{-2}\,\text{s}^{-1}$, and (b) after both X-ray and K-band selection with a spectroscopic magnitude limit of $K_{lim} = 19.5\,\text{mag}$. Contours are at 0.1, 5.0, 10.0, 15.0, 20.0, 25.0, 30.0 deg^{-2}.

see the same distance down the luminosity function in both B and K and therefore detect the same objects. Obviously, for obscured objects, more are detected in K. For shallower X-ray samples, you detect all the unobscured objects in both B and K, whatever limits you choose, and therefore once the obscuration sets in, fewer objects are detected in the optical. However, as the constraint of an optical limit has a stronger effect than the infra-red limit for the obscured populations, due to the increased absorption at shorter wavelengths, this will combine with the narrower dispersion in f_X/f_K vs redshift, to make an even tighter relationship. (For this reason, we have not plotted this here.)

3.5.5 QSO distribution in the $B - K$ vs redshift plane

To compare the predictions from our models with the results of Webster et al. (1995), we now investigate the $B - K$ properties of X-ray selected QSOs. Webster et al. explain the narrow spread in $B - K$ colours for the LBQS optically-selected sample as due to the fact that any QSOs that are significantly reddened will drop out of the survey below the $B-$ band selection limit. Optically-selected QSOs therefore show an intrinsic colour in the range $2 < B - K < 4$, (compared with $B - K = 2.5, 3.4$ for $\alpha_{opt} = 0.3, 0.8$ respectively), which is consistent with the average spectral indices found in various samples of $\alpha_{opt} \sim 0.2 - 0.35$ (Neugebauer et al. 1987) or $\alpha_{opt} \sim 0.8$ (Francis 1993), where the relationship between α_{opt} and $B - K$ is described in Section 3.5. Then for the Webster et al. radio-selected sample, there is a range of optical colours due to dust, but since these QSOs are intrinsically bright, spectroscopic identifications will be possible for a larger range of columns, for which they remain within the sample.
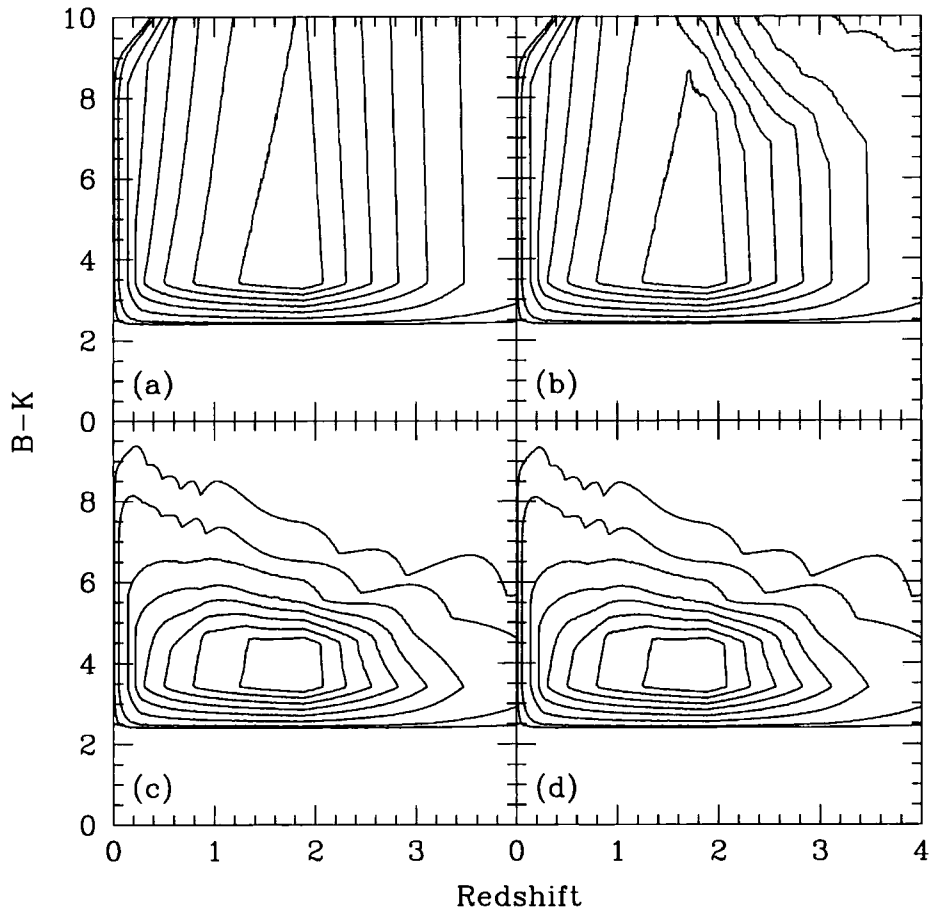
Figure 3.10: The distribution of AGN in the $B - K$ *vs* redshift plane (a) after X-ray selection with a flux limit of $S(0.5 - 2\,\text{keV}) = 5 \times 10^{-15}\,\text{erg}\,\text{cm}^{-2}\,\text{s}^{-1}$; (b) after both X-ray and K-band selection with an imaging magnitude limit of $K_{lim} = 19.5\,\text{mag}$; (c) after X-ray and B-band selection with a spectroscopic magnitude limit of $B_{lim} = 22.5\,\text{mag}$; (d) after selection at all three energies, ie, X-ray sources which are identified as candidates in the infra-red and which are bright enough in the optical to obtain a spectroscopic identification. Contours are at 0.1, 1, 5, 10, 15, 20, 25, 30 deg^{-2}. The application of all three selection criteria reproduces the observed tight correlation between X-ray and optical fluxes in such QSO samples, as in Fig. 1 from Boyle & Di Matteo (1995), although for this particular choice of flux limits, the primary constraint is from the B-band limit.

In Fig. 3.10, we show contour plots of the numbers of obscured AGN expected in the $B - K$ *vs* redshift plane. In panel (a), the distribution after X-ray selection of $S(0.5 - 2\,\text{keV}) > 5 \times 10^{-15}\,\text{erg}\,\text{cm}^{-2}\,\text{s}^{-1}$ alone is plotted, showing that QSOs can be found throughout the plane, with a peak at redshift $z \sim 2$ due to the evolution of the luminosity function. Panel (b) shows the effect on the X-ray sample of K-band selection with an imaging limit of $K \sim 19.5$. Low redshift objects are lost, along with some of the higher column, high redshift sources. Panel (c) shows the effect of imposing a B-band spectroscopic limit of $B \sim 22.5\,\text{mag}$ on the X-ray sample (no K-

selection). Here the majority of obscured objects are lost from the sample, at all redshifts. Finally, in panel (d), the three selection criteria are combined, giving a tight relationship, with a steep cut-off below the lower envelope of the $B - K$ distribution at around $B - K \sim 3.4$ ($\alpha_{opt} = 0.8$) and then a small dispersion towards redder colours. This shows that the dominant effect for the flux limits chosen here, is the B–band selection. For our X-ray selected QSO samples, we observe the range in $B - K$ colours found in radio-selected samples, but are limited due to the faintness of these sources, by the B–band spectroscopic limit. Increasing the B–band magnitude limit to $B \sim 24.5$ mag will enable more moderately absorbed QSOs to be identified as such. These will have redder colours and have a wider dispersion in $B - K$ colour, and are the faint counterparts to the red radio-quiet QSOs selected at bright X-ray fluxes by Kim & Elvis (1999).

3.5.6 Discussion

Future work is required in order to assess the contribution from the host galaxy light for obscured QSOs, which will have two primary effects. Firstly, if the host galaxy light dominates the nuclear emission, then the source may be extended and therefore will not satisfy the stellar criterion for identification as a candidate QSO. Secondly, the host galaxy light will have a different spectral shape to that of the QSO emission, thereby changing the observed optical/infra-red colours. The presence of on-going star-formation in the host galaxy will complicate the situation still further. In addition, there is evidence to suggest that the host galaxy luminosity is correlated with the luminosity of the QSO (McLeod & Rieke 1994a, 1994b, 1995), but as yet this relationship is not well constrained. Masci, Webster & Francis (1998) assess the contribution from a stellar component to the optical/infra-red colours of a radio-selected sample of red QSOs, and find that the observed red colours are not due to contamination by the host galaxy. We anticipate that the inclusion of the host galaxy properties into our models should not affect our broad conclusions.

3.5.7 Future surveys

With the advent of large near infra-red arrays, comparable to the mosaics of CCD detectors which are well established at optical wavelengths, it is now possible to undertake deep near infra-red QSO surveys over wide areas. The Omega-Prime camera is a dedicated wide-field near infra-red imager at prime focus on the Calar Alto 3.5-m telescope. This uses a 1024×1024 HgCdTe array, sensitive in the range $1 - 2.5\mu$m, J–, H– and K–bands. The image scale is $0\rlap{.}''4$/pix, giving a field-of-view of $6.8' \times 6.8'$. The new Cambridge Infra-Red Survey Instrument (CIRSI; Beckett et al. 1997) comprises four such 1024×1024 HgCdTe arrays, enabling even wider area coverage. At prime

focus on the 4.2-m William Herschel Telescope, the image scale of $0''\!.32$/pix gives a field-of-view of $\sim 20'$ on a side, and at prime focus of the 2.5-m Isaac Newton Telescope, a $\sim 30'$ field is attainable with a pixel scale of $0''\!.46$/pix. These telescopes are not optimised for use in the infra-red, and therefore background emission from the telescope itself makes observing at the longest wavelengths, *i.e.*, the K–band, very difficult with both Omega-Prime and CIRSI. However, K–band observations are possible with this camera on the 2.5-m Las Campanas du Pont Telescope, which is fitted with thermal baffling to reduce telescope emission, and cold fore-optics are being developed.

Arrays of this kind will enable efficient candidate selection for identification programs for deep *AXAF* and *XMM* observations. In addition, K–selected surveys of QSOs, to limits of $K \sim 20$ mag, will also be possible, extending the established UVX method of QSO selection (Shanks et al. 1983; Schmidt & Green 1983; Boyle et al. 1985). These will use multicolour selection techniques, analogous to the UVX method at shorter wavelengths, which rely on the fact that QSOs are *redder* than stars in the near infra-red, as well as being bluer than stars at near ultra-violet wavelengths (Warren, in preparation). In this way, QSO candidates can be distinguished from stars by their position in the $V - J$ *vs* $J - K$ plane. Unlike the UVX method, which by definition selects only blue objects, moderately obscured, reddened QSOs can be detected in this way.

3.6 Conclusions

We have shown here that the tight correlation between X-ray and optical luminosities does not rule out the existence of a large population of obscured QSOs, but instead can be explained by selection effects in the samples used. At low redshift, QSOs suffer both optical and X-ray absorption and therefore an obscured QSO may not appear in an X-ray selected sample. At high redshift, obscured QSOs suffer substantial optical extinction and in this case, although the QSO host galaxy may be visible, the lack of broad lines will generally mean that the QSO will not be identified as such and therefore will not be included in the sample, as shown in Fig. 3.5(b).

Extending this investigation to near infra-red wavelengths, where the effect of dust obscuration is less pronounced, we have shown that although a very tight relation is produced in the f_X/f_K *vs* redshift plane, our models predict a wide range in $B - K$ colours. This result for radio-quiet AGN is in agreement with the spread in $B - K$ colours in a sample of radio-loud QSOs observed by Webster et al. (1995). At the same time, this remains consistent with the small dispersion in the observed f_X/f_B *vs* redshift relation from Boyle & Di Matteo (1995). The precise spread in
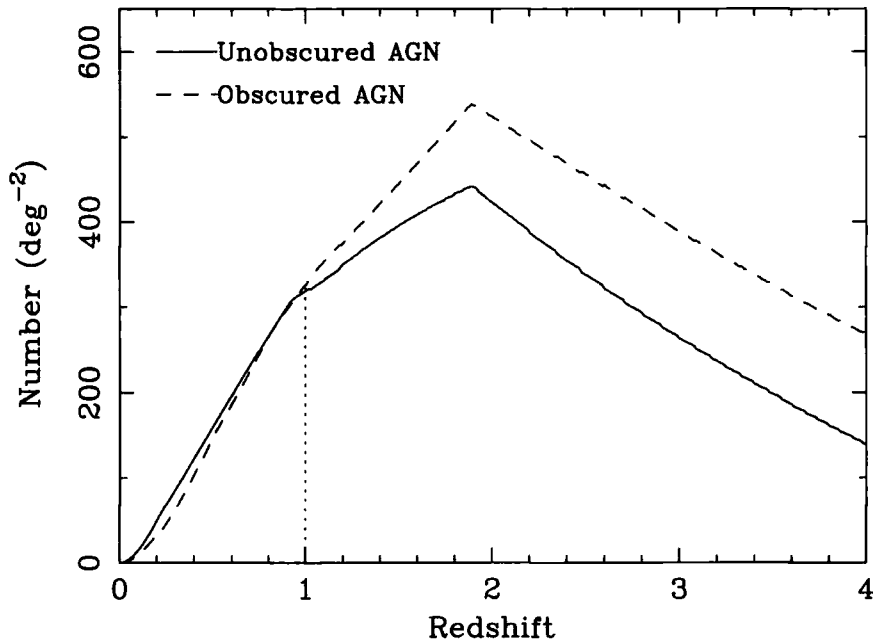
Figure 3.11: Prediction of the $n(z)$ relation for a deep *AXAF* X-ray survey, to a flux limit of $S(0.4 - 6\,\text{keV}) > 10^{-15}\,\text{erg}\,\text{cm}^{-2}\,\text{s}^{-1}$, using power-law evolution, $q_0 = 0.0$ parameters. The diagram shows the relative numbers of obscured and unobscured sources, as detailed in Table 3.3. Unobscured sources detected as broad-line AGN with $B < 24.5$ mag, are shown by the solid line. Galaxies and blank field sources, which are obscured such that any nuclear flux has $B > 24.5$ mag, are shown by the dashed line. The division between galaxies and blank fields is made at $z \sim 1$ (dotted line).

$B - K$ colours predicted by our models is heavily dependent on the spectroscopic magnitude limit in the optical, since this is primarily where the identification of sources will occur.

In Section 3.3, we have further shown that the predicted numbers of moderately obscured, low luminosity galaxies are in approximate agreement with the numbers of low redshift X-ray galaxies that are observed over a wide range of fluxes. A feature of the obscured QSO model is that a certain proportion of blank field X-ray sources are also predicted. These will predominantly be high redshift objects which will be detectable in the X-ray even with a relatively large column $(N_H \sim 10^{22}\,\text{cm}^{-2})$ but will have more than ten magnitudes of (observed) B-band absorption. For *ASCA* and *BeppoSAX* hard X-ray surveys, $(S > 5 \times 10^{-14}\,\text{erg}\,\text{cm}^{-2}\,\text{s}^{-1}, B < 22.5\,\text{mag})$, we predict that ~ 25 per cent of X-ray sources lie at $z > 1.0$, and hence would probably class as blank fields, in agreement with observations.

At the depths attainable by forthcoming *AXAF* surveys, there are striking differences between the numbers of high redshift sources predicted by our different evolution models for obscured QSOs. However, this is primarily due to the assumed cosmology, *i.e.*, volume effects. Table 3.3 shows that the $q_0 = 0$ model predicts that obscured QSOs at $z > 1$ will constitute ~ 50 per cent

of the total *AXAF* source counts, which in the optical will appear as blank fields with no broad emission line objects visible at $B < 24.5$ mag. Fig. 3.11 shows the relative numbers of obscured and unobscured QSOs predicted as a function of redshift by our canonical power-law evolution, $q_0 = 0.0$ model, POW(0.0), where those obscured QSOs at $z < 1$ correspond to galaxies and NELGs, and those at $z > 1$ are blank fields. Fig. 3.11 also confirms that obscured AGN outnumber unobscured AGN at $z > 1$. The tilted column distribution used for our $q_0 = 0.5$ model predicts an even higher fraction of blank field sources, ~ 65 per cent.

The numbers of high redshift sources detected in these new deep surveys will show whether the redshift cutoff in the luminosity evolution is a real effect or purely an artifact of existing data. If QSOs continue to evolve in luminosity to much higher redshifts than previously thought, then obscured QSOs will totally dominate the X-ray number counts at very faint fluxes, to an even greater extent than already seen in Table 3.3. The observed redshift cutoff may be due to absorption effects however, as although at soft energies it is comparatively straightforward to detect high redshift obscured sources, this is outweighed by the difficulties in getting an optical identification. Fewer high redshift objects are therefore detected.

We have shown that our obscured QSO model can give good fits to the XRB spectrum, LogN:LogS, the numbers of blank field sources, etc., and are not ruled out by the observed narrow dispersion in X-ray/optical flux ratios. However, tests of the model are still required, and we have made predictions of the numbers of QSOs, NELGs and blank fields that may be detected in a deep X-ray survey with *AXAF*. A direct test of the model will also be afforded by observing NELGs and blank field X-ray sources in the near infra-red where the effects of absorption are less, to search for obscured nuclei which are invisible in the optical. A program of near infra-red imaging of counterparts to individual X-ray sources has been undertaken with this aim in mind, and the results will be described in Chapter 5.

Further, in Chapter 4, we aim to test these model predictions by going to sub-mm wavelengths. A dusty torus will be heated by the absorption of X-rays, and this energy is re-emitted in the thermal infra-red which, particularly for high redshift objects, will be readily detectable in the sub-mm by the new SCUBA camera on the James Clerk Maxwell Telescope. We shall also use our model to predict the contribution of obscured QSOs to the far infra-red background and compare them with the measured values available at present, and this may well provide a further strong constraint on the total number of very highly absorbed QSOs that may exist.

References

Allen C. W., 1973, *Astrophysical Quantities*. The Athalone Press

Antonucci R., 1993, ARA&A, 31, 473

Barvainis R., 1993, ApJ, 412, 513

Beckett M. G., Mackay C. D., MCMahon R. G., Parry I. R., Piche F., Ellis R. S., 1997, SPIE Proc., 2871, 1152

Boyle B. J., Di Matteo T., 1995, MNRAS, 277, L63

Boyle B. J., Fong R., Shanks T., Clowes R. G., 1985, MNRAS, 216, 623

Boyle B. J., Georgantopoulos I., Blair A. J., Stewart G. C., Griffiths R. E., Shanks T., Gunn K. F., Almaini O., 1998a, MNRAS, 296, 1

Boyle B. J., Wilkes B. J., Elvis M., 1997, MNRAS, 285, 511

Comastri A., Setti G., Zamorani G., Hasinger G., 1995, A&A, 296, 1

Francis P. J., 1993, ApJ, 407, 519

Georgantopoulos I., Stewart G. C., Shanks T., Boyle B. J., Griffiths R. E., 1996, MNRAS, 280, 276

Granato G. L., Danese L., Franceschini A., 1997, ApJ, 486, 147

Green P. J. et al., 1995, ApJ, 450, 51

Hasinger G., Burg R., Giacconi R., Schmidt M., Trümper J., Zamorani G., 1998, A&A, 329, 482

Hewett P. C., Foltz C. B., Chaffee F. H., Francis P. J., Weymann R. J., Morris S. L., Anderson S. F., Macalpine G. M., 1991, AJ, 101, 1121

Howarth I. D., 1983, MNRAS, 203, 301

Kim D. W., Elvis M., 1999, ApJ accepted. (astro-ph/9811406)

Laor A., Fiore F., Elvis M., Wilkes B. J., McDowell J. C., 1997, ApJ, 477, 93

Madau P., Ghisellini G., Fabian A., 1994, MNRAS, 270, L17

Masci F., Webster R., Francis P., 1998, MNRAS, 301, 975

McLeod K. K., Rieke G. H., 1994a, ApJ, 420, 58

McLeod K. K., Rieke G. H., 1994b, ApJ, 431, 137

McLeod K. K., Rieke G. H., 1995, ApJ, 441, 96

Morris S. L., Weymann R. J., Anderson S. F., Hewett P. C., Francis P. J., Foltz C. B., Chaffee F. H., Macalpine G. M., 1991, AJ, 102, 1627

Morrison R., McCammon D., 1983, ApJ, 270, 119

Neugebauer G., Green R. F., Matthews K., Schmidt M., Soifer B. T., Bennett J., 1987, ApJS, 63, 615

Piccinotti G., Mushotzky R. F., Boldt E. A., Holt S. S., Marshall F. E., Serlemitsos P. J., Shafer R. A., 1982, ApJ, 253, 485

Schmidt M., Green R. F., 1983, ApJ, 269, 352

Schmidt M. et al., 1998, A&A, 329, 495

Seaton M. J., 1979, MNRAS, 187, 73P

Shanks T., Fong R., Green M. R., Clowes R. G., Savage A., 1983, MNRAS, 203, 181

Tananbaum H. et al., 1979, ApJL, 234, L9

Warren S. J., 1999, in preparation.

Webster R. L., Francis P. J., Peterson B. A., Drinkwater M. J., Masci F. J., 1995, Nat, 375, 469

Yuan W., Brinkmann W., Siebert J., Voges W., 1998a, A&A, 330, 108

Yuan W., Siebert J., Brinkmann W., 1998b, A&A, 334, 498

Zombeck M. V., 1990, *Handbook of Space Astronomy & Astrophysics, 2nd edition.* Cambridge University Press

Chapter 4

Implications of the

Obscured QSO Model at

Sub-mm & Far Infra-Red

Wavelengths

BRIEF ABSTRACT. In this Chapter, we outline the recent advances in the field of sub-millimetre astronomy, describing the observational data and the nature of the sub-mm sources detected so far. We then discuss properties of obscured AGN at sub-mm wavelengths, and compare our model predictions to the sub-mm source counts and the intensity of the far infra-red background. We make predictions for a proposed large area sub-mm survey, and describe how future developments in both ground- and space-based technology will enable us to test these models.

4.1 Motivation

Studies of galaxy evolution at high redshift have made dramatic progress in recent years. Madau et al. (1996) made estimates of the star-formation rate with cosmic time using ultra-violet and optically selected samples of galaxies, and claim to have detected a peak at a redshift of $z \sim 1 - 2$. However, evidence from local starburst galaxies (Meurer et al. 1997) suggests that a large fraction of the star-formation in the most luminous systems is obscured by dust, and is therefore undetected at shorter wavelengths. The energy absorbed by this dust is then re-radiated in the far infra-red. New sub-mm surveys of the high redshift Universe support this suggestion, detecting large populations of dust-obscured sources. In studies of Lyman break galaxies at redshifts $z \sim 4$, Steidel et al. (1999) assume that dust is present in galaxies at all redshifts, and

find no evidence for a decline in the star-formation rate at high redshift. There is therefore much debate over exactly how large a fraction of the star-formation in the Universe has occurred within massive dusty galaxies, and hence when galaxies were formed. However, sub-mm surveys are not easily interpreted, since far infra-red emission from these distant dusty galaxies could be powered by either starbursts or by AGN. Indeed, even for well-studied local examples, *e.g.*, Arp 220 and Markarian 231 (Downes & Solomon 1998), there is still discussion over the contribution to the far infra-red luminosity from highly obscured AGN. For highly obscured sources, it is not possible to use the usual observational signatures to discriminate between starbursts and AGN, and therefore hard X-ray data are required in order to distinguish between these two mechanisms. It is vital that the issue of AGN contamination in samples of sub-mm sources is fully understood, and here we attempt to predict the extent of the AGN contribution in the sub-mm regime.

It has been known for some time that some ultraluminous infra-red galaxies (ULIRGs), which are strongly star-forming, dusty galaxies, also contain buried QSO nuclei. Images of ULIRGs in polarized light have shown highly anisotropic structure, such as that observed in the *IRAS* galaxy, F10214+4724, (Lawrence et al. 1993). Similar polarization structure is seen in Seyfert 2s and high redshift radio galaxies, which is thought to be indicative of non-uniform illumination consistent with the Unified Model of AGN. Optical spectropolarimetric studies of ULIRGs have detected broad emission lines in polarized light in addition to a highly polarized continuum, which again is typical of QSOs (*e.g.*, F10214+4724: Jannuzi et al. 1994; Goodrich et al. 1996; and F15307+3252: Hines et al. 1995). From this, it has been inferred that the QSO and ULIRG phenomena are closely related, with ULIRGs being postulated as being Type 2 objects, or "QSO-2s" (Hines 1998).

Genzel et al. (1998) have made *ISO* observations of ULIRGs in order to determine which is the dominant emission mechanism at FIR wavelengths. They find that $\sim$ 75 per cent are powered by star-formation, while the remaining $\sim$ 25 per cent are AGN. Rigopoulou, Lawrence & Rowan-Robinson (1996) observe a sample of ten ultraluminous *IRAS* galaxies at both sub-mm wavelengths and soft X-ray energies, to investigate the properties of the spectral energy distributions (SED). They find that these galaxies are X-ray quiet with respect to the large far infra-red emission, with SEDs that are well fitted by a starburst model. Although the SEDs are inconsistent with conventional, unobscured QSOs, two of these galaxies are known to contain active nuclei, one of which, Markarian 231, is a broad absorption line (BAL) QSO (Boksenberg et al. 1977), which has a face-on molecular gas disc (Downes & Solomon 1998). For these two sources, and the eight sources for which there is no obvious evidence for AGN activity, the weak soft X-ray emission

may be due to the starburst component. However, scattered X-rays from an obscured AGN cannot be ruled out. A massive dusty torus will also contain huge amounts of molecular gas, and therefore by definition will also be a prime site for star-formation. It has become increasingly evident that both AGN and starburst activity are often present in the same object, and therefore it is naïve to assume that the two processes are either independent or mutually exclusive.

Huge advances have been made recently in the field of sub-mm astronomy, most notably with the advent of SCUBA, the Sub-mm Common User Bolometer Array (Gear & Cunningham 1994; Holland et al. 1999), on the James Clark Maxwell Telescope (JCMT). SCUBA makes gains of ~ 300 over previous instruments, by virtue of its increased sensitivity, efficiency, and multiplexing capabilities. In a SCUBA sub-mm survey of four distant clusters of galaxies (Smail, Ivison & Blain 1997), the brightest source, SMM 02399-0136, was found to be a hyperluminous, active galaxy at redshift $z = 2.8$ (Ivison et al. 1998). Frayer et al. (1998) compare the measured L_{FIR}/L'_{CO} ratio of this high redshift galaxy, SMM 02399-0136 (Ivison et al. 1998), to that of the local starburst, Arp 220, and find that it is twice as high. Since the FIR emission from Arp 220 is purely from merger-induced star-formation, they infer that approximately half of the FIR emission from SMM 02399-0136 must therefore be due to a dust-enshrouded AGN. Further examples include the ultraluminous BALQSO, APM 08279+5255, which at $z \sim 3.9$ is apparently the most luminous object currently known (Lewis et al. 1998), and the sub-mm source B 1933+503, thought to be a high redshift ($z > 2$) dusty radio quasar (Chapman et al. 1999).

One of the central features of our obscured QSO models is the presence of large amounts of gas and dust surrounding the active nucleus, providing the means of absorbing a large fraction of the intrinsic radiation and affecting the observed properties in the optical and X-ray regimes. But this energy must escape somewhere, and through heating of the dust, the absorbed flux is re-radiated at far infra-red (FIR) wavelengths, providing an important test of the models. The amounts of dust that we have invoked are quite considerable, and combined with the huge quantity of energy that must be radiated, plus the wide redshift distribution of these sources, would imply a substantial contribution to the FIR/sub-mm background radiation and source counts.

In the next Section, we describe the latest measurements of the spectrum and intensity of the far infra-red background, and recent observations of the sub-mm source counts. Section 4.3 discusses how our obscured AGN model can be extended to these longer wavelengths, and describes how the emission from the obscuring dust torus has been modelled. The results are presented in Section 4.4, and are compared with the observed sub-mm number counts and the intensity of the far infra-red background at these wavelengths. We discuss the implications of our results in Section 4.5,

and make predictions for the number-redshift relation for future 850μm surveys in Section 4.6. We conclude by describing some of the technological advances due to be implemented in the near future for both ground- and space-based facilities.

4.2 Far Infra-red and Sub-mm Observations

It is extremely difficult to measure the extragalactic far infra-red background (FIRB), due to the presence of foreground components from interplanetary zodiacal dust emission (peaking at $\sim 20\mu$m) and interstellar dust emission from our Galaxy (peaking at $\sim 150\mu$m). This zodiacal and galactic contamination must be carefully modelled, and subtracted to leave the extragalactic background. In addition, the cosmic microwave background (CMB) also contributes at these wavelengths, peaking at ~ 1 mm, and this must also be accounted for. Once these components have been accurately modelled and removed, it should then be possible to detect any extragalactic FIRB.

The first detection of the FIRB was claimed by Puget et al. (1996), who used data from the *Far Infra-red Absolute Spectrometer* (*FIRAS*) on board the *Cosmic Background Explorer* (*COBE*), which operated in the wavelength range 150μm $< \lambda < 5000\mu$m with constant $\Delta\nu$ resolution of $\sim 0.8\,\mathrm{cm}^{-1}$. They took advantage of the FIR window from $200 - 800\mu$m, between the peaks of the zodiacal emission and the CMB, to minimise the contamination from these sources, and found that the intensity of the extragalactic background has the form:

$$\nu I_\nu \simeq 3.4 \left(\frac{\lambda}{400\mu m}\right)^{-3} \times 10^{-9}\,\mathrm{W\,m^{-2}\,sr^{-1}}, \qquad 400\mu m < \lambda < 1000\mu m,$$

and flattens at shorter wavelengths (see Fig. 4.1). More recent measurements have been made by Schlegel, Finkbeiner & Davis (1998), Hauser et al. (1998) and Fixsen et al. (1998) using the *Diffuse Infra-red Background Explorer* (*DIRBE*), also on board *COBE*, at shorter wavelengths. The results differ at shorter wavelengths, with intensities from Schlegel et al. (1998) of:

$$\nu I_\nu = \begin{cases} (17 \pm 4) \times 10^{-9}\,\mathrm{W\,m^{-2}\,sr^{-1}} & \lambda = 240\mu m, \\ (32 \pm 13) \times 10^{-9}\,\mathrm{W\,m^{-2}\,sr^{-1}} & \lambda = 140\mu m, \end{cases}$$

and from Hauser et al. (1998) of:

$$\nu I_\nu = \begin{cases} (14 \pm 3) \times 10^{-9}\,\mathrm{W\,m^{-2}\,sr^{-1}} & \lambda = 240\mu m, \\ (25 \pm 7) \times 10^{-9}\,\mathrm{W\,m^{-2}\,sr^{-1}} & \lambda = 140\mu m, \end{cases}$$

whereas Fixsen et al. (1998) find that the relationship:

$$I_\nu = (1.3 \pm 0.4) \times 10^{-5}(\nu/\nu_o)^{0.64\pm0.12}B_\nu(18.5 \pm 1.2\,\mathrm{K}),$$
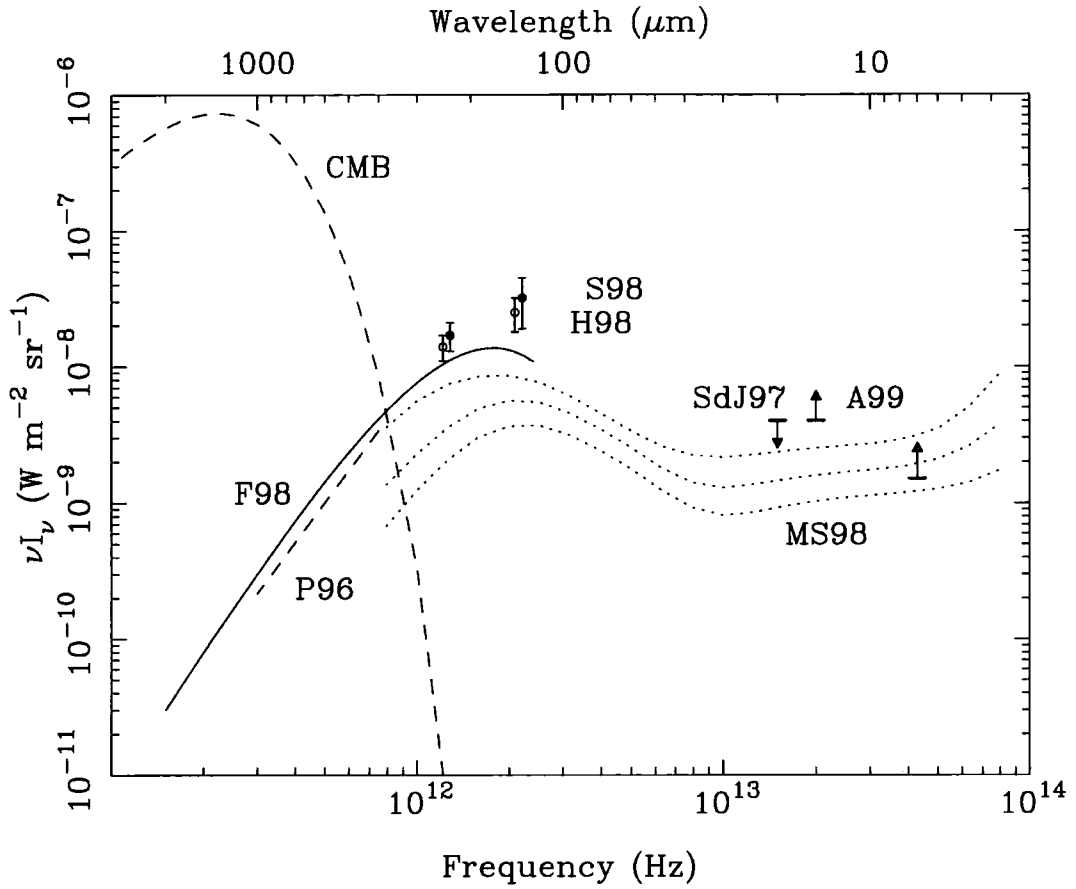
Figure 4.1: The latest measurements and estimates of the extragalactic FIRB, compared with the *COBE* measurement of the Cosmic Microwave Background (CMB; Mather et al. 1994). F98 - Fixsen et al. (1998); P96 - Puget et al. (1996); H98 - Hauser et al. (1998); S98 - Schlegel et al. (1998); SdJ97 - Stecker & De Jager (1997); A99 - Altieri et al. (1999). See text for details of the measurements. MS98 denotes the model predictions of Malkan & Stecker 1998.

gives good agreement over the range $125 < \lambda < 2000 \mu$m, where $\nu_o = 100\,\mathrm{cm}^{-1}$, and B_ν is the Planck function. This gives:

$$\nu I_\nu = \begin{cases} 5.03 \times 10^{-10}\,\mathrm{W\,m^{-2}\,sr^{-1}} & \lambda = 850\mu\mathrm{m}, \\ 1.08 \times 10^{-8}\,\mathrm{W\,m^{-2}\,sr^{-1}} & \lambda = 240\mu\mathrm{m}, \\ 1.26 \times 10^{-8}\,\mathrm{W\,m^{-2}\,sr^{-1}} & \lambda = 140\mu\mathrm{m}. \end{cases}$$

The above measurements of the FIRB from 1 mm to 1μm are plotted in Fig. 4.1, and compared with the black-body spectrum of the CMB.

At even shorter wavelengths, indirect methods are required to estimate the mid infra-red background (MIRB), expected to have an intensity of 0.1 per cent of the zodiacal emission. A lower limit can be found using the *ISOCAM* 7μm and 15μm number counts, by integrating the total contribution from resolved sources (Altieri et al. 1999). They find that $\nu I_\nu(7\mu\mathrm{m}) = (2 \pm 0.5) \times 10^{-9}\,\mathrm{W\,m^{-2}\,sr^{-1}}$ and $\nu I_\nu(15\mu\mathrm{m}) = (5 \pm 1) \times 10^{-9}\,\mathrm{W\,m^{-2}\,sr^{-1}}$. This can then be

combined with upper limits obtained by probing the MIRB with very high energy (VHE) γ-rays (Stecker & De Jager 1997). At TeV energies, γ-ray photons interact with MIRB photons forming electron-positron pairs,

$$\gamma_{VHE} + \gamma_{IR} = e^+ + e^-,$$

thereby attenuating the TeV flux from extragalactic objects such as blazars, in direct proportion to the distance travelled by the radiation. Stecker & De Jager (1997) use VHE observations of the active galaxy Mrk421 in order to constrain the 20μm background to $\nu I_\nu < 4 \times 10^{-9}\,\mathrm{W\,m^{-2}\,sr^{-1}}$.

Malkan & Stecker (1998) use an empirical method to predict the intensity of the extragalactic infra-red background at wavelengths 4μm $< \lambda < 400\mu$m. The measured *IRAS* galaxy luminosity functions at 12μm and 60μm are combined with the known correlations between these luminosities and near infra-red fluxes, which avoids using some of the assumptions present in spectral evolution models. The estimated background spectrum found by this method is fairly flat, $\nu I_\nu \sim 2 - 3 \times 10^{-9}\,\mathrm{W\,m^{-2}\,sr^{-1}}$, with a peak of $\nu I_\nu \sim 6 - 8 \times 10^{-9}\,\mathrm{W\,m^{-2}\,sr^{-1}}$ at around 200μm. An extrapolation to longer wavelengths gives $0.8 - 2.5 \times 10^{-9}\,\mathrm{W\,m^{-2}\,sr^{-1}}$ (450μm) and $0.2 - 0.8 \times 10^{-9}\,\mathrm{W\,m^{-2}\,sr^{-1}}$ (850μm), consistent with that measured by Puget et al. (1996). In Figure 4.1, we show their predictions for the background spectrum due to galaxies, extrapolated from the *IRAS* 60μm luminosity function, for three different evolutionary scenarios: pure luminosity evolution (PLE), $L \propto (1+z)^\gamma$, with $\gamma = 3.1$, up to a cut-off redshift, $z_{cut} = 2$, and passive evolution thereafter, to a maximum redshift, $z_{max} = 4$ (upper line); PLE with $\gamma = 3.1$, $z_{cut} = 1$ and $z_{max} = 4$ (middle line); and a conservative estimate of PLE with $\gamma = 2.0$, $z_{cut} = 1$ and $z_{max} = 4$ (lower line). (Many thanks to Dr Mathew Malkan for supplying me with the digitised form of these data).

There are several surveys currently in progress with the aim of resolving the source populations contributing to the sub-mm background. These surveys take advantage of the increased sensitivity and resolution now available with the SCUBA camera on the JCMT. SCUBA has two arrays of bolometers which can be used simultaneously. A dichroic beamsplitter is used to send the light to the SW array (91 pixels, $450/350\mu$m, HPBW[1] $7''\!\!.5@450\mu$m) and the LW array (37 pixels, $850/750\mu$m, HPBW $14''\!\!.7@850\mu$m), each with a field of view of $2'\!\!.3$. SCUBA also contains two single pixel bolometers at 1.3 mm and 2.0 mm, which require independent observations, but together with the 450μm and 850μm arrays, enable the coverage of a wide spectral range.

---

[1] HPBW: Half Power Beam Width.
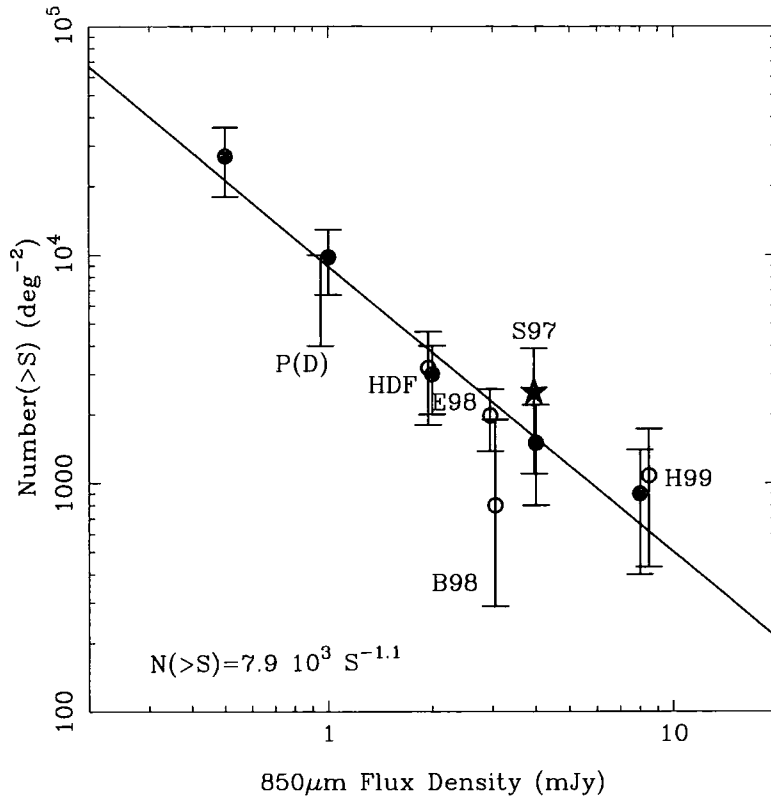
Figure 4.2: The current status of 850μm source counts, together with a power-law fit to the 0.5 $-$ 10 mJy data of $N(> S) = 7.9 \times 10^3 S^{-1.1}$, from Smail et al. (1998). The filled circles show the results of the SCUBA Lens Survey (Blain et al. 1999b), and the other points are as labelled: S97 - Smail, Ivison & Blain (1997); B98 - Barger et al. (1998); H99 - Holland et al. (1999); E98 - Eales et al. (1998); HDF, P(D) - Hughes et al. (1998a).

SCUBA sub-mm surveys can be divided into two types, the first being pointed observations of blank fields (Hughes et al. 1998a; Barger et al. 1998; Eales et al. 1998). The second strategy is to make pointed observations of clusters of galaxies, in order to take advantage of the gravitational amplification due to the lensing mass of the cluster (Smail, Ivison & Blain 1997). In this way, sources can be detected that would be fainter than the flux limit possible without the amplification factor, and in addition, due to the magnification of the source plane, there are fewer problems with source confusion. The 850μm data currently published are plotted in Fig. 4.2, together with a power-law fit of $N(> S) = 7.9 \times 10^3 S^{-1.1}$, from Smail et al. (1998). In the next section, we will compare the predictions of our obscured QSO models with these data.

A third type of sub-mm survey investigates the sub-mm properties of specific classes of objects selected at other wavelengths, for example, low redshift galaxies (Dunne et al. in preparation). Hughes et al. (1998b) are undertaking SCUBA observations of a sample of high redshift, steep spectrum radio-loud AGN, and early results for a sub-sample of objects find tentative evidence

for evolution of sub-mm luminosity with redshift. Omont et al. (1996) used the IRAM 30 m telescope to observe a sample of 22 high redshift ($z > 4$) radio-quiet QSOs at 1.25 mm, six of which were detected with fluxes between 2.5 and 10 mJy. These results also showed evidence for enhanced millimetre emission from QSOs with either broad *absorption* lines (BAL), or weak *emission* lines. BALQSOs are thought to be undergoing enhanced star-formation (Lipari, Terlevich & Macchetto 1993), and dust in their nuclei has been inferred from the observed reddening (Sprayberry & Foltz 1992). Omont et al. interpret their results for the weak emission line QSOs and BALQSOs as due to increased levels of star-formation, but this can also be explained within our current framework of obscured QSOs.

These recent measurements of both the spectrum of the far infra-red background, and the sub-mm number counts, now provide strict constraints with which to test theories of galaxy evolution, star-formation history, etc. It is known that a large fraction of sub-mm sources are starburst galaxies, and that there is a significant contribution from AGN. In the SCUBA Lens Survey (Smail et al. 1998) sample of sub-mm sources, at least 20 per cent were found to show evidence for AGN activity (Barger et al. submitted). In the next Section, we investigate the implications of the obscured AGN hypothesis, by modelling their properties at sub-mm wavelengths. In Section 4.4, we predict the number of such sources expected from our models, and put limits on their contribution to the far infra-red background.

4.3 Modelling

The aim here is to use our obscured AGN models developed in Chapter 2 in order to make self-consistent predictions at sub-mm wavelengths. We assume that all the luminosity absorbed at high energies, is then reprocessed and emitted at lower energies, with a known thermal spectrum. The fluxes expected from such objects can then be estimated, from which we can predict sub-mm source counts and their contribution to the far infra-red background. The assumptions we have made are the following:

- The intrinsic $0.3 - 3.5$ keV X-ray luminosity of each source is known, and is assumed to come from the zero-redshift X-ray luminosity function, with parameters as described in Table 2.1.

- The column density, N_H, perceived by the optical/ultra-violet/X-radiation is assumed to be a measure of the intrinsic amount of dust present, and is not affected significantly by the viewing angle. The covering factor, f_{cov}, of this obscuring material is defined to be the fraction of lines of sight for which a constant N_H is seen, and the remaining lines of sight are unobscured.

Wavelength (Å)
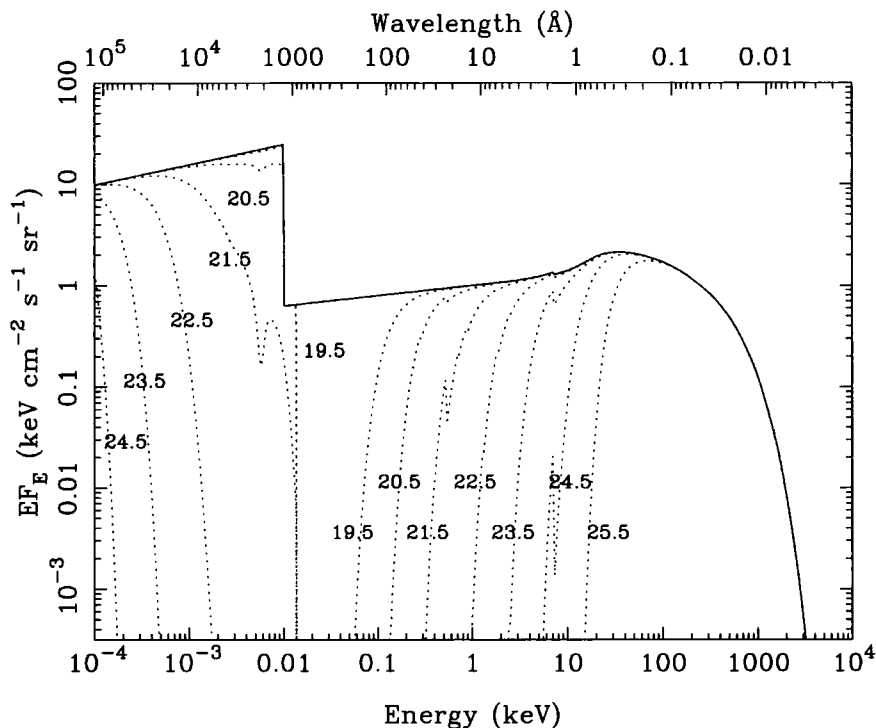
Figure 4.3: The canonical QSO spectrum of $\alpha_{opt} = 0.8$, $\alpha_x = 0.9$ plus reflection with an e-folding energy of 360 keV, and a spectral break at 0.01 keV (solid line, normalized to $F(1\,\text{keV}) = 1\,\text{keV}\,\text{cm}^{-2}\,\text{s}^{-1}\,\text{sr}^{-1}$). The transmitted spectra are shown as dotted lines, with the column density marked in units of $\log(N_H/\text{cm}^{-2})$. The X-ray opacity is due to photo-electric absorption, and the optical/ultra-violet opacity is provided by dust extinction.

- All the absorbed flux goes into heating up the dust and gas in the obscuring medium, whatever the assumed geometry, which is then re-radiated isotropically in the thermal infra-red.

4.3.1 Canonical X-ray/optical QSO spectrum

The intrinsic QSO spectrum, $F(E)$, is assumed to consist of two power-laws, with spectral indices $\alpha_x = 0.9$ (Nandra & Pounds 1994) and $\alpha_{opt} = 0.8$ (Francis 1993), and relative normalization defined by a power-law of slope $\alpha_{ox} = 1.5$ joining 2 keV and 2500 Å, as described in Section 3.4 (Tananbaum et al. 1979; Yuan et al. 1998a). The behaviour of the spectrum between these two regimes is not well known however. Zheng et al. (1997) investigate the far ultra-violet properties of a sample of high redshift QSOs with the *Hubble Space Telescope*. They find that the radio-quiet QSO spectrum can be approximated by a broken power-law, where the spectral break occurs at ~ 1050 Å (~ 0.01 keV), the spectral index at longer wavelengths is $\alpha_{opt} \sim 0.86\pm0.01$ (*c.f.* $\alpha_{opt} \sim 0.8$ used here), steepening significantly to shorter wavelengths. (See also Laor et al. 1997). For simplicity, we therefore assume that the spectral break can be approximated by a step discontinuity

at 0.01 keV. Our assumed canonical QSO spectral energy distribution (SED) is shown by the solid line in Figure 4.3.

4.3.2 Absorbed X-ray/optical QSO spectrum

The next step is to estimate the absorbed luminosity, $L_{\rm abs}$, responsible for the heating of the torus. This is done by calculating the transmitted flux, which escapes from the nucleus unattenuated, and subtracting this from the total emission of the central engine, thereby finding the amount of energy which is absorbed. The transmitted spectrum, $F_{\rm trans}(E)$, is calculated for each column density as follows:

At X-ray energies, the opacity is dominated by photo-electric absorption at columns of $N_H < 10^{24}\,{\rm cm}^{-2}$. However, once the column density increases to $N_H > 10^{24}\,{\rm cm}^{-2}$, then the obscuring medium becomes Compton thick due to electron scattering, such that the effective optical depth is:

$$\tau_{eff} = \tau_{ph} + \tau_{es}.$$

Since the absorbed fraction of the luminosity is almost unity above $N_H \sim 10^{24}\,{\rm cm}^{-2}$ due to photo-electric absorption alone (shown later in Fig. 4.4), we do not take electron scattering into account here as it does not affect our results significantly. The photo-electric absorption coefficients (Morrison & McCammon 1983) and the electron scattering cross-sections can be evaluated using XSPEC (Arnaud 1996). In the optical, the dust extinction laws (Howarth 1983; Seaton 1979) described in Section 3.2 (Equation 3.2) are used to calculate the transmitted spectrum. A constant gas to dust ratio is implicitly assumed here. The resulting SEDs, $E\,F_{\rm trans}(E)$, are shown as dotted lines in Fig. 4.3. As the column increases, so does the amount of the continuum which is destroyed by these processes. The absorbed luminosity can then be calculated from:

$$L_{\rm abs} = f_{cov} \int_{E_{min}}^{E_{max}} [F(E) - F_{\rm trans}(E)]\,{\rm d}E,$$

integrating between limits $E_{min} = 10^{-4}\,{\rm keV}$ ($\sim 10^5\,$Å or $10\,\mu{\rm m}$), which corresponds to the low energy end of the optical power-law, and $E_{max} = 10^4\,{\rm keV}$, which is above the high energy cut-off of the X-ray spectrum. The range of intrinsic luminosities is defined by the X-ray luminosity function (XLF), so the absorbed luminosity is normalized by the known X-ray luminosity, L_X:

$$L_X = \int_{0.3\,{\rm keV}}^{3.5\,{\rm keV}} F(E){\rm d}E.$$

The fraction of the luminosity which is absorbed can then be calculated from:

$$f_{\rm abs} = \frac{L_{\rm abs}}{L_{\rm tot}} = 1 - \frac{\int F_{\rm trans}(E)\,{\rm d}E}{\int F(E)\,{\rm d}E}.$$

again integrating between E_{min} and E_{max}. Fig. 4.4 shows how the absorbed fraction increases with column density, saturating above $N_H \sim 10^{25}\,\mathrm{cm}^{-2}$. This is due to the fact that once the column gets to such a level, no radiation whatsoever can escape unaffected from the nucleus, and all the emitted energy goes into heating up the obscuring medium.

An alternative way to think about this is the following. The absorbed luminosity can be approximated by calculating the energy at which the optical depth is unity for each process as a function of the column density, and then we assume that all the luminosity emitted between these two energies is absorbed. Using the relationship $\tau(E) = \sigma(E)N_H$, the cross-section scales as $\sigma(E) = 1/N_H$, for an optical depth of unity. The absorbed luminosity is then calculated from:

$$L_{\mathrm{abs}} = f_{cov} \int_{E(\tau_{opt}=1)}^{E(\tau_x=1)} F(E)\,\mathrm{d}E.$$

The values obtained for $E(\tau_x = 1)$ and $E(\tau_{opt} = 1)$ are shown in Table 4.1, together with the fractional absorbed luminosity. It can clearly be seen that f_{abs} increases with column density until it saturates above $N_H \sim 10^{25}\,\mathrm{cm}^{-2}$.

4.3.3 Far infra-red QSO spectrum

Finally, we assume that all the absorbed radiation, L_{abs}, has to escape as thermal emission from the dust in the far infra-red, and therefore that $L_{\mathrm{FIR}} = L_{\mathrm{abs}}$. We also assume that the FIR luminosity is isotropic, and therefore that the received flux is independent of viewing angle. For the case for which the obscuring medium is also isotropic, this is a realistic assumption, as self-shielding of the inner regions means that only radiation from the outer, cooler layers of dust will be received. However, for a toroidal geometry (*e.g.*, $f_{cov} \sim 0.5$), radiation from the hot dust in the innermost regions will be able to escape from the top of the torus, and for face-on viewing angles, the spectrum will be broadened due to the superposition of components at a range of different dust temperatures (Pier & Krolik 1992). This has the effect of boosting the flux at short wavelengths ($\lesssim 10\mu$m) but does not change the spectrum significantly at the wavelengths at which we are primarily concerned ($\gtrsim 100\mu$m), as the hot emission component makes little contribution, and the torus is optically thick. As the true geometry is still unclear, neglecting this effect means that the predictions from our models at short wavelengths should be taken to be lower limits. We therefore choose to approximate our obscuring medium by isothermal dust, emitting isotropically.

By convention, at these energies, frequency units are used, and we write:

$$L_{\mathrm{FIR}} = \int P(\nu_e)\,\mathrm{d}\nu_e.$$
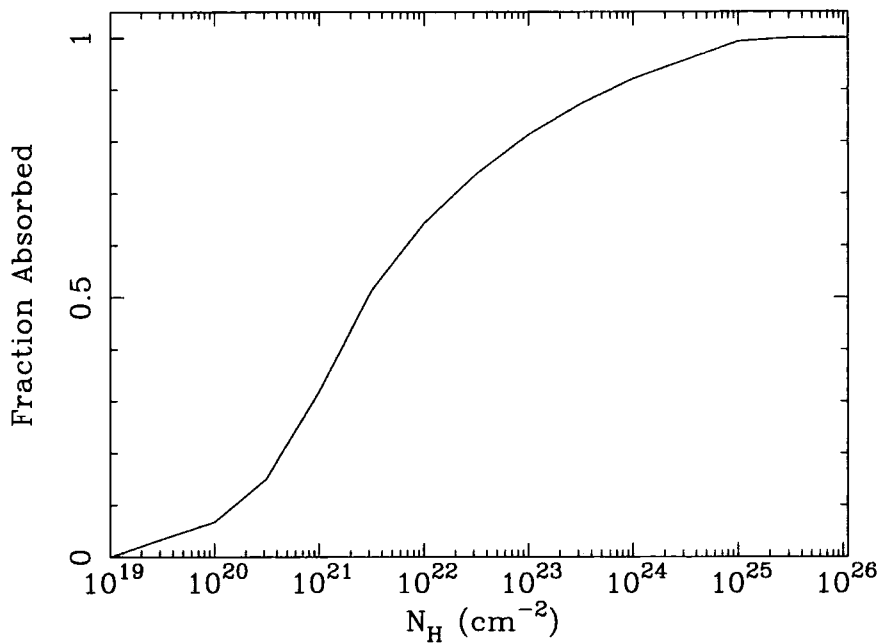
Figure 4.4: The fraction of the total X-ray and optical luminosity absorbed, as a function of the column density, N_H, for a covering factor of unity. Once the column is as high as $N_H \sim 10^{25}$ cm^{-2}, effectively all the energy is absorbed. For $f_{cov} = 0.5$, the fraction absorbed will be half that shown here.

N_H	σ	$E(\tau_X = 1)$	$E(\tau_{\mathrm{opt}} = 1)$		$L_{\mathrm{abs}}/L_{\mathrm{tot}}$
(cm^{-2})	(cm^2)	(keV)	(keV)	(Å)	
3.16×10^{19}	3.16×10^{-20}	0.12	3.81×10^{-2}	325	0.035
1.00×10^{20}	1.00×10^{-20}	0.19	2.36×10^{-2}	525	0.067
3.16×10^{20}	3.16×10^{-21}	0.30	1.47×10^{-2}	846	0.150
1.00×10^{21}	1.00×10^{-21}	0.45	4.56×10^{-3}	2,700	0.319
3.16×10^{21}	3.16×10^{-22}	0.90	1.63×10^{-3}	7,600	0.513
1.00×10^{22}	1.00×10^{-22}	1.42	8.36×10^{-4}	14,800	0.642
3.16×10^{22}	3.16×10^{-23}	2.24	4.66×10^{-4}	26,600	0.737
1.00×10^{23}	1.00×10^{-23}	3.46	2.73×10^{-4}	45,420	0.813
3.16×10^{23}	3.16×10^{-24}	5.19	1.70×10^{-4}	72,940	0.872
1.00×10^{24}	1.00×10^{-24}	9.83	1.15×10^{-4}	107,800	0.921
3.16×10^{24}	3.16×10^{-25}	14.45	8.70×10^{-5}	142,500	0.957
1.00×10^{25}	1.00×10^{-25}	21.22	7.50×10^{-5}	165,300	0.993

Table 4.1. The energies at which the optical depth of unity is obtained, for both photo-electric absorption, $E(\tau_x = 1)$, and dust extinction, $E(\tau_{opt} = 1)$, as a function of column density, N_H, and the corresponding cross-section, σ. The fraction of the total X-ray and optical luminosity, $f_{abs} = L_{abs}/L_{tot}$ is also shown, for a covering factor $f_{cov} = 1$. The values for $f_{cov} = 0.5$ are half that for $f_{cov} = 1$.

The Planck function for a black-body, $B(\nu, T)$, has the following form:

$$B(\nu, T) = \frac{2h\nu^3}{c^2} \left\{ \exp\left(\frac{h\nu}{kT}\right) - 1 \right\}^{-1}, \tag{4.1}$$

where h is Planck's constant, k is Boltzmann's constant, and T is the temperature. Assuming optically thin dust emission, the Planck function is modified by an opacity law, where the opacity depends on both the dust grain composition and the size and shape distribution of the grains, and which can be parametrized as $\kappa_d \propto \nu^\beta$. The effect of varying β is shown in Fig. 4.5, where $\beta = 0$ corresponds to pure black-body emission (optically thick), and values of β from the literature vary in the range $1 < \beta < 2$ (optically thin). By measuring the apparent spectral index of the dust below the peak of the sub-mm emission, an indication of the opacity can be obtained, since a pure black-body satisfies the Rayleigh-Jeans law for $h\nu \ll kT$:

$$B(\nu, T) = \frac{2\nu^2}{c^2} kT,$$

and therefore has a spectral index of $\alpha = 2$, where here we take $S \propto \nu^\alpha$. For optically thin dust, the spectrum is much steeper and $\alpha > 2$. Following Cimatti et al. (1997), we use the opacity law:

$$\kappa_d = 0.15 \left(\frac{\nu_e}{250\,\mathrm{GHz}}\right)^2 \mathrm{cm^2\,g^{-1}}.$$

The dust temperature is taken to be in the range $30\,\mathrm{K} < T_d < 70\,\mathrm{K}$ (Haas et al. 1998; Benford et al. 1998, 1999). In Fig. 4.6, we show the effect on the received sub-mm flux of changing T_d while keeping the emitted FIR luminosity, L_{FIR}, constant. If the temperature is increased, the luminosity also increases, and therefore the total normalization must be reduced in order to keep L_{FIR} constant, and vice versa.

The emitted power, $P(\nu_e)$, can therefore be parametrized as follows:

$$P(\nu_e) = 4\pi\kappa_d(\nu_e) B(\nu_e, T_d) M_d, \tag{4.2}$$

To calculate the received flux from such a source, we use the relationship:

$$S(\nu_o)\,\mathrm{d}\nu_o = \frac{P(\nu_e)}{4\pi D_L^2}\,\mathrm{d}\nu_e = (1 + z)\frac{P(\nu_e)}{4\pi D_L^2}\,\mathrm{d}\nu_o,$$

where D_L is the luminosity distance and $\mathrm{d}\nu_e = (1 + z)\,\mathrm{d}\nu_o$, to give:

$$S(\nu_o) = \frac{(1 + z)\kappa_d(\nu_e) B(\nu_e, T_d) M_d}{D_L^2}. \tag{4.3}$$

To calculate the integrated source counts as a function of flux density, we then use the same method as in Section 2.3, starting from the $0.3 - 3.5\,\mathrm{keV}$ XLF, and using the above relationships between L_X and $S(\nu_o)$. Note that in the sub-mm regime, traditionally flux *density* is used, with units of Janskys, $(1\,\mathrm{Jy} = 10^{-23}\,\mathrm{erg\,cm^{-2}\,s^{-1}\,Hz^{-1}})$, rather than the broad-band flux used at X-ray energies (units: $\mathrm{erg\,cm^{-2}\,s^{-1}}$), or optical magnitudes.
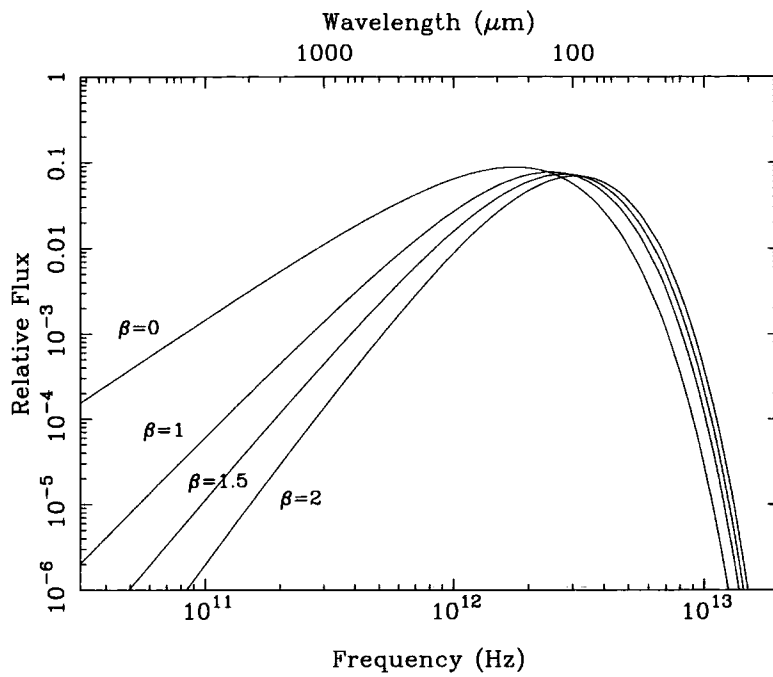
Figure 4.5: The effect on the FIR spectrum of varying the β parameter used to describe the opacity law, $\kappa_d \propto \nu^\beta$. The emission from $10^7\,M_\odot$ of dust with a temperature of $T_d = 30\,K$ is constrained to have the same total luminosity, L_{FIR}, in each case. Pure black-body emission has $\beta = 0$ and values used in the literature lie in the range $1 < \beta < 2$.
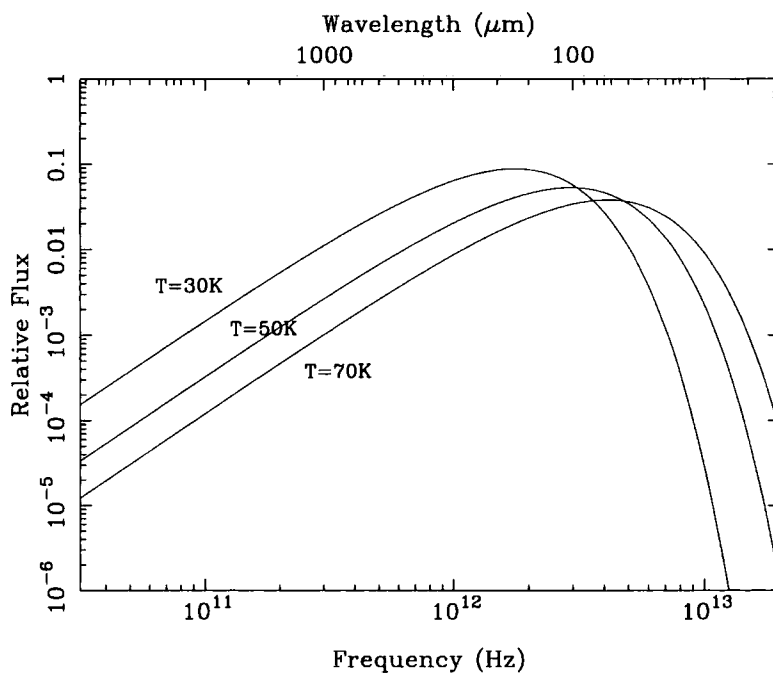
Figure 4.6: The effect of varying the dust temperature on the FIR spectrum due to $10^7\,M_\odot$ of dust, with an opacity parameter $\beta = 0$. The total luminosity, L_{FIR}, is constrained to be the same in each case.

Model	f_{cov}	z_{max}	T_d (K)	I_Q ($10^{-11}\,\mathrm{W\,m^{-2}\,sr^{-1}}$)	I_Q/I_{FIRB} (%)
POW(0.0)	1.0	5	30	8.70	17.4
POW(0.5)	1.0	5	30	3.80	7.6
POL(0.0)	1.0	5	30	5.41	10.8
POL(0.5)	1.0	5	30	2.23	4.5
POW(0.0)	0.5	5	30	6.85	13.2
POW(0.5)	0.5	5	30	3.00	6.0
POL(0.0)	0.5	5	30	4.08	8.2
POL(0.5)	0.5	5	30	1.75	3.5
POW(0.0)	1.0	2	30	1.30	2.6
POW(0.0)	1.0	10	30	16.4	32.9
POW(0.0)	1.0	5	50	1.04	2.1
POW(0.0)	1.0	5	70	0.149	0.3
POW(0.5)t	1.0	5	30	7.57	15.1
POL(0.0)t	1.0	5	30	4.45	8.9
POW(0.5)t	0.5	5	30	5.24	10.5
POL(0.0)t	0.5	5	30	3.05	6.1

Table 4.2. The contribution to the intensity of the FIRB at 850μm predicted by our obscured AGN model. The parameters used are as described in the text, where we have investigated the effects of changing the X-ray luminosity function and evolution, the covering factor of the obscuring medium f_{cov} and its temperature T_d, and the maximum redshift z_{max}. The predictions are compared with the observed 850μm background intensity from Fixsen et al. (1998) of $I_{\mathrm{FIRB}} = 5.03 \times 10^{-10}\ \mathrm{W\,m^{-2}\,sr^{-1}}$.

4.4 Sub-mm predictions

Here we investigate the contribution to the sub-mm source counts and the far infra-red background predicted by our obscured AGN model. We look at the effects of changing certain parameters, such as the covering factor and temperature of the obscuring medium, the luminosity evolution of the AGN, and the maximum redshift at which these sources exist. At present, these parameters are not well constrained, particularly at high redshift. However, despite evidence that the space density of QSOs declines beyond $z \sim 3$ (Shaver et al. 1996), we know that QSOs exist at high redshift. New search techniques are discovering more such objects all the time, for instance the three QSOs found recently by the SDSS Collaboration (Fan et al. 1998), all with redshifts in the range $4.75 < z < 5.0$. As we are using luminosity functions and evolutionary models determined from X-ray selected QSOs, these have diverging properties above $z \sim 2$, and can therefore be taken to span the range of likely properties. By invoking the most extreme cases, we are able
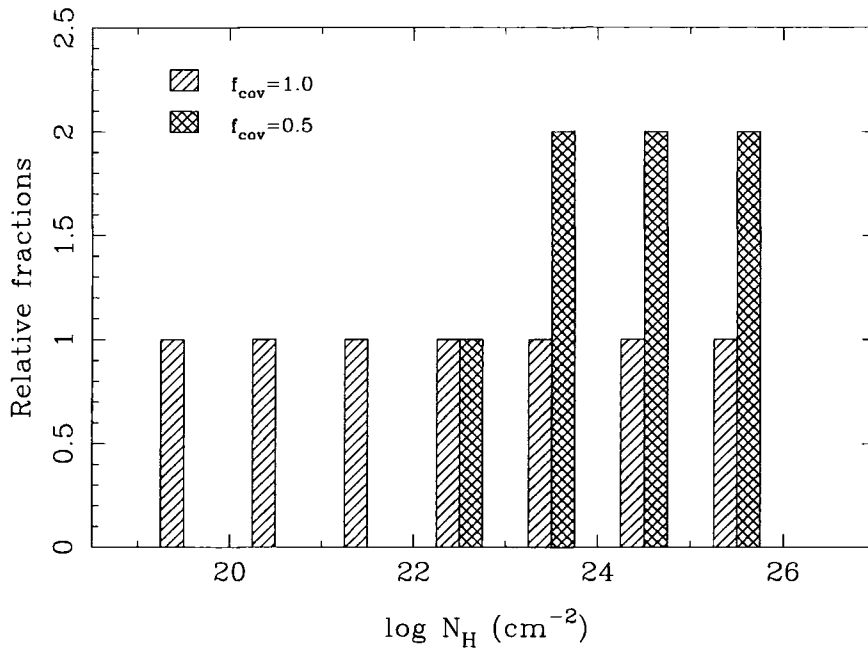
Figure 4.7: Comparisons of two different intrinsic column density distributions of obscured QSO populations, which give rise to the same *perceived* flat distribution. For an isotropic absorber, the covering factor is unity, *i.e.*, $f_{cov} = 1$, and therefore an intrinsic flat distribution will also be perceived as flat (hatched regions); however, for an absorber for which $f_{cov} = 0.5$, a larger number of obscured sources are required, as half will be observed to be unobscured (cross-hatched regions); the two distributions are shown slightly offset from one another for clarity. For the tilted distribution of columns used in $q_0 = 0.5$ scenarios, a similar correction must be made when $f_{cov} = 0.5$ is assumed.

to put firm upper limits on the obscured AGN contribution to both the source counts and FIRB intensity.

4.4.1 The covering factor of the absorbing material

As described earlier, in order to remain consistent with the assumed flat column distribution used in Chapters 2 and 3, we must also consider the covering factor of the obscuring material, as this affects the intrinsic distribution of column densities. Here, we take two examples, first that the obscuring material is isotropic, *i.e.*, with a covering factor $f_{cov} = 1$, and secondly that a torus covers half the sky as perceived by the nucleus for all sources, *i.e.*, $f_{cov} = 0.5$. We assume that these two values will span the true range of covering factors. The intrinsic distributions giving rise to a *perceived* flat column distribution are shown in Fig. 4.7.

A method for differentiating between these two cases, and constraining the geometry of the obscuring material in AGN, is to observe a sample of QSOs to determine the fraction which are highly luminous at sub-mm wavelengths. By definition, very little dust exists along the line-of

sight to broad-line QSOs. Therefore, if the absorbing medium is isotropic, the dust content of broad-line QSOs must be intrinsically low, with low sub-mm emission. However, for a toroidal structure in the spirit of the Unified Model (Antonucci 1993), broad-line QSOs could contain large amounts of dust in a plane perpendicular to the line of sight. This is consistent with the large infra-red bump observed by Sanders et al. (1989) in the 3000 Å to 300μm spectrum of a sample of Palomar Green QSOs (Schmidt & Green 1983). Therefore, if all QSOs contain large quantities of dust, they will be strong sub-mm sources. Proposed sub-mm observations of X-ray selected QSOs using SCUBA/JCMT will shed further light on this question in the near future.

4.4.2 The effects of changing the XLF parameters

We first investigate the predicted source counts for the obscured QSO models used in Section 2.1, with a flat distribution of columns, integrated over redshifts $0 < z < 5$. The X-ray luminosity function use the power-law and polynomial evolution models from Boyle et al. (1994), for both $q_0 = 0.0$ and $q_0 = 0.5$ cosmologies. The parameters of these models are detailed in Table 2.1.

First, we take as our fiducial model a power-law prescription for the luminosity evolution, and a $q_0 = 0.0$ cosmology, which we denote as POW(0.0). This model will be used hereafter, unless stated otherwise. In Fig. 4.8, we show the source counts predicted by this model, compared with the SCUBA data described in Section 4.2 and Fig. 4.2. A covering factor of $f_{cov} = 1$ is assumed, for a dust temperature of $T_d = 30$ K, integrated over $0 < z < 5$. The contribution from each population of obscured QSOs is shown by a dashed line, with the total source counts denoted by a solid line. The reverse trend to that observed at X-ray energies is seen here: the populations with the smallest column densities give the lowest sub-mm fluxes, with the high column density populations dominating the sub-mm source counts due to the large dust masses present. This model predicts ~ 20 per cent of the source counts at 2 mJy, and flattens off at fainter fluxes, but will provide ~ 17 per cent of the FIRB at 850μm.

In Fig. 4.9, the predictions for all four Boyle et al. models are shown, for covering factors of (a) $f_{cov} = 1$ and (b) $f_{cov} = 0.5$, using the intrinsic column distribution that each covering factor implies. As expected, the low q_0 models give a much larger contribution to the source counts than the $q_0 = 0.5$ models, due to volume effects. Taking the measured value for the 850μm FIRB intensity of $I_{FIRB} = 5.0 \times 10^{-10}$ W m^{-2} sr^{-1} from Fixsen et al. (1998), we calculate the fraction of the FIRB which can be accounted for by our obscured QSOs. Low q_0 models provide $\sim 8 - 17$ per cent of the FIRB intensity, compared with $\sim 3 - 8$ per cent for the $q_0 = 0.5$ models, as shown in Table 4.2.
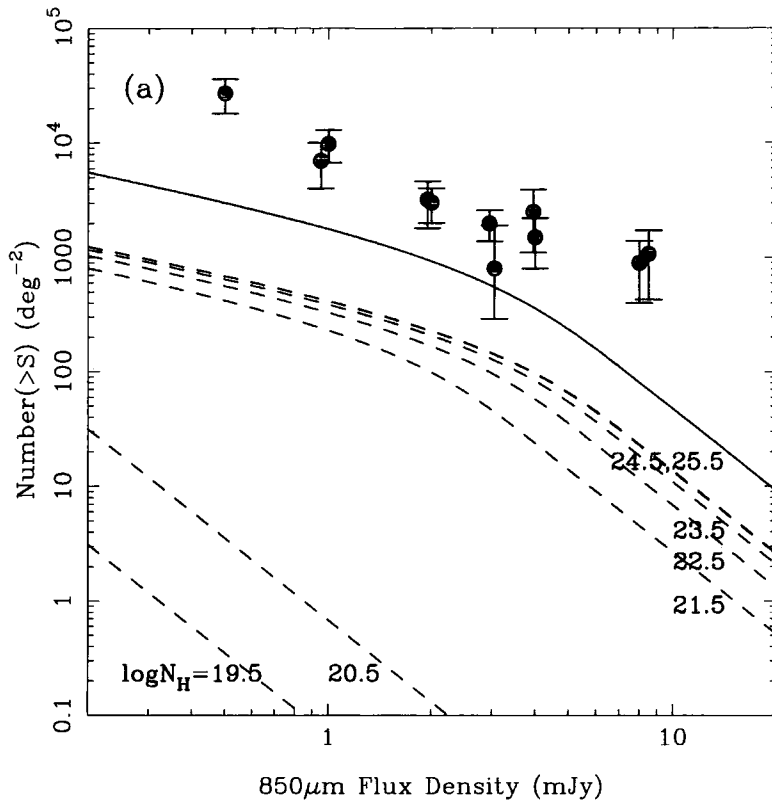
Figure 4.8: Predicted 850μm source counts of obscured QSOs, compared with the observed counts as described in Fig. 4.2. A dust temperature of $T_d = 30$ K and a covering factor $f_{cov} = 1$ is assumed, integrated over $0 < z < 5$, for power-law luminosity evolution and $q_0 = 0.0$, model POW(0.0). The contribution from each individual population of obscured QSOs is shown as a separate dashed line, marked with the column density, and the total is shown by the solid line. In contrast to the X-ray number counts, here the biggest contribution comes from the most highly obscured objects, since these contain the largest amounts of dust. This model accounts for ~ 17 per cent of the FIRB.

The difference in the predicted number counts and background intensity between the $f_{cov} = 1$ and $f_{cov} = 0.5$ cases is due to the increased intrinsic far infra-red luminosity of sources which have an isotropic absorbing medium, as a greater fraction of the nuclear radiation is intercepted. These intrinsically brighter sources are therefore detected at higher fluxes, increasing the bright-end number counts. However, at faint fluxes, the predictions are similar for both assumed covering factors, implying that we are observing high redshift objects, which by definition will be the most luminous sources in either case.

For an isotropic covering medium, the predicted source counts of obscured AGN at 2 mJy account for between 8 and 20 per cent of the total counts, whereas for the anisotropic case, the numbers drop by about a third, since the objects are less luminous. The contribution to the intensity of the FIRB is $\sim 3 - 13$ per cent in the $f_{cov} = 0.5$ case, which is about 25 per cent lower than the $\sim 4 - 17$ per cent predicted for the $f_{cov} = 1$ case.
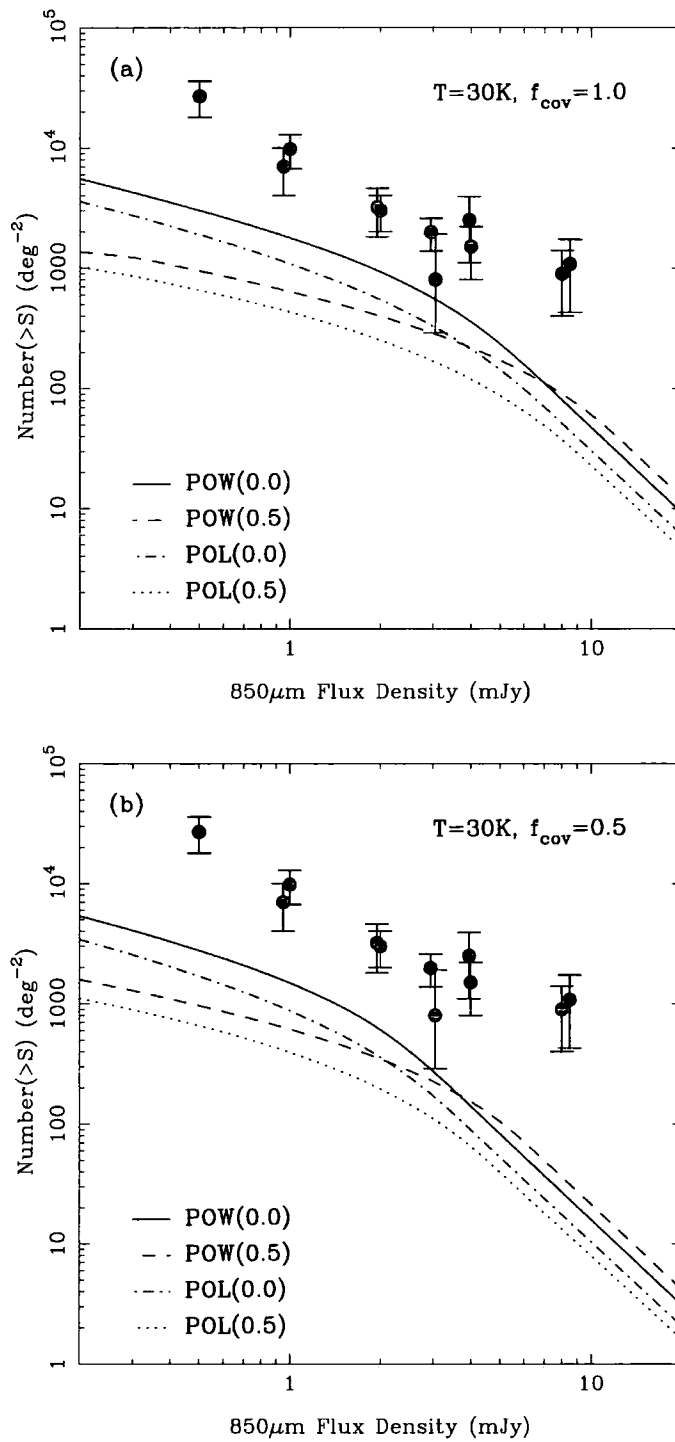
Figure 4.9: Total predicted 850μm source counts of obscured QSOs for models using power-law and polynomial evolution, $q_0 = 0.0$ and $q_0 = 0.5$ cosmologies, compared with the observed sub-mm counts as described in Fig. 4.2. A covering factor of (a) $f_{cov} = 1$, and (b) $f_{cov} = 0.5$, is assumed, with a dust temperature of $T_d = 30$ K, integrated over $0 < z < 5$. These models can account for between 17 per cent (POW(0.0), $f_{cov} = 1$) and 4 per cent (POL(0.5), $f_{cov} = 0.5$) of the FIRB. Note the change of scale with respect to Fig. 4.8.

4.4.3 The effects of changing z_{max} and T_d

If we were to assume that obscured QSOs exist out to redshift $z_{max} \sim 10$, then we can make a much larger contribution to the source counts and FIRB intensity, as shown for $T_d = 30\,\mathrm{K}$ and $f_{cov} = 1$ in Fig. 4.10(a). However, it is difficult to envisage a scenario in which large numbers of dusty QSOs form at such early epochs (Efstathiou & Rees 1988), and therefore this places a useful constraint on the maximum contribution such models can provide. Obscured QSOs from $0 < z < 10$ could contribute over 30 per cent of the Fixsen et al. (1998) measurement of I_{FIRB}.

There are very few complete sub-mm surveys of AGN at low and high redshifts in the literature, with enough data to constrain the dust temperatures in such objects. The uncertainties involved in making such estimates are high, where assumptions have to be made about the cosmology, the dust masses and the opacities, and in addition, observations at several different wavelengths are required in order to start to put limits on the parameters in the models. Treating the dust as isothermal is likely to be an oversimplification, but will be adequate for our purposes, and therefore we estimate that the range $30\,\mathrm{K} < T_d < 70\,\mathrm{K}$ should span the most probable temperatures.

For each column density used, the FIR luminosity is in effect fixed by the known amount of nuclear X-ray and optical luminosity which has been absorbed. Changing the temperature must therefore affect the flux received, as shown in Fig. 4.6. This is equivalent to saying that if we increase the temperature of the dust, the mass of the dust must be decreased in order to keep L_{FIR} constant. As the temperature is increased, the peak of the thermal radiation moves to higher frequencies, thereby reducing the intensity of the source at sub-mm energies. In Fig. 4.10(b), we show the effect of varying the temperature on the sub-mm counts, where the highest number of sub-mm sources are observed for the model with the lowest dust temperature. If the dust around most AGN is warm, $T_d \sim 70$, then the contribution to the $850\mu\mathrm{m}$ FIRB will be negligible, whereas at $100\mu\mathrm{m}$, their impact will be more significant.

4.4.4 Tilted column distributions for $q_0 = 0.5$ models

One further test here for the obscured QSO model is to look at the tilted distribution of column densities, which was invoked in order to obtain a better fit to the XRB for high density, $q_0 = 0.5$, models for the XLF. By skewing the distribution of objects towards higher column densities, this could have the effect of overpredicting the source counts and background intensity. However, in Fig. 4.11, it can be seen that the source counts predicted with this distribution for a range of models lie well below the observed counts, and flatten off towards fainter fluxes, again primarily due to
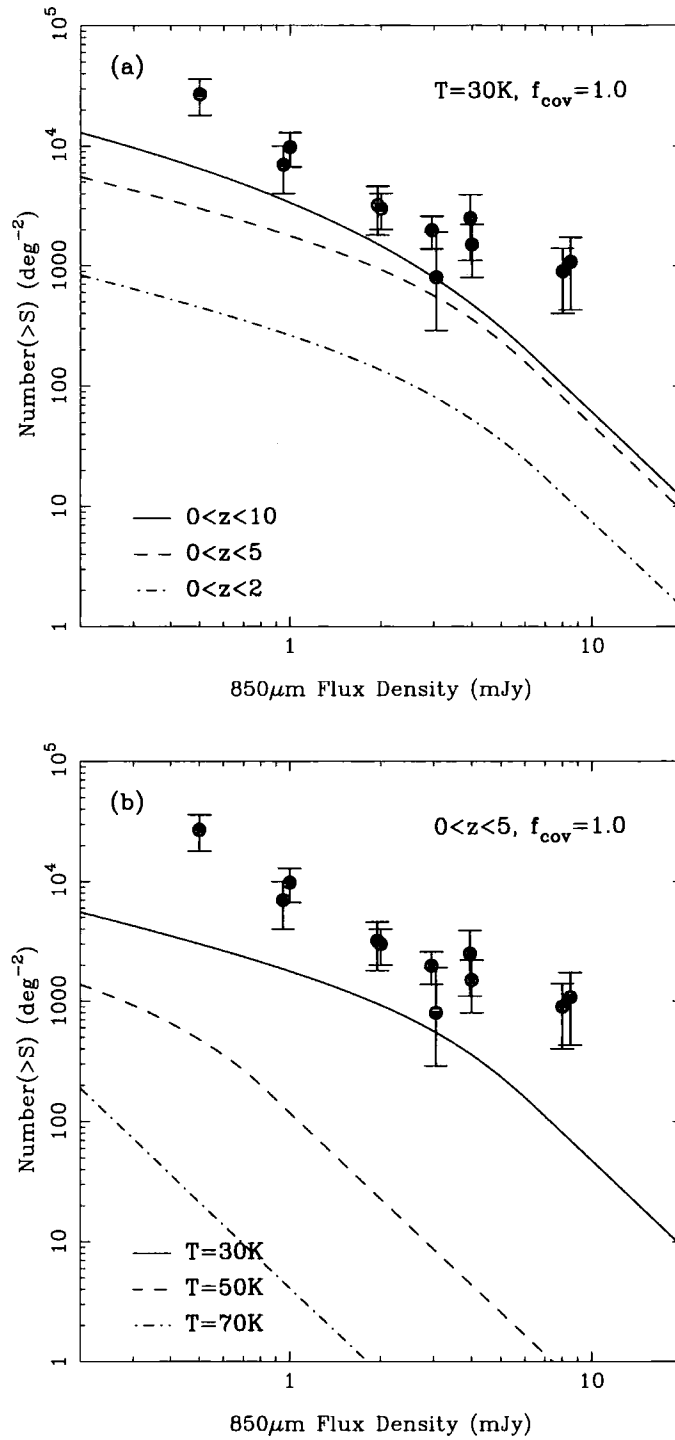
Figure 4.10: (a) The effect on the observed 850μm source counts, of varying the maximum redshift, z_{max}, for dust at T_d = 30 K, for z_{max} = 2, 5 and 10. (b) The effect on the observed 850μm source counts, of varying the dust temperature between T_d = 30 K and T_d = 70 K, over redshifts 0 < z < 5. In both cases, parameters for our fiducial model POW(0.0) have been used, for seven populations with a flat column distribution, and a covering factor f_{cov} = 1.
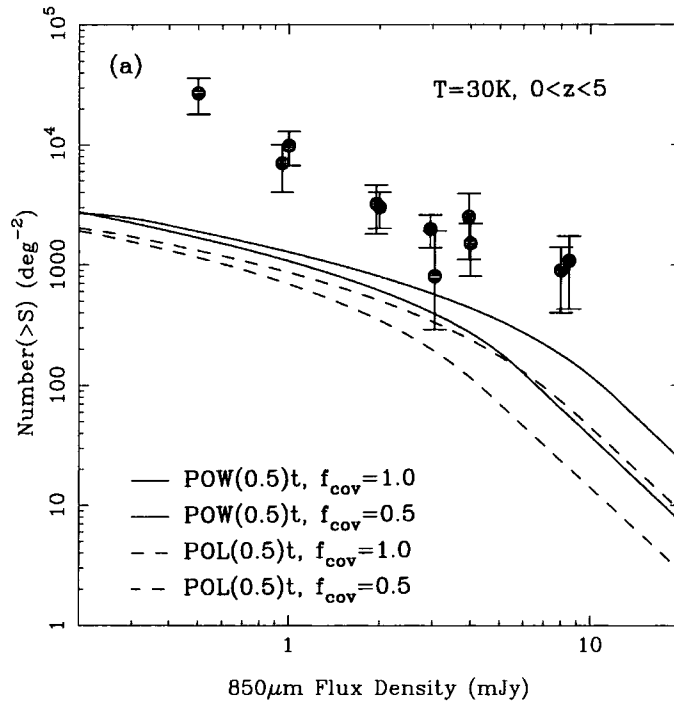
Figure 4.11: The predicted total source counts for the $q_0 = 0.5$ models, for power-law (solid lines) and polynomial (dashed lines) luminosity evolution, using a tilted distribution of column densities as described in Section 2.6. Predictions for both a covering factor of $f_{cov} = 1$ (bold lines) and $f_{cov} = 0.5$ (thin lines) have been plotted, using $T_d = 30$ K and $z_{max} = 5$.

volume effects. The maximum contribution to I_{FIRB} from these models is ~ 15 per cent, for model POW(0.5)t with $T_d = 30$ K and $f_{cov} = 1$.

4.4.5 Number-redshift distributions

In Fig. 4.12, we plot the number-redshift distributions predicted by our obscured QSO models, for an 850μm survey to 2 mJy (*c.f.* the 1σ confusion limit for the JCMT/SCUBA of 0.44 mJy beam^{-1}; Blain, Ivison & Smail 1998). Again, we use a dust temperature of $T_d = 30$ K, and consider sources out to redshift $z_{max} = 5$, and make predictions for both (a) $f_{cov} = 1$ and (b) $f_{cov} = 0.5$. We have taken four models with a flat column distribution of seven populations of obscured AGN, and two models using a tilted distribution of six populations, as described in Section 2.6 (all for $f_{cov} = 0.5$). In the $q_0 = 0.0$ cosmology, the number of sub-mm sources predicted at redshifts $z > 3$ is much higher than for $q_0 = 0.5$, consistent with the steeper faint-end slope of the LogN:LogS relation for a low q_0 universe. It will be very straightforward to distinguish between the two types of luminosity evolution, power-law vs polynomial, once more identifications become available, due to the fact that it is as easy to detect a sub-mm source at high
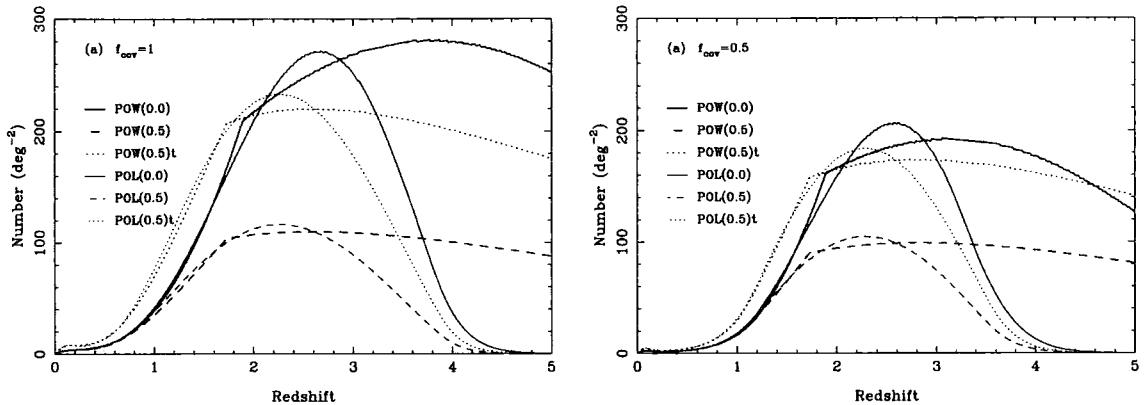
Figure 4.12: Predicted number-redshift distribution for an 850μm survey to $2\,$mJy, of obscured QSOS with $T_d = 30\,$K, and $z_{max} = 5$, for covering factors of (a) $f_{cov} = 1$, and (b) $f_{cov} = 0.5$. Note the higher number densities predicted for low q_0 models.

redshift as at low redshift, and therefore if large numbers of high redshift obscured QSOs exist, they will be found in deep SCUBA surveys.

The follow-up identification programs for the latest SCUBA sub-mm surveys are nearing completion, and the source catalogues will soon be published. We shall therefore be able to compare the numbers of AGN detected with the redshift distributions predicted by our models. It is interesting to note that ~ 10 per cent of the optical counterparts to sub-mm sources are classified as Extremely Red Objects (EROs) (Smail et al. in preparation), which are found in $K-$band images of the SCUBA error boxes. Deep radio maps provide more accurate positional information than the SCUBA maps, assuming that the radio and sub-mm emission is due to the same mechanism, and the ERO counterparts are confirmed by the radio data. It will be very difficult to obtain spectroscopic redshift information about these objects, even with a 10-m class telescope such as Keck, as they are so faint in the optical, with $I \gg 25$. However, near infra-red spectroscopy has been used successfully to obtain a redshift of $z = 1.44$ for the ERO HR10 (Dey et al. 1999). Potentially, these could be examples of very highly obscured AGN at high redshift, for which in the optical and near infra-red we see the dusty host galaxy (hence the very red colours), and only see evidence for the AGN through the sub-mm and radio emission. Future deep surveys with *AXAF* and *XMM*, such as the proposed *AXAF* and SCUBA observations of the SSA 13 field (Cowie et al.), will provide a vital test of these theories, in searching for faint X-ray emission associated with these sources. However, unlike in the sub-mm regime, the X-ray k-correction is not working in our favour, and if we assume that these sources are at high redshift, then this is still an extremely ambitious project.
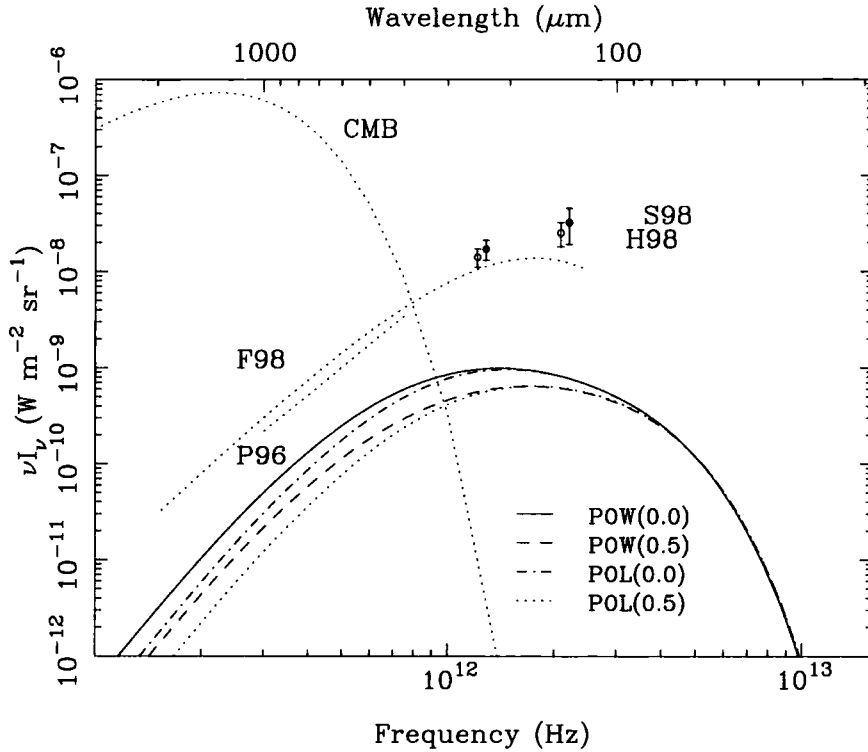
Figure 4.13: The predicted contribution to the FIRB from seven populations of obscured AGN with a flat column distribution, using power-law and polynomial luminosity evolution, for both $q_0 = 0.0$ and $q_0 = 0.5$ cosmologies, as labelled. A covering factor $f_{cov} = 1$ is used, with a dust temperature $T_d = 30$ K, integrated over redshifts $0 < z < 5$. The data are as described in Figure 4.1: CMB - Cosmic Microwave Background, Mather et al. (1994); F98 - Fixsen et al. (1998); P96 - Puget et al. (1996); H98 - Hauser et al. (1998); S98 - Schlegel et al. (1998).

4.4.6 Predicted spectrum of the far infra-red/sub-mm background

We have shown from the sub-mm number counts predicted from our models that obscured AGN provide a small but non-negligible fraction of the intensity of the far infra-red background at 850μm, ranging from 1 to 33 per cent. Fig. 4.13 shows the spectrum predicted from our flat distribution of column densities using a covering factor $f_{cov} = 1$, a dust temperature $T_d = 30$ K, and integrated over redshifts $0 < z < 5$. It can be seen that all four models predict the same intensity at high frequencies. This is to be expected, as the emission here is dominated by low redshift objects for which the rest-frame peak of the 30 K thermal spectrum is at $\sim 100\mu$m. Since the model parameters have been obtained from fits of the X-ray luminosity function to X-ray selected QSOs from *ROSAT* and the *Einstein* EMSS, which have relatively low median redshifts of $z \sim 1.5$ and $z \sim 0.2$ respectively, we would expect the predictions to diverge at high redshift and therefore low frequencies.
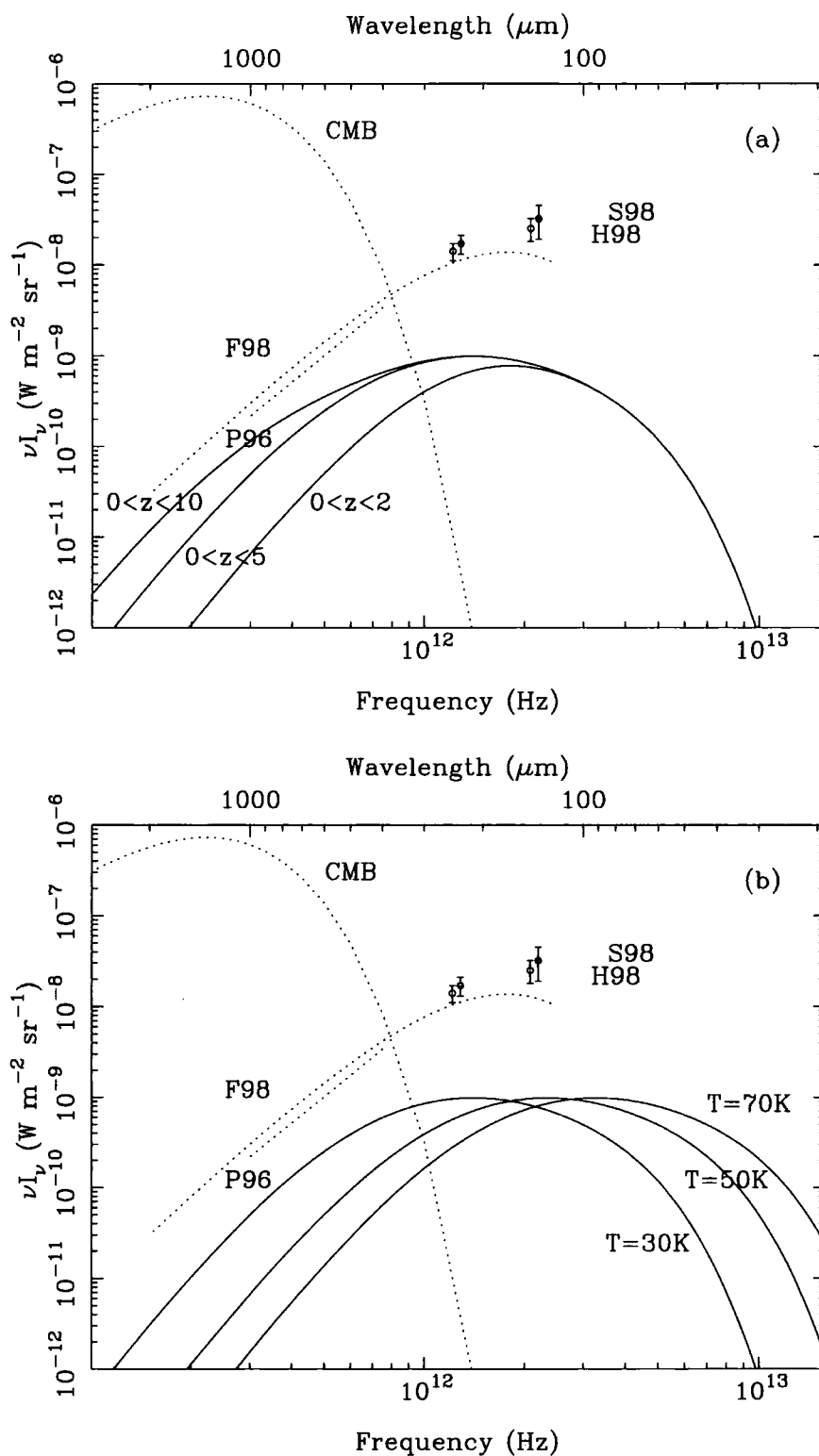
Figure 4.14: (a) The effect on the predicted FIRB spectrum of varying the maximum redshift, z_{max}, for dust at $T_d = 30\,\mathrm{K}$, for $z_{max} = 2,5$ and 10. (b) The effect on the predicted FIRB spectrum of varying the dust temperature between $T_d = 30\,\mathrm{K}$ and $T_d = 70\,\mathrm{K}$, over redshifts $0 < z < 5$. In both cases, our fiducial model has been used, for seven populations with a flat column distribution, and a covering factor $f_{cov} = 1$. The data are as described in Fig. 4.1.

In Fig. 4.14, we show the effects of changing the maximum redshift and the dust temperature used in the models. In panel (a), it can be seen that the low redshift sources contribute at higher frequencies around 100μm, whereas the high redshift sources account for the largest fraction of the FIRB intensity at 850μm. In panel (b), we show how as the dust temperature is increased, the peak of the predicted FIRB background moves to higher energies. The integrated luminosity is fixed by the amount of absorbed nuclear X-ray and optical radiation, and is independent of temperature. Since this is a spectral energy distribution diagram, in which equal areas mean equal energies, then the predicted intensities for each model are identical after a shift along the frequency axis. A dust temperature of $T_d \sim 40$ K would give the maximum contribution to the peak of the observed FIRB.

4.5 Discussion

The first question to address is what these sub-mm sources will look like at other wavelengths. Compared with the majority of the X-ray source population, sub-mm sources have much higher dust masses and therefore much higher column densities. Hence in general, the optical and X-ray nuclear emission will be totally obscured, and the counterparts are likely to appear like relatively "normal" galaxies. These galaxies may perhaps have narrow emission lines in their optical spectra, possibly of high ionization species, or may look very dusty from their optical and infra-red colours. However, if the obscuring material is not assumed to be isotropic, then a fraction of these highly obscured sources will be orientated such that our line of sight lies within the opening angle of the torus, and therefore the X-ray and optical nuclear flux will escape unattenuated, while simultaneously a large sub-mm flux is detected from the dust in the torus.

Identifying the optical counterparts to sub-mm sources has similar problems to those encountered with X-ray data, in that the point-spread function of the telescope is large (HPBW $= 14''.7@850\mu$m for SCUBA/JCMT) and the pointing accuracy can vary with distance of the source from the pointing calibrators. A number of plausible counterparts can lie in the error box of the source, and in order to ascertain which is correct, deep radio maps of sub-mm survey fields have been taken (Ivison et al. in preparation; Richards 1999) as sub-mm sources often have associated radio emission. Star-formation regions are expected to contain many supernova remnants, which are known to be strong radio emitters. Relativistic electrons accelerated by shocks in the supernova remnant interact with magnetic fields in the inter-stellar medium, producing synchrotron radiation. Although only approximately ten per cent of AGN are radio loud, the remaining ninety per cent are not radio-silent, and therefore are likely to be detected as very faint, μJy sources in extremely

deep radio maps. The high angular resolution of the radio data combined with the fact that radio emission is not affected by the presence of dust, means that optical counterparts to the sub-mm sources can be found in a much less ambiguous manner.

However, once the counterpart has been found, the mechanism giving rise to the sub-mm emission must then be determined. By assuming that for starburst galaxies, the star-formation rate controls both the radio emission and the thermal sub-mm emission, Carilli & Yun (1999) use the radio to sub-mm spectral index as a redshift indicator. If an independent measure of the source redshift can be obtained however, then the radio to sub-mm spectral index can be used to infer whether there is any additional contribution to either component due to the presence of an AGN. A radio-loud AGN will have proportionally higher radio emission than a starburst galaxy, whereas an obscured radio-quiet AGN will have lower radio and higher sub-mm emission, and therefore the radio to sub-mm spectral index can be used as a discriminant.

At present, there is little information available with which to constrain the dust temperature or range of temperatures that should be adopted for our models. Here, we have assumed that T_d remains constant with redshift, but as shown in Fig. 4.10, the temperature affects the predicted source counts significantly. The advent of larger samples of AGN at both low and high redshifts with multi-wavelength FIR/sub-mm data will enable any evolution of the dust temperature to be constrained.

Having chosen to keep T_d constant with redshift, and a universal opacity law, the only unconstrained parameter defining the luminosity is therefore the dust mass, M_d, (see Eqn 4.2). Therefore, since the FIR luminosity is directly related to the X-ray luminosity, which we have modelled to undergo pure luminosity evolution with redshift, then one possible interpretation is that the dust mass also evolves with redshift, with the form:

$$M_d \propto (1 + z)^3.$$

If the dust mass does not scale with the luminosity, then in order for our models to hold, there must be a balance between dust mass and temperature, with the mass compensating for changes in temperature.

Assuming that large amounts of star-formation is occurring simultaneously in any medium obscuring our QSOs, it would also be possible to add in the contribution to the sub-mm flux due to this additional component. Estimates of the relative contributions vary, and are bound to differ between individual objects, but a reasonable assumption would be that ~ 50 per cent comes from the AGN and ~ 50 per cent comes from the star-formation (Frayer et al. 1998). If we therefore

chose to include a comparable contribution from star-formation in our models, this would cause all our estimated sub-mm fluxes to double, increasing the source counts and predicted FIRB intensity considerably.

A further consideration is the question of whether the assumption of constant gas to dust ratio at all redshifts is appropriate. For a QSO, there exists a radius within which the radiation field is so intense that dust particles will not survive, the so-called dust sublimation radius. Granato, Danese & Franceschini (1997) proposed that a significant quantity of gas exists inside the dust sublimation radius, and that a large proportion of the photo-electric absorption occurs within this region. This would have the effect of reducing the dust masses calculated using the column densities inferred from the observed photo-electric absorption at X-ray energies. This would in turn, lower the sub-mm fluxes from obscured AGN, cutting their contribution to the source counts and the intensity of the FIR background. However, the calculation of the gas to dust ratio for SMM 02399-0136 at redshift $z = 2.8$ by Frayer et al. (1998), and SMM 14011+0252 at redshift $z = 2.6$ Frayer et al. (1999), from measurements of CO line emission combined with the sub-mm flux, gives a value similar to that found in nearby galaxies, from which they infer that CO emitting sources at high-redshift have already undergone significant chemical evolution. We have therefore chosen to adopt a constant gas to dust ratio in our models, since at present the available observations are insufficient to constrain any suitable alternatives.

4.6 Future observational tests of the models

The next decade promises to bring enormous advances in our knowledge of this subject, with the advent of many innovative instruments, combined with the light-gathering capacity of 8- and 10-m class telescopes, plus the new generation of satellite-borne detectors.

In the near infra-red, large area surveys will be possible with the Cambridge Infra-Red Survey Instrument (CIRSI; Beckett et al. 1997), which is a wide-field camera consisting of four HgCdTe 1024×1024 detectors, designed for use on the William Herschel, Isaac Newton and Las Campanas du Pont Telescopes. This instrument will be ideal for performing follow-up observations for existing and future X-ray surveys, enabling whole area coverage rather than the pointed observations used previously. In the far infra-red, the FIRBACK survey (Lagache 1998) is a project using an *ISOPHOT* 175μm survey of 4 deg^2 of sky at high Galactic latitudes, with the aim of determining the source populations making up the far infra-red background.

In the sub-mm regime, a proposed wide area survey with SCUBA plans to cover a subset of the European Large Area *ISO* Survey region (ELAIS; Oliver et al. 1998) of around 640 square
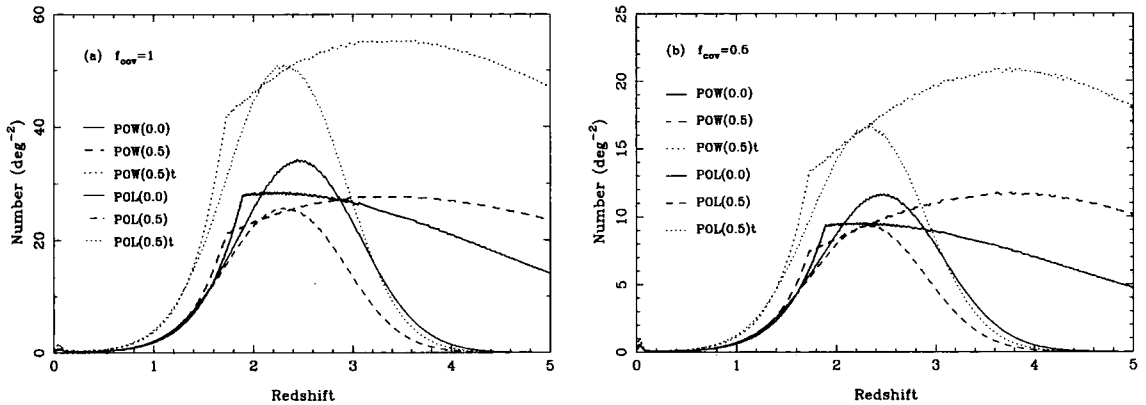
Figure 4.15: Predicted number-redshift distribution for an 850μm survey to 8 mJy, of obscured QSOS with $T_d = 30$ K, and $z_{max} = 5$, for (a) $f_{cov} = 1$ and (b) $f_{cov} = 0.5$. As in Fig. 4.12, we plot the $q_0 = 0$ models (solid lines) and $q_0 = 0.5$ models (dashed lines) for seven populations with a flat column distribution, and the tilted $q_0 = 0.5$ models with six populations (dotted lines). The power-law models are plotted with bold lines in each case, and the polynomial models are plotted with thin lines.

arcminutes (0.178 deg^2). The survey will have a brighter flux limit than existing deep pencil-beam surveys, and aims for a 3σ detection threshold of ~ 8 mJy, from which ~ 40 sources are expected. Our predictions for the number-redshift distribution for such a survey are presented in Fig. 4.15(a) for $f_{cov} = 1$, with the more conservative predictions using $f_{cov} = 0.5$ in Figure 4.15(b). The expected number of sources ranges between ~ 14 deg^{-2} (POL(0.5), $f_{cov} = 0.5$, $z_{max} = 5$) and ~ 180 deg^{-2} (POW(0.5)t, $f_{cov} = 1$, $z_{max} = 5$), depending on the evolution and column density distribution used in the model. However, if we take the more likely scenario in which the obscuring torus is also a site of active star-formation, and the sub-mm flux of each component is comparable (Frayer et al. 1998), then this survey will be able to detect 8 mJy sources with a flux of only 4 mJy due to the AGN plus 4 mJy from the starburst, and therefore the number of obscured AGN expected may be as high as ~ 400 deg^{-2}, far in excess of that anticipated.

The development of ground-based sub-millimetre and millimetre arrays will enable deep interferometric observations at extremely high spatial resolution. Forthcoming facilities include the European Large Southern Array (LSA; Booth 1997), and the National Radio Astronomy Observatory (NRAO) Millimetre Array (MMA; Brown 1996). These will provide arcsecond imaging at wavelengths between 350μm and 10 mm, with up to ~ 10 milli-arcsecond resolution using the longest baselines. Similar projects include the Japanese Large Millimetre and Sub-millimetre Array (LMSA; Ishiguro 1996).

Dramatic increases in our knowledge will be possible with the launch of a number of proposed satellite-borne observatories. The NASA *Space Infra-Red Telescope Facility* (*SIRTF*;

Werner 1998), scheduled for 2001, is a 0.85 m telescope, with imaging and spectroscopic capabilities in the range $3 - 180\mu$m. The ESA *Far Infra-Red and Sub-millimetre Telescope* (*FIRST*; Pilbratt 1993; Genzel 1997) due for launch in 2007, is a 3.5 m telescope which will perform photometry and spectroscopy at far infra-red and sub-mm wavelengths ($80 - 670\mu$m). Space-based observations enjoy the advantages of a stable background, and coverage of the entire spectral range, due to the lack of atmospheric emission and absorption respectively. The *FIRST* mission will be complemented by SOFIA, which is a smaller telescope mounted on a jumbo-jet, similar to the Kuiper Airbourne Observatory. *FIRST* will be launched at the same time as *Planck* (Lawrence & Lange 1997), which is a descendant of *COBE*, designed to measure the fluctuations in the Cosmic Microwave Background across the whole sky, with precision of two parts in a million and an angular resolution of $10'$. The two satellites will operate from an orbit around the L2 Lagrangian point of the Earth-Sun system, providing very stable observing conditions. The equivalent NASA mission is the Microwave Anisotropy Probe (*MAP*; Bennett et al. 1997) due for launch in 2000, which aims to map the CMB to an accuracy of $\sim 20\mu$K, with an angular resolution of $\sim 0.3°$.

4.7 Conclusions

In this Chapter, we have extended our obscured QSO model for the X-ray background to the sub-millimetre regime, by considering the fate of the X-ray, ultra-violet and optical energy absorbed by the obscuring medium. This energy goes into heating up the dust in the obscuring material, which then radiates thermally at far infra-red and sub-millimetre wavelengths. We have modelled the obscuring medium as either isotropic or having a toroidal geometry, which then dictates the intrinsic column density distributions which are consistent with the line-of-sight distributions found from X-ray and optical observations.

Since the spectrum in the sub-mm is rising steeply to higher frequencies, the k-correction obtained is such that our obscured QSOs are equally visible for redshifts of $1 < z < 10$. We therefore use the observed sub-mm source counts at 850μm and the spectrum of the far infra-red background to constrain our models, by ensuring that the large quantities of cool dust invoked would not exceed the observed emission.

We have shown that a variety of plausible obscured AGN models, which provide good fits to the X-ray background spectrum and the number counts at soft and hard X-ray energies, are consistent with the observed sub-mm source counts and intensity of the FIRB. The models predict between 1 and 33 per cent of the FIRB intensity, and a similar fraction of the number counts, depending on

how extreme is the model, but with the more conservative models predicting between 5 and 15 per cent. This is in good agreement with the fact that the majority of sub-mm sources are identified as starburst galaxies, providing the complementary sources. In addition, the obscured AGN models may be a suitable candidate for the source of the sub-mm emission associated with EROs.

Finally, we have made predictions of the redshift distribution of sub-mm sources from our models, for both existing and proposed surveys, and described how combined X-ray and sub-mm survey data will be able to determine the extent of the obscured QSO contribution to cosmological backgrounds at both high and low energies.

References

Altieri B. et al., 1999, A&AL, 343, L65

Antonucci R., 1993, ARA&A, 31, 473

Arnaud K. A., 1996, in Jocoby G.H., Barnes J., eds, *Proc. of the ADASS V Conference*: ASP Conf. Series 101: San Francisco, Vol. 5, p. 17

Barger A. J., Cowie L. L., Sanders D. B., Fulton E., Taniguchi Y., Sato Y., Kawara K., Okuda H., 1998, Nat, 394, 248

Barger A. J., Cowie L. L., Smail I., Ivison R. J., Blain A. W., Kneib J. P., 1999, AJ submitted.

Beckett M. G., Mackay C. D., MCMahon R. G., Parry I. R., Piche F., Ellis R. S., 1997, SPIE Proc., 2871, 1152

Benford D. J., Cox P., Omont A., Phillips T. G., 1998, AAS Meeting, 192, 1104

Benford D. J., Cox P., Omont A., Phillips T. G., McMahon R. G., 1999, ApJL accepted. (astro-ph/9904277)

Bennett C. L. et al., 1997, American Astronomical Society Meeting, 191, 8701

Blain A. W., Ivison R. J., Smail I., 1998, MNRAS, 296, L29

Blain A. W., Kneib J. P., Ivison R. J., Smail I., 1999b, in preparation.

Boksenberg A., Carswell R. F., Allen D. A., Fosbury R. A. E., Penston M. V., Sargent W. L. W., 1977, MNRAS, 178, 451

Booth R., 1997, *Future Large Scale Facilities in Astronomy*, IAU Symposia, 9, E8

Boyle B. J., Shanks T., Georgantopoulos I., Stewart G. C., Griffiths R. E., 1994, MNRAS, 271, 639

Brown R. L., 1996, American Astronomical Society Meeting, 188, 4601

Carilli C. L., Yun M. S., 1999, ApJL, 513, L13

Chapman S. C., Scott D., Lewis G. F., Borys C., Fahlman G. G., 1999, MNRAS submitted. (astro-ph/9810444)

Cimatti A., Bianchi S., Ferrara A., Giovanardi C., 1997, MNRAS, 290, L43

Dey A., Graham J. R., Ivison R. J., Smail I., Wright G. S., Liu M., 1999, ApJ accepted. (astro-ph/9902044)

Downes D., Solomon P. M., 1998, ApJ, 507, 615

Dunne L., Eales S., 1999, in preparation.

Eales S., Lilly S., Gear W., Dunne L., Bond J. R., Hammer F., Le Fevre O., Crampton D., 1998, ApJL submitted. (astro-ph/9808040)

Efstathiou G., Rees M. J., 1988, MNRAS, 230, 5P

Fan X., Strauss M., SDSS Collaboration , 1998, *SDSS Press Release*

Fixsen D. J., Dwek E., Mather J. C., Bennett C. L., Shafer R. A., 1998, ApJ, 508, 123

Francis P. J., 1993, ApJ, 407, 519

Frayer D. T. et al., 1999, ApJL, 514, L13

Frayer D. T., Ivison R. J., Scoville N. Z., Yun M. S., Evans A. S., Smail I., Blain A. W., Kneib J. P., 1998, ApJL, 506, L7

Gear W. K., Cunningham C. R., 1994, SPIE Proc., 2198, 613

Genzel R., 1997, in ASP Conf. Series 124: *Diffuse Infrared Radiation and the IRTS*, San Fransisco, p. 465

Genzel R. et al., 1998, ApJ, 498, 579

Goodrich R. W., Miller J. S., Martel A., Cohen M. H., Tran H. D., Ogle P. M., Vermeulen R. C., 1996, ApJL, 456, L9

Granato G. L., Danese L., Franceschini A., 1997, ApJ, 486, 147

Haas M., Chini R., Meisenheimer K., Stickel M., Lemke D., Klaas U., Kreysa E., 1998, ApJL, 503, L109

Hauser M. G. et al., 1998, ApJ, 508, 25

Hines D. C., 1998, American Astronomical Society Meeting, 193, 2704

Hines D. C., Schmidt G. D., Smith P. S., Cutri R. M., Low F. J., 1995, ApJL, 450, L1

Holland W. S. et al., 1999, MNRAS, 303, 659

Howarth I. D., 1983, MNRAS, 203, 301

Hughes D. H. et al., 1998a, Nat, 394, 241

Hughes D. H., Dunlop J. S., Archibald E. N., Rawlings S., 1998b, in *The Birth of Galaxies*: Xth Rencontres de Blois. (astro-ph/9810253)

Ishiguro M., 1996, IAU Symposia, 170, 239

Ivison R. J., Smail I., Blain A. W., Kneib J. P., 1999, in preparation.

Ivison R. J., Smail I., Le Borgne J. F., Blain A. W., Kneib J. P., Bezecourt J., Kerr T. H., Davies J. K., 1998, MNRAS, 298, 583

Jannuzi B. T., Elston R., Schmidt G. D., Smith P. S., Stockman H. S., 1994, ApJL, 429, L49

Lagache G., 1998, in *Wide Field Surveys in Cosmology*, 14th IAP meeting, Editions Frontieres, p. 301

Laor A., Fiore F., Elvis M., Wilkes B. J., McDowell J. C., 1997, ApJ, 477, 93

Lawrence A. et al., 1993, MNRAS, 260, 28

Lawrence C. R., Lange A. E., 1997, American Astronomical Society Meeting, 191, 4120

Lewis G. F., Chapman S. C., Ibata R. A., Irwin M. J., Totten E. J., 1998, ApJL, 505, L1

Lipari S., Terlevich R., Macchetto F., 1993, ApJ, 406, 451

Madau P., Ferguson H. C., Dickinson M. E., Giavalisco M., Steidel C. C., Fruchter A., 1996, MNRAS, 283, 1388

Malkan M. A., Stecker F. W., 1998, ApJ, 496, 13

Mather J. C. et al., 1994, ApJ, 420, 439

Meurer G. R., Heckman T. M., Lehnert M. D., Leitherer C., Lowenthal J., 1997, AJ, 114, 54

Morrison R., McCammon D., 1983, ApJ, 270, 119

Nandra K., Pounds K. A., 1994, MNRAS, 268, 405

Oliver S. et al., 1998, in *Wide Field Surveys in Cosmology*, 14th IAP meeting, Editions Frontieres, p. 165

Omont A., McMahon R. G., Cox P., Kreysa E., Bergeron J., Pajot F., Storrie-Lombardi L. J., 1996, A&A, 315, 1

Pier E. A., Krolik J. H., 1992, ApJ, 401, 99

Pilbratt G., 1993, Advances in Space Research, 13, 912

Puget J. L., Abergel A., Bernard J. P., Boulanger F., Burton W. B., Desert F. X., Hartmann D., 1996, A&A, 308, L5

Richards E. A., 1999, ApJL, 513, L9

Rigopoulou D., Lawrence A., Rowan-Robinson M., 1996, MNRAS, 278, 1049

Sanders D. B., Phinney E. S., Neugebauer G., Soifer B. T., Matthews K., 1989, ApJ, 347, 29

Schlegel D. J., Finkbeiner D. P., Davis M., 1998, ApJ, 500, 525

Schmidt M., Green R. F., 1983, ApJ, 269, 352

Seaton M. J., 1979, MNRAS, 187, 73P

Shaver P. A., Wall J. V., Kellermann K. I., Jackson C. A., Hawkins M. R. S., 1996, Nat, 384, 439

Smail I., Ivison R. J., Blain A. W., 1997, ApJL, 490, L5

Smail I., Ivison R. J., Blain A. W., Kneib J. P., 1998, in *After the dark ages: when galaxies were young (the Universe at $2 < z < 5$).* (astro-ph/9810281)

Smail I., Ivison R. J., Cowie L. L., Blain A. W., Kneib J. P., Barger A. J., 1999, ApJL in preparation.

Sprayberry D., Foltz C. B., 1992, ApJ, 390, 39

Stecker F. W., De Jager O. C., 1997, in De Jager, O.C., ed, *Proc. Kruger National Park Intl. Workshop on TeV Gamma-Ray Astrophysics,* (Space Research Unit Potchefstroom U.), p. 39

Steidel C. C., Adelberger K. L., Giavalisco M., Dickinson M., Pettini M., 1999, ApJ submitted. (astro-ph/9811399)

Tananbaum H. et al., 1979, ApJL, 234, L9

Werner M. W., 1998, American Astronomical Society Meeting, 193, 2502

Yuan W., Brinkmann W., Siebert J., Voges W., 1998a, A&A, 330, 108

Zheng W., Kriss G. A., Telfer R. C., Grimes J. P., Davidsen A. F., 1997, ApJ, 475, 469

Chapter 5

Near Infra-Red Imaging

of X-ray Sources

ABSTRACT. Here we use the IRIS camera on the AAT to look for evidence of AGN activity in X-ray luminous galaxies, and to search for highly obscured counterparts to X-ray sources for which no optical counterpart exists. We also observe a sample of *ASCA* sources, in order to aid the selection of optical counterparts for follow-up spectroscopy.

5.1 Motivation: The Deep *ROSAT* Survey

5.1.1 Source Identification Techniques

The work described in this Chapter is an extension of an investigation into the origin of the X-ray background radiation in a deep soft X-ray survey, the Deep *ROSAT* Survey (Shanks et al., in preparation). The properties of the seven fields included in this survey and details of the *ROSAT* and *ASCA* observations are described in full in Section 1.3 and Table 1.1.

In the total survey area of $\sim 2.4 \, \mathrm{deg}^2$, over 400 sources are detected by *ROSAT* above a 4σ threshold of $S(0.5 - 2 \, \mathrm{keV}) \sim 4 \times 10^{-15} \, \mathrm{erg \, cm^{-2} \, s^{-1}}$, where the area surveyed is a function of the sensitivity. Known optical QSOs in the field were used to obtain very accurate co-ordinates for the X-ray images, then photographic plates were searched for likely optical counterparts within the $\sim 25''$ FWHM X-ray error box of each source. The nearest source within $30''$ and with a magnitude $b_J < 23$ was taken as being the most likely candidate. Optical spectra of these counterparts were then obtained using the AUTOFIB fibre-fed spectrograph (Sharples, Gray & Hatzidimitriou 1991) on the 3.9-m Anglo-Australian Telescope (AAT). Identifications have been obtained in this way for ~ 60 per cent of the sample of ~ 500 sources, which are catalogued in Shanks et al. (in preparation). The 1σ r.m.s. errors on the *ROSAT* positions are found to be of the order of $10''$.

This survey was extended to hard X-ray energies, $2 - 10 \, \mathrm{keV}$, with the acquisition of deep *ASCA* exposures of all seven *ROSAT* pointings. Sources are extracted from the central $20'$ radius of the *Gas Imaging Spectrometer* (*GIS*) image of each field, in order to match the *ROSAT* field of view. The mean flux limit attained is $S(2 - 10 \, \mathrm{keV}) \sim 5 \times 10^{-14} \, \mathrm{erg} \, \mathrm{cm}^{-2} \, \mathrm{s}^{-1}$. The point-spread function of *ASCA* is much broader than that of *ROSAT*, giving a 1σ error box of radius $\sim 60''$ r.m.s., and therefore it is much more difficult to determine the optical counterpart and hence the source of the X-ray emission. For this reason, the process by which identifications are obtained for *ASCA* sources starts by cross-correlation with known *ROSAT* sources, where positional coincidences of $< 90''$ are considered to be plausible, and the *ASCA* source is given the same identification as the *ROSAT* source. Of the three fields analysed so far, catalogued in Boyle et al. (1998a), a total of 26 sources were detected, with between 7 and 10 per field depending on the exposure time. Of these 26 sources, only three do not have an associated *ROSAT* counterpart within $90''$. A further three *ASCA* sources had more than one *ROSAT* source within $90''$, which is significantly in excess of the 8.5 matches expected on average, but means that a small fraction of the *ASCA/ROSAT* associations may be chance coincidences.

5.1.2 Determining the Nature of X-ray Luminous Galaxies

QSOs are known to be the dominant source population at soft X-ray energies, contributing between 30 and 50 per cent of the soft XRB (Shanks et al. 1991; Boyle et al. 1994). However, the Deep *ROSAT* Survey aims further to determine the nature of the source populations responsible for the remainder of the XRB, the origin of which is still not known for certain.

There is much evidence supporting the existence of a new source population which starts to dominate the X-ray source counts at faint fluxes where the QSO contribution becomes less important (Georgantopoulos et al. 1996). The observed *ROSAT* counts, if extrapolated to hard energies, lie significantly below the *ASCA* counts (Georgantopoulos et al. 1997). This provokes the question as to whether this additional source population, which dominates at higher energies and fainter fluxes, could provide the remaining 50 per cent of the soft X-ray background.

Many non-QSO *ROSAT* sources are identified with narrow emission-line galaxies, for which the X-ray emission mechanism is not certain, but could be due to AGN or starburst activity. Cross-correlation analyses between *ROSAT* X-ray background photons and $B < 23 \, \mathrm{mag}$ galaxies produces a strong signal (5σ), implying that galaxies contribute ~ 17 per cent of the XRB (Roche et al. 1995b). The spectra of X-ray luminous galaxies are found to be harder

than those of QSOs, and are postulated to be the source of the remainder of the XRB (Romero-Colmenero et al. 1996; Almaini et al. 1997; McHardy et al. 1998).

ASCA observations support the existence of an additional population of X-ray sources, as the source counts are three times higher than the *ROSAT* counts extrapolated using $\alpha_X = 1$ (Georgantopoulos et al. 1997). Of the 26 sources detected in the first three *ASCA* fields to be observed, half were broad-line QSOs, and a further six sources were associated with narrow emission-line galaxies. These QSOs and narrow-line galaxies have a combined contribution to the $2 - 10\,\mathrm{keV}$ XRB of $50 - 80$ per cent (Boyle et al. 1998a). In a fourth *ASCA* field, one of the brightest sources was identified as a Type 2 obscured AGN at redshift $z = 0.67$ (Boyle et al. 1998b), providing additional evidence that a population of Type 2 objects may contribute to the hard XRB.

Once a population of X-ray luminous galaxies is identified as being a major contributor to the X-ray background, particularly at hard energies, it is then necessary to determine the X-ray mechanism responsible for this emission, whether it be star-formation, AGN activity, or a combination of the two. A program of follow-up observations was instigated, in order to investigate these possibilities. In this Chapter, I describe near infra-red imaging observations which search for evidence of obscured AGN activity in X-ray luminous galaxies, and provide complementary data for the selection of counterparts to *ASCA* sources. In Chapters 6 and 7, I present related projects involving near infra-red spectroscopy and far infra-red photometry, undertaken with the aim of obtaining a more detailed understanding of the nature of the X-ray emission from these galaxies.

5.2 K-band Imaging

Here we observe samples of X-ray sources to determine whether the properties of the candidate optical counterparts assigned to the X-ray sources are consistent with the obscured QSO hypothesis. We also search for any other possible source for the X-ray counterpart, such as groups of galaxies or starbursts within the field. The X-ray sources chosen for near infra-red imaging observations can be broadly divided into three sub-samples as follows:

- Luminous X-ray galaxies selected from the Deep *ROSAT* Survey: We aim to search for the presence of nuclear activity in these galaxies in the near infra-red.

- Optically-blank sources selected from the Deep *ROSAT* Survey: Here we look for counterparts to X-ray sources which have red optical/near infra-red colours. We test whether the observed colours of candidate counterparts are consistent with the obscured QSO hypothesis.
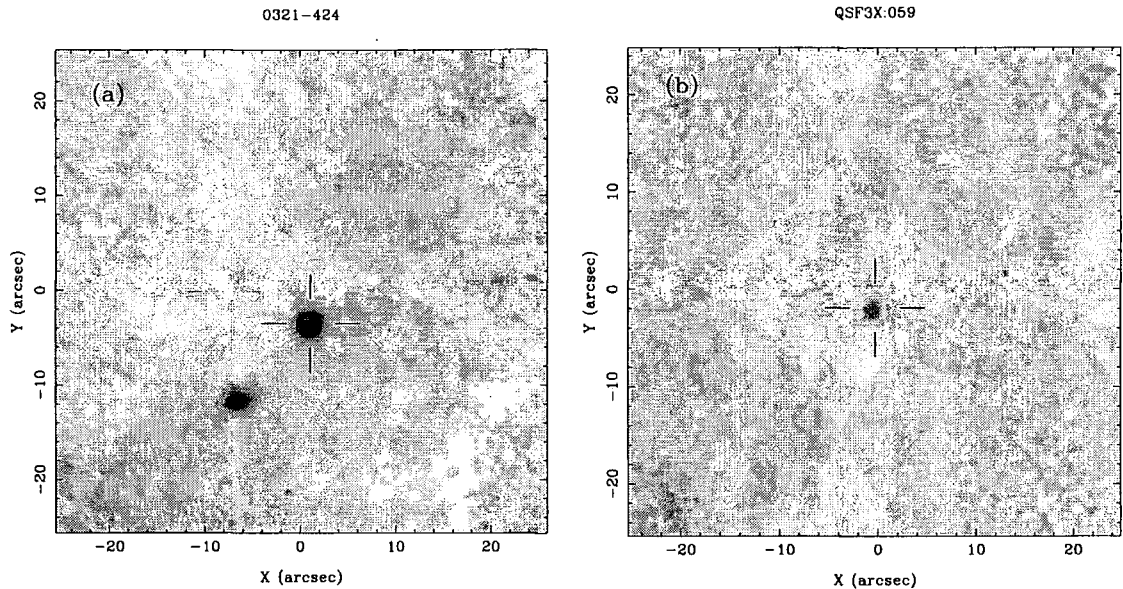
Figure 5.1: K–band images of broad-line QSOs 0321-424 and AXJ 0342.6-4404 (QSF3X:059) taken for comparison with $B - K$ colours of the X-ray galaxies.

- *ASCA* sources: The primary aim here is to select counterparts for optical spectroscopic follow-up of *ASCA* sources for which the source position is not well constrained. In addition, for those sources which have been assigned an optical identification, but for which the X-ray to optical offset is large, we observe the X-ray error box in order to look for very red counterparts.

5.2.1 Comparison QSOs

Two known QSOs were observed in addition to the three samples of X-ray sources, in order to obtain $B - K$ colours for broad-line QSOs for comparison with the X-ray galaxy colours.

0321-424 This radio-quiet optically-selected QSO at $z = 0.2$ is taken from the Veron-Cetty & Veron (1996) catalogue of QSOs and AGN, and has photographic $V = 16.6$ and $B = 17.3$. The IRIS image gives $K = 13.9$ and a colour of $B - K = 3.4$.

AXJ 0342.6-4404 (QSF3X:059) This X-ray selected QSO is taken from the Deep *ROSAT* Survey catalogue, and is also detected by *ASCA* (Boyle et al. 1998a). The redshift of this QSO is $z = 0.377$, with an optical magnitude of $B = 20.1$. IRIS imaging gave a near infra-red magnitude of $K = 16.6$ and a colour of $B - K = 3.5$.

These QSO $B - K$ colours are in excellent agreement with the value of $B - K \sim 3.4$ expected for an unobscured QSO with a power-law spectrum of spectral index $\alpha_{opt} \sim 0.8$, as described in Section 3.5.

5.2.2 X-ray luminous ROSAT galaxies

The first sample studied was a flux limited sample of galaxies from the Deep *ROSAT* Survey catalogue, with fluxes $S(0.5 - 2\,\mathrm{keV}) > 10^{-14}\,\mathrm{erg\,cm^{-2}\,s^{-1}}$ (as described in full in Almaini et al. 1996). The aim is to obtain $B - K$ colours for these galaxies, to identify unusually red galaxies, and to look for any nuclear point source component which would be indicative of an obscured active nucleus. As the extinction due to dust is higher in the blue, we would expect to be able to detect a nuclear component in the near infra-red more easily than in the optical. Moreover, the effective seeing is better in the near infra-red. The spectroscopic identifications for blue-selected counterparts were obtained from low-dispersion spectra taken with AUTOFIB and LDSS on the AAT. These comprise both emission- and absorption-line galaxies, and their properties are summarised in Table 5.1. Almaini et al. (1996) found that two of these galaxies, GSGP4X:069 and GSGP4X:091, have particularly hard *ROSAT* spectra which are not well fit by a pure power-law, and which could be a signature of absorption. Fitting these spectra with a typical QSO power-law photon index, $\Gamma = 2.2$, and intrinsic absorption at the redshift of the galaxy, gave much better agreement with the data, with best-fit column densities of $N_H = 2.7 \pm 1.9 \times 10^{21}\,\mathrm{cm^{-2}}$ and $7.5 \pm 1.8 \times 10^{21}\,\mathrm{cm^{-2}}$ respectively.

5.2.3 Hard spectrum ROSAT sources

Our second group of targets are *ROSAT* sources for which the X-ray spectrum is very hard. As described in Section 2.2, obscuration in QSOs has the effect of flattening an intrinsically steep QSO spectrum. Hard spectrum *ROSAT* sources are therefore the most likely obscured AGN candidates. Since the associated extinction by dust has less effect at longer wavelengths, we expect that while the counterparts to these X-ray sources are optically faint, they may well be infra-red bright, causing very red optical/near infra-red colours. We use this fact to aid our identification process. At faint optical magnitudes, the sky density of galaxies becomes sufficiently high that at least one faint galaxy will lie in the *ROSAT* X-ray error circle purely by chance. It is not feasible to take spectra of large numbers of supposedly "ordinary" faint galaxies, and we therefore take a near infra-red image of the X-ray error circle, in order to identify potential counterparts as those with "unusual" optical/infra-red colours, which have a much lower sky density.

Our targets in this case were chosen to be *ROSAT* sources with hard spectra, which had non-QSO identifications and were generally fainter than the previous sample. The selection criteria used were firstly that the *ROSAT* flux should satisfy $S(0.5 - 2\,\mathrm{keV}) \gtrsim 10^{-14}\,\mathrm{erg\,cm^{-2}\,s^{-1}}$. Next, count rates were calculated for each source in three channels: $0.1 - 0.5\,\mathrm{keV}$, $0.5 - 1\,\mathrm{keV}$ and

Object Name	Optical position α (J2000) δ	ID	B (mag)	z	$S_{0.5-2\,\mathrm{keV}}$ ($\mathrm{erg\,cm^{-2}\,s^{-1}}$)	Γ	Date
GSGP4X:091	00 58 01.3 -27 53 10	NL	21.2	0.416	4.0×10^{-14}	0.14 ± 0.30	23/10/96
GSGP4X:017†	00 56 34.0 -27 29 51	Gal	18.7	0.105	3.7×10^{-14}	2.25 ± 0.09	25/10/96
QSF1X:020	03 41 20.8 -45 11 27	Gal	19.5	0.312	2.8×10^{-14}	1.95 ± 0.21	23/10/96
GSGP4X:048	00 57 17.1 -27 21 47	NL	20.4	0.155	2.7×10^{-14}	1.82 ± 0.15	25/10/96
SGP3X:006	00 54 03.7 -28 24 15	Gal	19.0	0.258	2.5×10^{-14}	1.62 ± 0.18	25/10/96
QSF1X:036	03 41 47.3 -44 38 51	NL	21.0	0.551	2.0×10^{-14}	2.49 ± 0.18	25/10/96
GSGP4X:069	00 57 36.8 -27 33 04	NL	20.5	0.213	1.3×10^{-14}	0.79 ± 0.51	23/10/96
GSGP4X:064	00 57 31.7 -27 23 19	Gal	18.0	0.097	1.2×10^{-14}	1.73 ± 0.35	23/10/96
SGP3X:033	00 55 00.4 -28 38 30	NL	18.6	0.195	1.0×10^{-14}	1.94 ± 0.24	25/10/96

†Also an *ASCA* source, with $2-10\,\mathrm{keV}$ flux of 3.3×10^{-3} cts/s.

Table 5.1. Properties of our sample of X-ray luminous *ROSAT* galaxies, with their identifications as either emission- or absorption-line galaxies (NL and Gal respectively), plus B–band magnitude and redshift information, $0.5-2\,\mathrm{keV}$ *ROSAT* flux and photon index, Γ, and the date of the IRIS observation. The intermediate pixel scale of $0\farcs27$/pixel was used in each case.

Object Name	ROSAT position α (J2000) δ	$S_{0.5-2\,\mathrm{keV}}$ $(\mathrm{erg\,cm^{-2}\,s^{-1}})$	HR	Date
GSGP4X:116	00 58 38.2 -27 35 53	1.1×10^{-14}	0.23 ± 0.18	25/10/96
SGP2X:024	00 51 48.2 -28 50 25	9.6×10^{-15}	0.24 ± 0.26	25/10/96
SGP2X:034	00 51 59.1 -29 10 08	1.5×10^{-14}	0.17 ± 0.22	23/10/96
SGP2X:036	00 52 00.9 -29 16 24	3.8×10^{-14}	0.08 ± 0.13	23/10/96
SGP2X:055	00 52 31.1 -29 18 49	2.8×10^{-14}	0.12 ± 0.16	23/10/96
SGP3X:048	00 55 36.2 -28 32 52	1.3×10^{-14}	0.14 ± 0.25	25/10/96
SGP3X:058	00 56 25.3 -28 18 36	1.9×10^{-14}	0.13 ± 0.20	25/10/96
QSF1X:070	03 43 15.8 -44 57 03	1.1×10^{-14}	0.20 ± 0.33	25/10/96
QSF3X:026	03 41 43.7 -44 02 37	3.2×10^{-14}	-0.04 ± 0.13	24/10/96
QSF3X:040	03 42 11.0 -43 48 56	2.7×10^{-14}	0.10 ± 0.15	23,24/10/96
QSF3X:044	03 42 15.5 -43 48 48	2.0×10^{-14}	0.18 ± 0.19	23/10/96

Table 5.2. Properties of our sample of hard-spectrum, optically-blank ROSAT sources, including ROSAT positions, $0.5 - 2\,\mathrm{keV}$ fluxes and hardness ratios (HR), plus the date of the IRIS observation. The intermediate pixel scale of $0''.27$/pixel was used in all cases, and an additional exposure was taken at $0''.79$/pixel for QSF3X:040. QSF3X:040 and QSF3X:044 did not have existing optical counterparts since they lie in a plate hole on the AAT plate used for the identification procedure.

$1 - 2\,\mathrm{keV}$, named $C1$, $C2$ and $C3$ respectively. A power-law spectrum was then fitted to these three channel spectra. Sources for which the spectral index was significantly harder than that of a typical QSO were taken as our targets. This resulted in a sample of thirteen X-ray sources, two of which are identified as galaxies and were already included in our galaxy sample (GSGP4X:091 and SGP3X:006). The remaining eleven were all observed with IRIS and their properties are summarised in Table 5.2. Since the photon indices for these sources are fairly poorly constrained, here we quote the hardness ratios, which relate the relative numbers of counts in the $0.5 - 1\,\mathrm{keV}$ and $1 - 2\,\mathrm{keV}$ channels as follows:

$$HR = \frac{C3 - C2}{C3 + C2}.$$

Harder spectra have more positive hardness ratios. A typical QSO photon index of $\Gamma \sim 2.2$ corresponds to a hardness ratio of $HR \sim -0.09$, and the photon index of the X-ray background, $\Gamma \sim 1.4$ corresponds to $HR \sim 0.1$.

5.2.4 ASCA *sources*

The third group of targets are taken from deep ASCA observations of ROSAT survey fields. While all seven ROSAT fields have now been observed by ASCA, at the time of these observations, only

| Object Name | | ASCA position | ROSAT position | Offset | Count rate | Date | Comments |
ASCA	ROSAT	α (J2000) δ	α (J2000) δ	(arcsec)	(10^{-3} ct s^{-1})		
AXJ 0056.5-2729	GSGP4X:017	00 56 31.1 -27 29 47	00 56 34.1 -27 30 09	45.5	3.30±1.14	24,25/10/96	Gal $z = 0.105$
AXJ 0056.8-2729	–	00 56 49.9 -27 29 28	–	–	1.90±0.88	24/10/96	
AXJ 0056.8-2733	GSGP4X:025	00 56 51.0 -27 33 09	00 56 49.9 -27 33 26	22.1	1.66±0.60	25/10/96	?
AXJ 0057.6-2731	GSGP4X:072	00 57 38.5 -27 31 13	00 57 42.9 -27 31 10	59.0	1.13±0.44	24/10/96	NL $z = 0.316$
AXJ 0057.8-2735	GSGP4X:077	00 57 48.4 -27 35 56	00 57 46.6 -27 35 35	31.5	0.87±0.37	23,24/10/96	?
AXJ 0058.2-2742	GSGP4X:100	00 58 11.9 -27 42 44	00 58 12.4 -27 42 17	26.9	1.70±0.64	23,24/10/96	NL
AXJ 0341.4-4410	QSF3X:021	03 41 23.0 -44 10 47	03 41 19.6 -44 10 36	37.3	1.01±0.29	23/10/96	Gal/Star?
AXJ 0341.8-4402	QSF3X:029	03 41 47.1 -44 02 24	03 41 43.7 -44 02 37	39.2	0.92±0.31	24/10/96	Not obs'd by AUTOFIB
AXJ 0341.8-4414	–	03 41 45.6 -44 14 07	–	–	1.00±0.31	24/10/96	
AXJ 0342.0-4410	QSF3X:037	03 42 01.1 -44 10 53	03 42 05.8 -44 09 50	80.7	1.26±0.28	24/10/96	Not obs'd by AUTOFIB
AXJ 0342.5-4409	QSF3X:052	03 42 32.4 -44 09 35	03 42 24.8 -44 09 36	81.8	0.92±0.37	24/10/96	Not obs'd by AUTOFIB

Table 5.3. Properties of our sample of ASCA sources, including both ASCA and ROSAT names and positions, and their separations. The ASCA count rates are taken from Georgantopoulos et al. (1997). The pixel scale used can be found from the observation date: intermediate (0″27/pix) - 23/10/96, and wide (0″79/pix) - 24/10/96. If there is an existing identification from the associated ROSAT source, this is shown in the comments. In three cases, a candidate had been selected for the ROSAT counterpart, but not been observed by AUTOFIB.

two fields visible in the Autumn semester had been observed, namely GSGP4 and QSF3. Our analysis here therefore concentrates on the sources in these two fields, which are expected to be representative of the whole *ASCA* population at this flux limit.

The *ASCA* sources have been cross-correlated with known *ROSAT* sources, and if a *ROSAT* source exists with a separation of $< 90''$, the *ASCA* source is given the same identification. In a number of cases, either the optical counterpart to the *ROSAT* source has not been observed, or there is no candidate counterpart. In other cases, there is no *ROSAT* source within $90''$, which here is termed a "blank" field. Table 5.3 summarises our targets in this group. We observed two blank fields, and five sources for which the corresponding *ROSAT* sources have either no optical counterpart or have not been observed with AUTOFIB. In addition, we have observed four sources for which the apparent candidate optical counterpart is a galaxy, in order to determine whether any alternative candidates emerge in the near infra-red.

5.3 IRIS K–band observations

The observations were taken during three nights at the 3.9-m Anglo-Australian Telescope (AAT) on 1996 October 23–25 (observers: K F Gunn, T Shanks, B J Boyle) with the Infra-Red Imager Spectrograph (IRIS; Allen 1993; Allen et al. 1993). Observing conditions were photometric on the first two nights, with some light cirrus on the final night. The average seeing ranged between $1.0'' - 1.5''$.

The IRIS camera is mounted at the Cassegrain focus of the AAT with either the $f/15$ or $f/36$ top end, and has both imaging and spectroscopic capabilities. IRIS uses a 128×128 HgCdTe array, with 60μm pixels, which is sensitive over the wavelength range $0.9 - 2.5\mu$m. Our observations were taken at $f/36$, allowing pixel scales of both $0\!''\!.79$/pixel ("wide") and $0\!''\!.27$/pixel ("intermediate"), and giving a field-of-view of $100''$ and $30''$ on a side, respectively. The broad band Kn filter was used, with transmission from $2.0 - 2.3\mu$m. This is a narrower filter than the conventional K–band filter, in order to minimise the "sky" contribution due to line emission from water vapour in the atmosphere at short wavelengths, and thermal emission from the telescope and optics at longer wavelengths.

Thirty minute exposures were taken of each target, reaching $Kn \sim 19$ mag. Separate offset sky frames were not required since our targets are not significantly extended in the infra-red. We therefore used a nine-point dither pattern (3×3), moving the target with respect to the detector by $8''$ each time, integrating for a total of 200 s in each position. Since in the near infra-red, the sky brightness is much higher than in the optical, the chip will saturate very quickly, and observations

of faint objects will always be background limited. The detector is therefore read out many times during each integration, and at the end of each of these "cycles", the detector is reset to the bias level, with the individual cycles averaged in real-time by the controller software. This is known as "Method 1", which has a read-out noise of $\sim 120e^-$, and is the recommended mode for broadband imaging. Here we used 20 cycles of 10 s each for the intermediate pixel scale, and 50 cycles of 4 s each for the wide pixel scale. The first cycle is always thrown away in order to remove an additional bias component which is present at the beginning of each integration, but which decays away after a few seconds. The nine frames can then be combined, using the median value of each pixel in order to perform the sky-subtraction, to create the final image.

The standard stars used to provide the magnitude calibration were taken from the list of fainter photometric southern standards from Carter & Meadows (1995). These stars had magnitudes and colours in the range $8.0 < K < 9.5$, $8.0 < J < 9.5$ and $-0.6 < J - K < 0.5$. Standards were observed throughout each night, dithered between two positions on the chip, over an airmass range of $1 - 1.35$, $1 - 1.25$ and $1 - 1.8$ on the first, second and third nights respectively. For the intermediate pixel scale, ten to twenty cycles of between 1.5 and 3 s each were used, depending on the magnitude of the standard, since IRIS suffers from severe remnance problems if saturation of the detector occurs. For the wide pixel scale, thirty cycles of 0.3 s were used, where for such a short exposure time, a small area or "window" of the chip can be used to give a faster read-out time, as the read-out and reset time of the full chip, ~ 1.5 s, is longer than the required integration time.

5.4 IRIS Data Reduction

The raw data frames were reduced using the AAO version 4.2.1 of the FIGARO software, following guidelines from the IRIS reduction manual (Allen 1992), with additional routines developed specifically for IRIS (prefixed with **iris-**) by Chris Tinney at the AAO. An independent reduction method was favoured over the pipeline reduction, as this gave better results by providing more control over the frames used for flat-fielding and sky-subtraction. The steps used are as follows:

- Saturated pixels: The chip has several hot pixels which are saturated, therefore we flag these as "bad" in order to avoid affecting any subsequent calculations.

- Dark frame: An average dark or *superdark* frame was created using **irismedsky**, by combining many dedicated dark frames for the Kn exposures. Since the dark current depends on the exposure time used, we have taken ten dark observations, each consisting of twenty co-added

cycles of 10 s each, to match the science Kn frames. These ten exposures are then combined by sigma-clipping at the 2σ level with two passes through the data, and then taking the average of the remaining data values. The dark current is sufficiently stable that the dark frames taken at the end of the night can be used for the whole night's observations.

- Dark subtraction & linearization: The measured pixel values are affected by a non-linear response of the output amplifier, and a correction for this must be applied. Each pixel is affected in the same way, but is a function of the total ADU in each pixel rather than the number of incident photons, and therefore the linearity correction must be performed before converting to electrons per pixel. Bias subtraction is included in the dark subtraction procedure. In Method 1, the bias level of the detector is set to $\sim 15,000$ ADU in odd columns and $\sim 23,000$ ADU in even columns. The task **irislin** is used to simultaneously linearise the data, subtract the superdark frame, and convert from ADU to electrons per pixel.

- Flat-fielding: Rather than taking dome-flats, the preferred method for flat-fielding is to combine the science frames in such a way as to create a *supersky* frame. This is due to the presence of dust particles on the Fabry lens, which appear as "doughnut" shapes in the images, as the lens is not far out of focus. These particles absorb at short wavelengths and radiate at long wavelengths, and therefore are seen in absorption in dome-flat frames, and appear bright against the sky. Using sky frames to flat-field the data is more consistent, as the illumination for the flats is the same as for the science frames, unlike when a lamp is used to illuminate the dome. In addition, the direction of illumination differs between dome and sky observations, which can cause structure in the dome-flat images which is not present in the science images. The supersky frame is created using **irismedsky** to combine all the (linearised, dark-subtracted) science frames for the night, or part of the night if the filters have been moved for standard observations. Here, the flat-field frame is created from ~ 50 frames taken from each half of each night. The flat-field frame is then normalised to the median in order to preserve counts.

- Sky subtraction: In the near infra-red, the sky brightness changes rapidly throughout the night, due to variations in both the water content of the atmosphere and the ambient temperature. In addition, the sky contribution also depends on the zenith distance of the source and on the position of the telescope. The frames used for sky subtraction must therefore be close to the science frames in both time and zenith distance, and as our targets are not significantly extended, we are able to use the science frames themselves for sky subtraction, since the targets are dithered between sub-exposures to lie on different parts of the chip. We therefore take the

nine flat-fielded frames for each target individually, and use **irismedsky** to combine them. The nine frames are multiplicatively scaled to have the same median value, then median-filtered by sigma-clipping at the 2σ level with two passes through the data. The average of each of the remaining data values is assigned to each pixel of the sky frame. The sky frame is normalised to the median value of each frame individually in turn, to account for the varying sky brightness, and is then subtracted, leaving only the signal from the target source.

- Mosaicing: The nine frames must then be combined to produce the final frame, using the mosaicing routine **irismos2**. Common stars and galaxies in each frame are identified and the relative offsets of each frame are calculated with respect to a base frame, on a grid of 3 sub-pixels per true pixel. The frames are then shifted and stacked, with the option of the final frame being at the original resolution or at the increased resolution using the sub-pixels.

- Magnitude calculation: The $K-$band magnitudes were calculated using the Starlink GAIA package, where the errors are calculated from the noise in the sky level, since the exposures are background limited. The instrumental magnitude is calculated from:

$$m_{\text{inst}} = -2.5 \log(\text{counts} - \text{sky}) - 2.5 \log(\text{exposure time}), \tag{5.1}$$

with the counts measured in an aperture of 20 or 8 pixels radius for the intermediate ($0\rlap{.}''27$/pix) and wide ($0\rlap{.}''79$/pix) pixel scales respectively. The sky background level is estimated from the mode in an annulus of radius $1.5 - 2$ times the radius of the source aperture. The atmospheric extinction as a function of airmass, $\kappa(\lambda)$, and the zero-point, ZP, have been estimated from the standard star observations, and therefore the true $K-$magnitudes are calculated from:

$$K = m_{\text{inst}} - \kappa(\lambda)\sec(z) - ZP. \tag{5.2}$$

An estimate for the zero-point is obtained using figures quoted in the IRIS manual (Allen 1993), for the expected flux from a zero magnitude star in the Kn-band of 5.2×10^8 ADU/s. Taking the gain of $9.5\,e^-$/ADU, the expected zero-point is $ZP = 25.77$. Comparing this with the values obtained for our data, we have $ZP = 25.74, 25.84, 25.58 \pm 0.05$ for nights 23, 24 and 25/10/96 respectively. The airmass correction derived from the standard star observations on the 23,25/10/96 were $\kappa(\lambda) = 0.257, 0.271$, whereas on 24/10/96, the range of airmasses was sufficient only to fit the zero-point.

5.5 Results

Here we present IRIS images of the *ROSAT* and *ASCA* X-ray sources described in Section 5.2. The IRIS images are in the conventional orientation, with North at the top and East to the left of each image. In Tables 5.4, 5.5, and 5.6, the *ROSAT*, *ASCA* and optical positions are given, together with the $B-$ band, $R-$ band and $K-$ band magnitudes of the optical counterparts, where available.

The optical data come from digital scans of photographic plates. For GSGP4, SGP2 and QSF3, we have deep $1° \times 1°$ AAT $B-$ band plates, measured by the COSMOS plate-measuring machine. For GSGP4, we also have a deep $R-$ band AAT plate, whereas for SGP2 and QSF3, the $R-$ band magnitudes are taken from shallower APM scans of $6° \times 6°$ Schmidt plates taken with the United Kingdom Schmidt Telescope. For QSF1 and SGP3, both $B-$ band and $R-$ band magnitudes are taken from the APM scans of Schmidt plates.

For completeness, we also mention spectroscopic identifications of some of the optical counterparts, which were obtained at a later date with the aid of the IRIS identifications. The spectroscopic observations were taken during two observing runs, the first being a fortnight after the infra-red imaging run, 1997 November 8–10 (observers: K F Gunn, B J Boyle, I Georgantopoulos), and the second a year later, 1997 September 2–4 (observers: K F Gunn, B J Boyle, T Shanks, R E Griffiths). The aim of these observations was to obtain identifications for the X-ray sources detected in our deep *ASCA* fields, and the results of the first run are presented in Boyle et al. (1998a). The observations were taken using the Low-Dispersion Survey Spectrograph (LDSS) on the AAT in long-slit mode, providing low-resolution spectra with sufficient signal-to-noise to obtain spectral classification and redshift information. For QSF3, deep radio maps were used by Boyle et al. (1998a) to confirm two of the identifications, AXJ 0341.8-4402 and AXJ 0342.0-4410, assuming that the source of the X-ray emission is also the source of the radio emission.

The errors on the quoted magnitudes are of comparable sizes. For the AAT magnitudes, the quoted value for r.m.s. deviation between the scanned and CCD magnitudes for the J1888 (SGP4) plate is $\sigma = 0.27$ mag for $b_J < 23.0$ mag (Jones et al. 1991). This value appears to be typical of both $B-$ and R-plates, measured in the same way. The errors on the APM magnitudes have a similar scatter, with $\sigma \sim 0.1$ mag at bright fluxes, increasing to $\sigma \sim 0.15$ mag at $b_J \sim 21$ mag (Croom 1997). The errors on the IRIS $K-$ band magnitudes are smaller than this, ~ 0.1 mag, even for the faintest sources, and we therefore estimate that the maximum error on the $B - K$ colours to be of the order of 0.3 mag.

5.5.1 X-ray luminous ROSAT galaxies

These observations are all centred on the *ROSAT* optical counterpart, unless specified otherwise, as most of the identifications are secure. However, for some of the sources where the X-ray/optical separation is quite large, we have centred the observation on the X-ray position, to search for red objects which are below the plate limit in the optical ($B \gtrsim 23$).
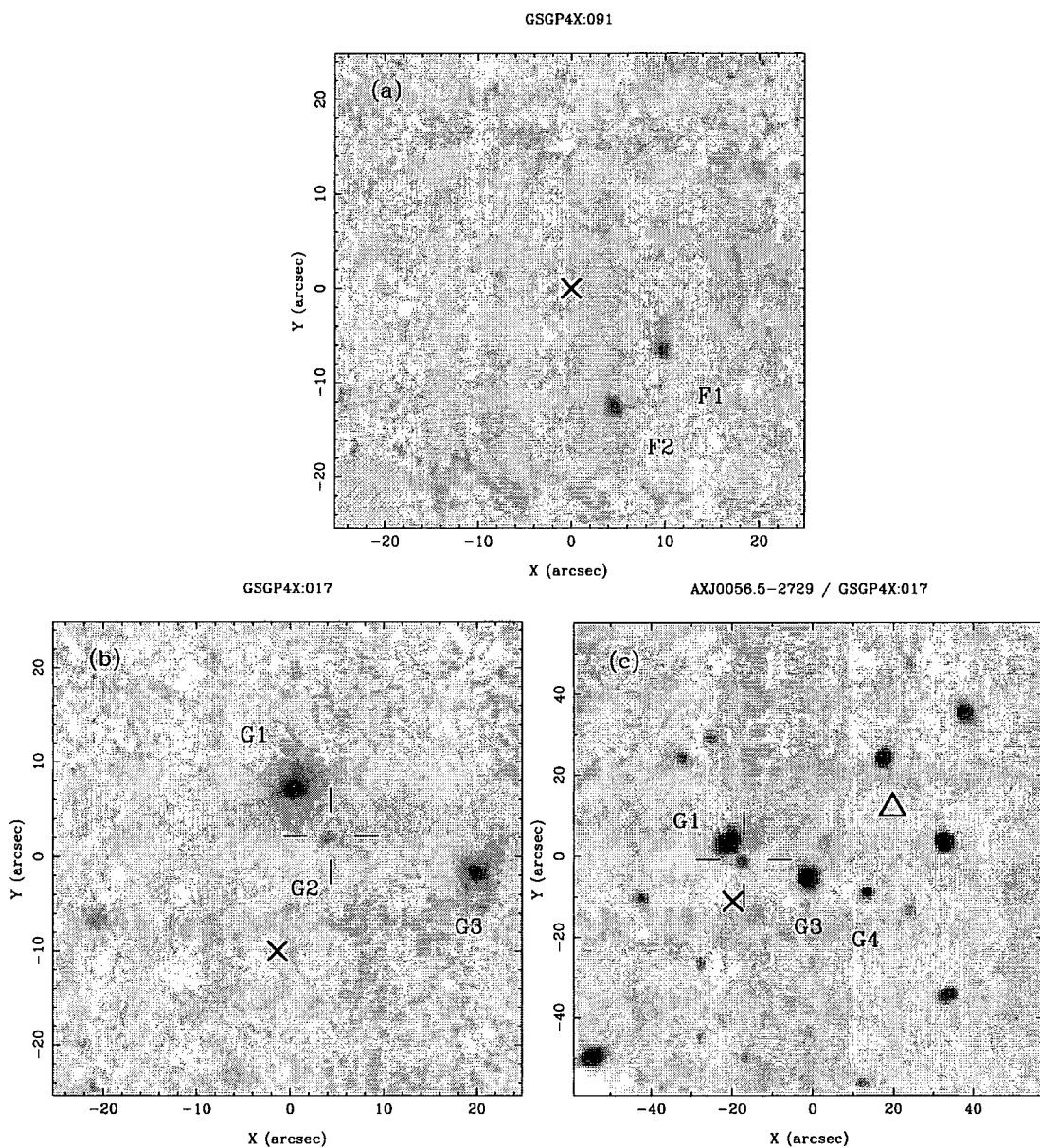
Figure 5.2: IRIS images of the sample of X-ray luminous *ROSAT* galaxies. In each case, the *ROSAT* centroid is denoted by an X, and the optical counterparts marked are described fully in the text. (a) GSGP4X:091, (b) and (c) GSGP4X:017/AXJ0056.5-2729.

Object Name	ROSAT position α (J2000) δ	#	Optical position α (J2000) δ	sgs	B (mag)	R (mag)	K (mag)	B − K (mag)	ID	z
GSGP4X:091	00 58 01.8 -27 53 03	F1	00 58 01.3 -27 53 10	?	21.2	19.7	16.8	4.4	NL	0.416
		F2	00 58 01.7 -27 53 16	?	22.4	19.9	16.1	6.3		
GSGP4X:017†	00 56 34.1 -27 30 10	G1	00 56 34.0 -27 29 51	g	18.7	17.1	14.5	> 4.2	Gal*	0.215
		G2	merged				16.3	> 2.4	**QSO***	**1.010**
		G3	00 56 32.6 -27 29 59	g	19.6	17.8	15.1	4.5	Gal*	0.219
QSF1X:020	03 41 19.9 -45 11 34		03 41 20.8 -45 11 27	s	19.5	18.0	15.4	4.1	Gal	0.312
GSGP4X:048	00 57 16.9 -27 21 36		00 57 17.1 -27 21 47	g	20.4	-	Cloudy	-	NL	0.155
SGP3X:006	00 54 04.0 -28 24 30		00 54 03.7 -28 24 15	m	19.0	16.5	> 14.4		Gal	0.258
			merged				> 14.4			
QSF1X:036	03 41 47.7 -44 38 43		03 41 47.3 -44 38 51	s	21.0	20.1	18.3	2.7	NL	0.551
GSGP4X:069	00 57 37.4 -27 33 07		00 57 36.8 -27 33 04	g	20.5	18.8	16.2	4.3	NL	0.213
GSGP4X:064	00 57 32.4 -27 23 18		00 57 31.7 -27 23 19	g	18.0	16.3	14.3	3.7	Gal	0.097
SGP3X:033	00 55 01.5 -28 38 22		00 55 00.4 -28 38 30	g	18.6	17.3	14.4	4.2	NL	0.195

*Identification from LDSS spectroscopy.

†Associated with the *ASCA* source AXJ 0056.5-2729, which has co-ordinates: 00 56 31.1 -27 29 47 (J2000), and is identified as a $z = 1.010$ QSO (in bold).

Table 5.4. IRIS results for the X-ray luminous *ROSAT* galaxies, showing X-ray and optical positions, B−, R− and K−band magnitudes, B − K colours, and the identifications and redshift of each source. The star-galaxy separation flag is from the *AAT* and APM photographic data, where stars, galaxies and merged objects are denoted by s,g and m respectively, and a ? denotes that the flag is undefined. If the flag differs between blue and red plates, or is undetermined on one plate, then both flags are included, in the form flag(blue)/flag(red).
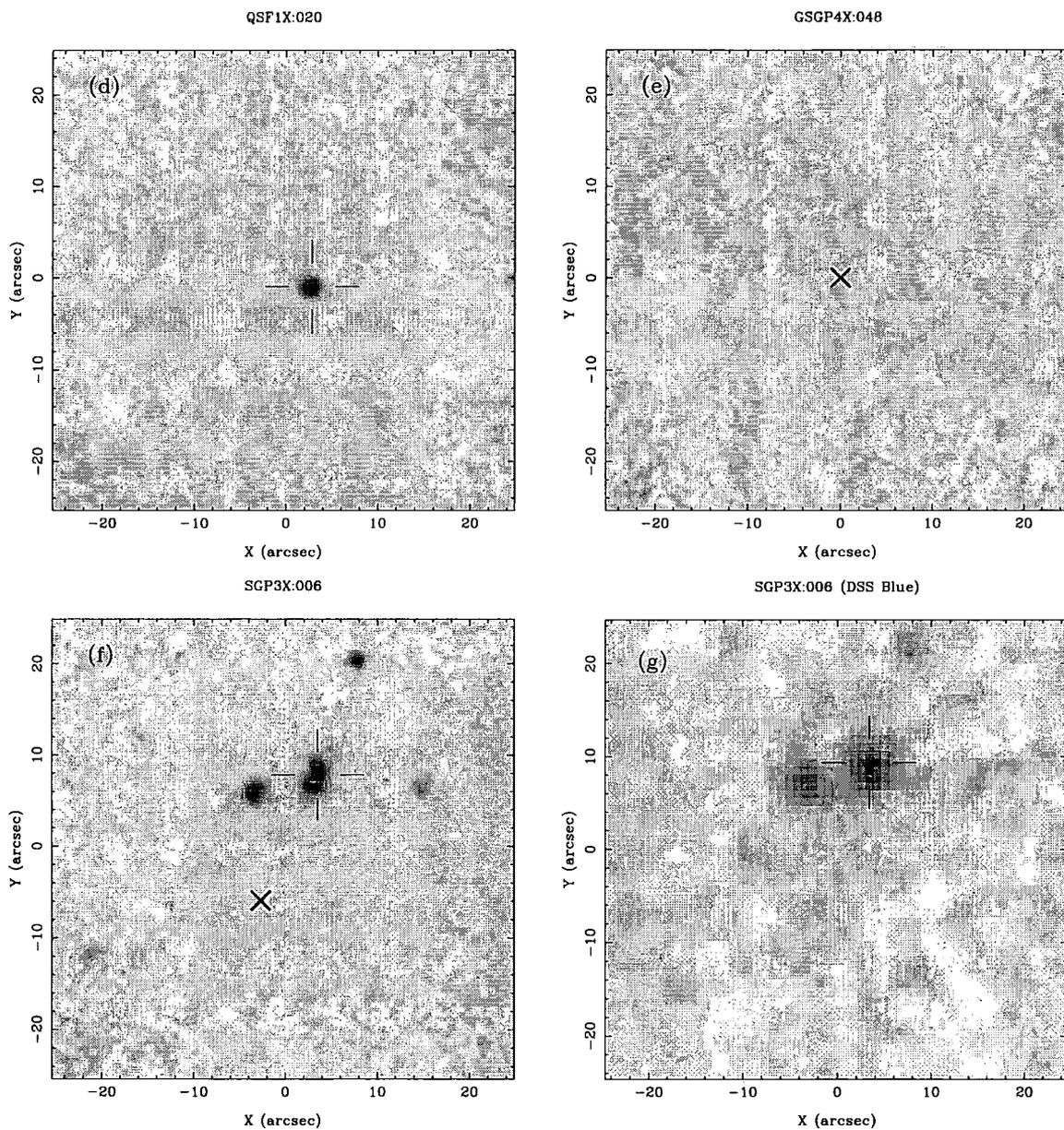
Figure 5.2: (cont.) (d) QSF1X:020, (e) GSGP4X:048, (f) SGP3X:006, with the DSS *B*–band image of the same source in (g).

QSF1X:036

GSGP4X:069

GSGP4X:064
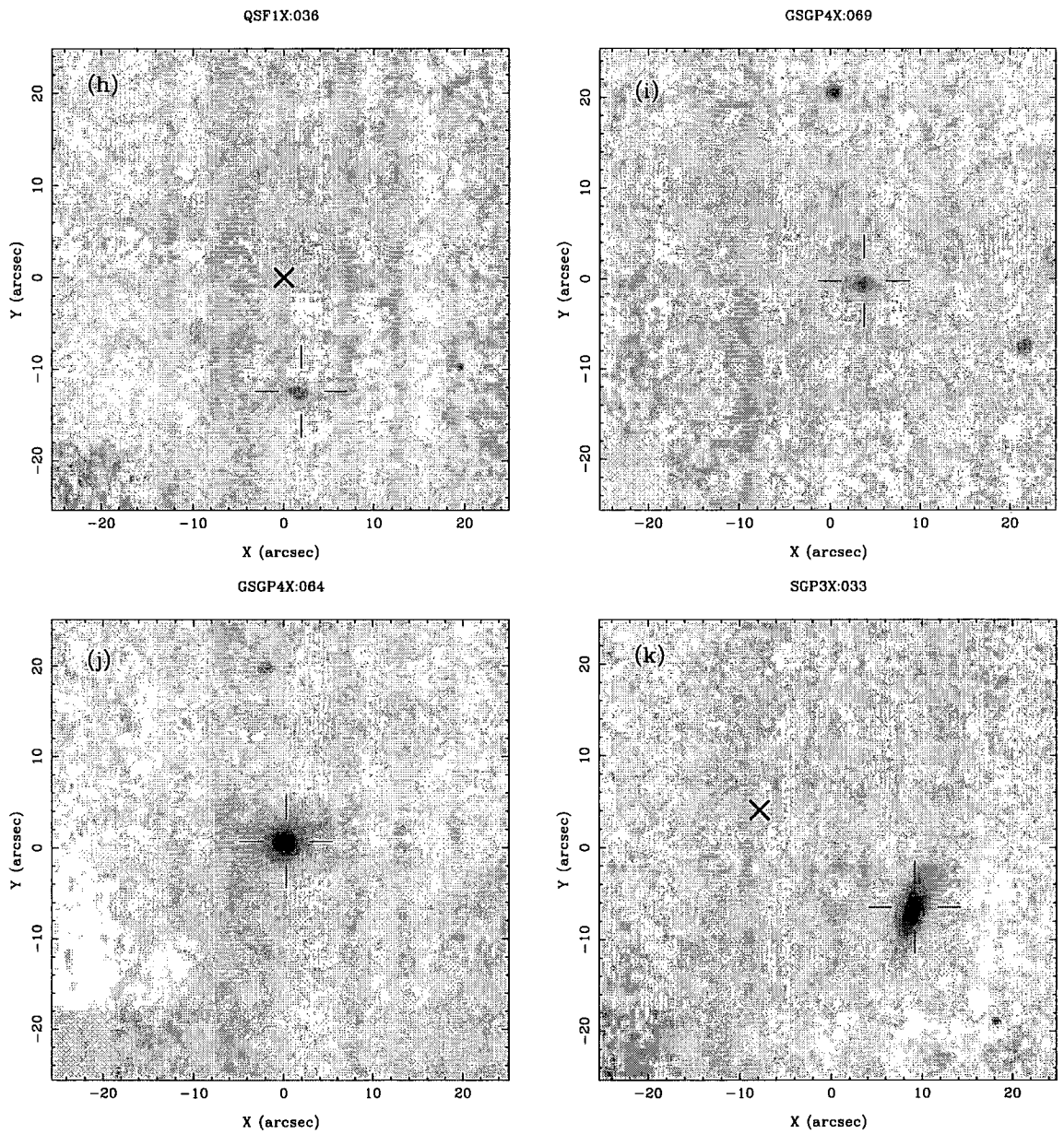
SGP3X:033

Figure 5.2: (cont.) (h) QSF1X:036, (i) GSGP4X:069, (j) GSGP4X:064, and (k) SGP3X:033.

GSGP4X:091 Fig. 5.2(a), centred on the *ROSAT* X-ray position, shows the optical counterpart marked F1, which is an emission line galaxy with $B - K = 4.4$ at $z = 0.416$. However, the object F2 to the south-east is very red, $B - K = 6.3$, for which we have not yet been able to obtain a spectroscopic identification. Both objects are consistent with being stellar, with FWHM $\sim 1''\!.3$. This X-ray source is extremely hard, with evidence for absorption, and therefore F2 is a more likely counterpart, with its red stellar nature being consistent with an obscured QSO. Further evidence comes from a detection of this source at 200μm with *ISO*, as will be described in full in Chapter 7.

GSGP4X:017 (AXJ 0056.5-2729) This source was initially identified in the *ROSAT* follow-up as a $z = 0.105$ galaxy, and we therefore took a high resolution near infra-red exposure of the galaxy, centred halfway between the X-ray and optical positions, to search for nuclear point sources, as shown in Fig. 5.2(b). This shows that the optical counterpart originally assigned to the *ROSAT* source from the AAT photographic data is in fact a blend of two objects, and consists of a brighter galaxy (G1), plus a fainter, point-like (FWHM $\sim 1''\!.2$) blue object (G2), five arcseconds to the south-west. As we only have a $B-$ band magnitude for the combined flux of these two objects, we obtain limits on the colours of $B - K > 4.2$ for G1 and $B - K > 2.4$ for G2.

Since this source was also detected at hard X-ray energies by *ASCA*, we took a second exposure at the wide pixel scale to cover the central region of the *ASCA* error circle. The observation was centred on a galaxy midway between the *ROSAT* and *ASCA* centroids (G3), as shown in Fig. 5.2(c). The two most likely counterparts from this image are the very blue stellar object (G2) to the east, and the red stellar object (G4) to the west of the central galaxy.

Subsequently, using LDSS on the AAT, a long-slit spectrum was taken of these two objects together with the central galaxy (G3). In addition, since the galaxy G1 is bright and extended, sufficient light fell down the slit to obtain a spectrum for this object also. This gave an identification for the blue stellar object (G2) of a $z = 1.010$ QSO, and redshifts for the two bright absorption-line galaxies of $z = 0.215$ and $z = 0.219$ (G1 and G3 respectively). The chance of finding two galaxies at similar redshifts, plus the noticeable overdensity of $K-$band sources in this field compared with other frames taken at the same Galactic latitude, suggests that there may be a group of galaxies in this field at $z \sim 0.22$. The red stellar object (G4) was too faint to obtain an identification, but in the light of having detected a QSO close to the *ROSAT* centroid, this is viewed as being the likely source of the X-ray emission at both soft and hard energies. This identification is consistent with the spectral index obtained from the *ROSAT* data, of $\Gamma = 2.25 \pm 0.09$, and the observed variability

in the X-ray light-curve (Almaini et al. 1999a), both of which are typical for a QSO. This source is also detected with *ISO* at 100μm (see Chapter 7).

Thermal bremsstrahlung from the group of galaxies at $z \sim 0.22$ could contribute to the overall X-ray emission for this source. The only other cluster present in the seven deep *ROSAT* survey fields stood out distinctly on a hardness ratio diagram (Roche et al. 1995a), in which the X-ray colours $C3/C2$ (the ratio of $1 - 2\,$keV counts to $0.5 - 1\,$keV counts) are plotted against $C2/C1$ (the ratio of $0.5 - 1\,$keV counts to $0.1 - 0.5\,$keV counts), which is not the case for the source considered here. Moreover, the X-ray source is not extended, which it should be if it is a cluster at this redshift, and therefore the possible group of galaxies is not likely to be the dominant source of X-ray emission in this case.

QSF1X:020 This *ROSAT* absorption-line galaxy at $z = 0.312$ has $B - K = 4.2$, and a stellar profile both in the optical, and in the IRIS image (FWHM $\sim 1\overset{''}{.}1$), as shown in Fig. 5.2(d). The X-ray spectrum is very steep, suggesting that this may be an unobscured QSO.

GSGP4X:048 This observation, centred on the X-ray position, was affected by the intermittent cloud present on night 3 of the run, and therefore nothing was detected to a limit of $K \sim 17.5$ (Fig. 5.2e).

SGP3X:006 This observation was centred halfway between the X-ray and optical positions, however no new infra-red bright counterparts were found nearer the X-ray position than the existing optical counterpart, which is a galaxy at $z = 0.258$. The IRIS image showed that this galaxy has multiple components, suggesting either merging or interacting galaxies. Comparing the IRIS image, Fig. 5.2(f), with the $B-$ band Digitized Sky Survey (DSS) image, Fig. 5.2(g), it can be seen that the central galaxy (marked) is more elongated in the $K-$band than in the $B-$ band , indicating that one component of this object is much redder than the other. LDSS spectroscopy was not able to disentangle the various contributions to obtain a separate identification for the red counterpart, but the red stellar nature of this component is extremely interesting within the obscured QSO framework.

QSF1X:036 The optical counterpart to this *ROSAT* source was identified as a $z = 0.551$ weak emission-line galaxy, however it was not conclusive as to whether this was the true object responsible for the X-ray emission. We therefore observed the X-ray centroid using IRIS, however no additional red counterparts were detected down to $K \sim 19$ (Fig. 5.2h). Subsequent follow-up with the *ROSAT High Resolution Imager* (*HRI*), which has superior spatial resolution to the *PSPC* at the expense of energy resolution, confirmed the $z = 0.551$ galaxy to be the correct identification (Griffiths et al. 1999, in preparation). For QSF1X:036, the optical counterpart is at the centre of

the *HRI* error circle, whereas for two further sources in the field, QSF1X:033 and QSF1X:064, the optical counterparts lie outside the *HRI* error circles, and hence can be rejected. QSF1X:036 is classified as stellar in the optical, and its colour of $B - K \sim 2.7$ is consistent with that of a QSO. The X-ray spectrum is very steep, $\Gamma \sim 2.5$, again similar to a QSO, and we therefore propose that this source may well have been mis-classified, and is in fact an unobscured QSO.

GSGP4X:069 The $z = 0.213$ emission-line galaxy marked in Fig. 5.2(i) has $B - K = 4.3$, and a FWHM $\sim 2''.0$. Both the optical classification and the $K-$band profile (see Fig. 5.5) are consistent with a galaxy identification, however the X-ray spectrum is extremely flat, with $\Gamma \sim 0.8$. These properties would be consistent with a dust-enshrouded QSO, which is invisible at both optical and near infra-red wavelengths, but which is detected at both 100 and 200μm by *ISO* (see Chapter 7).

GSGP4X:064 Fig. 5.2(j) shows this *ROSAT* absorption-line galaxy at $z = 0.097$, which has $B - K = 3.8$. This galaxy is resolved, with FWHM $\sim 1''.8$, however a nuclear point source is detected in the IRIS image, as will be shown in Fig. 5.5. The existence of a point source component, together with the very hard nature of the *ROSAT* spectrum, shows that this is consistent with the presence of an obscured AGN, particularly if there is no evidence for a nuclear component in the $B-$band .

SGP3X:033 The optical counterpart for this *ROSAT* source is a $z = 0.195$ emission-line galaxy, shown in Fig. 5.2(k). However, this galaxy lies $17''$ from the X-ray centroid, which is unusual for such a bright X-ray source, when the average *ROSAT* positional error is of the order of $\sim 10''$. We therefore observed a position halfway between the X-ray and optical positions, but no new infra-red bright sources were uncovered, down to $K \sim 19$. SGP3X:033 is the faintest X-ray source in this sample, but the low sky density of bright galaxies implies that the proposed galaxy counterpart is almost certainly the correct identification. The *ROSAT* spectrum is very steep, typical of a QSO, but no nuclear component is detected in the $K-$band image, and this therefore is a very puzzling object.

To summarise, in our sample of nine X-ray luminous galaxies, we have detected one positively identified QSO (GSGP4X:017), and two further sources whose optical colours and morphologies, and steep X-ray spectra, are consistent with the properties of unobscured QSOs (QSF1X:020 and QSF1X:036). For the four sources with the hardest *ROSAT* spectra (GSGP4X:091, SGP3X:006, GSGP4X:69 and GSGP4X:064), the observed optical and near infra-red colours and morphologies are not inconsistent with an obscured AGN origin for the X-ray emission. As will be described in Chapter 7, we also have *ISO* detections of GSGP4X:069 and GSGP4X:091, supporting the AGN nature of these objects. The galaxy which stands out as not consistent with this picture is

Object Name	ROSAT position α (J2000) δ	#	Optical position α (J2000) δ	sgs	B (mag)	K (mag)	B − K (mag)
GSGP4X:116	00 58 38.2 -27 35 53		00 58 36.7 -27 35 51	g	22.0	14.7	7.3
SGP2X:024	00 51 48.2 -28 50 25	P1	00 51 48.8 -28 50 28	g	23.2	17.9	5.3
		P2	00 51 48.7 -28 50 22	g	23.1	>19.0	<3.1
SGP2X:034	00 51 59.1 -29 10 08	Q1	00 52 00.9 -29 09 59	s	19.3	15.6	3.7
		Q2	00 51 59.1 -29 10 05	g	21.7	16.5	5.2
SGP2X:036	00 52 00.9 -29 16 24		00 52 01.2 -29 16 23	g	22.0	15.8	6.2
SGP2X:055		R1	00 52 32.6 -29 19 03	-	23.6	16.8	6.8
	00 52 31.1 -29 18 49	R2	00 52 32.1 -29 18 50	-	24.0	17.1	6.9
		R3	00 52 31.6 -29 18 45	g	21.7	16.6	5.1
		R4			-	16.7	>7.3
SGP3X:048	00 55 36.2 -28 32 52		00 55 36.1 -28 32 54	-	20.0	15.5	-
SGP3X:058	00 56 25.3 -28 18 36	a	00 56 24.3 -28 19 04		21.8	-	-
		S1			-	16.6	>5.9
		S2	00 56 25.0 -28 18 28	s	-	16.4	>6.1
		S3			-	17.2	>5.3
QSF1X:70	03 43 15.8 -44 57 03				b	-	-
QSF3X:26	03 41 31.3 -43 52 02	T1	03 41 31.2 -43 51 55	s	22.9	>19.0	<3.9
		T2	03 41 31.3 -43 51 30	s	17.1	14.6	2.5
		T3	03 41 31.9 -43 52 12	g	20.2	16.3	3.9
QSF3X:40	03 42 11.0 -43 48 56	H1	03 42 11.4 -43 49 09	-	-	16.0	>6.5
		H2	03 42 11.6 -43 49 25	s	21.3	15.7	5.6
		H3	03 42 14.8 -43 48 30	g	21.3	16.2	5.1
QSF3X:44	03 42 15.5 -43 48 48	H3	03 42 14.8 -43 48 30	g	21.3	16.2	5.1

[a] A possible identification for this source is a $z = 1.9$ QSO, which has an X-ray/optical offset of $30''\!.9$, and therefore is not visible on the IRIS image.

[b] Cloudy during IRIS observation.

Table 5.5. IRIS results for the hard-spectrum, optically-blank *ROSAT* sources, showing X-ray and optical positions, $B-$ and $K-$band magnitudes, and $B - K$ colours, where available. The # column indicates the numbering system used on the figures. The star-galaxy separation flag is from the AAT and APM photographic data, where stars and galaxies are denoted by s and g respectively, and a dash denotes that the flag is undetermined.

SGP3X:033, which has QSO-like X-ray properties, but no evidence for QSO activity in the optical or near infra-red.

5.5.2 Blank Field ROSAT Sources

These observations are all centred on the X-ray centroid, since in most cases, although a candidate optical counterpart has been proposed, the $B-$band magnitude is very faint, and a spectroscopic identification was not possible with AUTOFIB. Since at fainter magnitudes, the probability of finding an optical candidate close to the *ROSAT* centroid purely by chance becomes much higher, our aim here is to look for more unusual objects which, although faint, are more likely to be

the source of the X-ray emission. We are therefore searching for red objects ($B - K \gtrsim 5$) close to the X-ray position which are below the magnitude limit of the optical source material. The IRIS images of the eleven sources observed are shown in Fig. 5.3, and the measured $K-$ band magnitudes are listed in Table 5.5.

GSGP4X:116 This observation was affected by the light cirrus present at times on the third night of the run, making accurate sky-subtraction difficult, and giving rise to a very patchy image (Fig. 5.3a). However, it is still possible to compare the $K-$ images with $B-$band photographic and DSS data in order to obtain relative colours of the sources. The optical counterpart suggested initially, which is closest to the X-ray source, does not appear in the $K-$band image, whereas to the west of the image is an unusually red galaxy, with an estimated colour of $B - K \sim 7$. We propose that this object is a more likely counterpart, for which we require optical identification. The hard X-ray spectrum and the very red colour are consistent with obscured AGN properties.

SGP2X:024 The suggested optical counterpart in Fig. 5.3(b) is a $B = 23.2$ object, P1, for which there is no spectroscopic ID at present. The $K-$band image shows a second very faint object, P2, where neither P1 nor P2 stand out as being more likely candidates, both having $B - K$ colours typical of the field galaxy population. The X-ray emission could originate from either of these galaxies if due to a highly obscured AGN, as inferred from the flat X-ray spectrum.

SGP2X:034 Fig. 5.3(c) shows two objects. Q1 is bright and stellar, with $B - K \sim 3.7$, and Q2 is very faint, with $B - K \sim 5$, where Q1 is suitable for future follow-up spectroscopy.

SGP2X:036 Centred on the optical counterpart, Fig. 5.3(d) shows a very red object, $B - K \sim$ 6.4, which has a FWHM $\sim 1\rlap{.}{''}6$ in $\sim 1\rlap{.}{''}4$ seeing, and therefore it is uncertain whether this is consistent with being stellar or not. Although we have no redshift information to support this, there is a definite overdensity of faint galaxies around this counterpart compared with those in our other fields. If this was a cluster, we would also expect all the cluster members to have similar colours, but the $B-$band magnitudes are too faint to be able to test this. If this is a cluster, the $K-$ magnitude of the brightest cluster member can be used to estimate the redshift. Taking $K \sim 15.8$ and $B - K \sim 6.2$, we can infer a redshift of $z \gtrsim 0.6$ (Aragon-Salamanca, Baugh & Kauffmann 1998). However, if we assume that this galaxy contains an AGN, then the $B - K$ colour will be contaminated by AGN light. This is a prime candidate for CGS4 spectroscopy in the $J-$, $H-$ and $K-$bands.

SGP2X:055 Fig. 5.3(e) is centred on the X-ray position, and shows a group of four galaxies, all too faint for efficient LDSS follow-up. There are no obvious candidates for the X-ray emission,

but they all have very red colours, in particular R4, which has $B - K \gtrsim 7.3$, since it is not visible on the AAT plate.

SGP3X:048 In Fig. 5.3(f), a bright source is seen very close to the X-ray centroid which, although seen on the APM E plate ($R \sim 20$), is invisible on the APM O plate ($B > 22$), giving a very red colour of $B - K > 6.5$ ($B - R > 2$, $R - K \sim 4.5$). This, coupled with the hard X-ray spectrum, makes this an ideal obscured AGN candidate. This was observed using LDSS, but was too faint to obtain a reliable identification. The CGS4 K–band spectrum is presented in Chapter 6, showing a strong continuum but no obvious emission lines. If AGN activity is the source of the X-ray emission in this object, then it is likely to be highly obscured.

SGP3X:058 The suggested counterpart to this source is a $z = 1.90$ QSO ($B = 21.8$), but with an offset of $31''$ this is not certain. We therefore observed the position of the *ROSAT* centroid to search for further potential counterparts. Fig. 5.3(g) shows three bright-ish objects ($K \sim 16.5$), all with red colours of $B - K \sim 6$. Again, the red colours combined with the hard *ROSAT* spectrum are not inconsistent with an obscured AGN origin. The sky density of QSOs at $B = 21.8$ is $\sim 100 \deg^{-2}$, and one would expect ~ 0.025 QSOs in a patch of sky of $31''$ radius on average. It is unclear whether one of these faint galaxies or the QSO is the most likely source of the X-ray emission.

QSF1X:070 Cirrus during this observation reduced the sensitivity, and we detect no sources to a limit of $K \sim 17.5$ in the K–band image (Fig. 5.3h).

QSF3X:026 No unusually red objects are detected in this frame, Fig. 5.3(i), but close to the X-ray centroid is a very blue object, T1, which is not visible in the K–band image, and may therefore be the most likely counterpart. This was too faint for efficient LDSS follow-up. T2 is a bright stellar $B = 17.1$ object $32''$ away from the *ROSAT* centroid with a very blue colour, $B - K \sim 2.5$. The X-ray/optical offset is just larger than the $30''$ radius usually used, which is potentially why there is no identification for this object. QSF3X:026 is one of the softer sources in this sample, and could be consistent with an unobscured QSO. T3 is classified as a galaxy, $12''$ away, and has a $B - K \sim 3.9$, and therefore is unremarkable.

QSF3X:040 This source was observed twice, once at each pixel scale. Fig. 5.3(j) is an exposure at the intermediate pixel scale, centred on the *ROSAT* position, and shows a very red object, H1, $\sim$ $20''$ south of the X-ray centroid. The image taken using the wide pixel scale, Fig. 5.3(k), shows two sources to the south, H1 and H2, with comparable K–band magnitudes, where H1 is not visible in B. H1 and H2 have stellar profiles, where as H3 is resolved. Subsequent LDSS spectroscopy identified the blue source H2 as a late-type B star, but the red object was too faint to obtain an identification. However, if the star H2 is taken to be the source of the X-ray emission, the implied

X-ray/optical ratio is too high (Stocke et al. 1991), and therefore it is unlikely to be the correct counterpart. H1 is a far more plausible candidate for the true X-ray source, since its red stellar nature combined with the hard *ROSAT* spectrum is consistent with obscured AGN activity. (The K-band source to the north-east of this image, H3, is associated with QSF3X:044).

QSF3X:044 The optical counterpart for this source, H3, is a galaxy with $K = 16.2$, $B - K \sim$ 5.1, and no evidence for nuclear activity. The IRIS observation was centred halfway between the X-ray and optical positions, and is shown in Fig. 5.3(l). LDSS spectroscopy of this object was unsuccessful due to bad weather, and we therefore do not have an identification. If the X-ray emission here is due to AGN activity, then this source would be highly obscured.

To summarise, we have observed the X-ray error boxes of eleven *ROSAT* sources, and have found candidate counterparts with very red $B - K$ colours for five sources. The hard *ROSAT* spectra of these objects make them prime candidates for obscured AGN, and are suitable for further investigation in the future, in particular deep spectroscopic observations in both the optical and the near infra-red. QSF3X:026 is found to have an optical counterpart which is consistent with being an unobscured QSO, for which we require a spectroscopic classification. Although the remaining sources look unremarkable in the optical and near infra-red, this could either mean that they are unrelated to the X-ray emission and another fainter optical counterpart is responsible, or that they are potentially the host galaxies of highly obscured AGN.

5.5.3 ASCA *Sources*

The aim of these observations is to select candidate counterparts to the *ASCA* X-ray emission, on the basis of their unusual $B - K$ colours, both red and blue. In some cases, we are aided by the presence of an associated *ROSAT* detection, in which case we choose a pointing such that both the *ROSAT* centroid (or *ROSAT* optical counterpart) and the *ASCA* centroid are well placed in the field-of-view. When the two centroids are widely spaced, two observations are taken. In each case, the *ASCA* centroid is denoted by a triangle, and the *ROSAT* centroid is denoted by an X. As the *ASCA* 1σ error circle has a radius of $\sim 60''$, we use the wide pixel scale ($0\rlap{.}''79$/pix) to give a field-of-view which is $120''$ on a side, covering the region where the optical counterpart is most likely to be found.

Object Name	#	ASCA position α (J2000) δ	ROSAT position α (J2000) δ	Optical position α (J2000) δ	sgs	B (mag)	R (mag)	K (mag)	B − K (mag)	ID	z
AXJ0056.5-2729 (GSGP4X:017)	1	00 56 31.1 -27 29 47	00 56 34.1 -27 30 10	00 56 34.0 -27 29 51	g	18.7	17.1	> 14.5		Gal*	0.215
	2		—	merged				> 14.5		QSO*	1.010
	3			00 56 32.6 -27 29 59	g	19.6	17.8	15.1	4.5	Gal*	0.219
AXJ0056.8-2729	K1	00 56 49.9 -27 29 28		00 56 51.8 -27 28 56	g	19.1	17.3	14.8	4.3	NL	0.214
	K2			00 56 50.3 -27 29 33	s	23.2	20.9	17.8	5.4	NL	0.214
AXJ0056.8-2733 (GSGP4X:25)	1	00 56 51.0 -27 33 09	00 56 49.9 -27 33 26	00 56 50.0 -27 33 21		22.7		a		NL*	0.333
	2			00 56 52.2 -27 33 39		21.6		a		NL*	0.422
	3			00 56 48.8 -27 33 31		21.9		a		NL*	0.215
AXJ0057.6-2731 (GSGP4X:72)	r1	00 57 38.5 -27 31 13	00 57 42.9 -27 31 10	00 57 45.6 -27 31 17	g/s	21.7	19.8	16.5	5.2	NL¶	0.316
AXJ0057.8-2735 (GSGP4X:77)	L1	00 57 48.4 -27 35 56	00 57 46.5 -27 35 35	00 57 48.0 -27 35 53	g	19.2	17.8	15.2	4.0	Gal*	0.162
	L2			00 57 46.9 -27 35 35		22.9	22.0	18.9	4.0	QSO*	0.57
	L3			00 57 49.4 -27 36 21		18.5	16.7	14.5	4.0	Gal	0.163
AXJ0058.2-2742 (GSGP4X:100)	M1	00 58 11.9 -27 42 44	00 58 12.3 -27 42 18	00 58 11.8 -27 42 54	s	21.0	18.6	14.8	6.2	NL*	0.597
	M2			00 58 13.5 -27 42 10	g	22.2	20.7	21.1	1.1	QSO*	0.505
AXJ0341.4-4410 (QSF3X:21)	1	03 41 23.0 -44 10 47	03 41 19.6 -44 10 39	03 41 19.2 -44 10 29	s	21.1		16.3	4.8	QSO*	0.505
AXJ0341.8-4402 (QSF3X:29)	1	03 41 47.1 -44 02 24	03 41 43.7 -44 02 37	03 41 44.2 -44 02 48	g	21.3		18.8	2.5	NLRG*	0.354
AXJ0341.8-4414 (-)		03 41 45.6 -44 14 07		03 41 48.0 -44 14 41	s	20.30				b	
AXJ0342.0-4410 (QSF3X:37)		03 42 01.1 -44 10 53	03 42 05.8 -44 09 51	03 42 05.5 -44 09 42	s	21.3		18.7	2.6	QSO*	1.840
AXJ0342.5-4409 (QSF3X:52)	r1	03 42 32.4 -44 09 35	03 42 24.8 -44 09 37	03 42 24.1 -44 09 44	s	22.1	20.0	17.1	5.0		
	r2			03 42 24.7 -44 09 50	g	20.6	18.9	15.6	5.0		

aCloudy for IRIS observation.

bNo reliable counterpart.

Table 5.6. IRIS results for the *ASCA* sources, showing X-ray and optical positions, $B−$, $R−$ and $K−$band magnitudes, $B − K$ colours, and the identifications and redshift of each source. The star-galaxy separation flag is from the AAT and APM photographic data, where stars and galaxies are denoted by s and g respectively. If the flag differs between blue and red plates, or is undetermined on one plate, then both flags are included, in the form flag(blue)/flag(red).

GSGP4X:116

SGP2X:024

SGP2X:034

SGP2X:036
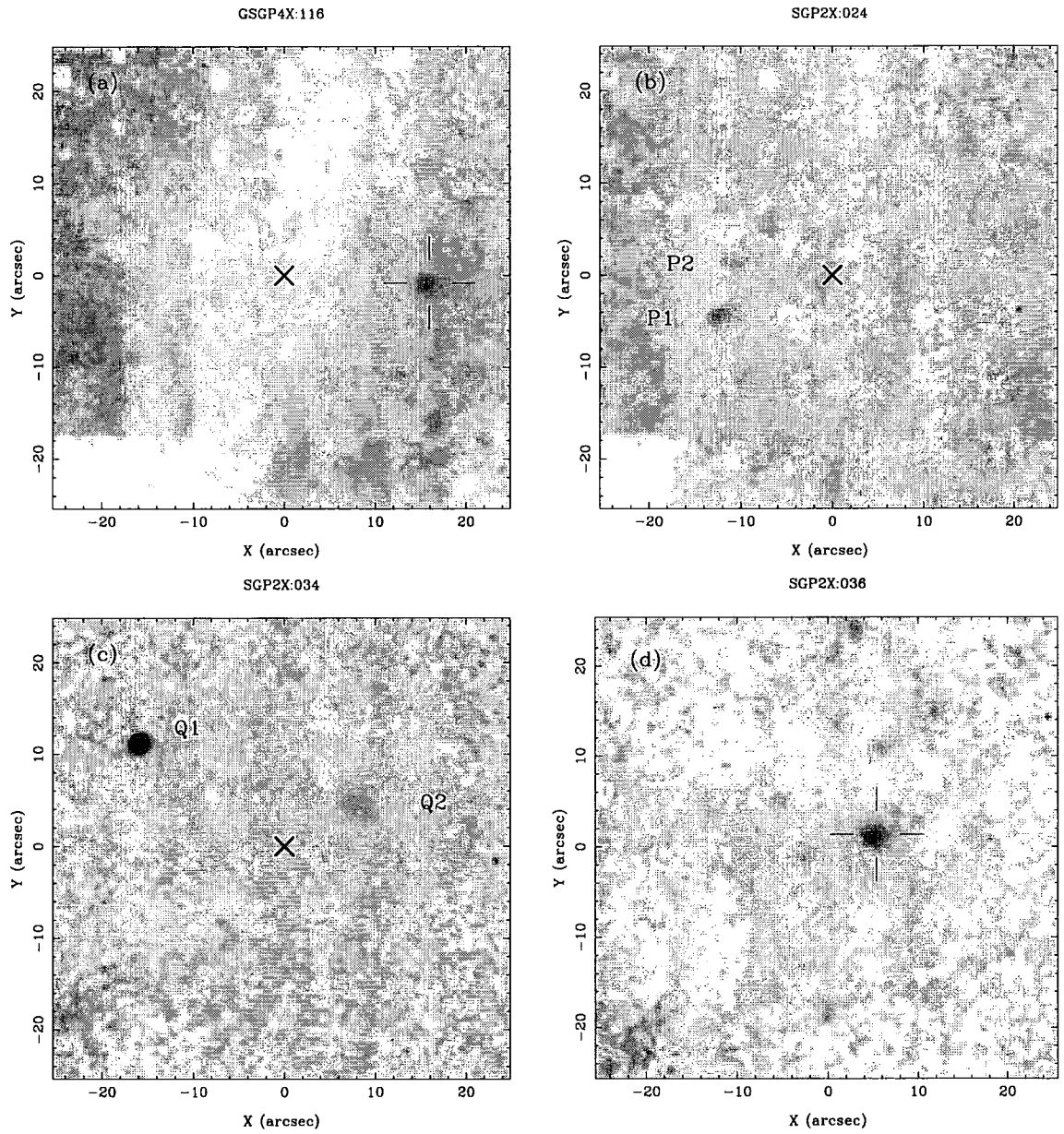
Figure 5.3: The eleven *blank* field *ROSAT* sources taken from the deep survey fields, GSGP4, SGP2, SGP3, QSF1 and QSF3. The X-ray centroid for each source is denoted by an X, and the marked optical counterparts are described in the text. (a) GSGP4X:116, (b) SGP2X:024, (c) SGP2X:034, (d) SGP2X:036.
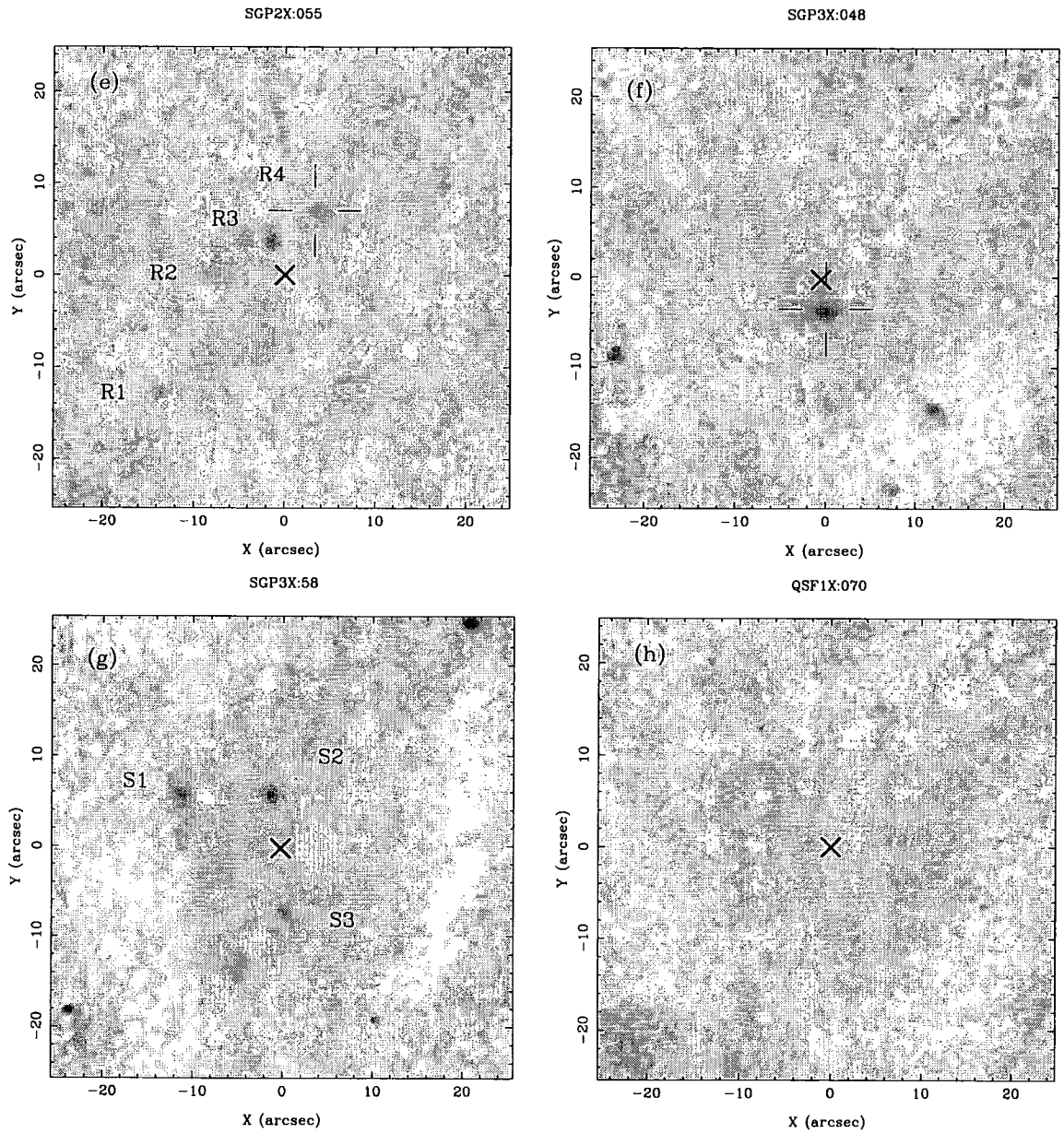
Figure 5.3: (cont.) (e) SGP2X:055, (f) SGP3X:048, (g) SGP3X:058, and (h) QSF1X:070.
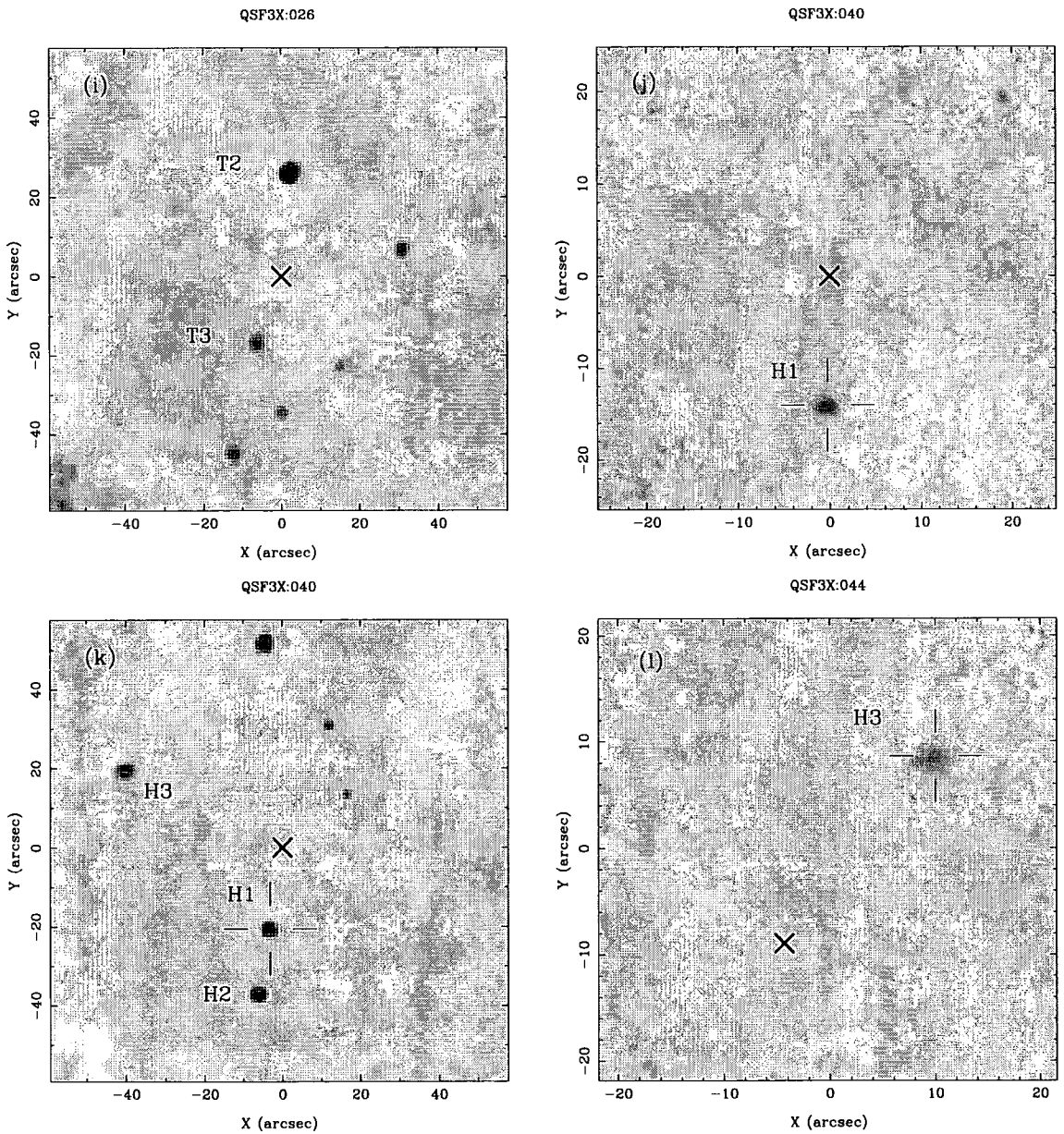
Figure 5.3: (cont.) (i) QSF3X:026, (j) QSF3X:040 – 0$''$.27/pix, (k) QSF3X:040 – 0$''$.79/pix, (l) QSF3X:044.
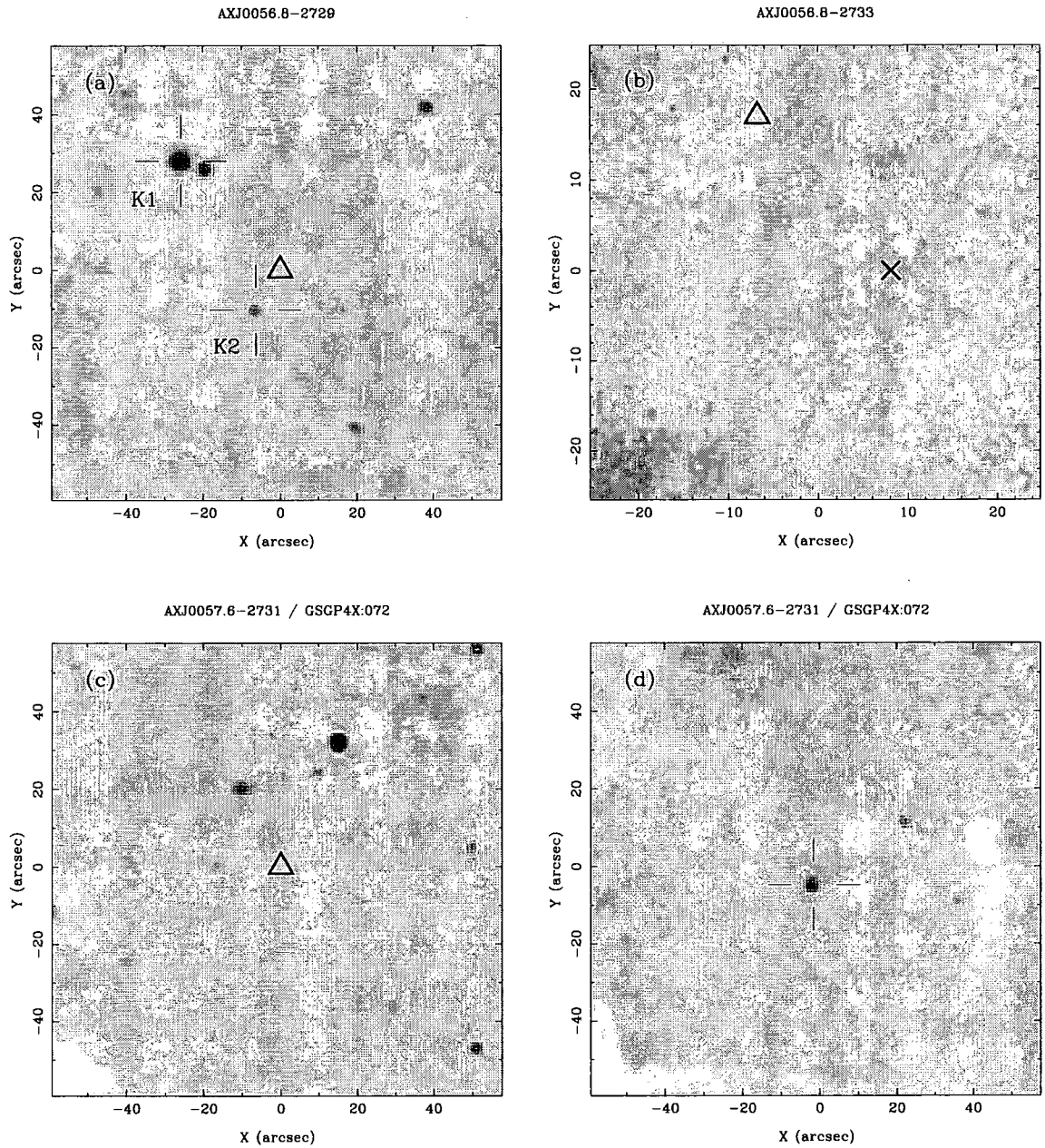
Figure 5.4: Ten *ASCA* sources taken from the deep survey fields, GSGP4 and QSF3 (the eleventh is shown in Fig.5.2(b) and (c)). The *ASCA* X-ray centroid for each source is denoted by a triangle, and if there is an associated *ROSAT* source, then this is denoted by an X. The observations were taken using both wide and intermediate pixel scales, therefore the axes of each frame are marked in arcseconds. The marked optical counterparts are as described in the text. (a) AXJ 0056.8-2729; (b) AXJ 0056.8-2733; (c) and (d) AXJ 0057.6-2731 (GSGP4X:072).
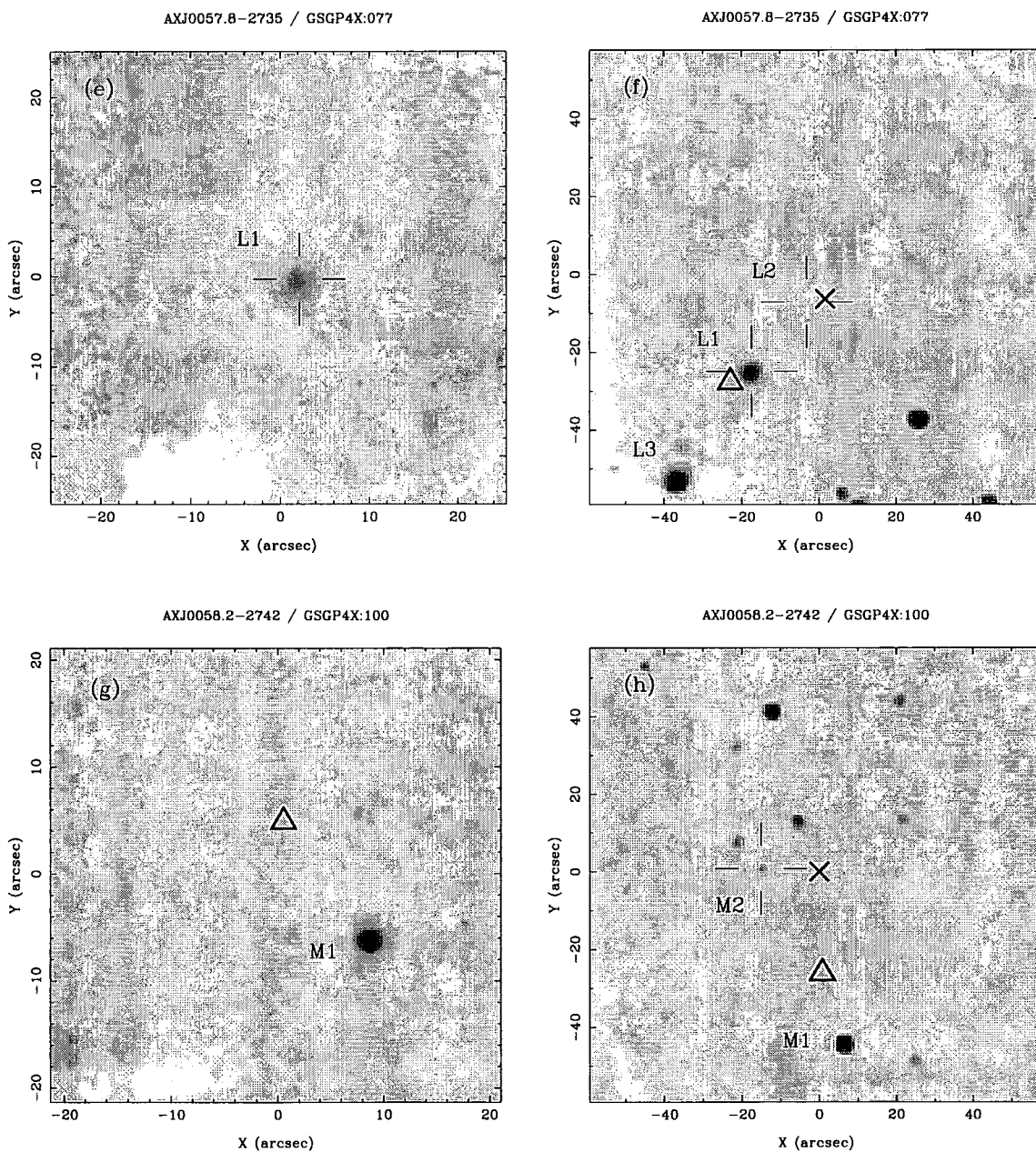
Figure 5.4: (cont.) (e) and (f) AXJ 0057.8-2735 (GSGP4X:077); (g) and (h) AXJ 0058.2-2742 (GSGP4X:100).
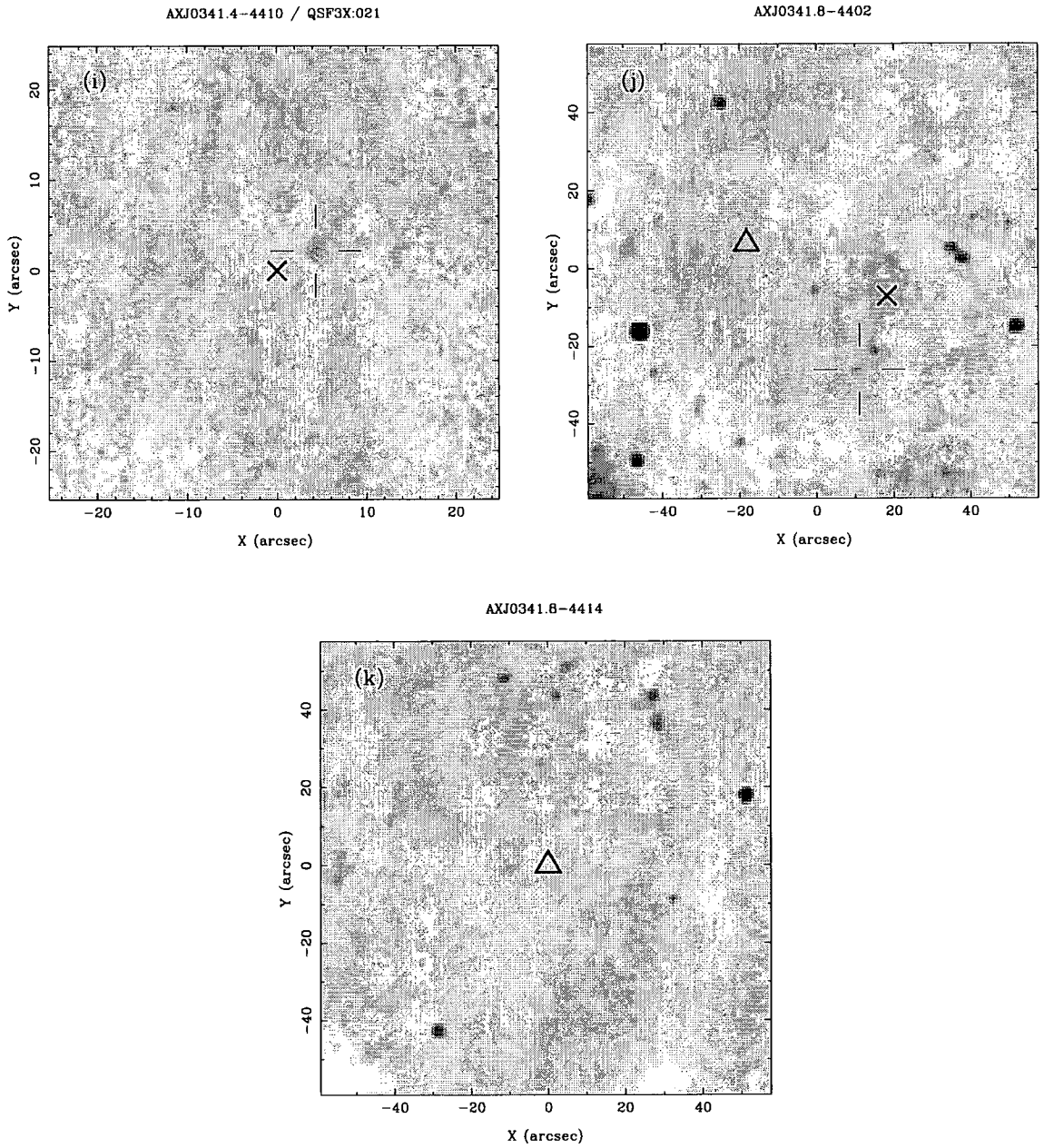
Figure 5.4: (cont.) (i) AXJ 0341.4-4410 (QSF3X:021); (j) AXJ 0341.8-4402 (QSF3X:029); (k) AXJ 0341.8-4414.
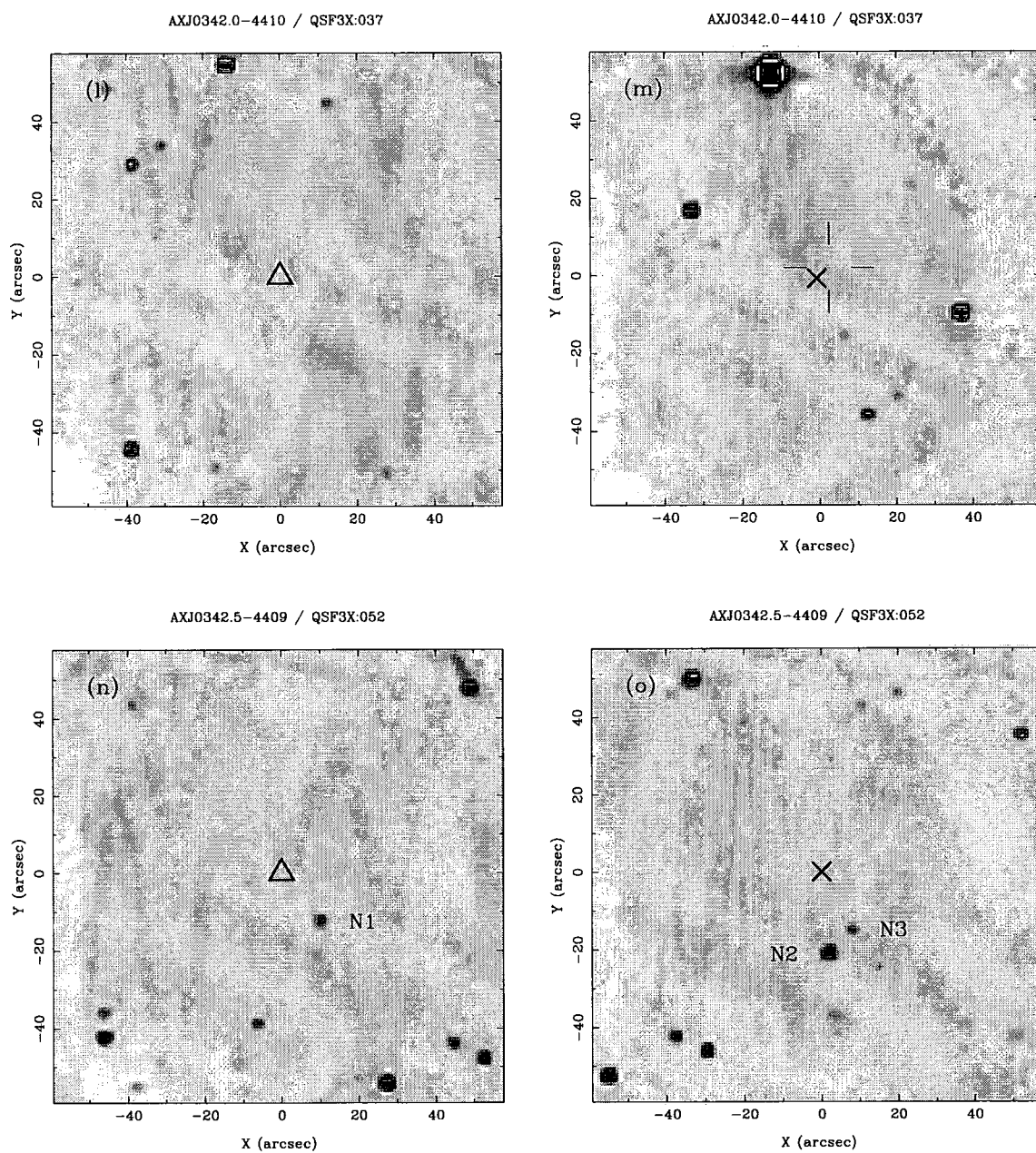
Figure 5.4: (cont.) (l) and (m) AXJ 0342.0-4410 (QSF3X:037); (n) and (o) AXJ 0342.5-4409 (QSF3X:052).

AXJ 0056.5-2729 (GSGP4X:017) See Fig. 5.2(b) and (c), and the earlier description of this source in Section 5.5.1, which discusses the results from the sample of X-ray luminous *ROSAT* galaxies.

AXJ 0056.8-2729 This source has no *ROSAT* counterpart which can be used to aid identification. The absence of a *ROSAT* detection either indicates variability between the two observations, or more interestingly, that the X-ray spectrum is very hard, implying that the source may be obscured. The IRIS observation, shown in Fig. 5.4(a), therefore covered the central part of the *ASCA* error circle, and highlighted two possible counterparts to the X-ray source. First, the nearest bright galaxy, K1, which lies $39''$ north-east of the *ASCA* centroid, and secondly the faint red object, K2, only $8''$ from the centroid, which has $B - K \sim 5.5$. LDSS follow-up shows that these galaxies are both narrow-emission line galaxies at $z = 0.214$, which could be part of a group or cluster, but no evidence for other galaxies in this structure can be seen for this on a $B-$band image taken at the same time as the spectrum. These galaxies have emission-line ratios typical of Seyfert galaxies (Boyle et al. 1998a). The red colour of K2 may indicate that this galaxy has additional near infra-red flux due to the presence of an obscured nucleus, which cannot be seen in the $B-$band flux or the optical spectrum.

AXJ 0056.8-2733 (GSGP4X:025) This observation was centred between the *ROSAT* and *ASCA* centroids, and was badly affected by cirrus during the exposure, hence no $K-$band sources can be detected in Fig. 5.4(b) to a limit of $K \sim 17.5$. However, subsequent LDSS spectroscopy showed that the counterpart to the X-ray source identified from the optical photographic plate is a narrow emission-line galaxy at $z = 0.333$, which lies $5''$ and $18''$ from the *ROSAT* and *ASCA* centroids respectively. At $B = 22.7$, this galaxy is too faint for a spectroscopic identification to have been obtained previously. The emission-line ratios for this galaxy show that it is consistent with a Seyfert 2 galaxy. Two further narrow-line galaxies were found within the *ASCA* error circle, with redshifts $z = 0.422$ and $z = 0.215$, but these lie at greater distances from both *ASCA* and *ROSAT* centroids, implying that the first galaxy is the most likely source of the emission.

AXJ 0057.6-2731 (GSGP4X:072) The nearest *ROSAT* source to the *ASCA* centroid is GSGP4X:072, which had already been identified as a narrow emission-line galaxy at $z = 0.316$. But since the *ASCA* centroid is $96''$ from this galaxy, the *ASCA* emission may be due to another source. We therefore observed two positions with the wide pixel scale, looking for alternative candidates, but nothing unusual was found. The first exposure was centred on the *ASCA* X-ray centroid, shown in Fig. 5.4(c), and the second was centred on the optical counterpart to the *ROSAT* source, Fig. 5.4(d). In addition, the situation here is confused by the fact that the X-ray source coincides with the outer parts of the spiral arms of the brightest galaxy in the GSGP4 field

($B = 13$). The X-ray emission is unlikely to be due to a source in this galaxy, such as an X-ray binary star, as the X-ray to optical flux ratio is not consistent with this idea. The $z = 0.316$ narrow-line galaxy is therefore still the most likely counterpart to the *ASCA* source, with any further investigation hampered by the presence of the spiral arms.

AXJ 0057.8-2735 (GSGP4X:077) This source was also observed twice, initially at high resolution, Fig. 5.4(e), centred on the galaxy L1 nearest to the *ASCA* centroid, and secondly using the wide pixel scale centred on the *ROSAT* optical counterpart L2, Fig. 5.4(f), which is a $z = 0.57$ QSO. No unusually red objects were found in either frame, and LDSS spectroscopy showed that the two nearby galaxies, L1 and L3, were absorption-line galaxies at redshifts $z = 0.162$ and $z = 0.163$ respectively, potentially a foreground group. The QSO is therefore the most plausible source of the X-ray emission.

AXJ 0058.2-2742 (GSGP4X:100) This source was observed twice, first at the intermediate pixel scale centred on the *ASCA* centroid, Fig. 5.4(g), and secondly at the wide pixel scale centred on the *ROSAT* position, Fig. 5.4(h). These observations produced several candidates for follow-up spectroscopy, in particular a very red source close to the *ASCA* position, M1, with $B - K = 6.2$, and a blue object nearer to the *ROSAT* position, M2. LDSS spectra of these objects found M1 to have a weak featureless continuum, for which no identification could be obtained, whereas M2 was found to be a narrow-line galaxy at $z = 0.597$. This galaxy is remarkable in that it shows extremely strong [OII] emission, with an equivalent width of $> 80\,\text{Å}$, and is therefore the source of the X-ray emission. In a direct optical image taken at the same time as the spectrum, M2 also appears to lie at the centre of a cluster, but this is not evident from the $K-$band image.

AXJ 0341.4-4410 (QSF3X:021) The optical counterpart of the *ROSAT* source corresponding to this *ASCA* source did not have a secure identification, and was thought possibly to be an F– or G–type star. The IRIS image centred on the *ROSAT* centroid, Fig. 5.4(i), shows that this optical counterpart is very red, with $B - K = 5.2$, with an LDSS spectrum confirming that this is indeed an unusual object: a $z = 0.505$ QSO with very weak emission lines, such that it is a borderline BL Lac.

AXJ 0341.8-4402 (QSF3X:029) This exposure was centred halfway between the *ROSAT* and *ASCA* centroids, as there was no existing likely candidate. However, the IRIS image in Fig. 5.4(j) contains a few faint objects, but nothing which stands out. LDSS spectroscopy of the blue object marked gave an identification of a narrow-line galaxy, which was subsequently found to be radio-loud (Boyle et al. 1998a), with a 20 cm flux of 298 mJy, showing that the X-ray emission is due to this narrow-line radio galaxy at $z = 0.354$.

AXJ 0341.8-4414 This source has no *ROSAT* counterpart which can be used to aid identification, and the image was therefore centred on the *ASCA* error box. However, the IRIS image shown in Fig. 5.4(k) did not uncover any likely counterparts for the X-ray emission, and therefore this source remains unidentified.

AXJ 0342.0-4410 (QSF3X:037) This field was observed twice, centred first on the *ASCA* centroid, Fig. 5.4(l), and secondly on the *ROSAT* centroid, Fig. 5.4(m), where the two X-ray centroids have a large separation of $81''$. These two images overlap: for orientation, we note that a group of three sources can be seen in both the top left hand corner of Fig. 5.4(l) and the bottom right hand corner of Fig. 5.4(m). There is a suggested counterpart to the *ROSAT* source at an offset of $8''$ from the X-ray position, but this had not been observed by AUTOFIB, and therefore no spectroscopic identification existed. No sources of note were present in the observation centred on the *ASCA* position, but the *ROSAT* counterpart, marked in Fig. 5.4(n), was found to be blue, with $B - K = 2.5$. An LDSS spectrum of this object showed this to be a $z = 1.840$ QSO, and later inspection of deep radio maps gave a 20 cm flux of 198 mJy (Boyle et al. 1998a). This identification is likely to be also associated with the *ASCA* emission, despite the large separation of $85''$ between *ASCA* centroid and optical counterpart.

AXJ 0342.5-4409 (QSF3X:052) Similarly, this object was observed twice, Figs 5.4(n) and 5.4(o) respectively, centred on the *ASCA* and *ROSAT* centroids in turn. The two centroids have a large separation of $82''$ east-west, and therefore the two images overlap by about $40''$. The *ASCA* image contains one red object to the south-west of the centroid, N1, but which is too faint for follow-up spectroscopy. However, the *ROSAT* image contains two galaxies, N2 and N3 with red colours, $B - K \sim 5$, which do not yet have spectroscopic identifications.

To summarise, we have used near infra-red imaging of the error circles of *ASCA* X-ray sources in order to identify the most likely candidates for the source of the X-ray emission. When these objects were bright enough in the optical, LDSS was used to obtain spectroscopic identifications, which led to two red and four blue counterparts being designated as the source of the X-ray emission (Boyle et al. 1998a). In two cases where the *ASCA* emission was thought to be associated with a known *ROSAT* source, but with a large separation between the two centroids, the IRIS images showed that there were no other more probable candidates near the *ASCA* emission, and therefore that it was most likely that the *ROSAT* and *ASCA* emission was due to the same source, and hence the *ASCA* source was assigned the *ROSAT* optical identification.

5.6 Discussion

5.6.1 Surface brightness profiles of three bright galaxies

For the three *ROSAT* X-ray galaxies which are bright and extended in the near infra-red, it is possible to fit their K–band surface brightness profile from the IRIS images, in order to search for possible nuclear components to the galaxy luminosity. This has been performed for galaxies GSGP4X:064, GSGP4X:069 and SGP3X:033 (Bell 1999, private communication), and the results are shown in Fig. 5.5. Each galaxy is fit with an exponential law, typical of a disc or spiral galaxy, plus a bulge or nuclear component, and the relative contribution from each component is allowed to vary.

For GSGP4X:064, there is a distinct unresolved nuclear component emerging at small radii, in excess of the disc seen at larger radii. By scaling the profile of QSF1X:20, which is unresolved, we can estimate the nuclear magnitude to be $K_{nuc} \sim 15.4$, compared with the total magnitude of $K_{tot} = 14.3$.

For the galaxies GSGP4X:069 and SGP3X:033, the surface brightness profile is well fit by a pure exponential law. In each, there may be a hint of a nuclear component, since there is a small excess above the fit at the smallest radii, where one would more usually expect a flattening due to the seeing profile. This is not conclusive however, and would require testing at much higher resolution. Using the same method as for GSGP4X:064, we scale a stellar PSF in order to estimate the maximum contribution from a nuclear point source in each galaxy that could be present without being detected. We therefore estimate for GSGP4X:069, $K_{nuc} \sim 17.8$ compared with $K_{tot} = 16.2$, and for SGP3X:033, $K_{nuc} \sim 15.4$ compared with $K_{tot} = 14.4$.

However, in each case, we do not have digital optical data with which to compare the K–band profiles, and therefore it is not possible at present to constrain the nuclear B– band magnitude in the same way.

5.6.2 Do all ROSAT galaxies host active nuclei?

The nine objects in this sample have a range of properties at both X-ray energies and at optical and near infra-red wavelengths. Here we attempt to draw some broad conclusions about the trends present in the data. The photon indices for these objects span a wide range, from very soft *ROSAT* spectra with $\Gamma > 2$, typical of a QSO, to very hard spectra, with $\Gamma < 1$, which would be more consistent with emission from an obscured central engine. We therefore discuss each of these sources in the context of its *ROSAT* spectrum.
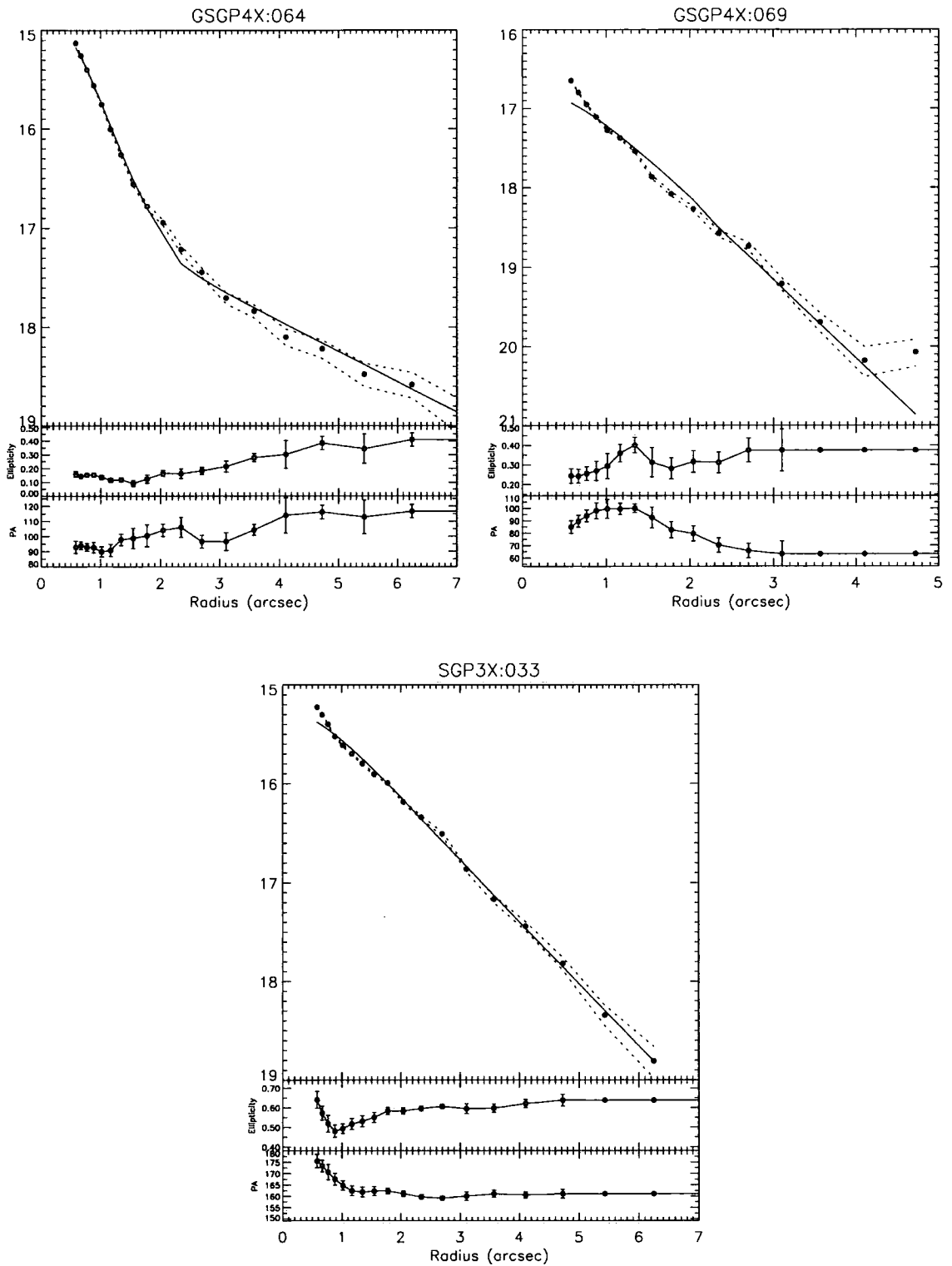
Figure 5.5: The surface brightness profiles fitted to the *ROSAT* galaxies, GSGP4X:064, GSGP4X:069 and SGP3X:033. GSGP4X:064 shows an exponential disc plus an nuclear point-source component, whereas GSGP4X:069 and SGP3X:033 can be fitted by an exponential disc alone (Bell 1999, private communication). The bottom two panels in each figure show the ellipticity and position angle of the galaxy.

The two galaxies with the steepest spectra are GSGP4X:017 and QSF1X:036, with $\Gamma = 2.25$ and 2.49 respectively. We have shown how our new near infra-red observations proved that GSGP4X:017 is in fact a $z = 1.010$ QSO, and not a low redshift galaxy as previously thought. The *ROSAT* photon index is then typical of a broad-line QSO, as is its blue $B - K$ colour. QSF1X:036 is only marginally resolved, and is very blue, with $B - K = 2.7$, however the optical identification is highly uncertain and further spectroscopy of this object may prove to be more illuminating.

GSGP4X:091 and GSGP4X:069 have the hardest spectra, with $\Gamma = 0.14$ and 0.79 respectively. Almaini et al. (1996) have shown that if an intrinsic QSO spectrum is assumed ($\Gamma \sim 2.2$), then absorbing columns of $N_H = 7.5$ and $2.7 \times 10^{21}\,\mathrm{cm}^{-2}$ at the redshift of the assumed optical counterpart galaxies ($z = 0.416$ and $z = 0.213$ respectively) are required in order to fit the data. There are two possible counterparts to GSGP4X:091, the first of which is a narrow line galaxy at $z = 0.416$. However, there is also a very red point source in the field, for which we have no identification, but is highly interesting within the obscured QSO framework. The near infra-red counterpart to GSGP4X:069 has an average $B - K$ colour and is resolved, which together with the hard spectrum may be indicative of large amounts of obscuration. The galaxies SGP3X:006 and GSGP4X:064 also have relatively hard spectra, with $\Gamma = 1.62$ and 1.73 respectively. The optical counterpart to SGP3X:006 is a multiple object, but a red point source is also found adjacent to the central object. GSGP4X:064 is a galaxy which contains a nuclear point-source component (see Section 5.6.1). Looking at the properties of these galaxies together, there is a tendency for the optical/near infra-red counterparts to flat spectrum X-ray sources to be point-like objects which are unusually red.

For the intermediate objects, QSF1X:020 has a stellar profile, and a moderate colour of $B - K = 4.2$. The bright galaxy SGP3X:033 is significantly extended, and has a large offset between the optical position and the *ROSAT* centroid. There are no other candidates in the IRIS image, and nothing stands out as being an obvious alternative on the photographic plate data. Finally, we do not have a K-band magnitude for GSGP4X:048, and therefore cannot say anything further about this galaxy.

We therefore propose a picture in which the X-ray emission in all these sources is due to the presence of an AGN: the steep spectrum objects being primarily broad-line QSOs with stellar profiles and blue optical/infra-red colours; and the flat spectrum objects hosting obscured AGN, with either red nuclear colours or no evidence for nuclear activity at all. In this framework, the intermediate spectrum objects have only moderate levels of absorption, and therefore the situation is not so clearly defined. However, it is well known that there are other X-ray emission mechanisms

contributing to the source counts in deep surveys such as this, and we do not attempt to account for all sources in this manner. It would be perfectly feasible for the X-ray emission in some objects to be primarily due to nuclear starburst activity in a galaxy. But we note that this still does not necessarily preclude the existence of AGN activity, as the starburst itself may provide a site for the obscuration seen in the X-ray spectra, and attenuating any emission from a broad-line region.

5.6.3 Individual sources of interest

A number of the sources in this sample are particularly curious objects, and merit further discussion here.

GSGP4X:091 is a bright, $S(0.5 - 2\,\mathrm{keV}) \sim 4 \times 10^{-14}\,\mathrm{erg\,cm^{-2}\,s^{-1}}$ X-ray source, and is interesting for two reasons, the first being its extremely hard *ROSAT* spectrum, $\Gamma \sim 0.14$, and the second being the observed variability in the *ROSAT* light-curve (Almaini et al. 1999a) from which the presence of AGN activity can be inferred. The proposed optical counterpart is a narrow emission-line galaxy at $z = 0.416$, with a colour of $B - K \sim 4.4$. Taking this to be the true redshift of the source, the X-ray spectrum can be fitted by an power-law of photon index $\Gamma \sim 2.2$, plus an intrinsic absorbing column of $N_H = 7.5 \pm 1.8 \times 10^{21}\,\mathrm{cm^{-2}}$. However, at a similar distance from the X-ray centroid, $\sim 13''$, lies a particularly red point source, with $K \sim 16.1$ and $B - K \sim 6.3$, for which we have no optical identification. The colours and magnitudes of this object are more consistent with an obscured source at $z \sim 0.5$ and $N_H \sim 5 \times 10^{21}\,\mathrm{cm^{-2}}$ than the proposed counterpart, which is bluer. It is difficult to constrain the redshift and column density with the information available however, and the possibility that this source lies at a much higher redshift cannot be ruled out. In this case, we would be seeing a contribution from the host galaxy in the optical, since even a small amount of obscuration would be enough to completely remove any nuclear emission at these energies. An optical spectrum is urgently needed for this red object, in order to discover which of the two sources hosts the AGN.

QSF1X:036 is identified with a $z = 0.551$ weak emission-line galaxy, while the steepness of the X-ray spectrum and the blue ($B - K \sim 2.7$) stellar nature of the optical counterpart are more consistent with a QSO origin for the X-ray emission. The confirmation from *ROSAT HRI* data that this optical source is the true counterpart to the X-ray emission (Griffiths et al. 1999, in preparation), only serves to heighten the necessity for obtaining a more reliable spectroscopic classification for this object. Of the two most plausible scenarios for this object, the first is that it has been mis-classified, and is in fact an unobscured QSO. The second possibility is that it is a heavily obscured object in which the X-ray emission is seen in scattered light only, thereby

explaining the steepness of the X-ray spectrum. In this case, the blue stellar nature of the optical counterpart is still unexplained. To differentiate between these two cases requires hard X-ray data. QSF1X:036 lies 85″ from an *ASCA* source, although the *ASCA* source has a closer *ROSAT* counterpart as well, and therefore more investigation is required before we can constrain the hard X-ray flux in this object (Boyle et al., in preparation).

SGP3X:033 in particular stands out from the picture outlined above, in that the associated optical counterpart to the X-ray source (shown in Fig. 5.2k) is not altogether convincing. We investigate whether the proposed counterpart is consistent with what is known from the X-ray data. Here, the initial concern is raised by the large offset between the X-ray and optical positions. In addition, although this is the faintest X-ray source in the sample, in the optical it is very bright. We therefore use the nuclear $K-$band magnitude estimated in Section 5.6.1, in order to see whether the effects of absorption would make the observed X-ray, optical and near infra-red properties consistent. Using the known relationships between X-ray and optical/near infra-red flux, we calculate that for an unobscured source with $S(0.5 - 2\,\mathrm{keV}) \sim 10^{-14}\,\mathrm{erg\,cm^{-2}\,s^{-1}}$, the expected $K-$band magnitude would be $K \sim 17.3$, where the dispersion in this relationship is $\sim 1\,\mathrm{mag}$. This compares with the limit placed on the nuclear component that could be present in this galaxy without being detected of $K_{\mathrm{nuc}} \sim 15.4$. It would therefore be very difficult to detect any nuclear component above the flux from starlight in the galaxy. However, if the X-ray source did not reside in such a bright galaxy, then it would be very straightforward to detect the $K-$band emission in our IRIS images.

If significant absorption is present in the nuclear regions of this galaxy, it is possible to increase the predicted nuclear K-magnitude, since the effect of absorption is greater in the X-ray than in the infra-red at low redshifts. For instance, a column of $N_H \sim 5 \times 10^{21}\,\mathrm{cm^{-2}}$ produces $\sim 0.5\,\mathrm{mag}$ more absorption in the X-ray than in the $K-$band, increasing the expected nuclear flux to $K \sim 16.8$, which is still too faint to be detected easily above the host galaxy. But this level of obscuration is inconsistent with the observed steep X-ray spectrum, unless we are seeing only scattered X-ray flux from the nucleus. In this case, no flux is transmitted directly due to the presence of a very high obscuring column, $N_H > 10^{24}\,\mathrm{cm^{-2}}$, and we see a fraction of the total luminosity scattered into the line of sight. This fraction can be of the order of one to ten per cent. Since scattering does not affect the energy of the photons, then the spectrum we see is steep, in line with the intrinsic spectrum. In the optical, the only way to see emission from the broad line region would also be in scattered light using polarimetry, making it even more difficult to detect above the host galaxy light. Hard X-ray observations could be used to test this scattered light hypothesis,

by looking for the transmitted spectrum at higher energies. Unfortunately, the *ASCA* observations of these fields are unlikely to be deep enough to detect such faint galaxies, unless the scattered fraction is sufficiently low to raise the intrinsic spectrum above the detection threshold. The *ASCA* observation of the SGP3 field has not yet been analysed, and so we have no hard X-ray flux or upper limit for SGP3X:033.

If however, we believe that the galaxy identification for SGP3X:033 is incorrect, then an alternative optical counterpart is required. This could potentially be a very high redshift obscured QSO, for which we see the unobscured part of the X-ray spectrum redshifted into the *ROSAT* band, but for which the nuclear emission in the optical is totally obliterated by the absorption. The host galaxy would be very faint due to the high redshift, and although detectable in deep optical imaging, would only be identified as the counterpart over any other faint galaxy if the X-ray position was known with much higher accuracy. For instance, if we postulate that our source is at $z \sim 2$, then for a column of $N_H \sim 10^{22}\,\mathrm{cm}^{-2}$, the X-ray absorption is negligible, whereas in the near infra-red it is $A_K \sim 3.4\,\mathrm{mag}$, making the predicted $K-$band magnitude $K \sim 20.8$, which is well below the limits of these observations. The situation is even worse at optical wavelengths, since the extinction is $A_B \sim 14\,\mathrm{mag}$.

The sky density of galaxies with $18 < B < 19$ is $\sim 30\,\mathrm{deg}^{-2}$ (Metcalfe et al. 1995), and therefore the probability of finding one such galaxy in a $30''$ radius *ROSAT* error circle is very small, and therefore this galaxy is still the most likely candidate for the source of the X-ray emission.

5.6.4 Blank field sources

Near infra-red imaging of the X-ray error box of *ROSAT* optically blank field sources has allowed us to pick up many red counterparts to the X-ray sources, potentially consistent with an obscured AGN origin for the X-ray emission. CGS4 spectroscopy in the $J-$, $H-$ and $K-$bands is required in order to obtain identifications for the counterparts, and in particular to look for broad emission lines indicative of the presence of an AGN. Some of the blank field sources are found still to be blank even in the $K-$band, in particular those sources with the hardest *ROSAT* spectra. These may well be sources for which the obscuration is sufficiently high to obliterate all evidence of nuclear activity in the near infra-red as well as in the optical. Further follow-up of these targets will be demanding, but should uncover whether these blank field sources are consistent with the obscured AGN hypothesis.

5.6.5 ASCA *sources*

The surprising result coming out of the *ASCA* identification program is that the majority of the sources are still optically blue QSOs (Boyle et al. 1998a). This is in line with the QSO population observed at softer energies with *ROSAT*. The sensitivity of *ASCA* is lower than *ROSAT*, and therefore it is proposed that at the flux limits obtained in the *ASCA* survey, the source counts are still dominated by bright, steep sources, *i.e.*, QSOs. Deeper hard X-ray observations such as with *AXAF* are therefore required to probe to the faint fluxes at which we anticipate that the hard spectrum obscured QSO population will start to make a significant contribution.

5.7 Conclusions

Here we have presented K–band imaging using IRIS on the AAT, of three samples of X-ray sources, including *ROSAT* X-ray luminous galaxies and sources with hard X-ray spectra, and *ASCA* sources both with and without identifications.

We have proposed a scenario in which the X-ray emission from all faint *ROSAT* galaxies is due to AGN activity, whether it is in comparatively unobscured QSOs, or highly absorbed sources in which nuclear X-ray emission is seen purely in scattered light. We describe the correlation which such a model would produce between the hardness ratio of the *ROSAT* spectrum and the $B - K$ colour of the optical counterpart. This proposed model is extreme, and it is therefore necessary to stress here that we are not trying to rule out any contribution from starburst activity or other X-ray emission mechanisms in these faint galaxies. However, the possibility that AGN reside in many of these galaxies cannot be ruled out by our observations, and it will be interesting to test this hypothesis further in the future. In Chapters 6 and 7, we present the results from two further projects searching for obscured AGN activity in samples of *ROSAT* galaxies. In the future, hard X-ray data on these galaxies will show whether the steep observed X-ray spectra are due to scattered light from an obscured AGN, a starburst component, or a combination of the two. Far infra-red observations will allow us to complete the picture which is beginning to emerge here, by testing for the presence of thermal emission from the obscuring media.

For our sample of hard spectrum *ROSAT* sources, we have shown that near infra-red imaging is a useful technique for identifying potential targets for future follow-up spectroscopy. Candidates with unusual optical to near infra-red colours are selected, in order to reduce the number of optically faint galaxies for which spectra would be required otherwise. By virtue of the selection on red $B - K$ colours from near infra-red data, the candidates are therefore very faint in the B–

band , and may require spectroscopic observations using both powerful 8m-class telescopes and CGS4 on UKIRT.

Regarding the *ASCA* sources, we conclude that $K-$band imaging is an effective method for reducing the number of candidates for optical follow-up spectroscopy. These observations have helped to identify four blue and two red sources, which after spectroscopic observations with LDSS have been assigned as the optical counterparts to *ASCA* sources. A further red counterpart was highlighted, but was not observed using LDSS. These seven sources represent a large fraction of the usable observations. Moreover in two cases for which there is an associated *ROSAT* source, but with a large offset from the *ASCA* centroid, the IRIS images were found to be empty of suitable candidates. This helped to confirm that the optical counterpart of the closest *ROSAT* source is also most likely to be the origin of the hard X-ray emission.

We therefore conclude that the use of $K-$band imaging data in the follow-up of deep X-ray surveys is a very valuable tool. The new generation of near infra-red cameras, such as CIRSI and Omega-Prime (described in more detail in Section 4.6), will enable more uniform and rigorous coverage of deep survey fields. In addition, it will be possible probe to the fainter magnitudes that will be required for the follow-up of deep surveys with *AXAF* and *XMM* .

References

Allen D. A., 1992, *IRIS Reduction Guide*. Anglo-Australian Observatory User Manual 30b

Allen D. A., 1993, *IRIS Users' Guide*. Anglo-Australian Observatory User Manual 30a

Allen D. A. et al., 1993, PASA, 10, 298

Almaini O., Lawrence A., Shanks T., Edge A., 1999a, MNRAS submitted.

Almaini O., Shanks T., Boyle B. J., Griffiths R. E., Roche N., Stewart G. C., Georgantopoulos I., 1996, MNRAS, 282, 295

Almaini O., Shanks T., Griffiths R. E., Boyle B. J., Roche N., Georgantopoulos I., Stewart G. C., 1997, MNRAS, 291, 372

Aragon-Salamanca A., Baugh C. M., Kauffmann G., 1998, MNRAS, 297, 427

Bell E. F., 1999, private communication.

Boyle B. J., Almaini O., Georgantopoulos I., Blair A. J., Stewart G. C., Griffiths R. E., Shanks T., Gunn K. F., 1998b, MNRAS, 297, L53

Boyle B. J., Georgantopoulos I., Blair A. J., Stewart G. C., Griffiths R. E., Shanks T., Gunn K. F., Almaini O., 1998a, MNRAS, 296, 1

Boyle B. J. et al., 1999, in preparation.

Boyle B. J., Shanks T., Georgantopoulos I., Stewart G. C., Griffiths R. E., 1994, MNRAS, 271, 639

Carter B., Meadows V., 1995, MNRAS, 276, 734

Croom S. M., 1997, PhD Thesis, University of Durham.

Georgantopoulos I., Stewart G. C., Blair A. J., Shanks T., Griffiths R. E., Boyle B. J., Almaini O., Roche N., 1997, MNRAS, 291, 203

Georgantopoulos I., Stewart G. C., Shanks T., Boyle B. J., Griffiths R. E., 1996, MNRAS, 280, 276

Griffiths R. E. et al., 1999, in preparation.

Jones L. R., Fong R., Shanks T., Ellis R. S., Peterson B. A., 1991, MNRAS, 249, 481

McHardy I. M. et al., 1998, MNRAS, 295, 641

Metcalfe N., Shanks T., Fong R., Roche N., 1995, MNRAS, 273, 257

Roche N., Shanks T., Almaini O., Boyle B. J., Georgantopoulos I., Stewart G. C., Griffiths R. E., 1995a, MNRAS, 276, 706

Roche N., Shanks T., Georgantopoulos I., Stewart G. C., Boyle B. J., Griffiths R. E., 1995b, MNRAS, 273, L15

Romero-Colmenero E., Branduardi-Raymont G., Carrera F. J., Jones L. R., Mason K. O., McHardy I. M., Mittaz J. P. D., 1996, MNRAS, 282, 94

Shanks T., Georgantopoulos I., Stewart G. C., Pounds K. A., Boyle B. J., Griffiths R. E., 1991, Nat, 353, 315

Shanks T. et al., 1999, in preparation.

Sharples R., Gray P., Hatzidimitriou D., 1991, *Autofib Manual*. Anglo-Australian Observatory User Manual 26

Stocke J. T., Morris S. L., Gioia I. M., Maccacaro T., Schild R., Wolter A., Fleming T. A., Henry J. P., 1991, ApJS, 76, 813

Veron-Cetty M. P., Veron P., 1996, European Southern Observatory Scientific Report, 17, 1

Chapter 6

Near Infra-Red Spectroscopy

of X-ray Luminous Galaxies

ABSTRACT. Here we use near infra-red spectroscopy to identify directly the presence of AGN activity in X-ray galaxies. We obtain CGS4/UKIRT spectra and search for broad Paschen α lines in galaxies from the Deep *ROSAT* Survey.

6.1 Introduction & Motivation

Here we describe spectroscopic observations undertaken at 2.2μm with the aim of detecting broad Paschen α emission lines in X-ray luminous galaxies. The detection of a broad component to Pa_α emission is indicative of AGN activity within a galaxy, obscured from sight at optical wavelengths.

The ratio of certain emission line luminosities can be used to provide a measure of the reddening present in an object, using the known wavelength dependence of absorption in the optical regime. The Balmer emission line, H_β, has a rest wavelength of $\lambda_{\mathrm{rest}} = 4861\,\text{Å}$, which lies bluewards of H_α at $\lambda_{\mathrm{rest}} = 6562\,\text{Å}$, and is therefore affected by absorption to a greater extent. The Balmer decrement, which is the ratio of H_α to H_β luminosities, is often used to estimate the reddening. For case B recombination, this ratio is predicted to be $\mathrm{H}_\alpha/\mathrm{H}_\beta = 2.8$. However, the intrinsic unreddened $\mathrm{H}_\alpha/\mathrm{H}_\beta$ ratio is not known for certain in the broad-line region (BLR), as the high densities present mean that collisional and self-absorption effects modify the ratio from the value of $\mathrm{H}_\alpha/\mathrm{H}_\beta$ predicted purely from case B recombination. Ward et al. (1988) use the observed correlation between Balmer decrement and hard X-ray/H_β ratio for a sample of hard X-ray selected AGN to determine that the average intrinsic ratio in the absence of dust is $\mathrm{H}_\alpha/\mathrm{H}_\beta = 3.5$. This value can then be used as a baseline against which the reddening in AGN can be measured. A Type 2 QSO found in the Deep *ROSAT* Survey, RXJ 1343.4+0001 (Almaini et al. 1995; Shanks et

al. 1995, 1996), was found to have $H_\alpha/H_\beta > 8.4$, from which an estimate of the reddening of $A_V > 3$ was obtained (Georgantopoulos et al. 1999).

However, H_α is still strongly affected by even a moderate obscuring column, and therefore in order to maximise the chance of detecting emission lines from the BLR, observations of Pa_α at the longer wavelength of $\lambda_{\mathrm{rest}} = 1.875\mu m$ are made instead. Although the Pa_α emission line is weaker, $H_\alpha/Pa_\alpha \sim 10$, this is more than compensated for by the differential reddening, $A_\lambda \propto 1/\lambda$, which gives a factor of approximately 14 in flux in favour of Pa_α. The search for broad Pa_α emission in the spectra of X-ray luminous galaxies is therefore an excellent strategy in our search for moderately obscured AGN.

The results presented here are preliminary, and have been used as an exploratory program with a view to expanding our observations to encompass a bigger sample of objects in the future.

6.2 Target Selection

The purpose of this spectroscopic campaign was to take $K-$band spectra of candidate obscured AGN at redshifts in the range $0.1 \lesssim z \lesssim 0.3$ for which Pa_α would lie at $\sim 2.2\mu m$, to search for broad components of this emission line. We therefore observed a sample of X-ray luminous galaxies, taken from the Deep $ROSAT$ Survey, for which the X-ray emission mechanism is not well understood, to determine whether obscured AGN could be the source of the X-ray emission. The properties of our targets are summarised in Table 6.1.

The first candidates considered for these observations were taken from the sample of bright $ROSAT$ galaxies (Almaini et al. 1996), as described in Section 5.2. The nine galaxies in this sample have $ROSAT$ fluxes of $S(0.5 - 2\,\mathrm{keV}) > 10^{-14}\,\mathrm{erg\,cm^{-2}\,s^{-1}}$. Two galaxies from the southern QSF1 field are too far south to be visible from UKIRT. Of the remaining seven galaxies, four are emission- rather than absorption-line galaxies and therefore are possible targets. However, GSGP4X:091 is not a feasible target, since at a redshift of $z = 0.416$, the observed wavelength, $\lambda_{\mathrm{obs}}(Pa_\alpha) = 2.655\mu m$, lies in an atmospheric absorption band. We therefore observed the remaining three galaxies, GSGP4X:048, GSGP4X:069 and SGP3X:033.

We next searched the sample of fainter X-ray galaxies from Almaini et al. (1996), for which the $ROSAT$ flux lies in the range $S(0.5 - 2\,\mathrm{keV}) > (0.1 - 1.0) \times 10^{-14}\,\mathrm{erg\,cm^{-2}\,s^{-1}}$. Of the fourteen galaxies in this sample, we chose to observe the two brightest galaxies which have hard $ROSAT$ spectral indices, an offset between the optical and X-ray positions of $< 10''$, and for which the optical spectrum showed narrow emission lines. The two galaxies which satisfied these criteria were SGP2X:025 and GSGP4X:109, at redshifts of $z = 0.202$ and 0.098 respectively.

Object Name	Optical position α (J2000) δ	z	$\lambda(Pa_\alpha)$ (μm)	$S_{0.5-2\,keV}$ (erg cm^{-2} s^{-1})	Γ	B (mag)	R (mag)	K (mag)	t_{exp} (sec)	Date
GSGP4X:048	00 57 17.1 -27 21 47	0.155	2.166	3.0×10^{-14}	1.82 ± 0.15	20.4	-	-	600	13,14/11/97[c]
GSGP4X:069	00 57 36.8 -27 33 04	0.213	2.274	8.5×10^{-15}	0.79 ± 0.51	20.5	18.8	16.2	2160	11/11/97
GSGP4X:109	00 58 24.4 -27 29 23	0.098	2.059	4.8×10^{-15}	0.77 ± 1.15[a]	16.9	15.7	-	1980	12,13/11/97[d]
SGP2X:025	00 51 51.4 -29 04 18	0.202	2.254	5.1×10^{-15}	-0.20 ± 0.82[a]	21.1	20.0	-	840	14/11/97
SGP3X:033	00 55 00.4 -28 38 30	0.195	2.241	1.2×10^{-14}	1.94 ± 0.24	18.6	17.3	14.4	1890	12/11/97
SGP3X:048	00 55 36.1 -28 32 54	?	-	1.3×10^{-14}	$\sim 1.2 \pm 0.8$[b]	-	20.0	15.5	1380	14/11/97

[a] Equivalent photon index obtained from the $0.5 - 2\,keV$ hardness ratio (Almaini et al. 1996).

[b] The hardness ratio for this source is 0.136, from which the estimated equivalent spectral index is $\Gamma \sim 1.2 \pm 0.8$ (Almaini, private communication).

[c] CGS4 observation partly affected by high humidity. Cloudy for IRIS observation, therefore no K−magnitude available.

[d] One reduced group on 13/11/97 affected by high humidity.

Table 6.1. Properties of the sample of X-ray luminous ROSAT galaxies observed by CGS4. Each galaxy has a narrow emission-line spectrum, with the exception of SGP3X:048, which has no spectroscopic identification. We give the redshift of each galaxy, and the expected wavelength of the Pa$_\alpha$ emission line, plus the ROSAT flux and photon index, and $B-$, $R-$ and K−magnitudes where available. The total exposure times and dates for the CGS4 observations are also listed.

In addition, we chose to observe the blank field *ROSAT* source, SGP3X:048, due to the extremely red $B - K$ colour of the proposed optical/near infra-red counterpart. Our IRIS observations gave a bright K-band magnitude of $K = 15.5$, whereas it is undetected on the APM blue plate, suggesting $B > 22$, which corresponds to $B - K > 6.5$. The object is detected on the APM R plate, with $R = 20.0$, giving again a red colour of $R - K = 4.5$. Although we do not have a spectroscopic identification of this galaxy at present, and therefore this observation was more exploratory, the red colour could be attributable to the presence either of a strong broad emission line in the K passband or strong reddening, and we aim to test these hypotheses. If the emission line present was Pa_α, then we estimate from the K-band magnitude that the fractional contribution from Pa_α would be 3.5 per cent.

The expected Pa_α flux can be estimated as a fraction of the continuum flux for each galaxy, using the following method. The relationship between hard X-ray luminosity and H_α flux was determined from a sample of hard X-ray selected AGN by Ward et al. (1988). These two quantities were used because of their lower sensitivity to absorption than soft X-rays and H_β flux. A linear correlation was found with $L_X(2 - 10\,\text{keV}) \sim 10 H_\alpha$. We use this correlation in our estimation of the Pa_α flux expected in each of our targets, together with the observed correlation, $L_X(2 - 10\,\text{keV}) \sim L_X(0.5 - 2\,\text{keV})$, and the ratio $H_\alpha/Pa_\alpha \sim 10$ predicted from case B recombination. This gives a relationship between the expected soft X-ray and Pa_α fluxes of $f_X(0.5 - 2\,\text{keV}) \sim 100 f(Pa_\alpha)$, and therefore the Pa_α flux can be estimated from the *ROSAT* fluxes that we have for each of these objects.

To maximise the chance of detecting broad Pa_α in these objects, we require that the Pa_α flux be large compared with the continuum flux. For example, for GSGP4X:069, the *ROSAT* flux is $f_X(0.5 - 2\,\text{keV}) = 8.5 \times 10^{-15}\,\text{erg cm}^{-2}\,\text{s}^{-1}$, which gives an estimate of $f(Pa_\alpha) = 1.3 \times 10^{-16}\,\text{erg cm}^{-2}\,\text{s}^{-1}$. Using the relationship between broad-band magnitude and continuum flux:

$$K = -2.5 \log f_\nu + 2.5 \log f_{\nu 0},$$

where for the K-band , $f_{\nu 0} = 4.17 \times 10^{-11}\,\text{erg s}^{-1}\,\text{cm}^{-2}\,\text{Å}^{-1}$, we calculate that $K = 16.23$ corresponds to $f_{\text{gal}} = 1.4 \times 10^{-17}\,\text{erg s}^{-1}\,\text{cm}^{-2}\,\text{Å}^{-1}$. Assuming that the broad component to the Pa_α emission line has a width of $3000\,\text{km s}^{-1}$, using $\delta v/c = \delta\lambda/\lambda$ gives a width of $227\,\text{Å}$ at $\lambda(Pa_\alpha) = 2.27\mu\text{m}$. Approximating the broad line by a rectangular box with this width allows us to estimate the fractional contribution of the broad line above the continuum flux. The K-magnitudes for GSGP4X:069 and SGP3X:033 are used to give estimates of the fractional Pa_α

flux of 4.1 and 1.1 per cent respectively. We estimate that the percentage contribution from Pa_α will be of the same order in the other four targets.

6.3 Observations

The observations were taken during four half nights at the 3.8-m United Kingdom Infra-Red Telescope (UKIRT), 1997 November 11–14 (observers: K F Gunn and O Almaini) with the Cooled Grating Spectrometer (CGS4; Wright 1994). Observing conditions on the whole were excellent, with typical seeing of $0''.5$ ($0''.3$ with tip-tilt correction). A short period during the third half-night was affected by high humidity, and we flag these observations in Table 6.1.

CGS4 contains a 256×256 InSb array, of which a sub-array of 256×178 is used for the long focal length camera. Both object and standard star observations were taken in non-destructive readout mode, ND_STARE. In this mode, measurements of the pixel voltage are taken throughout each sub-integration without affecting the voltage in each pixel, and a destructive read-out is taken at the end of each sub-integration in which the voltage is reset to the base level. The 40 lines/mm grating was used in first order, centred on 2.2μm in each case. The plate scale is $0''.61$/pixel giving a slit width of $1''.22$ (2 pixels). The observations were performed at first order, giving a dispersion of $2.4 \times 10^{-3}\mu$m/pix, and a wavelength coverage of $1.9 - 2.5\mu$m. Since there is only one wavelength resolution element per pixel, the detector was moved by half a pixel in the dispersion direction between exposures, thereby creating fully-sampled spectra. This is known as 2×1 resampling, and the resulting images are 512×178 pixels. Since our objects are not significantly extended compared with the slit length, it is possible to avoid using offset sky exposures, increasing the observing efficiency by a factor of two. The sky subtraction is performed by nodding the telescope between two positions on the slit, then subtracting the sky frame from the object frame in each object-sky pair. The object-sky pairs are then co-added to create the final frame. The object is initially centred on a certain row on the chip, chosen for the lack of hot or flickering pixels on this row and its neighbouring rows.

The technique used to acquire faint sources for CGS4 observations requires that the telescope should "peak-up" on a nearby bright source, and then use known offsets to move to the target. The "peaking-up" procedure involves spiralling around the bright source until the maximum intensity if observed by the tv camera. By definition, there are a lack of such bright stars in the South Galactic Pole region where all our targets lie, and therefore the offset distances were often quite large.

6.4 CGS4 Data Reduction

The raw data frames were reduced using the Starlink software CGS4DR. An image is stored for each detector position, so for 2×1 resampling, two images of dimensions 256×178 are created. These are combined into *reduced observations* or ro files, which have dimensions 512×178 ($2 * 256 \times 178$). The ro files are then divided into object-sky pairs for sky subtraction, then each object-sky pair is then co-added into one *reduced group* or rg file.

As the data were taken in ND_STARE mode, the bias is automatically accounted for, and linearization of the data is not required as for the array in CGS4, no nonlinearity is found up to $\sim 98\%$ of full-well capacity. Dark subtraction is not performed explicitly, as this effectively occurs during the creation of object-sky pairs. However, the images are flat-fielded, using the flat-field frame taken nearest in time. A 1D spectrum is taken from the (bias and dark subtracted) flat-field, and a low-order polynomial is fitted to it. This fit is then grown along the slit, and it is this 2D fit that is used to normalise the flat-field frame. This also removes the spectral signature of the black body calibration source used to illuminate the flat-field.

Once reduced group files have been created for each object and standard, then the spectra can be extracted. This is achieved using the following Starlink FIGARO procedures:

- Wavelength calibration of arcs: The tasks **extract, arc** and **iarc** are used to extract a 1-D spectrum from each arc frame, and the resulting spectrum is compared with that expected from the argon arc-lamp used. The 1-D spectrum is converted to a linear wavelength scale using **scrunch**, and then **iscrunch** is used to convert the whole arc frame onto $19,000 - 25,000\,\text{Å}$, which corrects for any residual tilt in the arc lines perpendicular to the dispersion direction.

- Wavelength calibration of object and standard frames: The arc frames closest in time on either side of the object or standard observations are used to calibrate each reduced group. The tasks **iscrunch** and **iscruni** are used, depending on whether one or two arc frames are used, and this again removes any tilt in the image.

- Curvature correction: Spectra taken with CGS4 can be seen to curve slightly along the chip, ie, the spatial position of the peak of the spectrum changes with wavelength, and this effect needs to be corrected for. As CGS4 is mounted at Cassegrain rather than floor-mounted, a small amount of flexure of the instrument occurs which means that the amount of curvature changes with zenith angle. The object frames are too faint for the position of the spectrum to be traced accurately along the chip, so the standard frame nearest in time is used. This therefore

means that both standard and object frames must be scrunched in the same way, onto the same wavelength scale.

Using the standard frame and **icur**, a point near the maximum of the positive spectrum is defined, and then the spectrum is traced using **sdist**. The standard frame must then be multiplied by -1 so that the negative spectrum can be traced in the same way (**sdist** cannot detect negative spectra). The results from both positive and negative spectra are combined, and used by **cdist** to correct both the standard and object frames for the curvature.

- Extraction of the spectrum: Using a subset region of each straightened image frame (to avoid messy edge effects), the whole spectrum is collapsed in the y-direction, in order to determine which rows contain the signal. For the standards, the aim is to collect as much of the flux as possible, as this is then used to flux-calibrate the object. However, for the object spectra, it is possible to look at different parts of the spatial profile, and in this way extract the spectrum from either the whole galaxy or just the nucleus. Once the rows containing the spectrum have been identified, then the tasks **profile** and **optextract** are used to extract the spectrum, using Horne's optimal extraction method (Horne 1986). This yields both positive and negative spectra, which can then be combined using **isub** (pos) (neg).

- Flux calibration: Each object spectrum is calibrated using a flux standard star observation taken nearby in time and at a similar airmass. This is to minimize the differences in the transmission of the atmospheric absorption bands present at these wavelengths, which are highly dependent on both the airmass and the water content of the atmosphere. At this stage, both the object and standard spectra are dominated by these atmospheric absorption bands, and so **scross** can be used to cross-correlate the positions of these bands to ensure that they lie in the same place and that there is no wavelength shift between object and standard observations. Any shift present can usually be measured in fractions of a pixel, and this can be corrected for (in the object frame, as more than one object can be calibrated using each standard) using **ishift**.

In order to use the task **irflux**, the object and standard spectra must have their wavelength scales measured in μm. This is achieved using KAPPA tasks **xcmult, axlabel** and **axunits**. The object frame should be scaled to the same exposure time as the standard star using **icmult**. Using **irconv**, the resulting spectrum can then be converted from Janskys into flux units of $\mathrm{W\,m^{-2}\,\mu m^{-1}}$.

- The sets of rg files for each individual object can then be combined, to increase the signal to noise. Each rg file is weighted by the exposure time, and then co-added. Any rg files which have been affected by high humidity or other problems are excluded.

- Line identification and fitting: The final spectrum is smoothed using **ixsmooth** and a Gaussian half width of 1 pixel in the wavelength direction. Then **gauss** is used to measure the parameters of any emission lines detected, or to place upper limits on emission lines not detected.

6.5 Spectroscopic Results

Here we present the results of these CGS4 spectroscopic observations. Figs 6.1 to 6.5 show the spectrum of each object. We give the raw spectra at the bottom of each plot and arbitrarily offset above this a version smoothed to the instrumental resolution. We now discuss each object in turn: **GSGP4X:109** Fig. 6.1 shows the co-added spectrum from the three individual observations of this object. A Pa_α emission line can clearly be seen at a wavelength of $2.059 \mu m$, however it is not strikingly broad. Fitting a Gaussian to the line gives a FWHM of $1030 \, \mathrm{km \, s^{-1}}$, which is on the borderline of the formal definition of a broad line for QSOs of FWHM $\gtrsim 1000 \, \mathrm{km \, s^{-1}}$. The observed flux in the Pa_α line is approximated from the height and FWHM of the emission line, giving $f(Pa_\alpha) = 3.4 \times 10^{-18} \, \mathrm{W \, m^{-2}}$.

However, for one of the individual observations of this object, a much broader line was detected in the spectrum of the nucleus of the galaxy, as shown in Fig. 6.2. Extensive tests have been performed to ensure that this is not due to poor flux calibration, since this in a portion of the spectrum affected by sky absorption bands, but the line was resilient and remained obvious when fluxed using several different calibration sources. We note however that although the existence of the line is convincing, the flux estimate of $f(Pa_\alpha) = 1.3 \times 10^{-18} \, \mathrm{W \, m^{-2}}$ is likely to be less reliable. This is greater than the flux predicted from the soft X-ray flux by a factor of ~ 15, and is probably contaminated by the presence of narrow Pa_α from the galaxy. Unfortunately, it is not possible to determine the relative contributions from the broad and narrow lines by fitting two components, since the data are not of sufficiently high signal-to-noise.

Due to the large offset distance involved in target acquisition for SGP sources, as described in Section 6.3, it is possible that for each individual observation of this source, a slightly different part of the galaxy was observed, only one of which covered the nucleus. In conditions of excellent seeing, this is even more likely, although using a slit width of $1''2$ slit should avoid this happening.
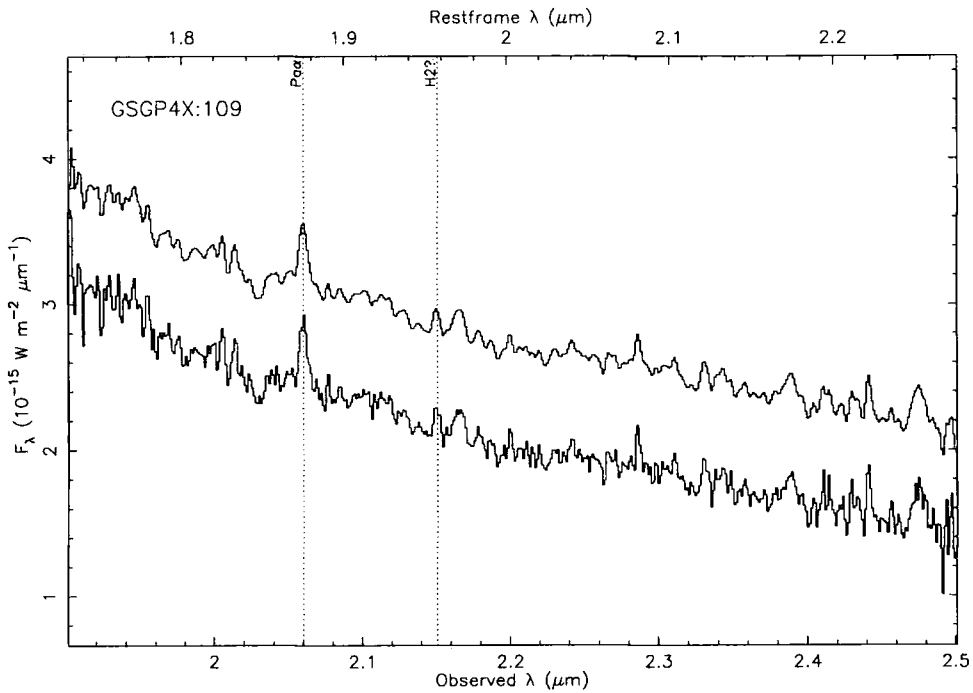
Figure 6.1: The K–band spectrum of GSGP4X:109, from three combined observations, with a total exposure time of 1500 s. A Pa_α emission line can be seen at $\lambda = 2.059\mu m$, which has a FWHM of $\sim 1000 \, km \, s^{-1}$. The continuum is very blue. The lower spectrum shows the raw spectrum; the upper spectrum has been smoothed to the instrumental resolution and offset by an arbitrary amount in flux for clarity.
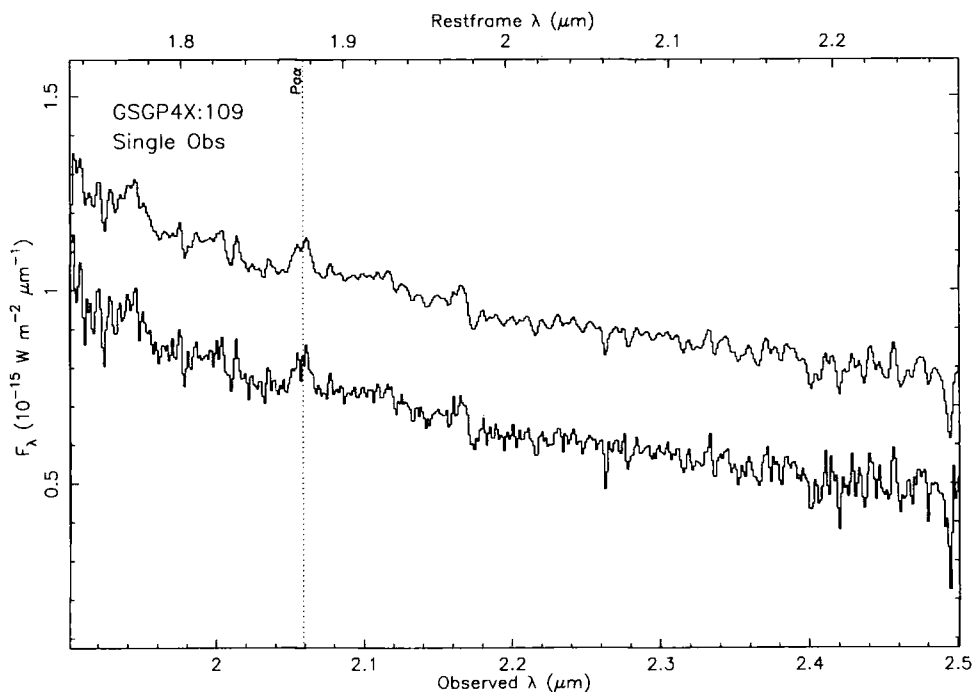
Figure 6.2: The K–band spectrum of the centre of GSGP4X:109, from a single observation of 660 s, showing a possible broader Pa_α emission line at $\lambda = 2.059\mu m$, with FWHM $\sim 2000 \, km \, s^{-1}$.
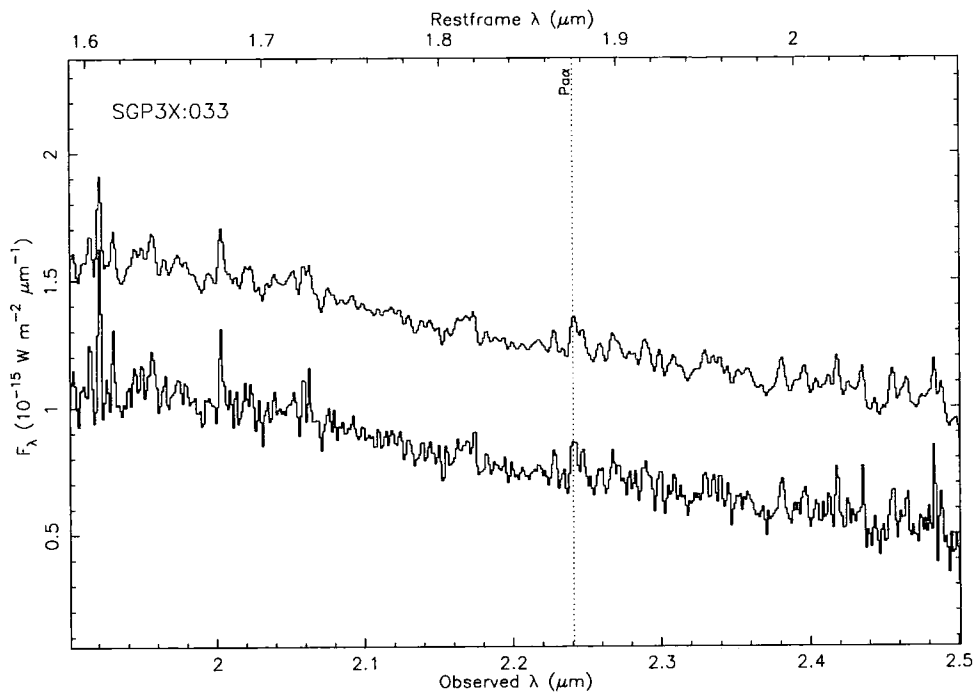
Figure 6.3: The K-band spectrum of SGP3X:033, showing a strong blue continuum, and possible Pa_α at $2.241\mu m$. The exposure time is $1890\,s$.
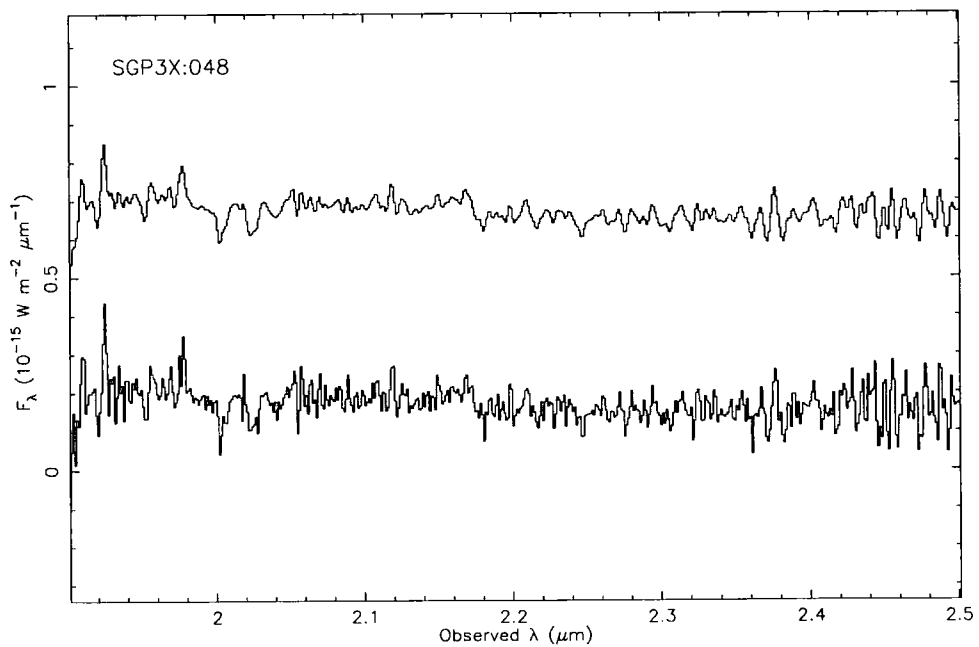
Figure 6.4: The K-band spectrum of SGP3X:048 for $t_{exp} = 1380\,s$, showing a strong red continuum, but no obvious broad or narrow emission lines.
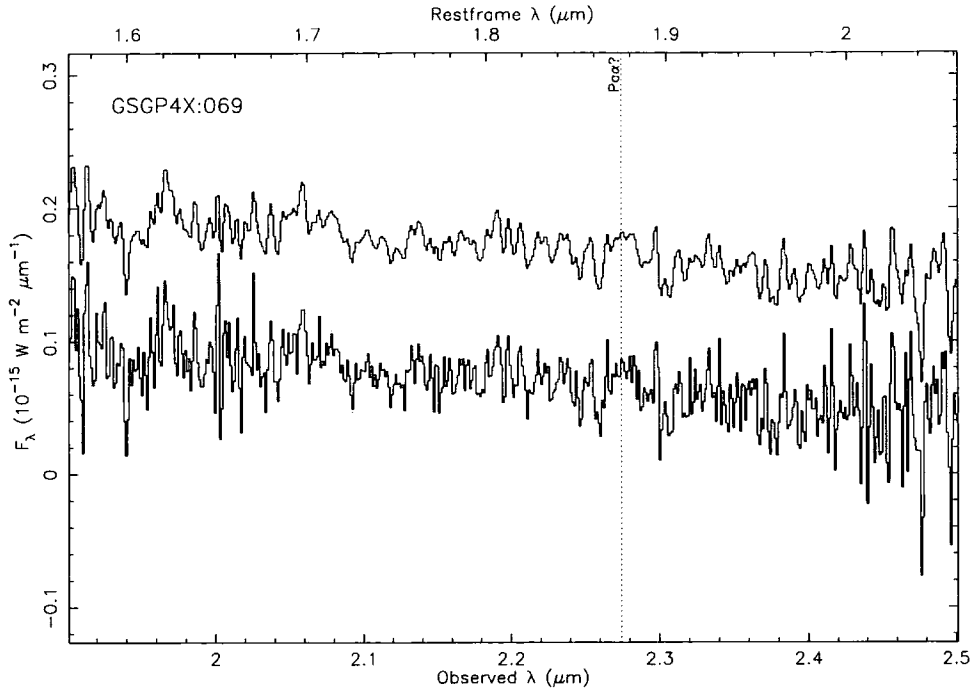
Figure 6.5: The K-band spectrum of GSGP4X:069, showing a red continuum. The exposure time is 2160 s. Pa$_\alpha$ emission is not obvious, but there is a definite excess close to the expected wavelength of $\lambda = 2.274\mu$m.

SGP3X:033 The spectrum of this galaxy is shown in Fig. 6.3. Possible Pa$_\alpha$ emission can be seen at 2.241μm, and perhaps [FeII] at 1.965μm, but this is very close to the edge of a sky band, and is slightly redshifted. Fitting a Gaussian to the Pa$_\alpha$ line gives a FWHM of 1260 km s^{-1}, which again is on the borderline of being defined as "broad". The measured flux in the line is $f(\text{Pa}_\alpha) = 1.1 \times 10^{-18}$ W m^{-2}, which in in excess of the value of $f(\text{Pa}_\alpha) = 1.8 \times 10^{-19}$ W m^{-2} estimated from the *ROSAT* flux. This makes it difficult to place limits on the obscuring column that could be present in this galaxy, particularly as the *ROSAT* spectrum is fitted by a steep power-law, of slope $\Gamma = 1.94 \pm 0.24$ (Almaini et al. 1996), which would imply that the X-ray emission is unaffected by absorption, and no nucleus is detected in the K-band image (see Chapter 5).

SGP3X:048 No strong emission lines were detected in the CGS4 spectrum shown in Fig. 6.4. However, a strong continuum can be seen, which is very red compared to the other sources in our sample, which is most likely what gives rise to the observed red $B - K$ colour of this galaxy. We therefore need to obtain an optical spectroscopic identification of this faint B-band source, in order to determine the nature of the emission mechanism in this object.

GSGP4X:069 Fig. 6.5 shows the spectrum of this galaxy, which has a red continuum and no obvious lines. Fitting a Gaussian to the excess emission nearest to the expected wavelength of the Pa$_\alpha$ emission line at $\lambda = 2.274\mu$m gives a FWHM of $\sim$ 2200 km s^{-1}, but this is offset slightly at

$\lambda = 2.276\mu$m. We therefore require additional observations of this object, in order to increase the signal-to-noise sufficiently to confirm or reject the presence of Pa_α emission. The K–band image of GSGP4X:069 shows that there is no evidence for a point-like nucleus in this object, and the hard *ROSAT* spectrum is consistent with the presence of a high level of obscuration.

GSGP4X:048 and **SGP2X:025** No continuum was detected. In the case of GSGP4X:048, this may be due to the increased humidity at the time of the CGS4 observation. However, in the absence of K–band magnitudes, both targets may be intrinsically faint at 2.2μm. In both cases, the observations might also have suffered from the problems inherent at high Galactic latitudes in the offset method of CGS4 target acquisition for faint sources.

6.6 Discussion

The nature of these observations have shown that it is very difficult to detect a broad component to Pa_α emission lines, and where we have made a tentative detection of such, the measured flux in the line is greater than that predicted from the *ROSAT* flux. This could be due to a number of reasons, the first of which being the possibility that the obscured AGN hypothesis is incorrect, and that an alternative explanation is required for the X-ray emission, such as starburst activity. However, we know for certain that some X-ray luminous galaxies harbour obscured AGN, with evidence from variability studies, spectropolarimetric observations, hard X-ray data, etc.. We therefore discuss a number of issues which may allow the lack of positive detections in these observations to remain consistent with an AGN origin for the X-ray emission of these galaxies.

By virtue of our selection criteria, these galaxies are narrow emission-line galaxies, and therefore are likely to have a narrow component to the Pa_α line. It is therefore very difficult to disentangle a weakly detected broad emission from the narrow line component. Furthermore, our predicted fluxes are estimated using two relationships, both of which have a significant intrinsic scatter. Starting from the hard X-ray luminosity, the scatter in the corresponding H_α luminosity is approximately an order of magnitude (Ward et al. 1988). The H_α/Pa_α ratio has a scatter of a factor of five around the case B predicted value of 10 (Soifer et al. 1981).

Perhaps most importantly however, we are taking as our starting point the soft X-ray flux, in order to estimate the hard X-ray luminosity. If we are assuming that the X-ray emission is due to AGN activity, and that we do not detect broad emission lines in the optical due to dusty material around the nucleus, then this same obscuring medium will also attenuate the X-ray flux. In this case, the measured *ROSAT* flux will be attenuated due to the absorption, and the true hard X-ray flux will be higher, in which case a brighter Pa_α line flux should be predicted. This could

be another reason to account for the predicted line fluxes being lower than the measured fluxes. However, as shown in Fig. 3.6, the ratio of X-ray to $K-$band flux is comparatively independent of column density in the redshift range we are dealing with here, of $0.1 \lesssim z \lesssim 0.3$. The X-ray absorption is greater than the $K-$band absorption, by a factor of ~ 2.5. If we preferred to invoke much higher column densities, then we would also require some other source for the observed soft X-ray emission, for instance either from a starburst, or scattered emission into the line of sight from a highly obscured AGN. Hard X-ray data are needed in order to discriminate between these two cases.

6.7 Conclusions

Our observations have shown that this is an effective but demanding method for searching for AGN activity in X-ray luminous galaxies. We have however succeeded in finding possible broad Pa_α emission in one out of six galaxies observed. However, there is only a very small range of obscuring columns for which broad Pa_α can be still observed while permitted emission lines in the optical spectrum are extinguished. For a low column density, broad lines will be visible at all wavelengths, whereas for high columns, no emission from the BLR will escape in the near infra-red, and then observations at even longer wavelength are required.

Nevertheless, this technique has already been proved to be very successful, with the discovery of an obscured AGN in an X-ray luminous galaxy detected in the *ROSAT* observation of the BJS864 field. The observations were taken during two half nights at UKIRT, 1997 February 3–4 (observer: O Almaini) with CGS4. The same observing strategy was used, namely spectroscopy at 2.2μm to search for broad Pa_α emission lines. One of the targets observed was F864X:052, which is optically identified as a narrow emission-line galaxy at $z = 0.103$, with $B = 17.6$. $K-$band imaging of this galaxy with IRCAM3 (Puxley et al. 1994) on UKIRT gave a magnitude of $K = 13.5$, and the image showed evidence for an offset point-like nucleus (Almaini 1999c, private communication). In the CGS4 spectrum of this object, only *narrow* Pa_α emission is detected, implying that if an AGN is present, the column density along the line of sight must be $N_H > 5 \times 10^{22}\,\mathrm{cm}^{-2}$ (Almaini et al. 1998). However, the forbidden line [Si VI] is detected in the spectrum, which is remarkable, as since the ionization potential of the [Si VI] coronal line is higher than $100\,\mathrm{eV}$, X-ray energies are required to create this species, and therefore its presence is indicative of AGN activity. The coronal line emission is thought to be produced in one or more of three distinct regions (Murayama & Taniguchi 1998). The inner edge of the obscuring torus has high density and a huge incident X-ray flux, however this region will only be visible in Type
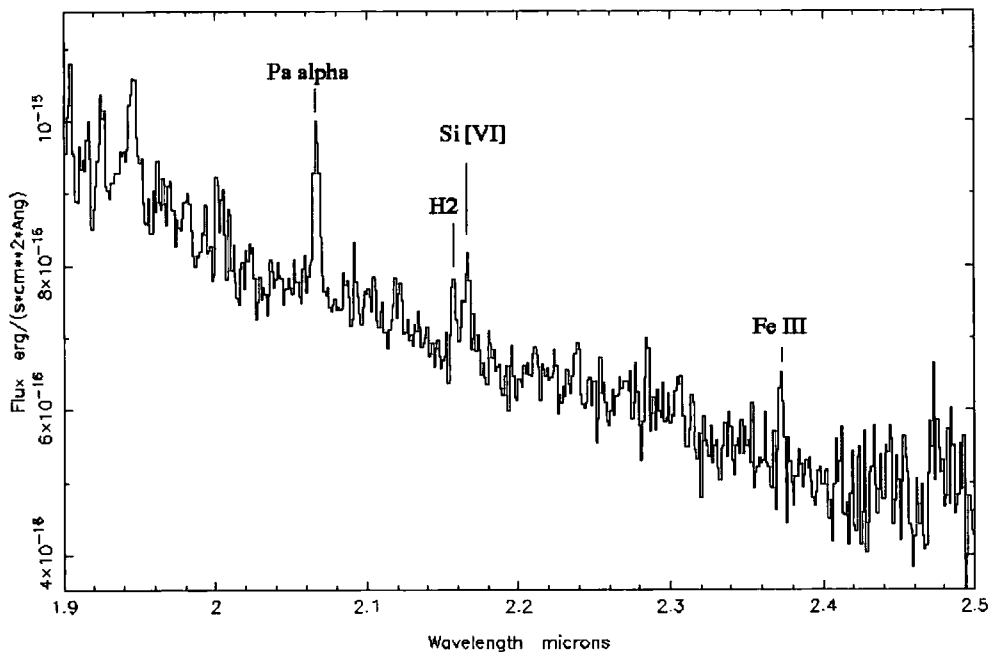
Figure 6.6: The CGS4 spectrum at $2.2\mu m$ of the narrow emission-line X-ray luminous galaxy, F864X:052, showing narrow Pa_α emission. Despite the lack of a broad component to the Pa_α emission line, the coronal line of [Si VI] shows that an AGN must present, in order to provide the intense radiation field necessary to create such high ionization species.

1 objects since by definition, the torus obscures emission in Type 2 objects. Clouds of material in the narrow line region are the second important site for coronal line emission, and the third component is from an extended low density medium on similar scales to the narrow line region. It is most likely that the [Si VI] emission seen in F864X:052 originates from one of these last two regions.

The lower limit placed on the column density present in F864X:052 therefore provokes the question as to the origin of its soft X-ray luminosity, since the same obscuring medium which attenuates the optical and near infra-red emission from the BLR will also produce significant photo-electric absorption of X-ray photons. One possible mechanism for the soft X-ray emission is that it is scattered light from the nucleus, in which case spectropolarimetry in the optical can be used to test this hypothesis, by searching for broad emission lines in polarized light. Alternatively, this could be one of a growing class of hybrid objects, in which both starburst and AGN activity are present, such as the narrow-line X-ray galaxy detected by Iwasawa et al. (1997). This is consistent with

the model in which the obscuration may actually be due to nuclear star-forming activity around a central AGN (Fabian et al. 1998). Either of these scenarios could also be true for GSGP4X:109.

Assuming that the X-ray emission in the sample of galaxies observed with CGS4, is due to the presence of an AGN, we can further test whether the lack of detections of broad Pa_α in these galaxies is due to the presence of obscuring material in the line of sight. Since we know that this method is sensitive to a restricted range of column densities, we now require hard X-ray spectroscopic data, such as will be possible with *AXAF* and in particular with *XMM*, so that firm limits can be placed on the column densities in these objects. It will then be possible to determine whether the level of obscuration is sufficient to cause the non-detection, or whether the presence of an AGN can be ruled out. Combining this with further infra-red spectroscopic observations in order to increase our sample size, and SCUBA photometry at sub-mm wavelengths to assess the amount of dust present, will enable a much clearer picture to emerge as to the energetics of X-ray luminous galaxies, and their contribution to the X-ray and far infra-red backgrounds.

The main conclusion that can be drawn from these observations is that the absence of a nucleus in $K-$band images of these targets correlates with the non-detection of broad lines in the CGS4 spectra. With the benefit of hindsight, no new results have been obtained from these spectroscopic data that could not have been inferred from the near infra-red imaging data. This means that our prime targets for future observations will be those found to have red point-like components. We would therefore like to extend these CGS4 observations to encompass a range of *ROSAT* sources. In particular, we would like to target the red stellar sources that have been identified from IRIS imaging as being potential counterparts to blank field *ROSAT* sources (as described in Chapter 5). The disadvantage to the blank field targets such as these is the lack of redshift information, but as they are often very bright in K, then it will be possible to obtain CGS4 spectra in the $J-$, $H-$ and $K-$bands, and obtain a spectroscopic redshift in that way. Objects of particular interest which have come out of our IRIS imaging program include the red stellar counterparts to GSGP4X:091 and SGP3X:006, the point-like nucleus in GSGP4X:064, and possibly QSF1X:036, which at present has a rather ambiguous identification.

In the next Chapter, we discuss far infra-red *ISO* observations searching for thermal emission in samples of X-ray luminous galaxies and QSOs detected by *ROSAT*, which would signify the presence of dusty material, predicted by the obscured AGN models.

References

Almaini O., 1999c, private communication.

Almaini O., Boyle B. J., Griffiths R. E., Shanks T., Stewart G. C., Georgantopoulos I., 1995, MNRAS, 277, L31

Almaini O., Shanks T., Boyle B. J., Griffiths R. E., Roche N., Stewart G. C., Georgantopoulos I., 1996, MNRAS, 282, 295

Almaini O., Shanks T., Gunn K. F., Boyle B. J., Georgantopoulos I., Griffiths R. E., Stewart G. C., Blair A. J., 1998, Astronomische Nachrichten, 319, 55

Fabian A. C., Barcons X., Almaini O., Iwasawa K., 1998, MNRAS, 297, L11

Georgantopoulos I., Almaini O., Shanks T., Stewart G. C., Griffiths R. E., Boyle B. J., Gunn K. F., 1999, MNRAS, 305, 125

Horne K., 1986, PASP, 98, 609

Iwasawa K., Fabian A. C., Brandt W. N., Crawford C. S., Almaini O., 1997, MNRAS, 291, L17

Murayama T., Taniguchi Y., 1998, ApJL, 497, L9

Puxley P. J., Sylvester J., Pickup D. A., Paterson M. J., Laird D. C., Atad-Ettedgui E. I., 1994, SPIE Proc., 2198, 350

Shanks T. et al., 1996, in Zimmerman U., Truemper J.E., Yorke H., eds, *Roentgenstrahlung from the Universe*, Vol. MPE Report 263, p. 341

Shanks T., Almaini O., Boyle B. J., Done C., Georgantopoulos I., Griffiths R. E., Rawlings S., Stewart G. C., 1995, Spectrum, Newsletter of the Royal Observatories, vol. 7, 7

Soifer B. T., Neugebauer G., Oke J. B., Matthews K., 1981, ApJ, 243, 369

Ward M. J., Done C., Fabian A. C., Tennant A. F., Shafer R. A., 1988, ApJ, 324, 767

Wright G. S., 1994, Experimental Astronomy, 3, 17

Chapter 7

Far Infra-Red Photometry

of *ROSAT* X-ray Sources

ABSTRACT. In this Chapter, we discuss a second extension of the Deep *ROSAT* Survey to determine the extent of dust reddening in X-ray galaxies and QSOs. This program of observations tests the obscured AGN hypothesis using far infra-red photometry of *ROSAT* X-ray galaxies and QSOs with *ISOPHOT* on the *Infra-red Space Observatory*. The aim here is to detect thermal emission from dusty obscuring material around active nuclei, which is predicted to make a significant contribution to the far infra-red background radiation.

7.1 The *ISO* Mission

The *Infra-red Space Observatory*[1] (*ISO*; Kessler et al. 1996) was launched in November 1995 and had a mission lifetime of 29 months, far in excess of the 18 months originally planned. The observatory finally ran out of helium coolant and was switched off in April 1998. The project was extremely ambitious, with the observatory containing a significant number of moving parts, to enable a large number of different filters, gratings and polarisers to be used in many different observing modes, including photometry, imaging and spectroscopy.

Our observations utilize *ISOPHOT* [2] (Lemke et al. 1996), the imaging photo-polarimeter on board *ISO*, and in particular the two photometric far infra-red cameras (PHT-C) which operate in the wavelength range $50 - 240\mu$m. The shorter wavelength array, C100, is a 3×3 pixel array made from Ge:Ga, with a pixel scale of $43''\!.5$/pixel. The long wavelength array, C200, is made from stressed Ge:Ga, and has 2×2 pixels with a scale $89''\!.4$/pixel. Characteristics of the filters are tabulated in Table 7.1.

---

[1]   *ISO* is an ESO project with instruments funded by ESA Member States with the participation of ISAS and NASA.

[2]   The *ISOPHOT* Consortium is led by the Max-Planck-Institute for Astronomy, Heidelberg.

Camera	Filter	λ_c	$\Delta\lambda$	f_{psf}
		(μm)	(μm)	
C100	60	60.8	23.9	0.69
C100	100	103.5	43.6	0.57
C200	160	174.0	89.4	0.64
C200	200	204.6	67.3	0.59

Table 7.1. PHT-C filter characteristics for the two FIR cameras, C100 and C200, where λ_c is the central wavelength, $\Delta\lambda$ is the rectangular width, and f_{psf} is the fractional intensity of a point source falling on one pixel of the detector, assuming the source is centred on that pixel.

The *ISO* mission was extremely successful. However, we note here that it was found that both the responsivity and sensitivity of the *ISOPHOT* detectors were seriously affected by the presence of ionizing radiation in orbit (Laureijs et al. 1996), and therefore the sensitivity achieved was lower than originally anticipated.

7.2 Target Selection

The aim of our *ISO* observations was to investigate the far infra-red properties of soft X-ray selected QSOs and galaxies. Candidates for FIR follow-up were chosen from our *ROSAT* catalogue to fall into one of two groups. The first was a sample of 20 X-ray galaxies, including both emission- and absorption-line galaxies, with redshifts in the range $0.09 < z < 0.42$, plus a cluster of galaxies at $z = 0.56$. We note however that, subsequent to these observations, one member of the galaxy sample (GSGP4X:017) was reclassified as a $z = 1.010$ QSO, as described in Section 5.5.1. The second sample contained a Type 2 obscured QSO at $z = 2.35$ from our survey, plus five comparison broad-line QSOs at redshifts in the range $1.2 < z < 2.5$.

In Table 7.2, we present the identification and redshift of each of the sources observed by *ISO*, together with the *ISO* observation number and date, and the on-source exposure times in each filter. The exposure times and filters used depended on the type of source, as summarised in Table 7.3. The galaxies were all observed at 60, 100 and 200μm, whereas the filters used for the QSOs depended on their redshift. The peak of the far infra-red emission for a low redshift QSO is expected to lie shortwards of $\sim 100\mu$m for a dust temperature of $T \sim 40$ K. This is then shifted to between 100 and 200μm for higher redshift QSOs. The filters used were therefore chosen in order to maximise the likelihood of a detection.

Object	Obs No	ID	Redshift	Obs date	On-source exposure times (sec)			
					60μm	100μm	160μm	200μm
GSGP4X:017[a]	38001601	QSO	1.010	01/12/96	64	64	-	128
GSGP4X:020	38001602	Gal	0.382	01/12/96	64	64	-	128
GSGP4X:032	38001603	Cl	0.561	01/12/96	64	64	-	128
GSGP4X:048	38001604	NL	0.155	01/12/96	64	64	-	128
GSGP4X:054	38603405	NL	0.21	07/12/96	64	64	-	128
GSGP4X:056	21600826	QSO	1.209	20/06/96	32	32	-	-
GSGP4X:057	38603406	NL	0.161	07/12/96	64	64	-	128
GSGP4X:064	38603407	Gal	0.097	07/12/96	64	64	-	128
GSGP4X:069	41401908	NL	0.213	04/01/97	64	64	-	128
GSGP4X:082	41401909	NL	0.204	04/01/97	64	64	-	128
GSGP4X:086	41401910	Gal	0.161	04/01/97	64	64	-	128
GSGP4X:091	38001512	NL	0.416	30/11/96	64	64	-	128
GSGP4X:094	41401911	NL	0.120	04/01/97	64	64	-	128
GSGP4X:101	21600823	QSO	2.485	20/06/96	-	128	-	128
GSGP4X:109	38001513	NL	0.098	30/11/96	64	64	-	128
GSGP4X:114	38001514	NL	0.211	01/12/96	64	64	-	128
F864X:012	23101121	NL	0.10	05/07/96	64	64	-	128
F864X:039	26001816	Gal	0.126	03/08/96	64	64	-	128
F864X:051	23101120	NL	0.25	05/07/96	64	64	-	128
F864X:052	26001815	NL	0.103	03/08/96	64	64	-	128
F864X:054	26001818	NL	0.089	03/08/96	64	64	-	128
F864X:065	26001925	QSO	1.96	03/08/96	-	128	-	128
F864X:066	26001924	QSO	1.89	03/08/96	-	128	-	128
F864X:077	25402719	QSO	1.97	28/07/96	128	128	-	128
F864X:078	26001817	Gal	0.15	03/08/96	64	64	-	128
F864X:086	25402732	NLQSO	2.35	28/07/96	128	128	64	128
F864X:129	23101122	Gal	0.328	05/07/96	64	64	-	128

[a]GSGP4X:017 was originally identified as a $z = 0.105$ absorption line galaxy, and therefore the *ISOPHOT* exposure times are those for a galaxy, and not for a low redshift QSO.

Table 7.2. Details of the *ISO* observations of a sample of X-ray luminous galaxies and QSOs, taken from the deep *ROSAT* survey fields, GSGP4 and BJS864. We present the the identification and redshift of each of the sources, together with the *ISO* observation number and date, and the on-source exposure times in each filter.

Object		On-source exposure times (sec)			
		60μm	100μm	160μm	200μm
Galaxies/Cluster		64	64	-	128
Low-z QSO	GSGP4X:056	32	32	-	-
High-z QSOs	GSGP4X:101	-	128	-	128
	F864X:065	-	128	-	128
	F864X:066	-	128	-	128
	F864X:077	128	128	-	128
Type 2 QSO	F864X:086	128	128	64	128

Table 7.3. Summary of the exposure times and filters used for each class of sources.

The uncertainties involved in predicting the expected far infra-red (FIR) flux from our X-ray galaxies and QSOs are considerable. Assumptions have to made about the FIR emission mechanism, whether primarily starburst or AGN, and the mass and temperature of dust present, etc. However, it is possible to make a reasonable estimate of the FIR flux in the following way. Griffiths & Padovani (1990) and David, Jones & Forman (1992) investigated the relationship between soft X-ray and 60μm FIR luminosities for samples of bright *IRAS* galaxies. These studies found that there was a strong correlation between the two quantities, of the form $L_X \propto L_{FIR}^{\epsilon}$, with $0.7 < \epsilon < 1$. Since ϵ is close to or equal to unity, then it is possible to use the mean value of the X-ray to 60μm ratio from the Griffiths & Padovani *IRAS* sample for our estimate:

$$\log \left(\frac{L_X(0.5 - 3\,\mathrm{keV})}{L_{60}} \right) = -3.32 \pm 0.10.$$

ROSAT fluxes are measured in the $0.5 - 2\,\mathrm{keV}$ band, and we therefore use the conversion factor of 0.77 (calculated using a spectral index of $\alpha = 1$) to relate the $0.5 - 3\,\mathrm{keV}$ band to the *ROSAT* band. This gives:

$$\log \left(\frac{L_X(0.5 - 2\,\mathrm{keV})}{L_{60}} \right) = \log \left(\frac{0.77\,L_X(0.5 - 3\,\mathrm{keV})}{L_{60}} \right)$$
$$= \log \left(\frac{L_X(0.5 - 3\,\mathrm{keV})}{L_{60}} \right) - 0.11$$
$$\simeq -3.43.$$

which is equivalent to:

$$L_{60} = 2.7 \times 10^3 \, L_X(0.5 - 2\,\mathrm{keV}), \tag{7.1}$$

where the same relationship holds in flux units. The average flux of a *ROSAT* galaxy is of the order of $S(0.5 - 2\,\mathrm{keV}) \sim 10^{-14}\,\mathrm{erg\,cm^{-2}\,s^{-1}}$, which from Eqn 7.1 corresponds to a 60μm flux

of $S_{60} \sim 2.7 \times 10^{-11}\,\mathrm{erg\,cm^{-2}\,s^{-1}}$. Using $1\,\mathrm{Jy} = 10^{-23}\,\mathrm{erg\,cm^{-2}\,s^{-1}\,Hz^{-1}}$ and $\nu(60\mu\mathrm{m}) = 5 \times 10^{12}\,\mathrm{Hz}$, this figure can be converted to an expected 60μm flux *density* of $\sim 0.5\,\mathrm{Jy}$. Since we do not yet know the properties of X-ray selected galaxies in the far infra-red, we take zero to be our lower limit to the flux estimate. In addition, we do not know at what wavelength the peak of the emission lies, and therefore the expected flux at 100 or 200μm could be lower or higher than the 60μm flux. We therefore use the same estimate for each wavelength observed, and assume an uncertainty on this estimate of the same order, *i.e.*, $S_{60,100,200} \sim 0.5 \pm 0.5\,\mathrm{Jy}$.

For the QSOs, the expected FIR flux was estimated from the B–band magnitude using a spectral index of $\alpha = 1.1$, connecting the *IRAS* and optical QSO flux densities.

7.3 The *ISOPHOT* observing strategy

The *ISOPHOT* observations were performed in the rectangular chopped mode, used for single pointing photometry, in which the satellite points to halfway between the target (on-source) and the nearby sky background (off-source) positions, and a chopping mirror moves in order to direct the beam from either the on- and off- source positions onto the detector. The chopper throw distance used for all our observations is $180''$, alternating between the two positions, starting with the off-source. Advantages of this observing method are that it is efficient in time, and that long term detector drifts can be cancelled out. The disadvantages however, were found by the *ISO* Mission Support Team to be considerable, which led to the phasing out of this mode of observation soon after our observations were started. This has meant that the photometric calibration is not yet completed in full, as described further in Section 7.4, although it is not expected that increases in the calibration accuracy will change our results significantly.

The data are taken in non-destructive readout mode, which means that many measurements of the voltage are taken during each integration, without affecting the voltage across each pixel, thereby creating a "ramp" of voltage against time for which the incident flux is proportional to the slope of the ramp. One destructive readout is taken at the end of each ramp, at which time the voltage in the pixel is reset to the base value. This is shown in cartoon form in Fig. 7.1. Integration times for each ramp of 1 s (8 s) are used for the C100 (C200) detectors respectively, with 4 ramps off-source followed by 4 on-source. For instance, for the galaxies, this process is repeated 16(4) times, making an on-source exposure time of 64 s (128 s), and a total exposure time of 128 s (256 s) respectively. The exposure times used for each class of source are listed in Table 7.3.
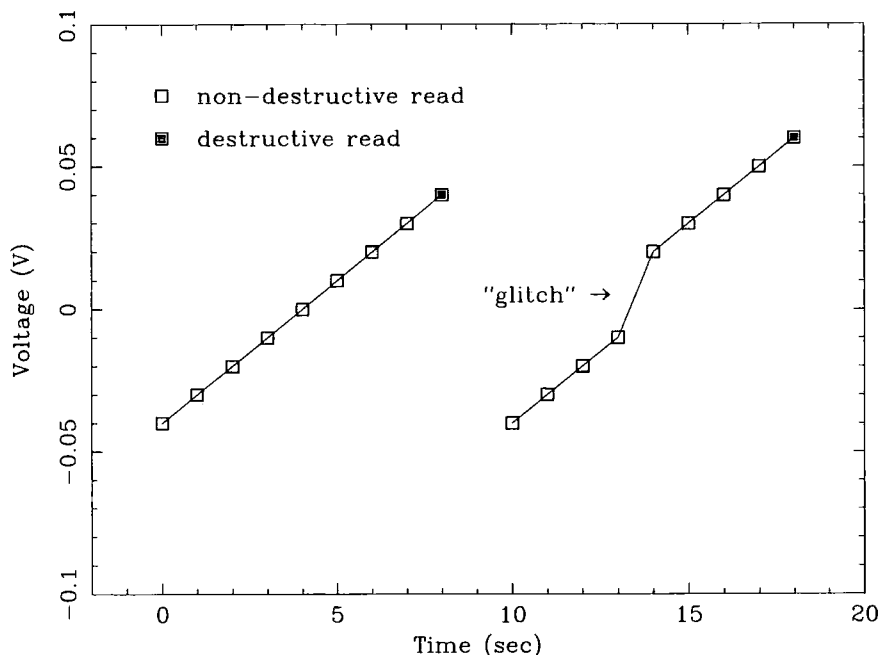
Figure 7.1: Cartoon showing the ramps created by the non-destructive readout technique. The first ramp shows the increase in voltage with time in a pixel, where the open squares denote non-destructive reads, and the filled square denotes a destructive read, at which point the voltage is reset to a base value. The second ramp shows the effect of a particle hit, or "glitch", in the detector. The slope of the ramp stays constant, with a discontinuity in voltage at the instant of the hit.

7.4 *ISO* Data Reduction

The raw *ISOPHOT* data were reduced using the dedicated reduction software package, PHT Interactive Analysis (PIA; Gabriel et al. 1997)[3]. The UK *ISO* Support Centre was consulted extensively for advice on the optimum methods for reducing faint source data. Following the standard reduction procedures in general, we customised the default parameters in order to maximise the detection efficiency for our particular data. The reduction steps used are as follows:

- Linearization: The response of the PHT detectors is slightly non-linear with the intensity of the incident flux, and internal calibration files are used to correct the ramps for this effect.

- Removal of the effects of cosmic particle hits: When the detector is hit by a cosmic ray, this causes a step between consecutive readouts in a ramp, known as a "glitch", which must be removed before calculating the signal. The effect of a glitch is shown in the second ramp in Fig. 7.1. As the duration of the event is usually short, the slope of the ramp afterwards is similar to the slope beforehand, and therefore it is not necessary to discard the entire ramp.

---

[3] PIA is a joint development by the ESA Astrophysics Division and the ISOPHOT Consortium.

Instead, a "single threshold ramp deglitching" procedure is applied to each ramp separately, to identify each glitch and collapse the data as if the glitch had not occurred. This process happens interactively, such that the parameters used can be tuned to suit each application. In our case, we tested both the default threshold value of 4.5σ, and also the more stringent level of 2.0σ as advised for very faint sources by the *ISO* support team. It was found that the 2.0σ method gave more reliable results, and therefore it is this set of measurements which is presented here.

- Determination of the signal-per-ramp: The output of the detectors is shown as the voltage as a function of time, with the slope of the ramp being steeper for higher signals. Therefore each ramp is fitted with a first order polynomial, ignoring the first and last few readouts as these may be affected by electronic effects, and this gives the signal in units of volts per second, as a function of time throughout the duration of the exposure.

- Reset interval correction: The output signal is dependent slightly on the reset interval, which is the ramp integration time, and therefore a correction for this effect must be applied.

- Secondary deglitching: Some cosmic particle events temporarily increase the sensitivity of the detector, thereby affecting the signal. These hits are removed on a statistical basis by PIA.

- Drift handling: The detectors show transient drifts in signal, due to changes in the dark current, etc., during different parts of the orbit. The PIA stability recognition procedure is used, which corrects for large scale variations only.

- Determination of the signal-per-chopper-plateau: The average signal for each section of the observation is then calculated, for each off- and on-source chopper positions. The signal is measured in Volts per second, and plotted as a function of time.

- Vignetting correction: For large chopper throws, such as that used here ($180''$), the detectors are partly vignetted by the telescope. The vignetting effects are different for the on- and off-source positions, and are more significant for the C200 detector which is physically larger than the C100 detector. Internal calibration files are used to calculate and correct for the flux lost by this effect.

- Power calibration: The signal ($V\,s^{-1}$) for each chopper position, both off- and on-source, is now converted to in-band power (W), taking account of the variation of the detector responsivity during an orbit. There are two faint calibration sources (FCS) present, and measurements of these are taken after each observation. Unlike the rectangular chopping method used here, the

majority of observations, *i.e.*, those performed in either staring or raster scan mode, use only one FCS. Therefore until recently, there has only been sufficient data to fully calibrate this first FSC. Only after the end of the *ISO* mission was enough data available to start fully calibrating the second FCS, and this will not be completed by the Mission Support Team until mid-1999. In the chopping mode used here, both FCSs are used, therefore in the meantime, we have used the default detector responsivities contained in internal calibration files in order to calculate the in-band power.

- Background subtraction: In chopped measurements, internal background subtraction is used, in which the off-source measurement is subtracted from the on-source measurement. The off-source position is observed first and the on-source position second, in all of our observations. The background also includes the dark current, which is why we did not perform a dark subtraction procedure earlier on, as this would have increased the errors.

- Extract flux density: The nine(four) pixels of the C100(C200) detector are combined into one measurement, correcting for flux lost between pixels and the point spread function. Error calculations include these adjustments, but purely reflect the errors on the combination of the measurements and do not include systematics. However, as a check, we use a method suggested by the UK *ISO* Support Centre, in which the variation in the flux measurements for each ramp can be used to provide an independent estimate of the errors involved in the final quoted flux. Q_1 and Q_3, the first and third quartiles on the measured flux in a pixel over all the ramps, can be used to give very conservative error estimates:

$$e = \sqrt{\sum_{i=1}^{n} \left(\frac{Q_3 - Q_1}{2} \right)_i^2} \tag{7.2}$$

where i counts over the number of pixels, n. The errors estimated in this way are of the order of, or smaller than, the PIA error from combining all the measurements, and we therefore adopt the PIA errors in determining the significance of our detections.

- Once the measurements for each source at each wavelength have been reduced, the output can be plotted. It is possible at this stage to adjust the fluxes using a colour correction to account for the spectral shape of the source. This can be done either by assuming a black body spectrum at a certain temperature, or a power-law spectrum, but our sources are too faint for this step to be warranted.

7.5 Results

We present the results of the *ISOPHOT* observations in Tables 7.4 and 7.5 for the samples of X-ray galaxies and QSOs respectively. The detection significances for the combined sample are summarised in Table 7.6.

7.5.1 The X-ray luminous galaxies

Of the nineteen X-ray luminous galaxies in our sample, six were detected with a significance of greater than 2.5σ in one or more wavebands, using the conservative PIA errors. The cluster of galaxies was not detected. It is interesting to note that all six galaxies detected were narrow emission-line galaxies. In addition, for the detected sources, very hard spectra can be inferred from the hardness ratios, albeit with very large errors. These also tend to be the brightest sources, suggesting a possible correlation with the hard X-ray flux. We therefore discuss each of these sources in turn.

GSGP4X:091 is detected by *ISOPHOT* with a significance of 2.9σ at 200μm[4], with a flux density of 0.160 ± 0.056 Jy. The originally proposed optical counterpart to the X-ray source is a narrow emission-line galaxy at $z = 0.416$, but as discussed in Chapter 5, an alternative candidate has been found from the $K-$band image of the field, which has $K = 16.1$ and is very red, $B - K \sim 6.3$. This may be a more plausible counterpart, since the significant variability observed in the *ROSAT* light-curve implies a QSO origin for the X-ray emission, and therefore this source is thought to contain an obscured AGN (Almaini et al. 1999a).

Almaini et al. (1996) find that this galaxy has a very hard *ROSAT* spectrum, which can be fitted with a power-law of photon index $\Gamma = 0.14 \pm 0.30$. If the intrinsic spectrum of the galaxy is constrained to be that of a typical QSO, with $\Gamma = 2.2$, then they estimate that the flattening would arise from a column density of $N_H = 7.5 \pm 1.8 \times 10^{21}$ cm^{-2} at the redshift of the $z = 0.416$ galaxy. Without an estimate of the redshift of the red counterpart, no estimate can be obtained of the column required to produce the flat X-ray spectrum. The far infra-red emission detected here is likely to be associated with the material producing the absorption in the X-ray spectrum. Since we have a firm detection at 200μm, we also mention that there is a marginal detection at 60μm of 0.182 ± 0.089 Jy (2.0σ), and that the 100μm flux density is 0.112 ± 0.060 Jy (1.9σ).

---

[4]   The C100 and C200 filters have central wavelengths slightly offset from those used to name the filter. This effect is greatest for the 160μm filter, which has a central wavelength of 174μm, as shown in Table 7.1. These central wavelengths should be used when fitting spectra to the measured flux densities, etc, however for our purposes we quote the filter names only.

Object	ID	Redshift	$S_{0.5-2\,\mathrm{keV}}$ (erg cm^{-2} s^{-1})	HR	S_{60} (Jy)	σ	S_{100} (Jy)	σ	S_{200} (Jy)	σ
GSGP4X:091	NL	0.416	4.0×10^{-14}	0.28 ± 0.09	0.182 ± 0.089	2.0	0.112 ± 0.060	-	0.160 ± 0.056	2.9
GSGP4X:048	NL	0.155	2.7×10^{-14}	-0.05 ± 0.11	0.121 ± 0.084	-	-0.043 ± 0.063	-	-0.226 ± 0.073	-
F864X:012	NL	0.10	2.5×10^{-14}	-0.21 ± 0.13	-0.084 ± 0.220	-	-0.022 ± 0.150	-	-0.007 ± 0.130	-
GSGP4X:032	Cl	0.561	2.5×10^{-14}	-0.15 ± 0.09	0.096 ± 0.100	-	-0.069 ± 0.061	-	-0.460 ± 0.097	-
GSGP4X:069	NL	0.213	1.3×10^{-14}	-0.08 ± 0.17	0.114 ± 0.110	-	0.223 ± 0.083	2.7	0.249 ± 0.091	2.7
GSGP4X:064	Gal	0.097	1.2×10^{-14}	-0.40 ± 0.21	-0.036 ± 0.099	-	0.090 ± 0.071	-	0.151 ± 0.120	-
GSGP4X:114	NL	0.211	8.6×10^{-15}	0.25 ± 0.25	-0.030 ± 0.066	-	-0.024 ± 0.067	-	-0.508 ± 0.110	-
F864X:052	NL	0.103	8.2×10^{-15}	0.52 ± 0.31	-0.189 ± 0.073	-	0.188 ± 0.066	2.8	-0.121 ± 0.100	-
GSGP4X:094	NL	0.120	7.7×10^{-15}	-0.32 ± 0.23	-0.145 ± 0.110	-	-0.013 ± 0.070	-	-0.076 ± 0.140	-
F864X:039	Gal	0.126	6.6×10^{-15}	-0.71 ± 0.32	-0.404 ± 0.140	-	-0.137 ± 0.066	-	-0.083 ± 0.043	-
F864X:078	Gal	0.15	6.5×10^{-15}	-0.35 ± 0.29	-0.173 ± 0.086	-	0.079 ± 0.085	-	-0.070 ± 0.083	-
F864X:054	NL	0.089	5.6×10^{-15}	-0.32 ± 0.31	-0.269 ± 0.110	-	-0.061 ± 0.077	-	-0.045 ± 0.063	-
GSGP4X:109	NL	0.098	5.3×10^{-15}	0.29 ± 0.34	-0.162 ± 0.120	-	0.277 ± 0.061	4.5	0.096 ± 0.051	-
GSGP4X:086	Gal	0.161	5.3×10^{-15}	-0.02 ± 0.33	-0.053 ± 0.110	-	-0.015 ± 0.079	-	-0.092 ± 0.054	-
F864X:051	NL	0.25	5.0×10^{-15}	0.45 ± 0.33	-0.061 ± 0.190	-	0.287 ± 0.170	-	-0.089 ± 0.230	-
GSGP4X:020	Gal	0.382	4.8×10^{-15}	-0.42 ± 0.34	0.025 ± 0.078	-	-0.175 ± 0.068	-	-0.460 ± 0.097	-
GSGP4X:082	NL	0.204	4.1×10^{-15}	0.34 ± 0.45	-0.064 ± 0.110	-	-0.043 ± 0.064	-	0.212 ± 0.081	2.6
GSGP4X:054	NL	0.21	2.9×10^{-15}	-0.29 ± 0.47	-0.125 ± 0.077	-	-0.031 ± 0.058	-	-0.192 ± 0.100	-
GSGP4X:057	NL	0.161	2.1×10^{-15}	0.33 ± 0.63	0.010 ± 0.091	-	0.011 ± 0.064	-	0.274 ± 0.093	2.9
F864X:129	Gal	0.328	^{a}		0.191 ± 0.300	-	0.394 ± 0.210	-	0.000 ± 0.100	-

^{a}F864X:129 lies outside of the 20′ radius central region of the ROSAT field, and we therefore do not have an accurate flux or hardness ratio available for this source.

Table 7.4. The results of the ISOPHOT photometry of our sample of nineteen X-ray luminous ROSAT galaxies and one cluster. The source identifications and redshifts, plus the ROSAT 0.5 2 keV fluxes and hardness ratios are listed, plus the ISOPHOT flux densities, measured in the 60, 100 and 200μm filters.

Object	ID	Redshift	$S_{0.5-2\,keV}$ (erg cm^{-2} s^{-1})	HR	S_{60} (Jy)	σ	S_{100} (Jy)	σ	S_{200} (Jy)	σ
GSGP4X:017	QSO	1.010	3.7×10^{-14}	-0.16 ± 0.01	-0.104 ± 0.086	-	0.175 ± 0.062	2.8	0.054 ± 0.082	-
GSGP4X:056	QSO	1.209	3.4×10^{-14}	-0.01 ± 0.09	0.233 ± 0.250	-	0.143 ± 0.170	-		
F864X:086	NLQSO	2.35	3.3×10^{-14}	0.11 ± 0.11	-0.195 ± 0.085	-	0.022 ± 0.059	-	0.191 ± 0.120	-
"	"	"	"	"	S_{160}:		0.155 ± 0.064	2.4		
F864X:066	QSO	1.89	1.2×10^{-14}	-0.07 ± 0.19			-0.051 ± 0.052	-	0.064 ± 0.093	-
GSGP4X:101	QSO	2.485	1.2×10^{-14}	-0.12 ± 0.19			0.009 ± 0.065	-	0.034 ± 0.150	-
F864X:077	QSO	1.97	8.9×10^{-15}	0.03 ± 0.22	-0.275 ± 0.092	-	-0.046 ± 0.056	-	-0.078 ± 0.100	-
F864X:065	QSO	1.96	4.2×10^{-15}	-0.18 ± 0.40			-0.086 ± 0.053	-	-0.199 ± 0.067	-

Table 7.5. The results of the *ISOPHOT* photometry of our sample of *ROSAT* QSOs: four high redshift QSOs ($z \sim 2$), two low redshift QSOs ($z \sim 1$), and a high redshift Type 2 QSO. The source identifications and redshifts, plus the *ROSAT* 0.5 2 keV fluxes and hardness ratios are listed, plus the *ISOPHOT* flux densities, measured in the 60, 100 and 200μm filters. In addition, the 160μm flux density is presented for the Type 2 QSO, F864X:086.

Object	ID	Redshift	Detection significance			
			60μm	100μm	160μm	200μm
GSGP4X:091	NL	0.416	2.0	-		2.9
GSGP4X:017	QSO	1.010	-	2.8		-
GSGP4X:056	QSO	1.209	-	-		
F864X:086	NLQSO	2.35	-	-	2.4	-
GSGP4X:048	NL	0.155	-	-		-
F864X:012	NL	0.10	-	-		-
GSGP4X:032	Cl	0.561	-	-		-
GSGP4X:069	NL	0.213	-	2.7		2.7
GSGP4X:064	Gal	0.097	-	-		-
F864X:066	QSO	1.89		-		-
GSGP4X:101	QSO	2.485		-		-
F864X:077	QSO	1.97	-	-		-
GSGP4X:114	NL	0.211	-	-		-
F864X:052	NL	0.103	-	2.8		-
GSGP4X:094	NL	0.120	-	-		-
F864X:039	Gal	0.126	-	-		-
F864X:078	Gal	0.15	-	-		-
F864X:054	NL	0.089	-	-		-
GSGP4X:109	NL	0.098	-	4.5		-
GSGP4X:086	Gal	0.161	-	-		-
F864X:051	NL	0.25	-	-		-
GSGP4X:020	Gal	0.382	-	-		-
F864X:065	QSO	1.96		-		-
GSGP4X:082	NL	0.204	-	-		2.6
GSGP4X:054	NL	0.21	-	-		-
GSGP4X:057	NL	0.161	-	-		2.9
F864X:129	Gal	0.328	-	-		-

Table 7.6. Summary of the detections obtained with *ISOPHOT*, where the sources are listed in order of decreasing *ROSAT* flux. The detection significances are obtained using the 2.0σ glitch rejection threshold. A dash indicates those sources for which the detection is < 2σ, and any filters for which data were not taken are left blank.

GSGP4X:069 is the only source to be detected in both the 100 and 200μm bands, at a 2.7σ level in both cases. The observed flux densities are 0.223 ± 0.083 Jy and 0.249 ± 0.091 Jy respectively. CGS4 spectroscopy of this object was unable to clearly detect the presence of broad Pa$_\alpha$ emission, although there is evidence for excess emission in the region of the spectrum where we would expect to see this line. As with GSGP4X:091, Almaini et al. (1996) find that this galaxy has a very
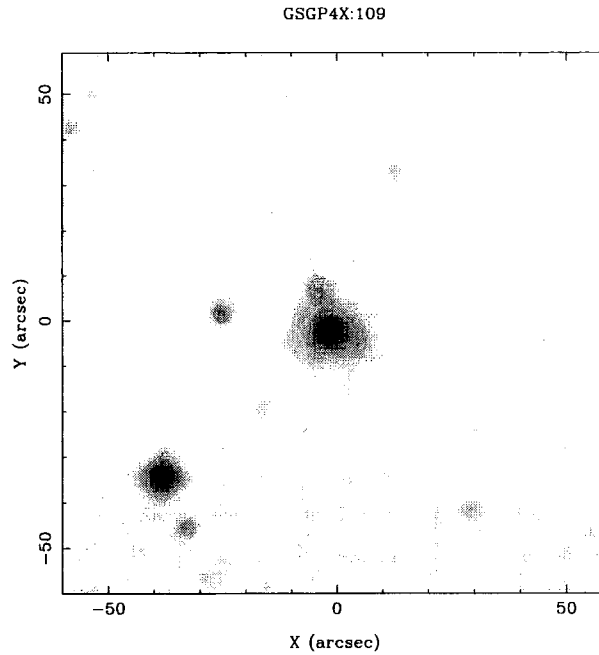
GSGP4X:109

Figure 7.2: B–band image of GSGP4X:109, taken from the Digitized Sky Survey. This is a bright, $B = 13.9$ mag narrow emission-line galaxy at $z = 0.098$. The image shows a companion galaxy and some evidence for potential interaction or merger activity.

hard spectrum, with $\Gamma = 0.79 \pm 0.51$, or a column density of $N_H = 2.7 \pm 1.9 \times 10^{21}\,\mathrm{cm}^{-2}$ intrinsic to the galaxy, for a $\Gamma = 2.2$ spectrum. Again, we propose that we are detecting far infrared emission associated with the obscuring medium.

F864X:052 is a narrow emission-line galaxy at $z = 0.103$, for which the observed 100μm flux density is $0.188 \pm 0.066\,\mathrm{Jy}$, which is a 2.8σ detection. The ROSAT spectrum is very hard, with $HR = 0.52 \pm 0.31$, and this is the second brightest narrow-line galaxy observed on the F864 field. As described in Section 6.7, this galaxy is known to contain an obscured AGN, from the [Si VI] coronal line detected in the K–band spectrum (Almaini et al. 1998).

GSGP4X:109 was the most significant of the six detections, with a 100μm flux density of $0.277 \pm 0.061\,\mathrm{Jy}$ (4.5σ). It is also at the lowest redshift, $z = 0.098$, and is optically bright, classified as an Sb galaxy with $B = 16.9$ mag. A B–band image from the Digitized Sky Survey is shown in Fig. 7.2, which shows the presence of a companion or interacting galaxy. Section 6.5 describes the CGS4/UKIRT spectroscopic observations of GSGP4X:109, where the tentative detection of a broad component to the Pa_α emission line is discussed. This combined with the very hard ROSAT spectrum, $HR = 0.29 \pm 0.34$, is convincing evidence for the presence of AGN activity in this galaxy. It will be interesting to obtain a higher resolution optical image of this galaxy to search for a point-like nucleus.

GSGP4X:082 is detected at 2.6σ with a 200μm flux density of 0.212 $\pm$ 0.081 Jy, and has a hardness ratio of 0.34 $\pm$ 0.45. **GSGP4X:057** has a measured 200μm flux density of 0.274 $\pm$ 0.093 Jy (2.9σ), and again, possibly has a hard spectrum, with $HR = 0.33 \pm 0.63$. At present, we do not have any further evidence to support the hypothesis of AGN activity in these two galaxies.

7.5.2 The QSO sample

Of the six QSOs originally targeted by *ISOPHOT*, it is interesting to note that the only one to be detected in any of the wavebands is the Type 2 obscured QSO, F864X:086. This has a 160μm flux density of 0.155 $\pm$ 0.064 Jy, which is a marginal 2.4σ detection. We may be picking up the redshifted peak of the black-body emission from warm dust at $\sim$ 70 K. In addition, we were able to detect the source GSGP4X:017 at 2.8σ significance, with a 100μm flux density of 0.175 $\pm$ 0.062 Jy. This source is a QSO at redshift $z = 1.010$, that was classified initially as an absorption-line galaxy at $z = 0.105$, and was therefore in our sample of X-ray galaxies. It is also the second brightest X-ray source observed here. This erroneous classification meant that GSGP4X:017 was observed for 64 s in both the 60 and 100μm filters, rather than the 32 s used for the known $z \sim 1$ QSO in the sample. This increased exposure time may well have helped us to obtain this detection. The upper limits on the flux from the other broad-line QSOs obtained from these data is not sufficiently different from the detection of the obscured QSO, and therefore we cannot make any differentiation between the amounts of dust present in Type 1 and 2 QSOs. If future observations detect more unobscured QSOs like GSGP4X:017, then this supports the picture in which broad-line QSOs have similar properties to Type 2 objects at long wavelengths, , whereas their optical properties depend crucially on the viewing angle to the nucleus, as expected from the Unified Model of AGN (Antonucci 1993). If however, the *ISO* detection of GSGP4X:017 is contaminated by the presence of nearby emission-line galaxies, and the QSO has little intrinsic FIR emission, then a model in which any obscuring medium is isotropic is favoured. Forthcoming observations with SCUBA on the JCMT of both the Type 2 QSO and broad-line QSOs can be combined with these detections and upper limits in order to provide better constraints on their far infra-red properties.

7.6 Discussion

The *ISOPHOT* detections presented here are of modest significance, and therefore must be treated with care. Ideally, we would have liked to use these data to investigate thoroughly the relationship between X-ray and far infra-red luminosity, for our samples of faint X-ray selected galaxies and

QSOs. However, due to the lower sensitivity of *ISO* compared with that predicted before the launch, any sources detected are at a much lower significance than anticipated for the exposure times used. If we were to place upper limits on the FIR fluxes from sources which we do not detect, then using 3σ in our estimates would give upper limits of the same order as our detections. However, it is encouraging that the galaxies and QSOs that we do detect are consistent with the fluxes predicted, of $S_{60} \sim 0.5 \pm 0.5$ Jy, implying that the relationship seen at brighter X-ray and FIR fluxes is also likely to hold for fainter samples. Elvis et al. (1994), find that radio-quiet QSOs, with $V < 17$ and $z \sim 0.5$, have an average *IRAS* flux of ~ 1 Jy at 100μm, and we can therefore infer from the fainter optical magnitudes and higher redshifts of our targets that the expected flux will be lower than this. It is not possible to make any inferences about the temperature of the dust in these objects, but in the future it may be possible to combine these tentative detections and upper limits with sub-mm data to look at the spectral energy distributions of faint X-ray galaxies and QSOs.

Nevertheless, although we must be cautious with these data, it is still possible to use these detections in our investigation of the obscured AGN hypothesis. We have seen that for at least four of the X-ray galaxies detected by *ISO*, there is additional evidence for AGN activity and obscuration, which can be reinforced if the FIR flux is interpreted as thermal emission from the obscuring medium. Two of the brightest galaxies, GSGP4X:069 and GSGP4X:091, have X-ray spectra consistent with the presence of intrinsic obscuring material with columns of a few $\times 10^{21}$ cm^{-2}. The analysis of X-ray variability is only possible for the brighter galaxies in this sample at present, with significant variability detected in GSGP4X:091 (Almaini et al. 1999a). Near infra-red spectroscopy of GSGP4X:109 showed some evidence for the presence of broad Pa$_\alpha$ emission, and detected [Si VI] emission in F864X:052, both properties being consistent with an AGN origin for the observed X-ray emission.

7.7 Future prospects

Future observations with *AXAF* and *XMM*, with their vastly superior capabilities, will be able to resolve many current dilemmas. In particular, the spatial resolution of *AXAF* will be able to show without doubt whether these optical galaxies are the true counterparts of the X-ray emission, which is often still the subject of much debate. *XMM* will have sufficient photon collecting area not only to produce high quality X-ray spectra, but will also be able to provide light-curves of these faint galaxies. This will allow the X-ray emission mechanism to be determined with a high degree of accuracy, whether it be due to AGN activity, starbursts, or a mixture of the two.

Proposed satellite-borne far infra-red telescopes, *SIRTF* and *FIRST*, described in more detail in Section 4.6, will revolutionise our knowledge of the FIR properties of galaxies and QSOs. Combining the information to be gained from these facilities with the advances in X-ray satellite technology on similar time-scales, will determine the relative contributions from AGN and star-formation activity in samples of objects selected in both regimes. Complementary observational programs such as these are vital, due to the interconnected nature of the source populations contributing to the source counts and background intensities at both X-ray and FIR energies.

7.8 Conclusions

Our results can be summarised as follows:

- The galaxies detected here by *ISO* can all be characterised as having narrow emission-line optical spectra.

- The sources detected tend to have the highest *ROSAT* fluxes, including two of the three brightest narrow-line galaxies in the GSGP4 field, and one out of the two brightest in F864.

- The galaxies detected also tend to have the hardest X-ray spectra. From this, we can infer a possible correlation between the FIR and hard X-ray flux, which we would like to test in the future with higher sensitivity and larger samples of objects.

- Both an unobscured QSO and an obscured QSO are detected, which is not inconsistent with the Unified Model of AGN, although an isotropic covering medium cannot be ruled out.

- The objects detected here by *ISO* often have supporting evidence from observations at other wavebands to support the existence of obscured AGN activity. For example, we have detected the known high redshift Type 2 QSO; the variable, hard spectrum *ROSAT* source, GSGP4X:091; the nearby galaxy GSGP4X:109, which has a possible broad component to the Pa_α emission line; and F864X:052, which is known to host an obscured AGN due to the presence of the [Si VI] coronal line in its $K-$band spectrum.

We therefore conclude that these observations support the hypothesis that the X-ray emission in a significant fraction of the faint galaxies detected in deep *ROSAT* surveys, is due to the presence of AGN activity, in many cases obscured by large quantities of dust.

References

Almaini O., Lawrence A., Shanks T., Edge A., 1999a, MNRAS submitted.

Almaini O., Shanks T., Boyle B. J., Griffiths R. E., Roche N., Stewart G. C., Georgantopoulos I., 1996, MNRAS, 282, 295

Almaini O., Shanks T., Gunn K. F., Boyle B. J., Georgantopoulos I., Griffiths R. E., Stewart G. C., Blair A. J., 1998, Astronomische Nachrichten, 319, 55

Antonucci R., 1993, ARA&A, 31, 473

David L. P., Jones C., Forman W., 1992, ApJ, 388, 82

Elvis M. et al., 1994, ApJS, 95, 1

Gabriel C., Acosta-Pulido J., Heinrichsen I., Morris H., Tai W. M., 1997, in Hunt G., Payne H.E., eds, *Proc. of the ADASS VI Conference*: ASP Conf. Series 125: San Francisco, Vol. 6, p. 108

Griffiths R. E., Padovani P., 1990, ApJ, 360, 483

Kessler M. F. et al., 1996, A&A, 315, L27

Laureijs R. J., Klaas U., Lemke D., Herbstmeier U., Abraham P., 1996, Addendum to *ISOPHOT* Observer's Manual. *ISOPHOT* Consortium

Lemke D. et al., 1996, A&A, 315, L64

Chapter 8

A *BeppoSAX* Observation

of a Deep *ROSAT* Survey Field

ABSTRACT. Here, we present the preliminary results from a new 100 ks *BeppoSAX* hard X-ray observation of one of the fields from the Deep *ROSAT* Survey, BJS864. *BeppoSAX* has hard X-ray sensitivity comparable to *ASCA* and a field of view similar to *ROSAT*. *BeppoSAX* observations therefore provide a new route to test the hypothesis of an obscured QSO origin for the hard X-ray background.

8.1 *BeppoSAX* observations of BJS864

The X-ray satellite *BeppoSAX*[1] (Boella et al. 1997), launched on April 30 1996, is a joint project for the Italian Space Agency, the Netherlands Agency for Aerospace Programs, and the Space Science Department of ESA. *BeppoSAX* has a wide spectral coverage of $0.1 - 200$ keV, with imaging capabilities below 10 keV. The instrumentation on board *BeppoSAX* includes four different types of Narrow Field Instruments (NFI). Firstly, there are three *Medium Energy Concentrator Spectrometers* (*MECS*), which are position sensitive, gas scintillation proportional counters, which detect X-rays in the energy band $1.3 - 10$ keV. The *Low Energy Concentrator Spectrometer* (*LECS*), is identical to the *MECS*, but with a thin window, enabling soft < 1 keV photons to penetrate to the detector, and giving an energy range of $0.1 - 10$ keV. However, the thin window means that the camera can only be operated at certain sun angles, to avoid being dominated by solar emission, thereby drastically reducing the available exposure time with respect to the *MECS*. In addition, the *MECS* 1 detector failed shortly after launch, meaning that all subsequent observations were performed with just the *MECS* 2 and *MECS* 3 detectors. This has resulted in the availability of only two-thirds the collecting area originally envisaged, with the consequent

---

[1] *BeppoSAX*: *Satellite per Astronomia X "Beppo"*, named in honour of Giuseppe "Beppo" Occhialini.

Satellite	Instrument	Exp. Time	Date
ROSAT	*PSPC*	52466 s	1/93
ASCA	*GIS*	89426 s	1/98
BeppoSAX	*LECS*	29333 s	1/98
BeppoSAX	*MECS*	82825 s	1/98

Table 8.1. Summary of the exposure times and dates of the *ROSAT, ASCA* and *BeppoSAX* X-ray observations of the field BJS864. The co-ordinates of the field centre are 13 43 43.0 -00 15 00 (J2000) in each case, and the Galactic column density in the direction of this pointing is $N_H = 2.6 \times 10^{19}$ cm^{-2}.

reduction in sensitivity. The two other NFI instruments are both collimated detectors: the *High Pressure Gas Scintillation Proportional Counter* (*HPGSPC*), which has high spectral resolution, but rather poor sensitivity in the $4 - 120$ keV range, and the *Phoswich Detector System* (*PDS*), which has much higher sensitivity over the $15 - 300$ keV bandpass.

8.2 The Data

The Deep *ROSAT* Survey Collaboration was awarded an 100 ks *BeppoSAX* observation of the survey field BJS864, using the NFI instruments *LECS* and *MECS*. The *BeppoSAX* observation was performed between 1998 January 15–17, having been delayed from the previous year due to technical problems with the attitude control of the satellite. At the time of the proposal, the existing data for the field included *ROSAT* soft X-ray data, and large quantities of optical imaging and spectroscopic data for source identification requirements. The *ASCA* observation was performed subsequently, and we therefore use this image for comparison with the *BeppoSAX* results only. The X-ray data now available for this field are summarised in Table 8.1.

8.3 Preliminary Results

Here we use the SAX Data Analysis System (SAXDAS) linearized and cleaned event files (Rev.1.1) produced at the *BeppoSAX* Science Data Center, which results in total exposure times of $82,825$ s and $29,333$ s for the *MECS* and *LECS* images (Figs 8.1 and 8.2) respectively. These can be compared with the *ROSAT* $0.5 - 2$ keV (Fig. 8.3) and *ASCA* $2 - 10$ keV (Fig. 8.4) images of the same field.

The exposure time for the *LECS* observation was shorter than the *MECS* exposure due to the sun-angle constraints described earlier. The total number of photons detected is therefore extremely small, and in order to make out any sources at all, considerable rebinning and smoothing of the
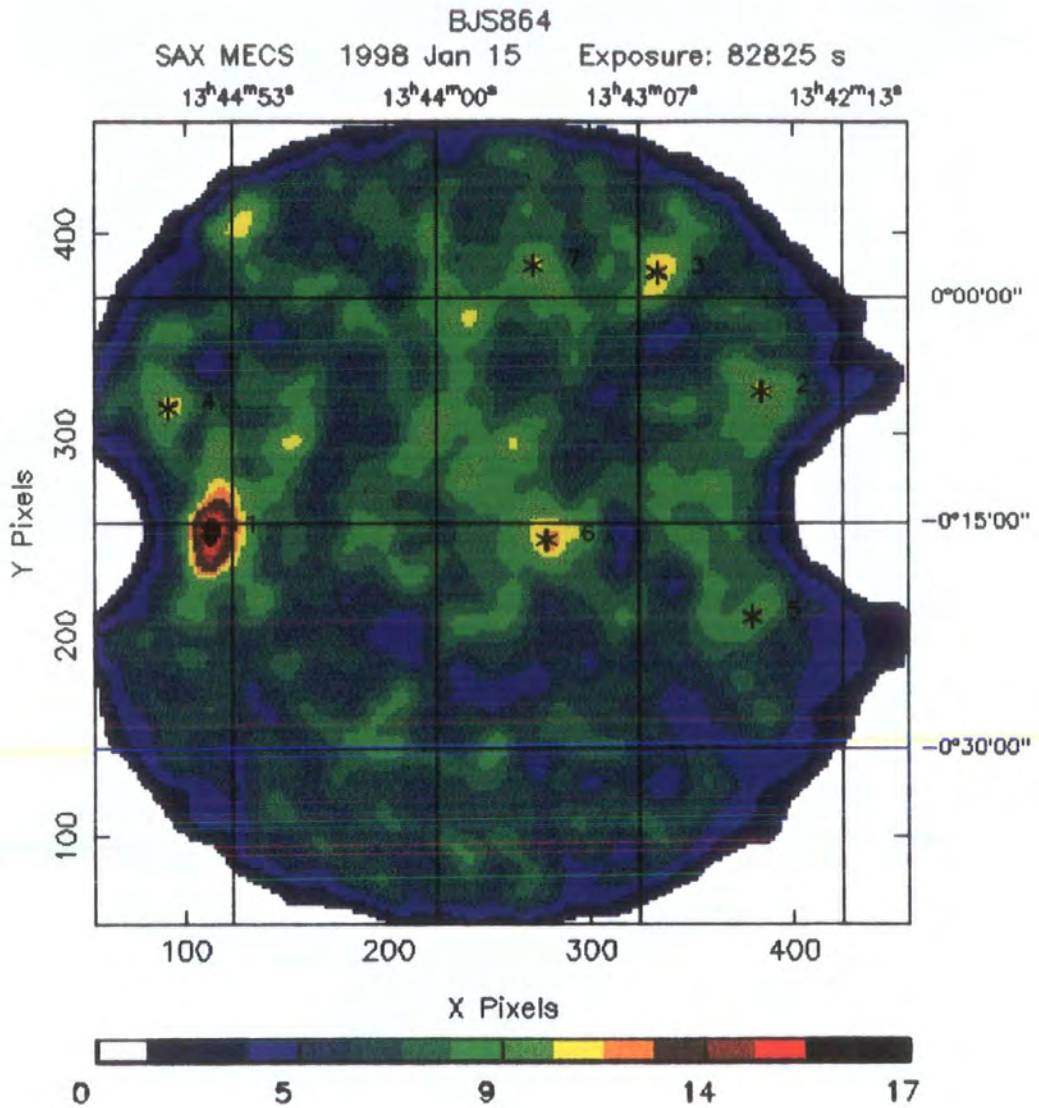
Figure 8.1: The *BeppoSAX* mosaiced image from the *MECS* 2 and *MECS* 3 detectors, with the six sources detected marked with crosses, and numbered 1–6. In addition, we have also marked the source closest to the position of the Type 2 QSO RXJ 1343.4+0001, which is numbered 7.
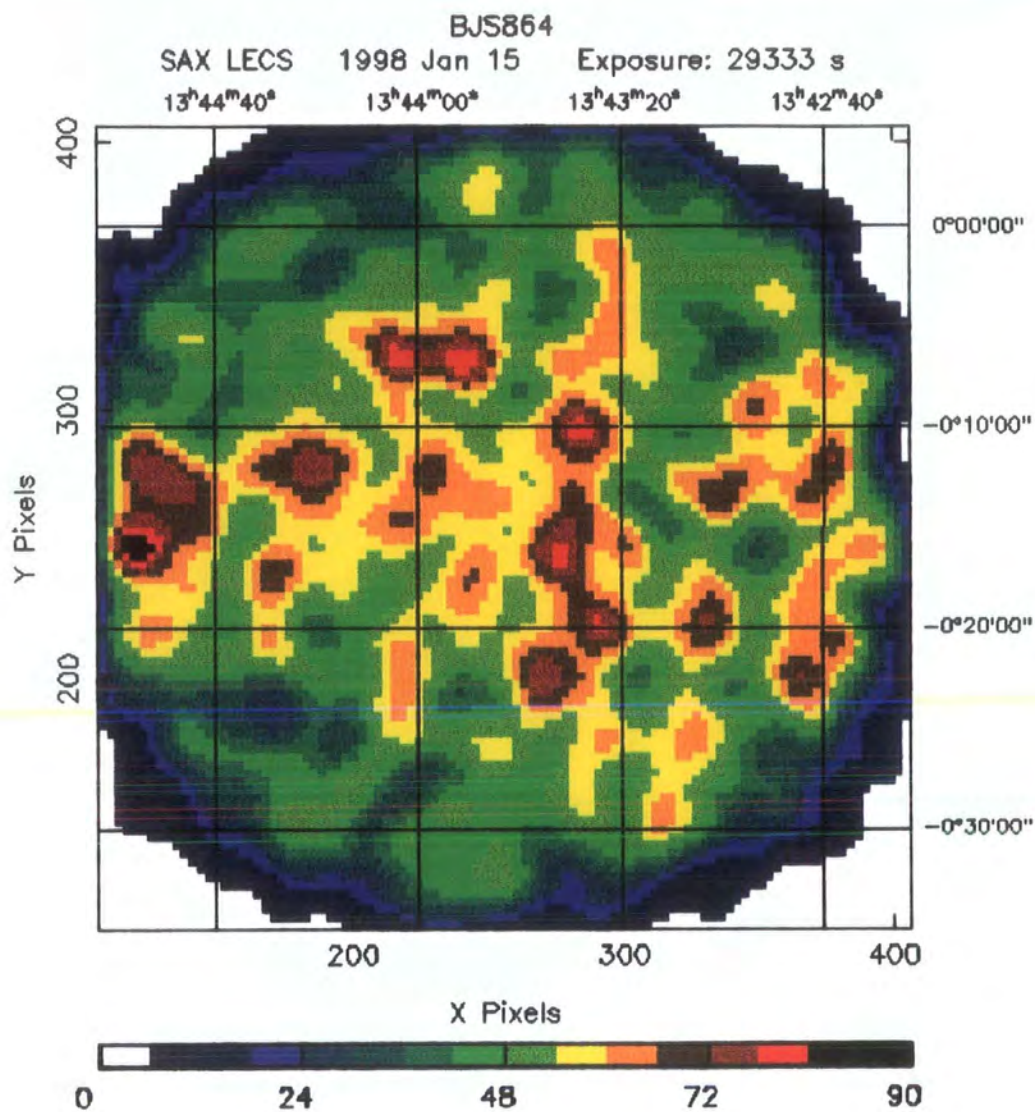
Figure 8.2: The *BeppoSAX* image from the *LECS* detector.
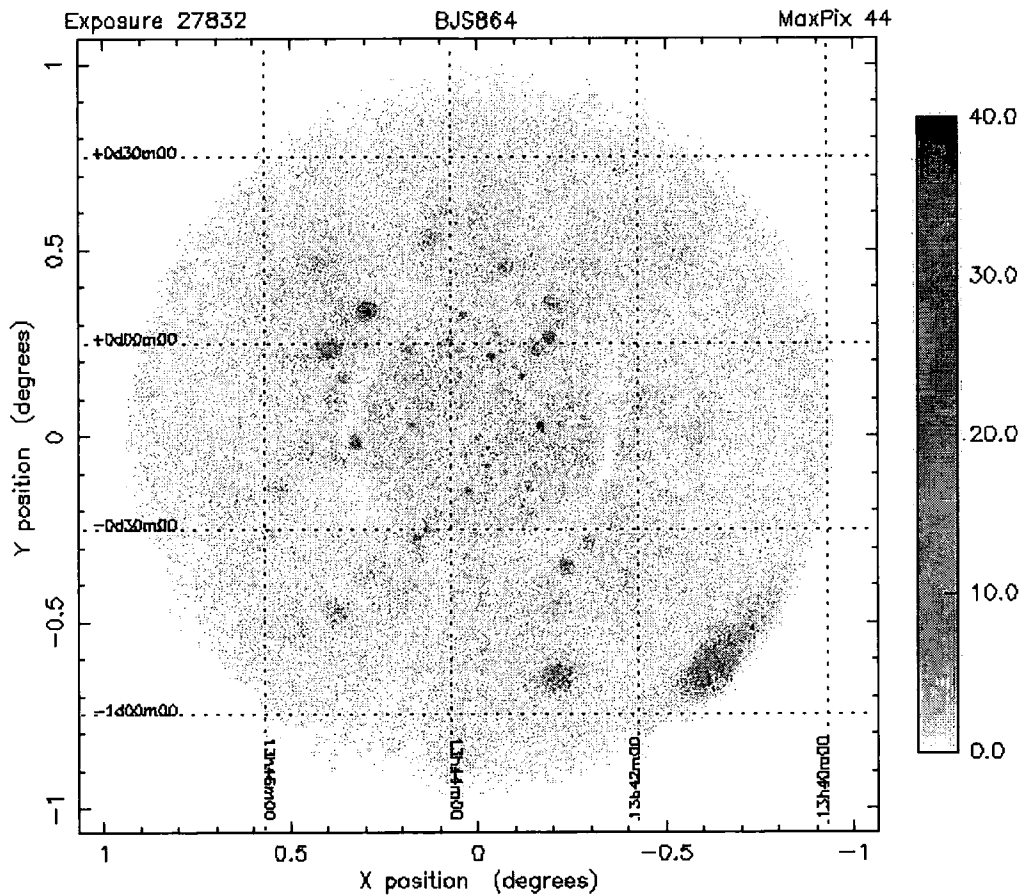
Figure 8.3: *ROSAT* PSPC image of the field BJS864 in the broad band 0.1 − 2.4 keV. The whole field is approximately 2° across, and the shadow cast by the central support structure can be seen. In the Deep *ROSAT* Survey, sources were extracted from the central 20′ radius, which is where the point-spread function is optimised, and is unaffected by shadowing by the central support.

Figure 8.4: *ASCA GIS* 2 and *GIS* 3 mosaic of the field BJS864, in the energy range $2-10\,\mathrm{keV}$. Five sources are marked, and numbered 1–5: these are referred to in the text as $A1-A5$ to distinguish them from the *BeppoSAX* sources.

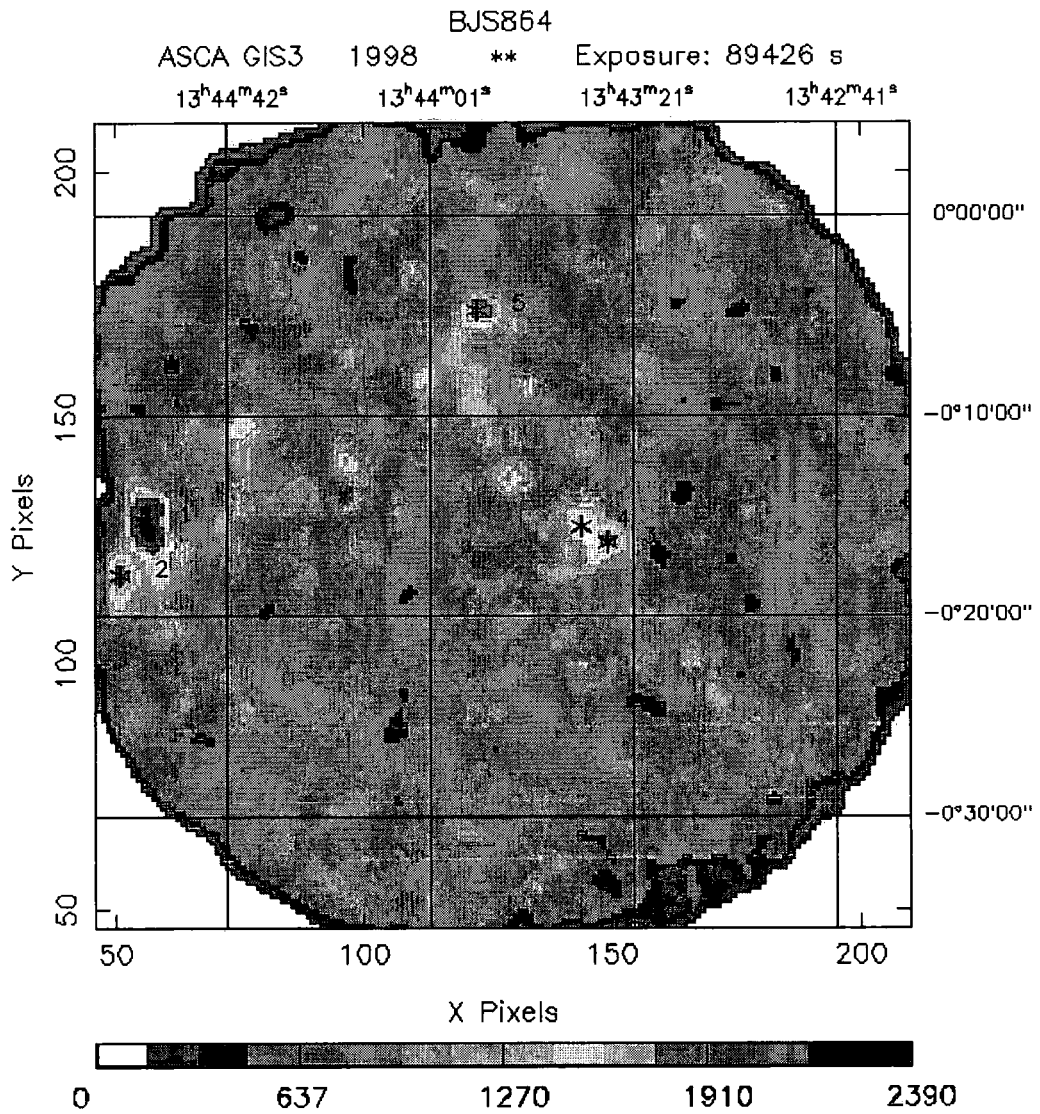| Source	Count rate 10^{-3}ct s^{-1}	Position x	y	Vignetting Correction	Position α (J2000) δ	Error box (arcsec)	S/N
SAX864:01	8.72 ± 0.91	117.1	237.9	2.80	13 44 57.3 -00 17 24.6	184	9.56
SAX864:02	5.31 ± 0.73	369.4	311.5	2.52	13 42 42.7 -00 07 36.2	184	7.26
SAX864:03	5.85 ± 0.91	332.5	384.3	3.00	13 43 02.4 +00 02 06.1	200	6.43
SAX864:04	4.05 ± 0.99	92.0	320.3	3.63	13 45 10.6 -00 06 25.7	184	4.07
SAX864:05	3.18 ± 0.71	381.6	218.6	2.61	13 42 36.2 -00 19 59.1	184	4.51
SAX864:06	1.25 ± 0.34	280.9	252.7	1.10	13 43 29.9 -00 15 26.1	200	3.62

Table 8.2. Sources detected above 3σ significance in the *MECS* image of the field BJS864, using the pipeline reduction procedure on SAXDAS linearized and cleaned event files (Rev.1.1) produced at the BeppoSAX Science Data Center. The count rate for each source is listed, together with the (x, y) pixel co-ordinates, the vignetting correction applied, and the signal-to-noise ratio. The (x, y) position has been converted into J2000 (α, δ).

image are required. This results in the loss of positional accuracy, to the extent that no correspondence can be found with known *ROSAT* sources. We therefore do not try to identify sources in this image here, but will use the data in the future in order to look at the spectra of the sources detected in the *MECS* image.

The sources extracted from the *MECS* data using the pipeline reduction facility are presented in Table 8.2, together with photon count rates and positions. We then compared the positions of these six sources with the *ROSAT* source catalogue for this field (Shanks et al. in preparation). For five of the six sources, we found associated *ROSAT* sources within 140 arcseconds of the *BeppoSAX* centroid, but in each case the offset was quite large. When we recalculated the position of each centroid, but still using only positional information from the headers, and no additional rotations or translations to the images, we found that our positions were significantly different to those obtained by the pipeline procedure. These measured differences ranged between $25''$ and $150''$, which is consistent with the point-spread function of the *MECS* detectors combined with the telescope optics, which has an 50 per cent encircled energy radius of $\sim 90''$ at 3 keV.

For the four sources for which the *BeppoSAX–ROSAT* offset were smallest, these offsets decreased for the new positions. For the fifth source, for which the initial association with a *ROSAT* source was most tenuous, the *BeppoSAX–ROSAT* offset increased, and this may well be a coincidental association.

We therefore present a revised *MECS* source list in Table 8.3, in which we give the new determination of the position for each *BeppoSAX* source, and the position of the corresponding

Source	BeppoSAX position α (J2000) δ	Optical position α (J2000) δ	d_{ox} ($''$)	ID	B (mag)	z
SAX864:01	13 44 58.7 -00 15 24.2	13 44 59.4 -00 16 00.4	38	QSO	17.8	0.244
SAX864:02	13 42 34.2 -00 06 09.4	13 42 34.6 -00 06 38.9	30	QSO	22.7	2.10
SAX864:03	13 43 01.4 +00 01 45.1	13 42 56.5 +00 00 56.8	88	QSO	19.8	0.804
SAX864:04	13 45 09.9 -00 07 15.1	–	–			
SAX864:05	13 42 36.6 -00 21 07.3	13 42 35.8 -00 17 49.9	198	?		
SAX864:06	13 43 30.6 -00 16 00.8	13 43 25.8 -00 16 13.3	73	BALQSO	19.6	1.511
T2QSO	13 43 33.1 +00 01 52.4	13 43 29.2 +00 01 32.8	62	NLQSO	22.0	2.35

Table 8.3. The provisional identification of the six sources identified in the pipeline reduction of the *BeppoSAX* observation of BJS864. For each source, we give the new determination of the *BeppoSAX* centroid position, and the co-ordinates of the corresponding optical counterpart, found through cross-correlation with the *ROSAT* source catalogue. We give the offset between the optical and X-ray positions, d_{ox}, together with the optical identification and redshift, where available. In addition, we list the tentative detection of the Type 2 QSO RXJ 1343.4+0001.

optical counterpart from the *ROSAT* catalogue, where available. We now describe each of the six sources in turn:

SAX864:01 This source corresponds to the brightest source in the *ROSAT* survey, F864X:017, which is a QSO from the Large Bright Quasar Survey (LBQS), at a redshift of $z = 0.244$. This has a *ROSAT* $0.5 - 2$ keV flux of 1.3×10^{-13} erg cm^{-2} s^{-1}, and an optical magnitude of $B = 17.8$ mag. The SAX centroid is $\sim 38''$ away from the *ROSAT* optical position. This source appears extended in the *BeppoSAX* image, which may either be due to the PSF degrading at large radii, or possibly the presence of an additional source, which has blended with the QSO emission.

SAX864:02 The *ROSAT* counterpart to this *BeppoSAX* source is F864X:089, which is $30''$ away. This is identified as a QSO at $z = 2.10$, with an optical magnitude of $B = 22.7$ mag.

SAX864:03 The closest *ROSAT* source is F864X:053, $\sim 88''$ away, which is a $B = 19.8$ mag QSO at redshift $z = 0.804$.

SAX864:04 This source lies outside of the central $20'$ radius of the *ROSAT* image, and therefore has no associated *ROSAT* source or optical identification. A $3' \times 3'$ Digitized Sky Survey image centred on the *BeppoSAX* X-ray centroid is shown in Fig. 8.5(a). There is nothing obvious in the centre of the field, but two bright galaxies lie $\sim 45''$ away, for which we require identifications. In addition, the near infra-red imaging techniques used successfully for the identification of *ASCA* sources, as described in Chapter 5, can be used to select candidates with unusual $B - K$ colours for future optical spectroscopic follow-up.
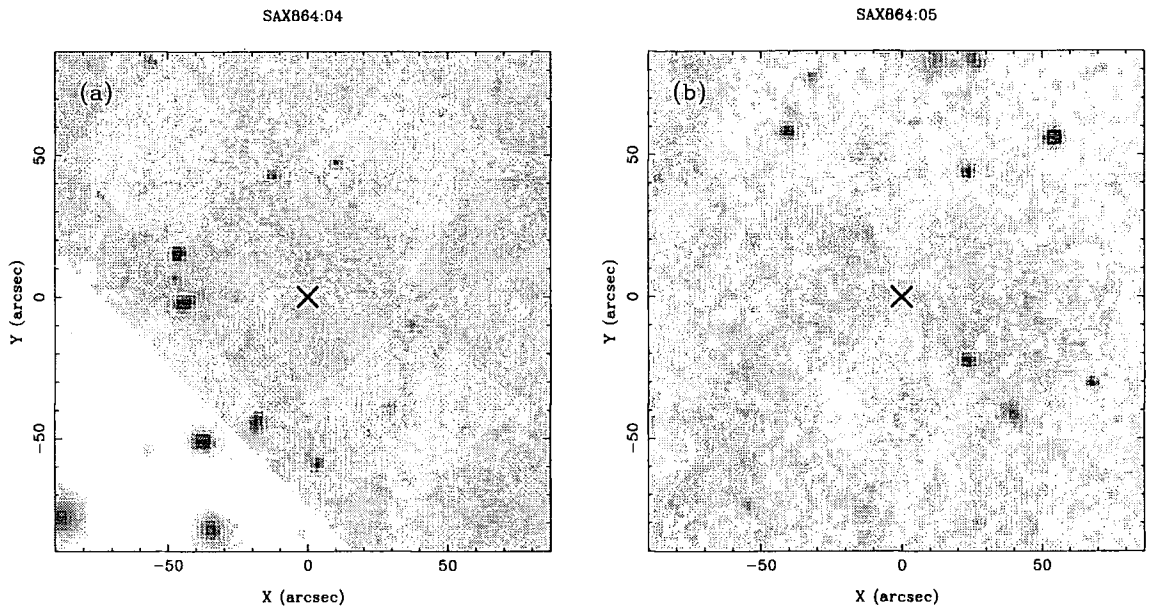
SAX864:04   SAX864:05

Figure 8.5: Digitized Sky Survey images of the X-ray error boxes for *BeppoSAX* sources (a) SAX864:04 and (b) SAX864:05. Each image is $3' \times 3'$, centred on the X-ray centroid.

SAX864:05 The closest *ROSAT* source lies $198''$ away, and has no spectroscopic identification. This source lies close to the edge of the field-of-view in both *ROSAT* and *BeppoSAX* images, which has several implications. Since the PSF deteriorates with off-axis angle, the positions are less well defined towards the edges of the field. However, the sources SAX864:02 and SAX864:03 are at similar off-axis angles, and have optical counterparts within $90''$, and therefore we believe that the positions are fairly accurate. It is therefore unclear as to whether the *ROSAT* source is the true counterpart to the *BeppoSAX* source, or whether a counterpart closer to the *BeppoSAX* position should be sought. A $3' \times 3'$ Digitized Sky Survey image centred on the *BeppoSAX* X-ray centroid is shown in Fig. 8.5(b). Candidates for follow-up spectroscopy will be selected from optical data using the UVX technique, and from near infra-red data by highlighting candidates with particularly red $B - K$ colours.

SAX864:06 The closest *ROSAT* counterparts to this source were F864X:039, which is an absorption-line galaxy at $z = 0.126$, $\sim 190''$ away, and F864X:040, which is a K-type star $112''$ away, neither of which are obvious candidates for the hard X-ray emission. However, this source was found to coincide with a QSO found in the initial optically selected QSO survey in this field, performed by Boyle, Jones & Shanks (1991). This QSO, F864:80, lies at only $77''$ from the *BeppoSAX* centroid, and more remarkably, is a member of the rare class of broad-absorption line BALQSOs. F864:80 has a photographic magnitude of $b_j = 19.64$, and lies at a redshift of $z = 1.511$. However, this source is particularly interesting since it is not detected in the

ROSAT PSPC observation, even at the 3σ level, despite being almost on-axis. This could be due to variability between the epochs of the two observations, since QSOs are known to exhibit both short- and long-term variability (see Mushotzky, Done & Pounds 1993 for a review). Short-term variability has been detected in the light-curves of X-ray selected QSOs from the *ROSAT* Deep Survey (Almaini et al. 1999a). An alternative explanation to the lack of a *ROSAT* detection for this source, is that it has an extremely hard spectrum. BALQSOs are known to have much weaker soft X-ray emission than non-BAL QSOs (Green & Mathur 1996). This gives a complicated picture of this object: a strong hard X-ray source, with little or no soft X-ray emission would imply significant amounts of obscuration. However in the optical spectrum, we can still see broad emission lines of Cɪɪɪ] and Cɪv, although the blue wing of the Cɪv emission line has been destroyed by the presence of a deep absorption line. This object is a prime candidate for our forthcoming follow-up SCUBA observations.

T2QSO For interest, we have marked the fluctuation (number 7) in the *BeppoSAX MECS* image which is closest to the Type 2 QSO RXJ 1343.4+0001, at redshift $z = 2.35$, identified in the Deep *ROSAT* Survey (Almaini et al. 1995; Shanks et al. 1995, 1996). Further work is required, in order to ascertain whether this is a true detection or just a fluctuation where we would hope to see a source.

8.4 Comparison with the *ASCA* data

In Fig. 8.4, we show the *ASCA* image of the field BJS864, also taken in 1998 January. Five sources are detected, numbered 1–5 on the plot, and we refer to them here as $A1–A5$ to distinguish them from the *BeppoSAX* sources. Here we give the optical identification for each *ASCA* source, plus the corresponding *BeppoSAX* source, if present:

$A1$: LBQS QSO at $z = 0.244$ (SAX864:01);

$A2$: A source very close to $A1$, which may be the cause of the extended nature of SAX864:01;

$A3$: The BALQSO at $z = 1.511$ (SAX864:06). The offset between the *ASCA* centroid for $A3$ and the optical position of the BALQSO is $3''$;

$A4$: Lies very close to $A3$ in the *ASCA* image, and does not correspond to any nearby *ROSAT* source. At present, it is not clear whether this pair of sources is due to two individual objects, or is a statistical fluctuation. Further work is required in order to determine whether $A4$ is a true source, a fluctuation, or due to the BALQSO.

*A*5: this source is not detected in the *BeppoSAX* image, probably since it lies underneath the window support structure[2], but when compared with the *ROSAT* catalogue, can be identified as a the source F864X:037 which is a $B = 20.3$ mag QSO at $z = 1.14$;

8.5 Discussion & Preliminary Conclusions

The primary result from the identification of the six sources present in the *BeppoSAX* observation of BJS864 field, is that they are predominantly QSOs. Three out of the six sources are identified as "normal" broad-line QSOs, and are also detected by *ROSAT*. This is a similar result to that obtained from the analysis of the source populations of three deep *ASCA* fields, by Boyle et al. (1998a), in which thirteen out of twenty-six *ASCA* sources were identified as QSOs, having broad emission lines.

In addition, we have detected a broad *absorption*-line QSO, which must either be extremely variable, or have a very hard spectrum, since this is not detected by *ROSAT*, even at the 3σ level. *ASCA* observations of a sample of eight BALQSOs detected only four objects, in exposure times of between 15 and 40 ks (Gallagher et al. 1999). These sources are still extremely weak above 2 keV, and the inferred column densities are very high, $N_H \gtrsim 5 \times 10^{23}\,\mathrm{cm}^{-2}$. Gallagher et al. find no correlation between optical brightness and hard X-ray flux for their sample of BALQSOs, which have optical magnitudes in the range $14.5 < B < 18.5$. This is consistent with the detection of SAX864:06, since at $B = 19.6$ is considerably fainter. It will be extremely interesting in the near future to be able to combine all the available data on this object, obtaining upper limits at soft energies from *ROSAT* and *LECS* data, and fluxes from both the *BeppoSAX* and *ASCA* exposures. In addition, we have been awarded time on the JCMT to make SCUBA sub-mm observations of a sample of candidate obscured AGN, of which this BALQSO is a member.

Of the remaining two sources, one lies outside of the central field-of-view of the *ROSAT* observation, and therefore has no corresponding *ROSAT* source, and the other has no compelling *ROSAT* association to aid the identification process, and therefore optical and infra-red imaging data are required to find suitable candidates for follow-up spectroscopy.

---

[2] The window support structure consists of a circular ring of $\sim 10'$ radius, plus four radial spokes. The four spokes are at angles of $45°$, $135°$, $225°$ and $315°$ from vertical respectively, for the roll angle applied for this observation.

References

Almaini O., Boyle B. J., Griffiths R. E., Shanks T., Stewart G. C., Georgantopoulos I., 1995, MNRAS, 277, L31

Almaini O., Lawrence A., Shanks T., Edge A., 1999a, MNRAS submitted.

Boella G., Butler R. C., Perola G. C., Piro L., Scarsi L., Bleeker J. A. M., 1997, A&AS, 122, 299

Boyle B. J., Georgantopoulos I., Blair A. J., Stewart G. C., Griffiths R. E., Shanks T., Gunn K. F., Almaini O., 1998a, MNRAS, 296, 1

Boyle B. J., Jones L. R., Shanks T., 1991, MNRAS, 251, 482

Gallagher S. C., Brandt W. N., Sambruna R. M., Mathur S., Yamasaki N., 1999, ApJ in press. (astro-ph/9902045)

Green P. J., Mathur S., 1996, ApJ, 462, 637

Mushotzky R. F., Done C., Pounds K. A., 1993, ARA&A, 31, 717

Shanks T. et al., 1996, in Zimmerman U., Truemper J.E., Yorke H., eds, *Roentgenstrahlung from the Universe*, Vol. MPE Report 263, p. 341

Shanks T., Almaini O., Boyle B. J., Done C., Georgantopoulos I., Griffiths R. E., Rawlings S., Stewart G. C., 1995, Spectrum, Newsletter of the Royal Observatories, vol. 7, 7

Shanks T. et al., 1999, in preparation.

Chapter 9

Conclusions

ABSTRACT. In this final Chapter, we summarise the results of this thesis, and discuss the exciting future prospects in this area of research.

In this thesis, we have presented a study of the properties of dust-enshrouded AGN, and their relevance to the X-ray and far infra-red background radiation. A self-consistent model of obscured AGN has been developed, and tested against existing observational constraints in the X-ray, optical and sub-millimetre regimes. Building upon this, a program of varied observations has been undertaken to test further these ideas. Here we present a short summary of the main results. We conclude by discussing the avenues open for the development of this subject in the future.

9.1 Obscured QSO Models for the XRB

We began this work by developing an obscured QSO model for the X-ray emission from obscured AGN, and their total contribution to the X-ray background. Our aim was to determine whether various contradicting observational results could be explained by the presence of selection effects in QSO samples, in particular those of Webster et al. (1995), Boyle & Di Matteo (1995) and Madau, Ghisellini & Fabian (1994). We tested obscured AGN models containing populations of sources with a wide range of intrinsic absorbing columns, and found that a simple prescription involving a flat distribution of column densities in the range $N_H \sim 10^{19.5} - 10^{25.5}$ was found to provide a good fit to the source counts both at soft and hard X-ray energies. This model was also found to be consistent with the observed spectral shape and intensity of the X-ray background radiation.

The advantages of our model over previous work is that the obscured QSO framework naturally incorporates the X-ray luminous galaxies detected in faint *ROSAT* surveys (Roche et al. 1995; Griffiths et al. 1996; McHardy et al. 1998). These galaxies define the faint end of the X-ray luminosity function from AGN, with modest obscuring columns of order $N_H < 10^{22}\,\mathrm{cm}^{-2}$. These

results apply in a low-density universe, with QSO luminosity evolution prescribed by a power-law dependence on redshift, $L_X \propto (1 + z)^\gamma$, up to some maximum redshift. In high density universes, the contribution from models using a flat column distribution to the source counts and XRB intensity is much lower, by a factor of about a third. It is necessary to tilt the column distribution to include a larger number of highly obscured sources in order to remain consistent with the observations.

9.1.1 Selection Effects in QSO Surveys

Our models have shown that obscured QSOs may outnumber unobscured QSOs by at least a factor of four to one. Thus there may be significant numbers of highly absorbed sources, releasing enormous amounts of energy via accretion, which have remained undetected in optical and soft X-ray surveys. Future hard X-ray surveys will provide further constraints on the numbers of such sources, with the measurement of source counts down to flux levels comparable to, or fainter than, those currently possible at soft X-ray energies, and the subsequent follow-up programs will identify the source populations which dominate at these faint fluxes.

We next used our obscured QSO model to investigate the presence of selection effects in both optical and X-ray QSO surveys, and find that the tight correlation between X-ray and optical luminosities may not necessarily preclude the existence of a large population of obscured QSOs. The effects of photo-electric absorption of X-rays by gas, and extinction in the optical from dust associated with the gas, combine to produce the observed narrow X-ray to optical relationship. At near infra-red wavelengths, where the effect of dust obscuration is less pronounced, we have shown that although we predict a very tight relation between X-ray and $K-$ band flux as a function of redshift, the range in $B - K$ colours of obscured AGN is still very broad, in agreement with observation.

The numbers of moderately obscured, low luminosity X-ray galaxies predicted by our models are in approximate agreement with the numbers of low redshift X-ray galaxies that are observed over a wide range of fluxes. A further consequence of the obscured AGN model is that a proportion of blank field X-ray sources are also predicted, which will be undetectable in CCD images. These are predominantly high redshift sources with a relatively large column ($N_H \sim 10^{22}\,\mathrm{cm^{-2}}$), still detectable in the X-ray, but with more than ten magnitudes of $B-$ band absorption. For current *ASCA* and *BeppoSAX* hard X-ray surveys, ($S > 5 \times 10^{-14}\,\mathrm{erg\,cm^{-2}\,s^{-1}}$, $B < 22.5\,\mathrm{mag}$), we predict that ~ 25 per cent of X-ray sources are blank fields, in agreement with observations. These sources are expected to lie at redshifts $z > 1.0$.

At the depths attainable by forthcoming *AXAF* surveys, we predict that obscured QSOs at $z > 1$ will constitute ~ 50 per cent of the total $0.4 - 6\,\text{keV}$ source counts, which in the optical will appear as blank fields with no broad emission line objects visible at $B \lesssim 24.5\,\text{mag}$. Tests of our obscured AGN model will come in the form of the deep survey data required for the *AXAF* source identification process, both in the optical using new large format CCD cameras, such as the Isaac Newton Telescope Wide Field Camera (Walton et al. 1998), and in the near infra-red, using the CIRSI (Beckett et al. 1997) and Omega-Prime cameras. The information derived in this way will provide the data against which to compare our predicted source counts and relative fractions of broad-line QSOs, narrow-line galaxies and blank fields at faint, hard X-ray fluxes. Since these deep surveys will be detecting large numbers of dust-enshrouded sources at high redshifts, then both radio and sub-mm data will be invaluable in cases where the obscuration is sufficient to obliterate any evidence of AGN activity in the optical and near infra-red.

9.1.2 Sub-mm & FIR predictions of Obscured AGN Models

An important consequence of our dust-enshrouded QSO model is the re-radiation at far infra-red wavelengths of the energy absorbed by the obscuring medium. Enormous quantities of X-ray, ultra-violet and optical photons are reprocessed in this way, leading to high far infra-red luminosities. Thus strong constraints on our model can be provided by observations in the part of the electro-magnetic spectrum dominated by thermal emission from dust.

We have modelled the properties of the obscuring medium in the dust-enshrouded AGN population using a distribution of column densities consistent with X-ray and optical observations, and predicted the sub-millimetre source counts expected. By making various assumptions, such as the temperature and the covering factor of the dust, the redshift distribution of the sources, etc., we have also estimated the maximum contribution that obscured AGN could make to the intensity of the far infra-red background (FIRB). We find that obscured AGN can provide up to thirty per cent of the sub-mm source counts and FIRB intensity at 850μm, when assuming more extreme parameters, such as a low dust temperature of $30\,\text{K}$, and a maximum redshift of $z \sim 10$, with a more conservative value of approximately ten per cent. Obscured QSOs account for a smaller fraction of the FIRB at 100μm due to the assumed spectrum. Nevertheless, this is a non-negligible fraction of the 850μm sub-mm population, and needs to be accounted for when using sub-mm data to derive the star-formation history of the Universe. Our predictions are in good agreement with the fraction of sub-mm sources identified with AGN in the latest surveys, and also with the fact that the complementary (and perhaps dominant) population in such surveys is found

to be starburst galaxies. The starburst and AGN phenomena are not mutually exclusive, and are highly likely to co-exist in a number of these sources, if only because stars are required to make dust. In addition, obscured populations of AGN may provide suitable candidates for the source of the sub-mm emission associated with extremely red objects (EROs; Hu & Ridgway 1994), which are a class of infra-red selected obscured galaxies. We have also made predictions of the expected redshift distribution of obscured AGN from our models, which can be tested when large completely identified samples of sub-mm sources become available.

The populations in our models contributing the largest fraction to the sub-mm source counts have the highest obscuring columns, and therefore are the hardest to detect in almost all other wavebands. Fortunately, the same k-correction effect which aids the detection of sub-mm sources out to extremely high redshifts, also acts in our favour for obscured sources in the hard X-ray regime (although this effect is not nearly as great as in the sub-mm where the k-correction is enough to compensate for cosmological dimming). At low redshift, even $2 - 10$ keV photons are severely attenuated by absorption, and it is difficult to detect highly obscured QSOs, apart from in scattered light. But at high redshift, the unabsorbed part of the spectrum is redshifted into the hard X-ray passband, increasing the chances of detection. The combination of *AXAF* hard X-ray and SCUBA sub-mm data will provide strong tests of the model predictions of the fraction of obscured QSOs, as well as giving insight into the nature of the sub-mm population. In this way, it will be possible to determine the extent of the obscured QSO contribution to cosmological backgrounds at both high and low energies.

9.2 An Observational Search for Obscured AGN

Having modelled the properties of populations of obscured AGN as a whole and compared these to existing datasets, we then undertook a program of observations designed to search for evidence of AGN activity responsible for the observed X-ray emission in samples of *ROSAT* and *ASCA* galaxies and QSOs.

9.2.1 Near infra-red imaging of X-ray sources

Our first project searched for counterparts to X-ray sources with unusual optical/near infra-red colours consistent with being point sources, which were previously undetected in the optical, in order to test for the presence of dust obscuration. To do this, we used IRIS on the AAT to take K–band images of three samples of X-ray sources, including *ROSAT* and *ASCA* X-ray luminous

galaxies and hard spectrum X-ray sources. Evidence of obscured activity has been discovered, in the form of red $B - K$ colours and the presence of unresolved counterparts to the X-ray sources.

From the results of these observations, we have proposed a scenario in which the X-ray emission from all faint *ROSAT* galaxies is due to AGN activity. This includes both comparatively unobscured QSOs, which have steep X-ray spectra and blue $B - K$ colours, and highly absorbed sources which have very hard X-ray spectra and red $B - K$ colours. The hypothesis that the $B - K$ colour of the optical counterpart appears to correlate with the hardness ratio of the *ROSAT* spectrum has been tested to see whether the observed sources fit into this framework. We find that the majority of sources are consistent with this hypothesis.

IRIS imaging to search for objects with unusual colours was also used as an effective method for reducing the number of candidates for optical follow-up spectroscopy of *ASCA* sources, for which the positional accuracy is not well constrained in the absence of an associated *ROSAT* source. In this way, we have identified six sources for subsequent LDSS observations, from which we were able to obtain spectroscopic classifications.

9.2.2 Near infra-red spectroscopy of X-ray luminous galaxies

Spectral observations in the near infra-red also provide tests of our model, by searching for broad emission lines from obscured AGN, which would be invisible in the optical. Hence, the second project used CGS4 on UKIRT to take K-band spectra of X-ray luminous *ROSAT* galaxies to search for the presence of broad Pa_α emission, which would be indicative of obscured AGN activity. We succeeded in possibly detecting one modestly broad line (FWHM $\sim 2000\,\mathrm{km\,s^{-1}}$) out of six galaxies observed. This is not inconsistent with the presence of obscured AGN in these galaxies, as this method is only sensitive to quite a narrow range of absorbing columns. For low columns, broad lines will be visible even at optical wavelengths, whereas for high columns, no broad components will be visible even in the infra-red. Similar observations of an X-ray luminous galaxy, F864X:052, revealed the presence of the coronal emission line [Si VI], which can only be produced in conditions of the intense radiation field surrounding an AGN, thereby providing firm evidence for an AGN origin for the emission in X-ray luminous galaxies.

9.2.3 Far infra-red photometry of X-ray luminous galaxies and QSOs

Moving into the far infra-red, our model can be tested by looking for thermal emission from dust re-radiating energy absorbed from higher energies. The third project therefore involves *ISOPHOT* observations searching for thermal emission in samples of *ROSAT* galaxies and QSOs, which

would indicate the presence of obscuring material, as predicted by our dust-enshrouded AGN model. The first sample included nineteen galaxies and one cluster, of which six were detected above a significance of 2.5σ in at least one waveband, all of which were narrow emission-line galaxies. Broadly speaking, these galaxies were found to be at the brighter end of the sample, and tended to have harder *ROSAT* spectra, consistent with the expected properties of obscured AGN. The second sample contained both unobscured QSOs, two at low ($z \sim 1$) and four at high ($z \sim 2$) redshifts, and an obscured Type 2 QSO at $z = 2.35$. Of these, the Type 2 QSO and a low redshift QSO are detected, from which it is too early to infer whether we can yet discriminate between the Unified Model of AGN, in which the properties of both Type 1 and Type 2 objects should be similar at long wavelengths, and a more isotropic geometry for the obscuring material, in which the optical properties are independent of viewing angle.

The *ISO* detection of $\sim 100\mu$m flux in two narrow-line galaxies for which there is conclusive proof of AGN activity via variability analysis (GSGP4X:091) and the detection of high ionization lines (F864X:052), confirms that there exists a significant population of obscured QSOs as invoked earlier to explain the origin of the X-ray background. These two objects in particular, when combined with the detection of the Type 2 QSO at high redshift, are almost certainly the first sightings of a hitherto undetected population of obscured QSOs, which are predicted to dominate the hard X-ray source populations at faint fluxes and contribute a significant fraction of the X-ray and far infra-red backgrounds. These observations herald the likely discovery of a massive population of dust-enshrouded AGN, which will be uncovered using the more sensitive X-ray, infra-red and sub-mm detectors in the future.

9.2.4 Summary

We therefore conclude that infra-red observations from $2 - 1000\mu$m support the hypothesis that the X-ray emission in a significant fraction of the faint galaxies detected in deep *ROSAT* surveys is due to the presence of AGN activity, in many cases obscured by large quantities of dust.

Although several other galaxies show no evidence of AGN activity, these tend to be fainter and have flatter X-ray spectra, and therefore may be so heavily obscured that they are invisible even in the near infra-red. These objects may be best detected in deeper far infra-red observations, aimed at detecting their dust emission. These sources are also expected to be strong sources at hard X-ray energies.

In at least two cases, the presence of AGN activity can be inferred in individual narrow-line galaxies from the detection of variability in the X-ray light-curve, or from near infra-red detec-

tions of broad or high ionization emission lines. These galaxies are also detected by *ISO*, which combined with these other observations, tends to support the presence of a significant population of obscured AGN.

9.3 Future Prospects

The most exciting new development in the very short-term, is the forthcoming launch of both the *AXAF* and *XMM* X-ray satellites. These have complementary capabilities, with *AXAF* providing the equivalent of the *Hubble Space Telescope* for X-ray astronomy, with arcsecond resolution possible over a wide field-of-view, and sensitive to very faint fluxes. *XMM* has an extremely large collecting area, and energy sensitive CCD detectors, enabling high resolution of very faint sources, with spatial resolution comparable to the *ROSAT HRI*. The source identification process will be performed using deep optical and near infra-red imaging data to select candidates for spectroscopic follow-up. This will be a much easier task that previously, due to the high spatial resolution of the X-ray telescopes. Full advantage can then be taken of the multiplexing capabilities of 8-m class telescopes, to obtain spectroscopic classification of the faint source populations expected.

Although on a longer time-scale, proposed satellite-borne telescopes, such as the optical/near infra-red Next Generation Space Telescope (NGST; Mather, Seery & Bely 1996) and the far infra-red *SIRTF* (Werner 1998) and *FIRST* (Pilbratt 1993; Genzel 1997), will revolutionise our knowledge of the FIR properties of galaxies and QSOs, from the optical all the way to $\sim 600\mu$m. Combining the information to be gained from these facilities at both near and far infra-red and X-ray energies, will determine the relative contributions from AGN and star-formation activity in samples of objects selected in both regimes. Complementary observational programs such as these are vital, due to the interconnected nature of the source populations contributing to the source counts and background intensities at both X-ray and FIR energies.

We therefore conclude that a multi-wavelength approach is vital in order to test the predictions of the obscured AGN model. In the short term, we are planning sub-mm observations of a sample of *ROSAT*, *ASCA* and *BeppoSAX* sources using SCUBA on the JCMT. We hope to determine whether both obscured and unobscured QSOs contain significant quantities of dust. We also aim to ascertain whether these X-ray luminous galaxies are powered by AGN activity, by detecting the thermal emission from dust enshrouding the nucleus. The joint interpretation of these various datasets will enable a much clearer picture to emerge as to the energetics of X-ray luminous galaxies and QSOs, and their contribution to the X-ray and far infra-red backgrounds.

References

Beckett M. G., Mackay C. D., MCMahon R. G., Parry I. R., Piche F., Ellis R. S., 1997, SPIE Proc., 2871, 1152

Boyle B. J., Di Matteo T., 1995, MNRAS, 277, L63

Genzel R., 1997, in ASP Conf. Series 124: *Diffuse Infrared Radiation and the IRTS*, San Fransisco, p. 465

Griffiths R. E., Della Ceca R., Georgantopoulos I., Boyle B. J., Stewart G. C., Shanks T., Fruscione A., 1996, MNRAS, 281, 71

Hu E. M., Ridgway S. E., 1994, AJ, 107, 1303

Madau P., Ghisellini G., Fabian A., 1994, MNRAS, 270, L17

Mather J. C., Seery B. D., Bely P. Y., 1996, SPIE Proc., 2807, 98

McHardy I. M. et al., 1998, MNRAS, 295, 641

Pilbratt G., 1993, Advances in Space Research, 13, 912

Roche N., Shanks T., Georgantopoulos I., Stewart G. C., Boyle B. J., Griffiths R. E., 1995, MNRAS, 273, L15

Walton N. A., Bunclark P. S., Fisher M. P., Gribbin F. J., Jones E. L., Rees P. C., Rixon G. T., 1998, SPIE Proc., 3351, 197

Webster R. L., Francis P. J., Peterson B. A., Drinkwater M. J., Masci F. J., 1995, Nat, 375, 469

Werner M. W., 1998, American Astronomical Society Meeting, 193, 2502

Bibliography

References

Allen C. W., 1973, *Astrophysical Quantities*. The Athalone Press

Allen D. A., 1992, *IRIS Reduction Guide*. Anglo-Australian Observatory User Manual 30b

Allen D. A., 1993, *IRIS Users' Guide*. Anglo-Australian Observatory User Manual 30a

Allen D. A. et al., 1993, PASA, 10, 298

Almaini O., 1999c, private communication.

Almaini O., Boyle B. J., Griffiths R. E., Shanks T., Stewart G. C., Georgantopoulos I., 1995, MNRAS, 277, L31

Almaini O., Gunn K. F., Shanks T., Boyle B. J., Georgantopoulos I., Stewart G. C., Griffiths R. E., 1999b, in preparation.

Almaini O., Lawrence A., Shanks T., Edge A., 1999a, MNRAS submitted.

Almaini O., Shanks T., Boyle B. J., Griffiths R. E., Roche N., Stewart G. C., Georgantopoulos I., 1996, MNRAS, 282, 295

Almaini O., Shanks T., Griffiths R. E., Boyle B. J., Roche N., Georgantopoulos I., Stewart G. C., 1997, MNRAS, 291, 372

Almaini O., Shanks T., Gunn K. F., Boyle B. J., Georgantopoulos I., Griffiths R. E., Stewart G. C., Blair A. J., 1998, Astronomische Nachrichten, 319, 55

Altieri B. et al., 1999, A&AL, 343, L65

Antonucci R., 1993, ARA&A, 31, 473

Antonucci R. R. J., Miller J. S., 1985, ApJ, 297, 621

Aragon-Salamanca A., Baugh C. M., Kauffmann G., 1998, MNRAS, 297, 427

Arnaud K. A., 1996, in Jocoby G.H., Barnes J., eds, *Proc. of the ADASS V Conference*: ASP Conf. Series 101: San Francisco, Vol. 5, p. 17

Barber C. R., Roberts T. P., Warwick R. S., 1996, MNRAS, 282, 157

Barger A. J., Cowie L. L., Sanders D. B., Fulton E., Taniguchi Y., Sato Y., Kawara K., Okuda H., 1998, Nat, 394, 248

Barger A. J., Cowie L. L., Smail I., Ivison R. J., Blain A. W., Kneib J. P., 1999, AJ submitted.

Barvainis R., 1993, ApJ, 412, 513

Beckett M. G., Mackay C. D., MCMahon R. G., Parry I. R., Piche F., Ellis R. S., 1997, SPIE Proc., 2871, 1152

Bell E. F., 1999, private communication.

Benford D. J., Cox P., Omont A., Phillips T. G., 1998, AAS Meeting, 192, 1104

Benford D. J., Cox P., Omont A., Phillips T. G., McMahon R. G., 1999, ApJL accepted. (astro-ph/9904277)

Bennett C. L. et al., 1997, American Astronomical Society Meeting, 191, 8701

Blain A. W., Ivison R. J., Smail I., 1998, MNRAS, 296, L29

Blain A. W., Kneib J. P., Ivison R. J., Smail I., 1999b, in preparation.

Boella G., Butler R. C., Perola G. C., Piro L., Scarsi L., Bleeker J. A. M., 1997, A&AS, 122, 299

Boksenberg A., Carswell R. F., Allen D. A., Fosbury R. A. E., Penston M. V., Sargent W. L. W., 1977, MNRAS, 178, 451

Booth R., 1997, *Future Large Scale Facilities in Astronomy*, IAU Symposia, 9, E8

Bower R. G. et al., 1996, MNRAS, 281, 59

Boyle B. J., Almaini O., Georgantopoulos I., Blair A. J., Stewart G. C., Griffiths R. E., Shanks T., Gunn K. F., 1998b, MNRAS, 297, L53

Boyle B. J., Di Matteo T., 1995, MNRAS, 277, L63

Boyle B. J., Fong R., Shanks T., Clowes R. G., 1985, MNRAS, 216, 623

Boyle B. J., Fong R., Shanks T., Peterson B. A., 1990, MNRAS, 243, 1

Boyle B. J., Georgantopoulos I., Blair A. J., Stewart G. C., Griffiths R. E., Shanks T., Gunn K. F., Almaini O., 1998a, MNRAS, 296, 1

Boyle B. J. et al., 1999, in preparation.

Boyle B. J., Griffiths R. E., Shanks T., Stewart G. C., Georgantopoulos I., 1993, MNRAS, 260, 49

Boyle B. J., Jones L. R., Shanks T., 1991, MNRAS, 251, 482

Boyle B. J., Shanks T., Georgantopoulos I., Stewart G. C., Griffiths R. E., 1994, MNRAS, 271, 639

Boyle B. J., Wilkes B. J., Elvis M., 1997, MNRAS, 285, 511

Brown R. L., 1996, American Astronomical Society Meeting, 188, 4601

Burrows D. N., Mendenhall J. A., 1991, Nat, 351, 629

Butcher J. A. et al., 1997, MNRAS, 291, 437

Carilli C. L., Yun M. S., 1999, ApJL, 513, L13

Carter B., Meadows V., 1995, MNRAS, 276, 734

Chapman S. C., Scott D., Lewis G. F., Borys C., Fahlman G. G., 1999, MNRAS submitted. (astro-ph/9810444)

Cimatti A., Bianchi S., Ferrara A., Giovanardi C., 1997, MNRAS, 290, L43

Comastri A., Setti G., Zamorani G., Hasinger G., 1995, A&A, 296, 1

Croom S. M., 1997, PhD Thesis, University of Durham.

Croom S. M., 1999, private communication.

David L. P., Jones C., Forman W., 1992, ApJ, 388, 82

De Zotti G., Boldt E. A., Marshall F. E., Swank J. H., Szymkowiak A. E., Cavaliere A., Danese L., Franceschini A., 1982, ApJ, 253, 47

Dey A., Graham J. R., Ivison R. J., Smail I., Wright G. S., Liu M., 1999, ApJ accepted. (astro-ph/9902044)

Di Matteo T., Esin A., Fabian A. C., Narayan R., 1999, MNRAS submitted. (astro-ph/9812134)

Di Matteo T., Fabian A. C., Rees M. J., Carilli C. L., Ivison R. J., 1998, MNRAS submitted. (astro-ph/9807245)

Done C., Madejski G. M., Smith D. A., 1996, ApJL, 463, L63

Downes D., Solomon P. M., 1998, ApJ, 507, 615

Dunne L., Eales S., 1999, in preparation.

Eales S., Lilly S., Gear W., Dunne L., Bond J. R., Hammer F., Le Fevre O., Crampton D., 1998, ApJL submitted. (astro-ph/9808040)

Efstathiou G., Rees M. J., 1988, MNRAS, 230, 5P

Elvis M. et al., 1994, ApJS, 95, 1

Esin A. A., McClintock J. E., Narayan R., 1997, ApJ, 489, 865

Fabian A. C., Barcons X., 1992, ARA&A, 30, 429

Fabian A. C., Barcons X., Almaini O., Iwasawa K., 1998, MNRAS, 297, L11

Fabian A. C., Iwasawa K., 1999, MNRAS, 303, L34

Fan X., Strauss M., SDSS Collaboration , 1998, *SDSS Press Release*

Fixsen D. J., Dwek E., Mather J. C., Bennett C. L., Shafer R. A., 1998, ApJ, 508, 123

Franceschini A., Vercellone S., Fabian A. C., 1998, MNRAS, 297, 817

Francis P. J., 1993, ApJ, 407, 519

Frayer D. T. et al., 1999, ApJL, 514, L13

Frayer D. T., Ivison R. J., Scoville N. Z., Yun M. S., Evans A. S., Smail I., Blain A. W., Kneib J. P., 1998, ApJL, 506, L7

Gabriel C., Acosta-Pulido J., Heinrichsen I., 1998, in Albrecht R., Hook R.N., Bushouse H.A., eds, *Proc. of the ADASS VII Conference*: ASP Conf. Series 145: San Francisco, Vol. 7, p. 165

Gabriel C., Acosta-Pulido J., Heinrichsen I., Morris H., Tai W. M., 1997, in Hunt G., Payne H.E., eds, *Proc. of the ADASS VI Conference*: ASP Conf. Series 125: San Francisco, Vol. 6, p. 108

Gallagher S. C., Brandt W. N., Sambruna R. M., Mathur S., Yamasaki N., 1999, ApJ in press. (astro-ph/9902045)

Gear W. K., Cunningham C. R., 1994, SPIE Proc., 2198, 613

Gendreau K., Yaqoob T., Mushotzky R., Fabian A., 1995a, American Astronomical Society Meeting, 187, 5007

Gendreau K. C. et al., 1995b, PASJ, 47, L5

Genzel R., 1997, in ASP Conf. Series 124: *Diffuse Infrared Radiation and the IRTS*, San Fransisco, p. 465

Genzel R. et al., 1998, ApJ, 498, 579

Georgantopoulos I., Almaini O., Shanks T., Stewart G. C., Griffiths R. E., Boyle B. J., Gunn K. F., 1999, MNRAS, 305, 125

Georgantopoulos I., Stewart G. C., Blair A. J., Shanks T., Griffiths R. E., Boyle B. J., Almaini O., Roche N., 1997, MNRAS, 291, 203

Georgantopoulos I., Stewart G. C., Shanks T., Boyle B. J., Griffiths R. E., 1996, MNRAS, 280, 276

Georgantopoulos I., Stewart G. C., Shanks T., Griffiths R. E., Boyle B. J., 1993, MNRAS, 262, 619

Giacconi R., Gursky H., Paolini F., Rossi B., 1962, Phys.Rev.Letters, 9, 439

Giommi P., Fiore F., Ricci D., Molendi S., Maccarone M. C., Comastri A., 1998, Nucl. Phys. Proc. Suppl., 69, 591

Goodrich R. W., Miller J. S., Martel A., Cohen M. H., Tran H. D., Ogle P. M., Vermeulen R. C., 1996, ApJL, 456, L9

Granato G. L., Danese L., Franceschini A., 1997, ApJ, 486, 147

Green P. J., Mathur S., 1996, ApJ, 462, 637

Green P. J. et al., 1995, ApJ, 450, 51

Greenhill L. J., Gwinn C. R., Antonucci R., Barvainis R., 1996, ApJL, 472, L21

Greenhill L. J., Jiang D. R., Moran J. M., Reid M. J., Lo K. Y., Claussen M. J., 1995, ApJ, 440, 619

Griffiths R. E., Della Ceca R., Georgantopoulos I., Boyle B. J., Stewart G. C., Shanks T., Fruscione A., 1996, MNRAS, 281, 71

Griffiths R. E. et al., 1983, ApJ, 269, 375

Griffiths R. E. et al., 1999, in preparation.

Griffiths R. E., Padovani P., 1990, ApJ, 360, 483

Gruber D. E., 1992, in Barcons X., Fabian A.C., eds, *The X-ray Background*, p. 44

Gunn K., Shanks T., 1998, Astronomische Nachrichten, 319, 66

Gunn K., Shanks T., 1999a, Advances in Space Research, in press.

Gunn K., Shanks T., 1999b, MNRAS submitted.

Haas M., Chini R., Meisenheimer K., Stickel M., Lemke D., Klaas U., Kreysa E., 1998, ApJL, 503, L109

Hasinger G., Burg R., Giacconi R., Schmidt M., Trümper J., Zamorani G., 1998, A&A, 329, 482

Hauser M. G. et al., 1998, ApJ, 508, 25

Hewett P. C., Foltz C. B., Chaffee F. H., Francis P. J., Weymann R. J., Morris S. L., Anderson S. F., Macalpine G. M., 1991, AJ, 101, 1121

Hines D. C., 1998, American Astronomical Society Meeting, 193, 2704

Hines D. C., Schmidt G. D., Smith P. S., Cutri R. M., Low F. J., 1995, ApJL, 450, L1

Holland W. S. et al., 1999, MNRAS, 303, 659

Horne K., 1986, PASP, 98, 609

Howarth I. D., 1983, MNRAS, 203, 301

Hu E. M., Ridgway S. E., 1994, AJ, 107, 1303

Hughes D. H. et al., 1998a, Nat, 394, 241

Hughes D. H., Dunlop J. S., Archibald E. N., Rawlings S., 1998b, in *The Birth of Galaxies*: Xth Rencontres de Blois. (astro-ph/9810253)

Inoue H., Kii T., Ogasaka Y., Takahashi T., Ueda Y., 1996, in Zimmerman U., Truemper J.E., Yorke H., eds, *Roentgenstrahlung from the Universe*, Vol. MPE Report 263, p. 323

Ishiguro M., 1996, IAU Symposia, 170, 239

Ivison R. J., Smail I., Blain A. W., Kneib J. P., 1999, in preparation.

Ivison R. J., Smail I., Le Borgne J. F., Blain A. W., Kneib J. P., Bezecourt J., Kerr T. H., Davies J. K., 1998, MNRAS, 298, 583

Iwasawa K., Fabian A. C., Brandt W. N., Crawford C. S., Almaini O., 1997, MNRAS, 291, L17

Jannuzi B. T., Elston R., Schmidt G. D., Smith P. S., Stockman H. S., 1994, ApJL, 429, L49

Jones L. R., Fong R., Shanks T., Ellis R. S., Peterson B. A., 1991, MNRAS, 249, 481

Kay L. E., Moran E. C., 1998, PASP, 110, 1003

Kessler M. F. et al., 1996, A&A, 315, L27

Kim D. W., Elvis M., 1999, ApJ accepted. (astro-ph/9811406)

Lagache G., 1998, in *Wide Field Surveys in Cosmology*, 14th IAP meeting, Editions Frontieres, p. 301

Laor A., Fiore F., Elvis M., Wilkes B. J., McDowell J. C., 1997, ApJ, 477, 93

Laureijs R. J., Klaas U., Lemke D., Herbstmeier U., Abraham P., 1996, Addendum to *ISOPHOT* Observer's Manual. *ISOPHOT* Consortium

Lawrence A., Papadakis I., 1993, ApJL, 414, L85

Lawrence A. et al., 1993, MNRAS, 260, 28

Lawrence C. R., Lange A. E., 1997, American Astronomical Society Meeting, 191, 4120

Lemke D. et al., 1996, A&A, 315, L64

Lewis G. F., Chapman S. C., Ibata R. A., Irwin M. J., Totten E. J., 1998, ApJL, 505, L1

Lipari S., Terlevich R., Macchetto F., 1993, ApJ, 406, 451

Madau P., Ferguson H. C., Dickinson M. E., Giavalisco M., Steidel C. C., Fruchter A., 1996, MNRAS, 283, 1388

Madau P., Ghisellini G., Fabian A., 1994, MNRAS, 270, L17

Malkan M. A., Stecker F. W., 1998, ApJ, 496, 13

Masci F., Webster R., Francis P., 1998, MNRAS, 301, 975

Mather J. C. et al., 1994, ApJ, 420, 439

Mather J. C. et al., 1990, ApJL, 354, L37

Mather J. C., Seery B. D., Bely P. Y., 1996, SPIE Proc., 2807, 98

Matt G., Fabian A. C., 1994, MNRAS, 267, 187

McHardy I. M. et al., 1998, MNRAS, 295, 641

McLeod K. K., Rieke G. H., 1994a, ApJ, 420, 58

McLeod K. K., Rieke G. H., 1994b, ApJ, 431, 137

McLeod K. K., Rieke G. H., 1995, ApJ, 441, 96

Metcalfe N., Shanks T., Fong R., Roche N., 1995, MNRAS, 273, 257

Meurer G. R., Heckman T. M., Lehnert M. D., Leitherer C., Lowenthal J., 1997, AJ, 114, 54

Miller J. S., Goodrich R. W., 1990, ApJ, 355, 456

Moritz P., Wennmacher A., Herbstmeier U., Mebold U., Egger R., Snowden S. L., 1998, A&A, 336, 682

Morris S. L., Weymann R. J., Anderson S. F., Hewett P. C., Francis P. J., Foltz C. B., Chaffee F. H., Macalpine G. M., 1991, AJ, 102, 1627

Morrison R., McCammon D., 1983, ApJ, 270, 119

Murayama T., Taniguchi Y., 1998, ApJL, 497, L9

Mushotzky R. F., Done C., Pounds K. A., 1993, ARA&A, 31, 717

Nandra K., Pounds K. A., 1994, MNRAS, 268, 405

Narayan R., Mahadevan R., Quataert E., 1998, *The Theory of Black Hole Accretion Discs*. Cambridge University Press

Neugebauer G., Green R. F., Matthews K., Schmidt M., Soifer B. T., Bennett J., 1987, ApJS, 63, 615

Ohta K., Yamada T., Nakanishi K., Ogasaka Y., Kii T., Hayashida K., 1996, ApJL, 458, L57

Oliver S. et al., 1998, in *Wide Field Surveys in Cosmology*, 14th IAP meeting, Editions Frontieres, p. 165

Omont A., McMahon R. G., Cox P., Kreysa E., Bergeron J., Pajot F., Storrie-Lombardi L. J., 1996, A&A, 315, 1

Osterbrock D. E., 1989, *Astrophysics of gaseous nebulae and active galactic nuclei*. University Science Books, University of Minnesota, Mill Valley, CA.

Penzias A. A., Wilson R. W., 1965, ApJ, 142, 419

Piccinotti G., Mushotzky R. F., Boldt E. A., Holt S. S., Marshall F. E., Serlemitsos P. J., Shafer R. A., 1982, ApJ, 253, 485

Pier E. A., Krolik J. H., 1992, ApJ, 401, 99

Pilbratt G., 1993, Advances in Space Research, 13, 912

Primini F. A., Murray S. S., Huchra J., Schild R., Burg R., Giacconi R., 1991, ApJ, 374, 440

Puget J. L., Abergel A., Bernard J. P., Boulanger F., Burton W. B., Desert F. X., Hartmann D., 1996, A&A, 308, L5

Puxley P. J., Sylvester J., Pickup D. A., Paterson M. J., Laird D. C., Atad-Ettedgui E. I., 1994, SPIE Proc., 2198, 350

Richards E. A., 1999, ApJL, 513, L9

Rigopoulou D., Lawrence A., Rowan-Robinson M., 1996, MNRAS, 278, 1049

Roche N., Griffiths R. E., Della Ceca R., Shanks T., Boyle B. J., Georgantopoulos I., Stewart G. C., 1996, MNRAS, 282, 820

Roche N., Shanks T., Almaini O., Boyle B. J., Georgantopoulos I., Stewart G. C., Griffiths R. E., 1995a, MNRAS, 276, 706

Roche N., Shanks T., Georgantopoulos I., Stewart G. C., Boyle B. J., Griffiths R. E., 1995b, MNRAS, 273, L15

Romero-Colmenero E., Branduardi-Raymont G., Carrera F. J., Jones L. R., Mason K. O., McHardy I. M., Mittaz J. P. D., 1996, MNRAS, 282, 94

Sanders D. B., Phinney E. S., Neugebauer G., Soifer B. T., Matthews K., 1989, ApJ, 347, 29

Schlegel D. J., Finkbeiner D. P., Davis M., 1998, ApJ, 500, 525

Schmidt M., Green R. F., 1983, ApJ, 269, 352

Schmidt M. et al., 1998, A&A, 329, 495

Schmitt J. H. M. M., Snowden S. L., Aschenbach B., Hasinger G., Pfeffermann E., Predehl P., Trümper J., 1991, Nat, 349, 583

Schwartz D., Gursky H., 1974, in *X-ray Astronomy*, eds. Giacconi R., Gursky H.; Reidel, Dordrecht; Astrophysics and Space Science Library. Volume 43, p, 359

Seaton M. J., 1979, MNRAS, 187, 73P

Shanks T. et al., 1996, in Zimmerman U., Truemper J.E., Yorke H., eds, *Roentgenstrahlung from the Universe*, Vol. MPE Report 263, p. 341

Shanks T., Almaini O., Boyle B. J., Done C., Georgantopoulos I., Griffiths R. E., Rawlings S., Stewart G. C., 1995, Spectrum, Newsletter of the Royal Observatories, vol. 7, 7

Shanks T., Fong R., Green M. R., Clowes R. G., Savage A., 1983, MNRAS, 203, 181

Shanks T., Georgantopoulos I., Stewart G. C., Pounds K. A., Boyle B. J., Griffiths R. E., 1991, Nat, 353, 315

Shanks T. et al., 1999, in preparation.

Sharples R., Gray P., Hatzidimitriou D., 1991, *Autofib Manual*. Anglo-Australian Observatory User Manual 26

Shaver P. A., Wall J. V., Kellermann K. I., Jackson C. A., Hawkins M. R. S., 1996, Nat, 384, 439

Smail I., Ivison R. J., Blain A. W., 1997, ApJL, 490, L5

Smail I., Ivison R. J., Blain A. W., Kneib J. P., 1998, in *After the dark ages: when galaxies were young (the Universe at* $2 < z < 5$*).* (astro-ph/9810281)

Smail I., Ivison R. J., Cowie L. L., Blain A. W., Kneib J. P., Barger A. J., 1999, ApJL in preparation.

Snowden S. L. et al., 1995, ApJ, 454, 643

Soifer B. T., Neugebauer G., Oke J. B., Matthews K., 1981, ApJ, 243, 369

Sprayberry D., Foltz C. B., 1992, ApJ, 390, 39

Stecker F. W., De Jager O. C., 1997, in De Jager, O.C., ed, *Proc. Kruger National Park Intl. Workshop on TeV Gamma-Ray Astrophysics,* (Space Research Unit Potchefstroom U.), p. 39

Steidel C. C., Adelberger K. L., Giavalisco M., Dickinson M., Pettini M., 1999, ApJ submitted. (astro-ph/9811399)

Stocke J. T., Liebert J., Gioia I. M., Maccacaro T., Griffiths R. E., Danziger I. J., Kunth D., Lub J., 1983, ApJ, 273, 458

Stocke J. T., Morris S. L., Gioia I. M., Maccacaro T., Schild R., Wolter A., Fleming T. A., Henry J. P., 1991, ApJS, 76, 813

Tanaka Y., Inoue H., Holt S. S., 1994, PASJ, 46, L37

Tananbaum H. et al., 1979, ApJL, 234, L9

Terlevich R., Tenorio-Tagle G., Franco J., Melnick J., 1992, MNRAS, 255, 713

Trümper J., 1982, Advances in Space Research, 2, 241

Trümper J., 1990, in *High resolution X-ray spectroscopy of cosmic plasmas,* Cambridge University Press, p. 291

Veilleux S., Osterbrock D. E., 1987, ApJS, 63, 295

Veron-Cetty M. P., Veron P., 1996, European Southern Observatory Scientific Report, 17, 1

Walton N. A., Bunclark P. S., Fisher M. P., Gribbin F. J., Jones E. L., Rees P. C., Rixon G. T., 1998, SPIE Proc., 3351, 197

Ward M. J., Done C., Fabian A. C., Tennant A. F., Shafer R. A., 1988, ApJ, 324, 767

Warren S. J., 1999, in preparation.

Webster R. L., Francis P. J., Peterson B. A., Drinkwater M. J., Masci F. J., 1995, Nat, 375, 469

Weinberg S., 1972, *Gravitation and cosmology: Principles and applications of the general theory of relativity.* New York: Wiley

Werner M. W., 1998, American Astronomical Society Meeting, 193, 2502

White N. E., Nagase F., Parmer A. N., 1995, in Lewin W. H. G., van Paradijs J., van den Heuvel E., eds, *X–Ray Binaries,* Cambridge: Cambridge Univ. Press, p. 1

White N. E., Swank J. H., Holt S. S., 1983, ApJ, 270, 711

Wright G. S., 1994, Experimental Astronomy, 3, 17

Yaqoob T., McKernan B., Ptak A., Nandra K., Serlemitsos P. J., 1997, ApJL, 490, L25

Yuan W., Brinkmann W., Siebert J., Voges W., 1998a, A&A, 330, 108

Yuan W., Siebert J., Brinkmann W., 1998b, A&A, 334, 498

Zheng W., Kriss G. A., Telfer R. C., Grimes J. P., Davidsen A. F., 1997, ApJ, 475, 469

Zombeck M. V., 1990, *Handbook of Space Astronomy & Astrophysics, 2nd edition.* Cambridge University Press